

無穩定構型蛋白質之摺疊、聚集與分子間交互作用

計畫類別： 個別型計畫  整合型計畫

計畫編號：NSC 97-2112-M-009-009-MY3

執行期間：97年08月01日至100年07月31日

執行機構及系所：國立交通大學生物科技學系

計畫主持人：張家靖

計畫參與人員：鄭財木、朱學亮、李星原、李子正、周靖淳、楊瑤貞、姜芳馨、  
張毓娟、陳虹璋、鍾偉賢、何昌翰、阮泓翔、曾憲儀

成果報告類型(依經費核定清單規定繳交)： 精簡報告  完整報告

本計畫除繳交成果報告外，另須繳交以下出國心得報告：

- 赴國外出差或研習心得報告
- 赴大陸地區出差或研習心得報告
- 出席國際學術會議心得報告
- 國際合作研究計畫國外研究報告

處理方式：除列管計畫及下列情形者外，得立即公開查詢

涉及專利或其他智慧財產權， 一年  二年後可公開查詢

中 華 民 國 100 年 10 月 15 日

目錄:	頁數
中文摘要	3
英文摘要	4
關鍵詞	4
<b>Part I: Folding of Human Intrinsic Disorder Proteins: Cyclin I and Securin</b>	
Abstract	5
Introduction	5
Material and Method	7
Results and discussion	10
Conclusion	12
Acknowledgments	12
References	13
Figure legends	14
Figures	15
<b>Part II: Structure and function restoration of intrinsically disordered protein human cyclin I (ceni)</b>	
Abstract	22
Keywords	22
Introduction	22
Material and Method	23
Results	26
Discussion	28
Acknowledgments	29
References	30
Table	32
Figure legends	33
Figures	34
<b>Part-III: Protein aggregation: competition reactions between self-stabilization and diffusion limited aggregation in solution</b>	
Abstract	42
Keywords	42
Introduction	43
Experimental section	44
Results	48
Discussion	50
Conclusion	53
Acknowledgments	53
References	54
Figure legends	56
Figures	57
附件	65

## 中文摘要

無穩定構型蛋白質(Intrinsically disordered protein, IDP)為蛋白質交互作用網絡之核心。然而其穩定予否則端賴其是否摺疊正確。本研究發現 IDP 摺疊仍依循著蛋白質摺疊似一階態轉變(first order-like state transition)模型。此外透過量測 IDP 之 Raman 與螢光光譜於摺疊中間體之變化解析，進一步驗證 IDP 之聚集沉澱符合摺疊與擴散速率限制聚集(diffusion limited aggregation)相拮抗之模型。相關研究“金屬硫蛋白與銅離子鍵結之水溶液構型解析”(IDP 之摺疊)，“heat shock protein 60 分子聚集之分析”(蛋白質-蛋白質交互作用)與“Haptoglobin Phenotypes 分子聚集之分析”(蛋白質-蛋白質交互作用)等論文分別已發表於 Biophysical Journal，Biochemistry Biophysics Research Communication 與 Nanotechnology 等知名生物物理與奈米科技之學術期刊中。另有“IDPs: cyclin I 與 securin 之摺疊研究”，“cyclin I 與 p21 分子間交互作用與功能之關聯”及“蛋白質摺疊與聚集之關聯”等論文已送交國際期刊發表審查中。

此外本實驗室運用摺疊完成之蛋白質與奈米鑽石相結合，產生高度生物相容且可偵測之單分子複合體。此一系列之成果為奈米科技應用於生物領域開啟新頁。為此本研究之相關成果分別發表於 Applied Physics Letters，Nanotechnology 與論文專書“Nanodiamonds: Applications in Biology and Nanoscale Medicine”中。當我們成功的完成蛋白質摺疊之反應我們發現倘若將蛋白質摺疊所需之變因如金屬離子等加以改變，則可合成出新功能之奈米生物材料此一成果發表於論文專書“Handbook of Nanophysics: Nanoelectronics and Nanophotonics”。相同的生物巨分子 DNA 於自組織之過程使其參雜  $Ni^{2+}$  將形成具半導體特性之新穎一維奈米生物材料 Ni-DNA。此一材料具有室溫下負微分電阻之特性，若搭配半導體製成將可為未來生物材料半導體元件，開創出一展新的領域。此一系列之研究為 Nanothechnology, Applied Physics Letters, 與 Biophysical Journal 所接受發表。其中送審論文將分部份臚列於本報告中。

## **Abstract:**

Intrinsically disordered protein (IDP) plays a vital role in the networks of protein-protein interactions. However, their stabilities rely on the process of folding. In this study, the folding reaction of IDPs are consistent with the “first order-like phase transition model”. By using Raman and fluorescence spectroscopy analysis of their folding intermediates, the reactions for protein folding and diffusion limited aggregation are competing with each other during the folding process. At the same time the related research achievements such as “Solution structure of Cu-chelated Metallothioneins” (MT is an IDP), “Characterizing the polymeric status of heat shock protein 60” (protein-protein interactions) and “Haptoglobin Phenotypes studies” (protein-protein interactions) are published in world renowned biophysical and nanotechnology related journals “Biophysical Journal”, “Biochemistry Biophysics Research Communication and Nanotechnology. At the same time, the research papers about, “IDPs: cyclin I and securin folding study”, “intermolecular interactions and function analysis between cyclin I and p21” and “Relationship between protein folding and aggregations” have been submitted to international Journals for publish.

Moreover, we have generated a biocompatible nanoparticle complex by combining the folded protein and nanodiamond and this complex can be monitored at the single molecular level. These achievements play important role in bio-nanotechnology research. These studies have been published in “Applied Physics Letters”, “Nanotechnology” and the book chapters in “Nanodiamonds: Applications in Biology and Nanoscale Medicine”, during the granted years. We found that the folding of protein may be affected by metal ions chelation and we can create a novel functional nanobiomaterials, this achievement has been published as a chapter in “Handbook of Nanophysics: Nanoelectronics and Nanophotonics”. Besides the protein, we also found that we can operate the DNA self-assembly process and add the Ni ions into the base-pairs of DNA as a Ni-DNA. This Ni-DNA acts like a semiconductor and can be used as novel nano-wire. Furthermore, this biomaterials possess the negative differential resistance property at room temperature. This bio-nano-wire can be used for biomaterial based semiconductor devices. These serials studies have been published in Nanotechnology, Applied Physics Letters, and Biophysical Journal, during the granted years. All submitted papers will be described following.

## **關鍵詞 (keywords)**

Intrinsic disordered protein, cyclin I, securing, over critical folding process, first order-like state transition

## **Part I: Folding of Human Intrinsic Disorder Proteins: Cyclin I and Securin**

### **Abstract**

Unlike regular protein, an intrinsic disordered protein possesses its function without stable tertiary structure; human cyclin I (Ccn1) and securin (PTTG1) are two cases of intrinsic disordered proteins. Both proteins were found in inclusion body of *E. coli*, a recombinant expression system. It is intriguing to know the common folding motif of these proteins. In this study, we found that the recombinant proteins can be folded continuously by an over critical folding process (on-path folding process). These proteins aggregated under off-path folding process. Differential scanning micro-calorimeter analysis indicated that both recombinant cyclin I and securin are intrinsic disordered proteins. However, the circular dichroism spectra denoted that cyclin I is a helical structure major protein; the securing contains no secondary structure at all. Functional analysis indicated that the folded cyclin I can directly bind with p21<sup>cip1/waf1</sup> under the condition with calcium ion and securing can bind with p53. Fluorescence spectra of both proteins indicate that both proteins possess tight hydrophobic core which can not be completely unwound in denaturing environment. Meanwhile, fluorescence spectra of folding intermediates of both proteins indicate that these hydrophobic motifs can be restored by an over critical folding process. These results prove that we have folded these intrinsic disordered proteins into their active form. Meanwhile, the hydrophobic motif may be the only or most important motif of intrinsic disordered protein.

### **Introduction**

Intrinsic disordered proteins are characterized by its flexible and dynamic tertiary structure even secondary structure [1]. In the recently years, the intrinsic disordered protein was found in cell signaling proteins and transcription factors [2], the large flexible regions in this class of proteins may have an advantage over fully folded proteins that can allow them to make more efficient physical functional interactions with their target partners, which may represent a mechanism for regulation of cellular processes [3, 4].

The biological functions of intrinsic disordered protein under physiological condition are interesting. Include the well-ordered conformation in a protein may no longer be required for functioning, and conformational flexibility in intrinsic disordered proteins may serve as specific functions [5, 6]. In some studies have suggested that the conformational flexibility in intrinsic disordered proteins under physiological conditions might allow them to interact with several different targets for specific functions [5, 7]. The

phenomenon indicates that the simple mechanism can regulate several cellular processes such as transcription and cell cycle control by the intrinsic disordered protein binding with other specific targets [8-10]. The intrinsic disordered proteins have an advantage in interacting with different target in response to inter and intra cellular environment to own different functions [11]. The structure characters are suitable for the environment in the different part of cell. Human securin [12] and cyclin I are intrinsic disordered protein and has been demonstrated the securin is a multifunction protein [13-17]. Over-expression of human securin protein (Pituitary tumor-transforming gene, PTTG1) has been reported in a variety of endocrine-related and nonendocrine-related tumors, including pituitary, thyroid, breast, ovarian, and uterine tumors, central nervous system, pulmonary system, and gastrointestinal system[18-24]. The expression level of securin protein corresponded with tumor invasion[25].

In the cell cycle progress, securin can bind to separase and inhibit the separation of sister chromatin. Securin is the target of the anaphase promoting complex (APC) and would be degradation before entering anaphase by polyubiquitinated which depended on the destruction sequences[26]. Expect the cell cycle regulation, securin involved in DNA damage repair[17], metabolism[27].

The functions of cyclin I protein are not clear expect of it can stabilize p21 [28] and active cdk5 [29] to avoid cell apoptosis. Cyclins, are famous cell cycle regulation family. Cyclins are regulatory subunits of cyclin dependent kinases (CDKs)[30]. The Cyclin-CDK complexes regulate cell mitosis[31]. The cyclins would be degraded at the end of each cell cycle stage via the ubiquitin system[32]. Cyclin I (Ccn1) contains a typical cyclin box at its N-terminal and it is similar to the ones of cyclin G and E. Meanwhile, it contains PEST sequences at its C-terminal. Unlike other cyclins, cyclin I's expression level is high in post-mitotic tissues, including heart, brain, and skeletal muscle, and it is expressed constantly during cell cycle progression. Therefore, the functions of cyclin I may be independent on the cell cycle [33]. However, cyclin I is expressed in human breast cancer and closely associated with VEGF and KDR expression[34] and protects podocytes to apoptosis by stabilization of p21[28]. It indicated that the function of cyclin I may be activated by interacting with other regulatory proteins

To understand the structure prosperity of intrinsic disordered protein, we use over critical folding method [35-38] to fold recombinant securin and cyclin I protein. By stepwise thermal equipment dialysis, we can analysis the structure change during folding process by analysis the folding intermediate.

We have demonstrated securin and cyclin I were native intrinsic disordered proteins by DSC measurement. The secondary structure of securin protein is not regular but in the cyclin I is helix major, it indicates the disordered tertiary structure may compose of regular or non-regular secondary structure. Moreover, the binding of cyclin I and p21 need calcium ion also showed that the functions of cyclin I protein is environment depend in the cell, especially during early apoptosis signal present. In this paper, we will discuss the function and structure relationship of securin and cyclin I protein, and demonstrate that the cyclin I stabilize p21 by directly binding.

## **Material and Method**

### **Cloning and expression of recombinant human cyclin I and securin**

The cDNA of cyclin I and securin were cloned from A549 cell line using the polymerase chain reaction (PCR) with

cyclin I forward (5'-CATATGAAGTTTCCAGGGCCTT-3'),

cyclin I reversed (5'-TGAAACTACATGACAGAAACAGG-3'),

securin forward (5'-CACCCATATGGCTACTCTGATCTATGTT-3'),

and securin reversed (5'-ATTTAAATATCTATGTCACAGCA-3') primers.

The PCR product of cyclin I was added an A in the 3' end by tag polymerase and then ligated into yTA vector. Digested yTA-cyclin I plasmid by Nde I and ligated the product into pET30a (Novagen, Darmstadt, Germany) vector. The securin PCR product was purified and ligated into pET200 vector. These plasmids were transformed into BL21(DE3).

The expression of securin and cyclin I were induced by 1mM IPTG at 37 °C for 16 h. The cells were broken by pressure (French-Press, Constant Systems [LTD](#), UK) and total cell lysate was washed with ddH<sub>2</sub>O then centrifuged at 15,000 g for 5minutes until the supernatant become clear. The inclusion body was obtained.

### **The folding process of cyclin I and securin**

Dissolved securin and cyclin I proteins in the denature buffer, vortex at 4°C overnight until the solution become clear. Filtered the solution by 0.22 µm filter to obtain the denatured protein. To avoid the protein aggregates in the folding process. The over critical folding method was used. All processes were in the 4°C.

### **Fluoresce intensity analysis indicated the folding stages**

Fluorescence of securin and cyclin I proteins in each folding intermediates U-M<sub>5</sub> (0.2 mg/mL) have been analysis. Fluorescence spectra were recorded in a Hitachi F-7000 fluorescence spectrophotometer (Hitachi, Tokyo, JP), using 1 cm square cuvettes thermostated at 25 °C. The protein solutions were excited at 280 nm, scan rate as 2400nm/minute, PMT value as 700V, excitation and emission slit was 10nm, and the emission was recorded at angle 90° to the excitation with a 2-nm bandwidth in the range 250-500 nm.

### **The CD spectra detect the secondary structure ratio**

CD spectra in UV region (260 – 200 nm) of U and M<sub>1-5</sub> were collected by Jasco J 720C spectropolarimeter (Jasco, Tokyo, JP) at 20°C. A 0.1 cm-light-path cuvette was used to reduce the light scattering. The CD spectrum was measured for each sample diluted with corresponding folding buffer and adjusted the concentration to 0.2mg/ml. Scanning speeds are 200 nm/min, data collected by 0.5nm/ point. The secondary structures were analyzed by the SELCON3 program.

### **Using DSC to measurement the tertiary structure stability**

N-DSC II (CSC, USA) interfaced with the computer equipped with an automatic data collection program was used for the experiments on thermal stability investigation of cyclin I and securin. Each solution of cyclin I and securin intermediates in corresponding folding buffer was adjusted to 2mg/ml. All samples were filtered and degassed under vacuum for 10-15 min with gentle stirring before being placed into cell. DSC experiments were performed at constant pressure 4 atm in order to avoid bubble formation. The temperature of samples was increasing with the constant scanning rate which was equal to 0.5 °C /min. The temperature range from 15 °C up to 95 °C.

### **The particle size analysis by DLS**

Dynamic light scattering (DLS) measurements were made using a goniometer from Brookhaven Instruments Corp. (BIC, Holtsville, NY) equipped with a diode-pumped laser (Coherent, Inc., U.S.) with a wavelength  $\lambda=532.15$  nm and power of 10 mW. The scattered light was collected at an angle 90°. The chamber temperature was controlled by water circulator. The autocorrelation function was computed using a digital correlator (BI9000), then analyzed with the non-negatively constructed least-squares (NNLS) method. The instrument performance was calibrated by measuring the DLS of standard suspensions of polystyrene beads ( $R_H = 68$  nm) (Polysciences, Warrington, PA). The correlation function obtained in DLS experiment as describe previously. The concentration of securin and cyclin I protein are 2 mg/ml, and all experiments were

conducted at 20 °C.

### **Analysis of protein interaction by far Western blot technique**

Recombinant securin and p53 (cyclin I and p21) were denatured and resolved on a 12 % SDS PAGE, then electrophoretically (100 V for 90 min. at 4°C) transferred to the a poly(vinylidene difluoride) membrane. The proteins were refolded by subsequent changing buffers from folding buffer 1 to 5. The membrane was washed twice in each buffer during 5 min and then incubated in blocking solution (10 mM Tris·HCl/100 mM NaCl/0.1% Tween-20, 5% non fat milk, pH= 8) for 30 min. at room temperature. The position of recombinant securin on the membrane was detected by mouse anti securin antibody (Santa Cruz, USA) that was recognized by goat anti mouse antibody. Supersignal West Pico Chemiluminescent Substrate (Pierce, Rockford, IL, USA) was used in order to enhance the chemiluminescence signal.

### **Isothermal titration calorimetry (ITC)**

The 2277 Thermal Activity Monitor (TAM, ThermoMetric AB, Sweden) has been used in order to determine the equilibrium constant  $K_a$  and reaction enthalpy  $\Delta H$  for binding p21 with cyclin I in the presence of calcium  $Ca^{2+}$  and for securin binding with p53. TAM utilizes the heat flow principle, where heat produced in a thermally-defined vessel flows away to establish thermal equilibrium with its surroundings. The sample was placed into the reaction measuring vessel which was surrounded by water thermostat for achievement thermal stability. The temperature in the thermostat was maintained constant to within  $\pm 2 \times 10^{-4}$  °C. Before escaping to the heat sink, heat from the sample was channeled through the Peltier elements acted as a thermoelectric generator.

The cyclin I (securin) solution in Tris buffer (10 mM, pH=8.8) with the volume of 2.8 ml and the protein concentration of 10  $\mu$ M was placed into the measuring vessel and titrated by addition of drops of p21 (p53) solution step by step with interval between two consecutive portions of 15 min. The volume of one portion of injected p21 solution with concentration 300  $\mu$ M was 10  $\mu$ l. The injection rate was 1  $\mu$ l/sec. Finally 200  $\mu$ l of p21 solution was added into the measuring vessel. The temperature of 25 °C was maintained during whole experiment. In order to clarify the role of calcium  $Ca^{2+}$  for p21 binding with cyclin I the same experiments was performed in the absence and in the presence of 1 $\mu$ M calcium chloride.

## **Results and discussion**

### **Pure and high yield recombinant protein can be obtained in the prokaryote expression system**

In the prokaryote expression system, the protein can be obtained in two major ways- soluble protein and inclusion body. The soluble proteins are usually called native form because the conformations of soluble proteins were approached to the lowest energy state in the native environment. In the inclusion body, the proteins were aggregation because the hydrophobic force and/or disulfide mis-linked. The induced proteins in inclusion body are higher yield and purity than proteins in the soluble form. We use over critical dialysis method to overcome the challenge that fold proteins from inclusion body to native state,.

We express the cyclin I and securin in the inclusion body by IPTG induction 16 hours (Fig. 1). The securin protein was obtained from inclusion body and purified by His-tag column after folding procedure. In the cyclin I protein, the high purity (>95%) and high yield (>200mg / L) cyclin I protein was obtained directly in the inclusion body. The securin and cyclin I proteins were identified by western blot and mass (data not show).

### **The hydrophobic core collapse during folding process**

The aromatic amino acids are more hydrophobic than hydrophilic in the water environment. When the protein in the native environment, the aromatic amino acids were form hydrophobic core by hydrophobic force to resistant the hydrophilic environment. The fluorescent will have higher intensity and blue shift when the hydrophobic core was getting more stable. During folding process, the hydrophobic core of protein would collapse and enhance the fluoresce intensity when excitation wavelength at 280nm. In the securin protein (Fig. 2 B), the highest fluoresce emission wavelength is observed in U (349nm). And the fluoresce emission wavelength was reduced following the folding process (M1 (347nm)=M2 (347nm)>M3 (345nm)>M4 (341nm)=M5 (341nm)). The fluoresce intensity are M5 (71a.u.)>M4 (69a.u.)>M3 (66a.u.)>M2 (51a.u.)>M1 (49a.u.)>U (11a.u.). All data indicated that the hydrophobic core of securin is getting more stable following folding procedure and approach to native form. The cyclin I protein (Fig 2 A) has the same phenomenon and indicated the hydrophobic core of cyclin I were also getting stable following the folding procedure.

### **The secondary structure analysis in the securin and cyclin I protein**

The secondary structure or protein is determined by its sequences. In the native environment, the protein

secondary structure is one feature to understand the protein conformation. In the folding process, each intermediate was adjusted to 0.2mg/ml and analysis its secondary structure composition by CD[39, 40] and analysis by SELCON3 program [41]. In the securin (Fig. 3 D), the highest helix ratio is present in the M2 (H (r)=23.1%, H (d)=18.2%) and sheet ratio in the M1 (S (r)=27.7%, S (d)=13.6%). But the ratio of random coil is the highest structure in each intermediate (U=54.9%, M1=48.8%, M2=42.6, M3=60.7%, M4=63.5%, M5=62.6%). This result indicated that the secondary structure of securin protein is flexible in the folding process and even in the native buffer. The cyclin I reveals opposite phenomenon (Fig. 3 C), all intermediates are helix major (H (r)=56%, H (d)=21%) and small amount of random coil (20%).

### **The tertiary structure stability measurement by DSC**

The thermal stability of folded cyclin I protein (M<sub>5</sub>) was investigated at 10mM tris buffer with different ions (Ca<sup>2+</sup>, Zn<sup>2+</sup>). The securin protein is in the same buffer condition except ions. The DSC profile in the securin and cyclin I in different ion condition showed no significant phase transition point. It indicated the securin and cyclin I have no stable tertiary structure. Lysozyme, a standard sample in the DSC experiment, as a positive control, showed the transition temperature at 77 °C in the M<sub>5</sub> buffer. Compare with lysozyme, securin, and cyclin I, the data indicated that the securin and cyclin I are intrinsic disordered proteins.

### **Particle size determine by DLS**

Dynamic light scattering (DLS) measurements were made on all folding intermediates of cyclin I and securin. When protein folding, the amino acid would form its unique secondary structure, tertiary structure, and even quaternary structure. With its structure formation, the protein would be more compact and reduce its size by intermolecular interaction. The protein size of folding intermediates is uniformity and single distribution, indicated that the folding process has reached an equilibrium state and the state of the protein is in a monomeric state. The hydrodynamic diameter ( $R_H$ ) of are reduced during folding pathway in securin and cyclin I and securin (Fig 4). This is consistent with the protein collapse model. Interesting, the M<sub>5</sub> of cyclin I protein with calcium is smaller than others. It indicates that the cyclin I protein will be more stable in the calcium environment.

### **Functional analysis in the folded recombinant protein**

We use far Western blot to analysis the activity of refolded recombinant protein. In Western blot, recombinant p53 can not be recognized by securin antibody. In the far Western blot, the protein had transfer

on the PVDF membrane after separated by SDS-PAGE. Refold the denatured protein on the membrane by modification TED method. Hybridize the membrane with refolded recombinant securin. The securin antibody then can recognize the securin protein in the p53 site because the securin has bind to p53. The BSA is negative control (Fig. 5).

## **Conclusion**

The protein expression and purification are basic and difficult part in the protein experiment. In the prokaryote expression system, the high purity and yield of securin and cyclin I protein can be obtained.

In the protein folding, three major tools would be used to detect the accuracy of folding process, hydrophobic core collapse detected by fluoresce, secondary structure analysis by CD, and amino acids reshuffled by NMR or crystallization. In the intrinsic disordered protein, it's hard to define the folding states by the crystallization or NMR because they do not have stable tertiary even secondary structure. We use far western blot and ITC to demonstrate the folded intrinsic disordered proteins are in the native state. The cyclin I and securin without clear phase transition when heating by DSC reveal they do not have stable tertiary structures. Interesting, in the CD analysis, the two intrinsic disordered proteins present signification difference in the secondary structure component. Cyclin I is helix major protein which similar to another cyclin family members but the securin protein is radon coli major structure. It reveals that the secondary structure of intrinsic disordered protein may not correspond with it tertiary structure. The helix of cyclin I protein was formed in the early stage and kept during folding process, but the most stable hydrophobic core of cyclin I was showed at final stage, similar with securin. The particle size of cyclin I and securin protein are reduced following the folding process. In the nature environments, the protein conformation would approach to the lowest energy state. The particle size of protein is also an indicator to survey the energy state of protein. Usually, the smaller size of protein in the nature environment indicates the lower energy state it is. The data of DLS is corresponded to the fluorescence result. Indicates the hydrophobic core and particle size may be an important indicator of intrinsic disordered protein folding.

## **Acknowledgements**

This project was supported by an NSC Grant (97-2112-M-009-009-YM3).

## References

- [1] A. K. Dunker *et al.*, *Journal of Molecular Graphics and Modelling* **19**, 26 (2001).
- [2] J. Liu *et al.*, *Biochemistry* **45**, 6873 (2006).
- [3] A. S. Garza, N. Ahmad, and R. Kumar, *Life Sciences* **84**, 189 (2009).
- [4] A. K. Dunker *et al.*, *Biochemistry* **41**, 6573 (2002).
- [5] C. J. O. A. K. D. Vladimir N. Uversky, *Journal of Molecular Recognition* **18**, 343 (2005).
- [6] H. J. Dyson, and P. E. Wright, *Nat Rev Mol Cell Biol* **6**, 197 (2005).
- [7] A. K. Dunker, and V. N. Uversky, *Nat Chem Biol* **4**, 229 (2008).
- [8] R. Kumar *et al.*, *Biochemistry* **43**, 3008 (2004).
- [9] D. D. Gajinder Pal Singh, *Proteins: Structure, Function, and Bioinformatics* **68**, 602 (2007).
- [10] I. J. McEwan *et al.*, *Biochemistry* **35**, 9584 (1996).
- [11] K. Sugase, H. J. Dyson, and P. E. Wright, *Nature* **447**, 1021 (2007).
- [12] V. Csizmok *et al.*, *Journal of the American Chemical Society* **130**, 16873 (2008).
- [13] H. Zou *et al.*, *Science* **285**, 418 (1999).
- [14] Y. Zhou *et al.*, *J. Biol. Chem.* **278**, 462 (2003).
- [15] F. Romero *et al.*, *Mol. Cell. Biol.* **24**, 2720 (2004).
- [16] L. Christopoulou, J. D. Moore, and C. Tyler-Smith, *Cancer Letters* **202**, 213 (2003).
- [17] F. Romero *et al.*, *Nucl. Acids Res.* **29**, 1300 (2001).
- [18] X. Zhang *et al.*, *J Clin Endocrinol Metab* **84**, 761 (1999).
- [19] A. P. Heaney *et al.*, *J Clin Endocrinol Metab* **86**, 5025 (2001).
- [20] C. Solbach *et al.*, *The Breast* **13**, 80 (2004).
- [21] R. Puri *et al.*, *Cancer Letters* **163**, 131 (2001).
- [22] S.-J. Tsai *et al.*, *J Clin Endocrinol Metab* **90**, 3715 (2005).
- [23] K. Chamaon *et al.*, *Biochemical and Biophysical Research Communications* **331**, 86 (2005).
- [24] A. P. Heaney *et al.*, *The Lancet* **355**, 716 (2000).
- [25] S. Ogbagabriel *et al.*, *Mod Pathol* **18**, 985 (2005).
- [26] Y. Mitsuhiro, *Genes to Cells* **5**, 1 (2000).
- [27] Z. Wang, R. Yu, and S. Melmed, *Mol Endocrinol* **15**, 1870 (2001).
- [28] S. V. Griffin *et al.*, *J. Biol. Chem.* **281**, 28048 (2006).
- [29] P. T. Brinkkoetter *et al.*, *The Journal of Clinical Investigation* **119**, 3089 (2009).
- [30] L. Hengst *et al.*, *Proceedings of the National Academy of Sciences of the United States of America* **91**, 5291 (1994).
- [31] G. Draetta, and D. Beach, *Cell* **54**, 17 (1988).
- [32] M. Glotzer, A. W. Murray, and M. W. Kirschner, *Nature* **349**, 132 (1991).
- [33] T. Nakamura *et al.*, *Experimental Cell Research* **221**, 534 (1995).
- [34] G. Landberg *et al.*, *Breast Cancer Research and Treatment* **89**, 313 (2005).
- [35] C.-C. Chang *et al.*, *Physical Review E* **70**, 011904 (2004).
- [36] Y.-L. Liu *et al.*, *Biochemical and Biophysical Research Communications* **306**, 59 (2003).
- [37] K.-J. Chang *et al.*, *The American Journal of Emergency Medicine* **21**, 247 (2003).
- [38] C.-C. Chang *et al.*, *Physical Review E* **66**, 021903 (2002).
- [39] B. A. W. Lee Whitmore, *Biopolymers* **89**, 392 (2008).

[40] N. J. Greenfield, Nat. Protocols **1**, 2876 (2007).

[41] J. Lees *et al.*, BMC Bioinformatics **7**, 507 (2006).

Figure legends:

Fig. 1 S=Supernatant I=Inclusion Body. The target proteins were expressed in the inclusion body.

Fig. 2 Fluorescence spectra of different intermediates of cyclin I (*A*) and securin (*B*) refolded in Tris buffer at 25 °C. The solid, dash, dot, dash dot, dash dot dot, and short dash lines are represented the spectra of cyclin I in the states U, M<sub>1</sub>, M<sub>2</sub>, M<sub>3</sub>, M<sub>4</sub> and M<sub>5</sub>, respectively.

Fig. 3 Circular dichroism profiles of cyclin I (*A*) and securin (*B*) intermediates during Tris refold buffer process at 20 °C. The solid, dash, dot, dash dot, dash dot dot, and short dash lines are represented the spectra of cyclin I in the states U, M<sub>1</sub>, M<sub>2</sub>, M<sub>3</sub>, M<sub>4</sub> and M<sub>5</sub>, respectively. Due to the high absorption background of urea in UV range the signal-to-noise ration is very low when the wavelength is lower than 220 nm of U, and is therefore not shown.

The CD profiles analysis by SELCON3 of folding intermediates of cyclin I (*C*) and securin (*D*) in Tris folding buffer. =M<sub>1</sub>; =M<sub>2</sub>; =M<sub>3</sub>; =M<sub>4</sub>; =M<sub>5</sub>, respectively.

Fig. 4 Secruin protein is analysis in the tris buffer.

Fig. 5 p53-securin and p21-cyclin I interaction were analyzed by Far Western blot. The securin antibody can't recognize the p53 protein. After incubate with securin protein, the securin antibody can recognize the securin signal which binding with p53 protein (*A*).

**Fig 1**

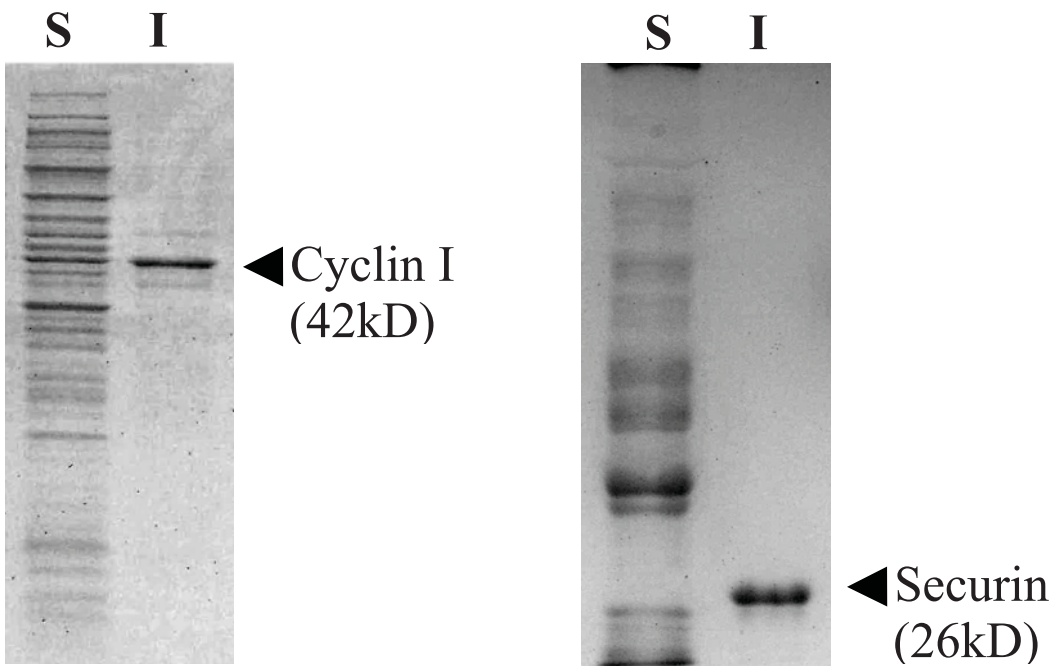


Fig 2

(A)

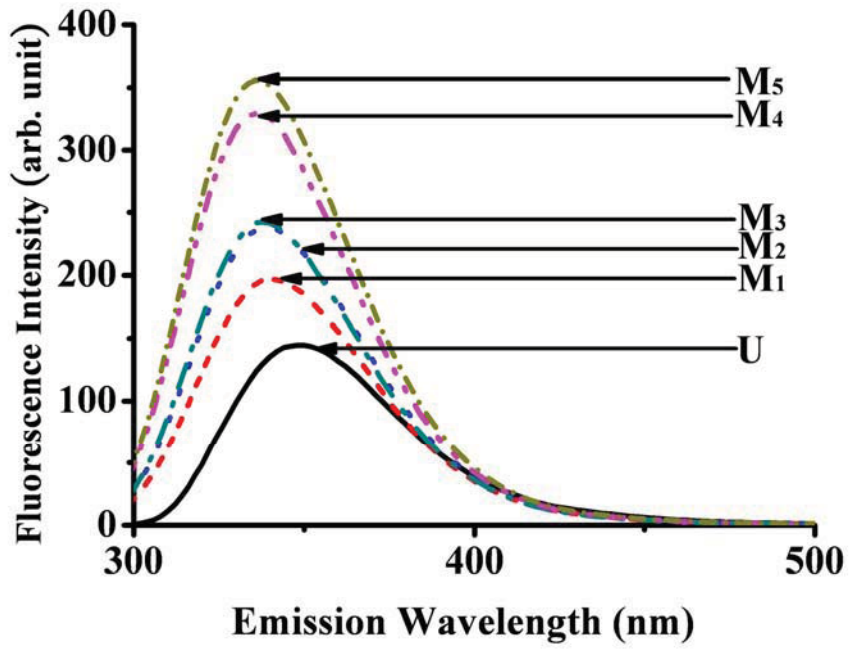


Fig 2

(B)

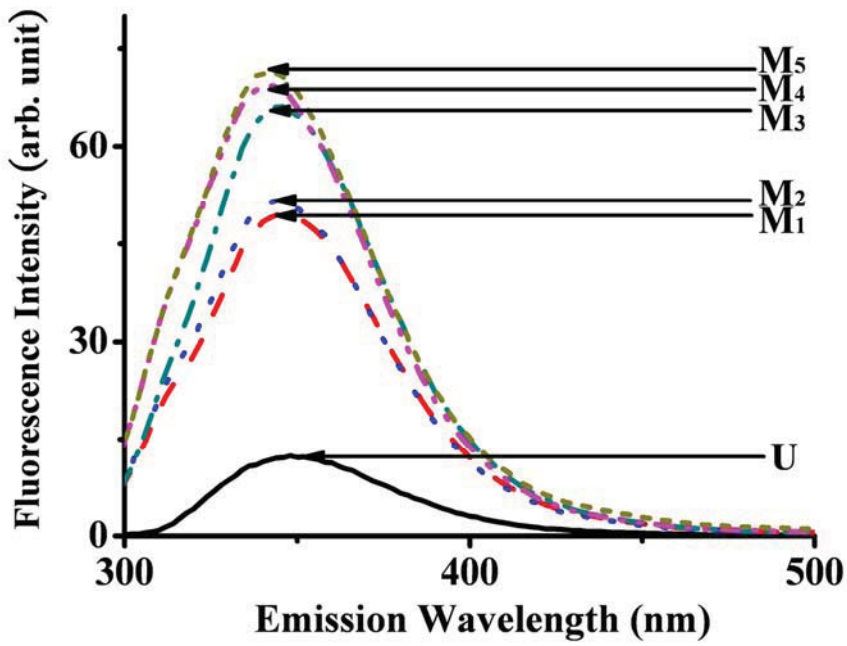


Fig 3

(A)

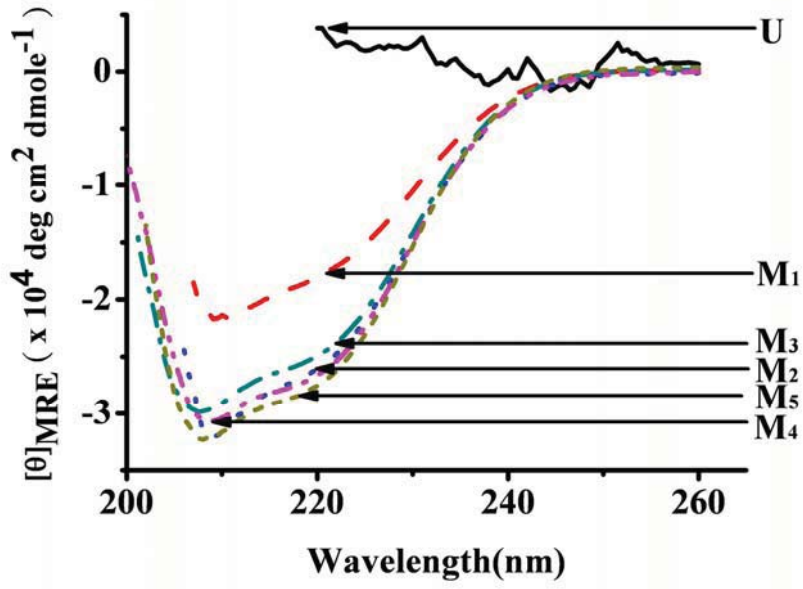


Fig 3

(B)

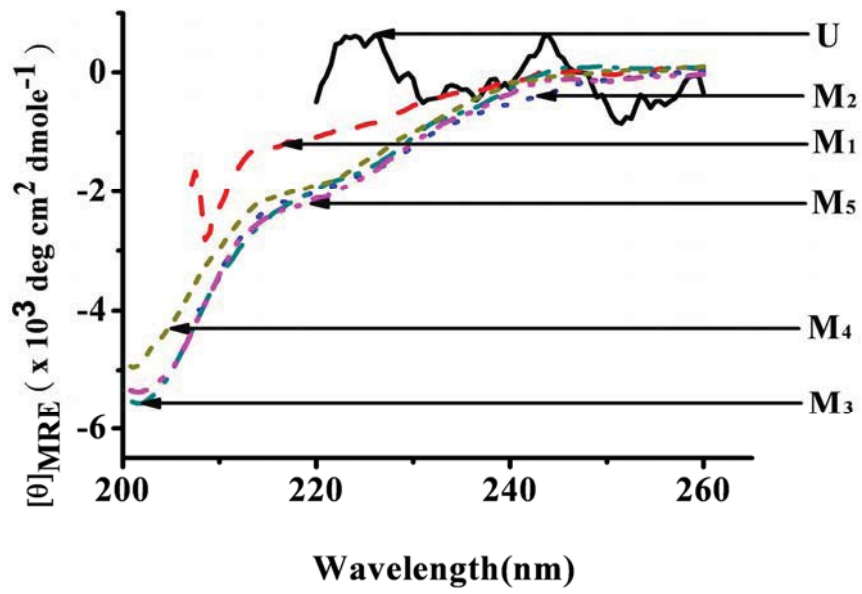


Fig 3

(C)

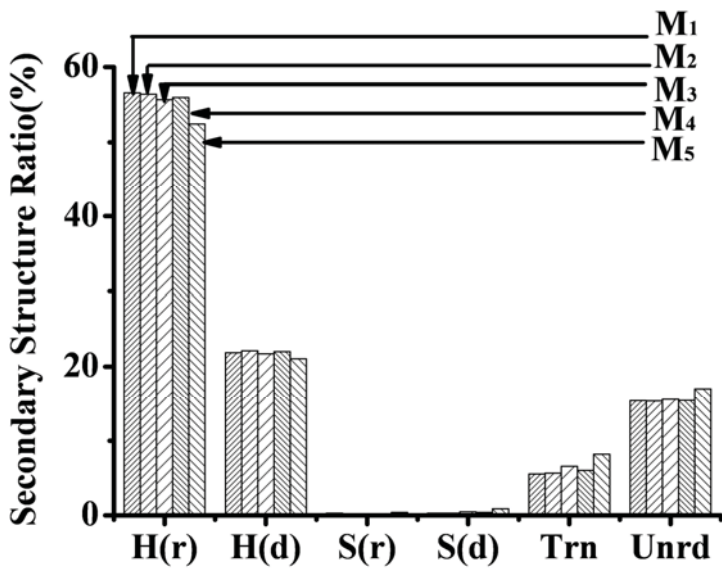


Fig 3

(D)

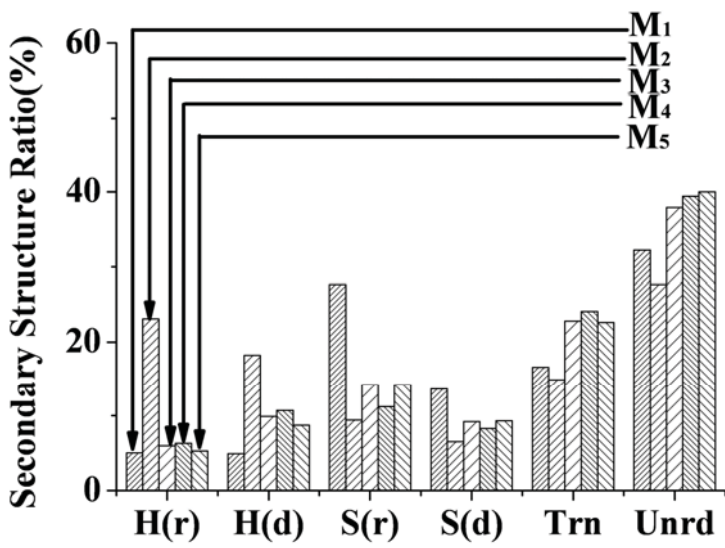




Fig 4

(A)

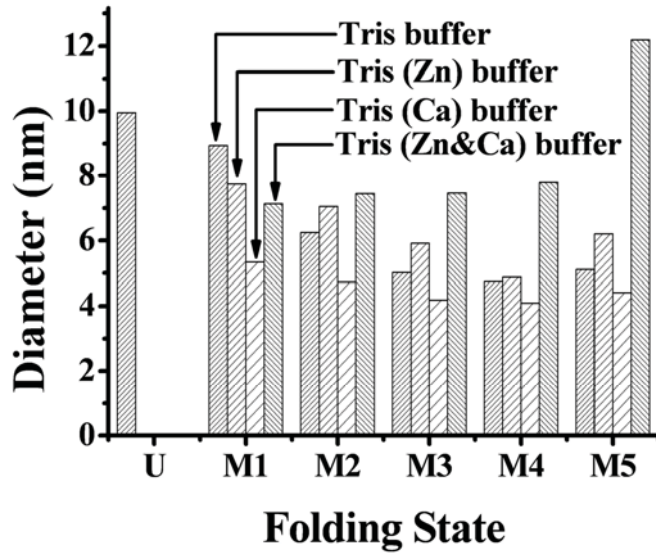
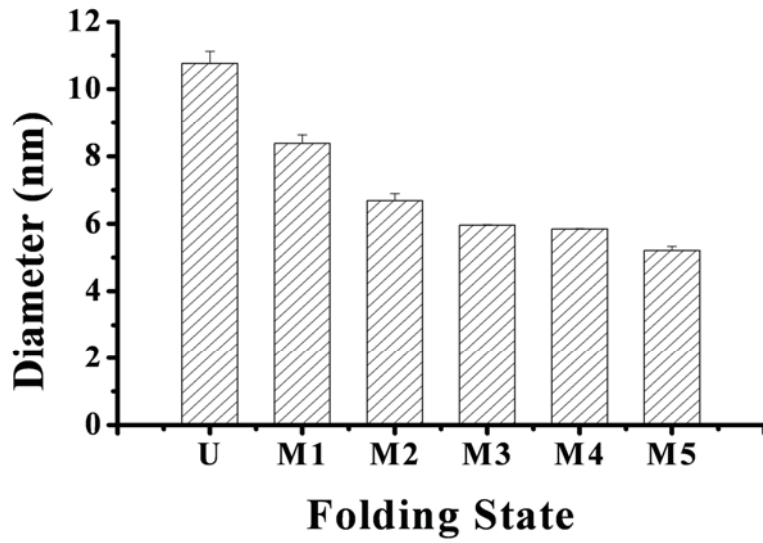
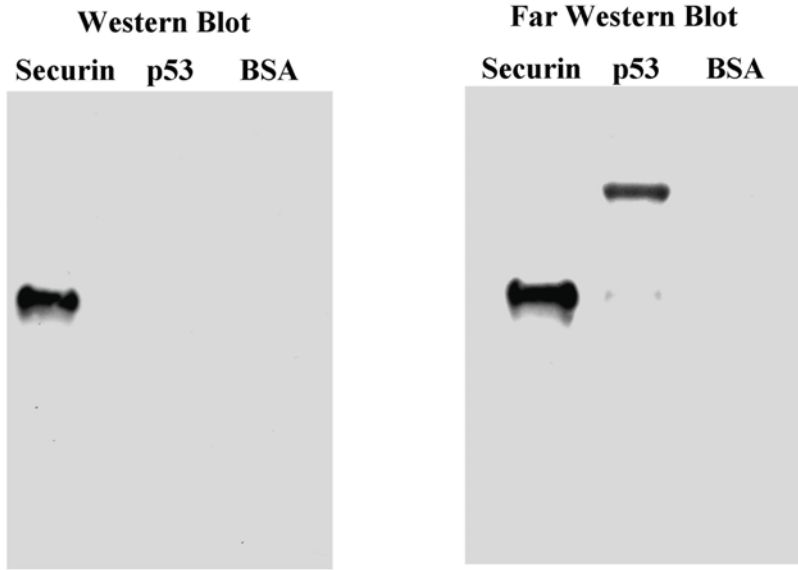


Fig 5

(B)



**Fig 5**



## **Abstract**

Cell cycle progression is controlled by a series of regulatory proteins, including members of the cyclin family. Cyclin I (Ccn1), a new member of the cyclin family, was identified in 1995 by Nakamura et al. It contains a typical cyclin box at the N-terminus and PEST sequences at the C-terminus. Interestingly, unlike other members of the cyclin family, the expression of cyclin I remains constant during cell cycle progression in post-mitotic tissues, so an understanding of the role of this protein in the cell remains unknown. In this study, recombinant human cyclin I was cloned, expressed, purified from inclusion bodies of *E.coli*, and refolded by an overcritical refolding process for structure-function analysis. According to analysis of circular dichroism spectra and differential scanning micro-calorimetry, we conclude that cyclin I is primarily a helical protein but without intra-molecular tertiary interactions, the characteristic of an intrinsically disordered protein. Far western blot analysis indicated that cyclin I can directly bind to p21<sup>cip1/waf1</sup>. Moreover, isothermal titration calorimetry analysis indicated that cyclin I and p21 could interact only in the presence of calcium ions. These results suggest that the function of cyclin I as an intrinsically disordered protein might regulate the activity of p21, another intrinsically disordered protein. This protein–protein interaction may rescue the cell from the apoptosis pathway.

Keywords: cyclin I, p21, intrinsically disordered protein, protein folding, calcium ion

## **Introduction**

The cell cycle is regulated by several complex pathways, including members of the well known cyclin family, named for their role in regulating cell cycle progression [1]. The cyclin family proteins are identified by their conserved “cyclin box” regions [2,3], and the activities of these proteins are regulated by the interaction of the cyclin box with cyclin-dependent kinase (CDK) [4]. At the end of each phase of the cell cycle, the cyclin protein is degraded by the ubiquitin system [5] and the cell progresses to the next stage of the cell cycle.

Cyclin I, a cyclin family member, was identified in 1995 by its conserved “cyclin box” and PEST sequences [6]. This cyclin box region of cyclin I protein is similar to cyclin G1 and G2; they are considered to

be a separate subgroup of the cyclin family [7]. Unlike other members of the cyclin family, cyclin I is similar to housekeeping genes, which are expressed constitutively [6,8] and are most abundant in post-mitotic tissues [6]. This expression profile of cyclin I implies that the functions of cyclin I may be different from regular cyclin family proteins that participate in the regulation of cell cycle progression [6]. Recent studies have indicated that cyclin I is expressed in human breast cancer and is closely associated with VEGF and KDR expression [9]. Additionally, cyclin I has been implicated in the protection of podocytes from apoptosis by stabilizing p21 from degradation [10]. Moreover, cyclin I can activate Cdk5 via protein-protein interactions, and regulate Bcl-2 and Bcl-xL expression in mouse podocytes and neurons to prevent cellular injury during apoptosis [11,12]. These multifunctional roles of cyclin I are similar to those of the intrinsically disordered proteins that have important roles in signal transduction and cellular regulation [13] and usually function as multi-functional proteins [14].

In this study, we have cloned the human cyclin I gene from the A549 cell line and recombinantly expressed the resulting protein in an *E.coli* expression system. The human cyclin I protein was expressed in inclusion bodies and refolded by an overcritical folding process [15-19]. Secondary and tertiary structure analysis indicated that the cyclin I protein is an intrinsically disordered protein with a major  $\alpha$ -helical secondary structure. Functional analysis indicated that cyclin I could bind to another well known intrinsically disordered protein, p21 [20], an interaction that was characterized by ultraviolet-visible (UV-VIS) spectroscopy, fluorescence spectroscopy, and isothermal titration calorimetry (ITC). This interaction was found to occur as a calcium-mediated process. We also demonstrated a principle that the function of one intrinsically disordered protein can be regulated by another intrinsically disordered protein via direct interaction.

## **Materials and Methods**

### **Materials and buffers.**

All chemicals were purchased from Merck Ltd. (Rahway, NJ). The denaturing/unfolding buffer contained 4.5 M urea with 10mM Tris base (pH=11.0), 0.1 M dithiothreitol (DTT), 0.1% mannitol and 0.5 mM pefabloc.

### **Cloning of recombinant human cyclin I**

The cDNA of cyclin I was amplified from A549 cell line using the polymerase chain reaction (PCR) with

cyclin I forward (5'-CATATGAAGTTTCCAGGGCCTT- 3') and cyclin I reversed (5'-TGAAACTACATGACAGAAACAGG -3') primers. The PCR product of cyclin I was added an A in the 3' end by tag polymerase and then ligated into yTA vector. Digested yTA-cyclin I plasmid by Nde I and ligated the product into pET30a vector (Novagen, Darmstadt, Germany). These plasmids were transformed into BL21 (DE3).

### **Recombinant expressed cyclin I**

Human cyclin I cDNA was constructed into the bacterial expression vector pET-30a (Novagen, Madison, WI) and then transformed into BL21(DE3) cells. The culture was incubated at 37°C and induced by 1 mM IPTG for 16 hours and then centrifuged at 12,000 g for 5 minutes. The pellet was suspended in 3 ml ddH<sub>2</sub>O and then disrupted by cell disruptor (Constant System Ltd. Northants, UK). Total cell lysate was centrifuged at 12,000 g for 5min. The cyclin I containing inclusion body was collected and washed with ddH<sub>2</sub>O twice.

Human recombinant p21 was produced with the similar approach which describe previously [21].

### **Unfolding and refolding of recombinant cyclin I by overcritical folding process**

The unfolded cyclin I with concentration 10 mg/ml was obtained by treating with denaturing/unfolded buffer. In order to avoid protein aggregation, the modified over-critical folding process was used [15-19,21]. Each of the folding intermediates was dialyzed against a particular folding buffer at 4 °C. All components of each refolding buffer are described in Table 1.

In order to study the divalent ions effect, we have investigated M<sub>1</sub>-M<sub>5</sub> intermediates in the presence of different ions: Ca<sup>2+</sup> (M<sub>1-5</sub>-Ca) and Zn<sup>2+</sup> (M<sub>1-5</sub>-Zn) that were prepared by dialysis of corresponding intermediates against folding buffers that included 1 μM ZnCl<sub>2</sub> and 1 μM CaCl<sub>2</sub> (R<sub>1</sub> buffer to R<sub>3</sub> buffer), and 1 mM ZnCl<sub>2</sub> and 1 mM CaCl<sub>2</sub> (R<sub>4</sub> buffer and R<sub>5</sub> buffer), respectively.

### **Fluorescence measurements**

Intrinsic fluorescence of unfolded cyclin I and its folding intermediates M<sub>1</sub>-M<sub>5</sub> have been investigated in the absence and in the presence of 1 mM ZnCl<sub>2</sub> and/or 1 mM CaCl<sub>2</sub>. Fluorescence spectra were recorded in the Hitachi F-7000 fluorescence spectrophotometer (Hitachi High Technologies, Tokyo, Japan), using 1 cm square cuvettes thermostated at 25 °C. The protein solutions were excited at 280 nm, and the emission was recorded at angle 90° to the excitation with a 5-nm bandwidth in the range from 300-450 nm with the 290 nm

long-pass filter.

### **CD analysis of cyclin I secondary structure**

CD spectra in far UV region (260 – 200 nm) of U, M<sub>1-5</sub>, M<sub>1-5</sub>-Zn and M<sub>1-5</sub>-Ca were determined by Jasco J 720C spectropolarimeter (Jasco Ltd., Tokyo, Japan) at 20°C with a 0.1 cm-light-path cuvette, the molar ellipticity [ $\theta$ ] (deg cm<sup>2</sup> dmol<sup>-1</sup>) was calculated base on the molecular weigh of cyclin I (M=42.557 kDa). The secondary structure of cyclin I and complexes of cyclin I with Zn<sup>2+</sup> or/and Ca<sup>2+</sup> were analyzed by the SELCON3 program [22,23].

### **Thermal stability monitored by differential scanning calorimetry (DSC)**

N-DSC II (Calorimetry Sciences Corporation, CSC, Lindon, UT,) interfaced with the computer equipped with an automatic data collection program was used for the experiments on thermal stability investigation of cyclin I and its complexes with the metals. Each solution of cyclin I intermediates in corresponding refolding buffer were adjusted to 2 mg/ml. All samples were filtered and degassed under vacuum for 5-10 minutes with gentle stirring before being placed into calorimetry cell. DSC experiments were performed at constant pressure 4 atm in order to avoid bubble formation. The temperature of samples was increasing with the constant scanning rate which was equal to 0.5 °C/min.

### **Analysis of size and shape of cyclin I by dynamic light scattering**

Dynamic light scattering (DLS) measurements were made using a goniometer from Brookhaven Instruments Corp. (BIC, Holtsville, NY) equipped with a diode-pumped laser (Coherent, Santa Clara, CA) with a wavelength  $\lambda=532.15$  nm and power at 10 mW. The scattered light was collected at an angle 90<sup>0</sup>. The chamber temperature was controlled at 20 °C by water circulator. The autocorrelation function was computed using a digital correlator (BI 9000, BIC, Holtsville, NY), then analyzed with the negatively constructed least-squares (NNLS) method.

### **Intermolecular interactions analysis between cyclin I and p21 by far Western blot technique**

Recombinant cyclin I and p21 were denatured and resolved on a 12 % SDS-PAGE, then electrotransferred to a poly vinylidene difluoride (PVDF) membrane with semi-dry transfer blots. The proteins were refolded on the PVDF by subsequent changing buffers from folding buffer 1 to 5 which

compounds are represented in Table. 1. The membrane was washed twice in each buffer during 5 min and then incubated in blocking solution (10 mM Tris·HCl/100 mM NaCl/0.1% Tween-20, 5% non fat milk, pH=7.5) for 30 minutes at room temperature. The recombinant p21 was detected by mouse anti p21 antibody (Santa Cruz Biotechnology, Santa Cruz, CA) that was recognized by goat anti mouse antibody. Chemiluminescent HRP substrates which purchase from (Millipore Corporation, Billerica, MA) was used to enhance the chemiluminescence signal. rEaGH was used as a negative control.

Far western blot technique, however, after incubation of the membrane in the blocking solution, the refolded human recombinant p21 (10 µg/ml in R<sub>5</sub> buffer with 1 µM CaCl<sub>2</sub>) was added and the membrane was gently shake for 2 hours at 4<sup>0</sup>C. The p21 and complex of p21 and cyclin I was detected by mouse anti p21 antibody as previously described.

### **Isothermal titration calorimetry (ITC) analysis the binding between p21 and cyclin I**

The 2277 Thermal Activity Monitor (TAM, ThermoMetric AB, Sweden) was used to determine the equilibrium constant  $K_a$  and reaction enthalpy  $\Delta H$  for p21 binding to cyclin I in the presence of calcium Ca<sup>2+</sup>. The cyclin I solution in concentration 10 µM which dissolved in Tris buffer (10 mM, pH=8.8) with the volume of 2.8 ml was placed into the measuring ample and titrated by addition of drops ,10 µl each, of p21 solution, in 300 µM, step by step with interval between two consecutive portions of 15 min. The injection rate was 1 µl/sec. Finally 200 µl of p21 solution was added into the measuring ample. The temperature of 25 °C was maintained during whole experiment. In order to clarify the role of calcium Ca<sup>2+</sup> for p21 binding with cyclin I the same experiments was performed in the absence and in the presence of 1 mM calcium chloride.

## **Results**

### **Secondary structure analysis of the intrinsically disordered protein cyclin I**

Secondary structure analysis has the unique feature of revealing the local conformation of proteins. The folding intermediate was adjusted to a concentration of 0.2 mg/ml and analysis of its secondary structural composition was performed by circular dichroism (CD) [24,25]. Figure 1 shows the CD profiles of folding intermediates of cyclin I from wavelengths 200 nm to 260 nm. The CD spectrum of cyclin I in the denatured state (U) showed no meaningful signal below 220 nm. In the M<sub>1</sub> to M<sub>5</sub> states, the CD profiles showed

significant negative peaks at 208 nm, the typical  $\alpha$ -helical signal for CD spectra (Figure 1A). By analyzing the CD profiles with the SELCON3 program [26], the secondary structure of cyclin I is predominately an  $\alpha$ -helical protein (50% to 70%), formed in the early stage of the folding process, along with several random coil segments (about 20%) but no  $\beta$ -sheet structure (Figure 1B).

### **Fluorescence analysis of cyclin I protein during the folding process**

Hydrophobic core formation is also a major characteristic of the cyclin I protein. The autofluorescence of various cyclin I folding intermediates was analyzed by fluorescence spectroscopy with excitation at 280 nm. In different cyclin I folding intermediates (Figure 2), the longest emission ( $\lambda_{\max}$ ) was observed in the denatured state (U; 348 nm) with a blue shift in the  $\lambda_{\max}$  following the progression of the folding process ( $M_1 = M_2$  [340 nm] >  $M_3 = M_4$  [338 nm] >  $M_5$  [336 nm]). Moreover, the fluorescence intensity increased following the progression of the folding process ( $M_5$  [356 a.u.] >  $M_4$  [330 a.u.] >  $M_3$  [242 a.u.] >  $M_2$  [237 a.u.] >  $M_1$  [197 a.u.] > U [144 a.u.]).

### **Particle size determination by DLS**

The particle size analysis by DLS (Table 2) demonstrates uniformity with a single distribution, indicating that the folding process has reached equilibrium and that the protein is in a monomeric state. However, the  $R_H$  of cyclin I folding intermediates is reduced during the folding process in metal ion-containing conditions. Moreover, the  $M_5$  state of cyclin I protein complexed with calcium ions is the smallest one of all folding intermediates.

### **Thermal stability analysis of intrinsically disordered protein cyclin**

The thermal stability of folded cyclin I ( $M_5$ ) was investigated by differential scanning calorimetry (DSC) with two ions ( $\text{Ca}^{2+}$ ,  $\text{Zn}^{2+}$ ). The DSC profiles of cyclin I in various ionic environments showed no significant phase-transition phenomena (Figure 3), even in the native state. The DSC profile of cyclin I suggests that cyclin I has no stable tertiary structure and is an intrinsically disordered protein when compared with a lysozyme control sample.

### **Cyclin I can bind to p21 directly when calcium ions are present**

A previous study demonstrated that cyclin I could stabilize p21 from degradation and prevent podocyte

cell apoptosis [10]. In this study, the ITC measurement demonstrated that cyclin I protein could bind to p21 directly when calcium ions are present (Figure 4A). The binding affinity ( $K_a$ ) is  $1.12 \times 10^7 \text{ M}^{-1}$ ,  $\Delta H$  is  $-90.35 \text{ kJ/mole}$ , and binding ratio between p21 and cyclin I is 1. However, cyclin I cannot bind to p21 in the calcium ion-free solution. Similar results were observed by Far western blot analysis, which indicated that p21 bound directly to cyclin I protein (Figure 4B) but not to the negative control rEaGH. Moreover, a calcium concentration of about 0.62 mM for cyclin I binding to p21 was required in UV-VIS spectroscopic (Figure 4C) and fluorescence spectroscopic (Figure 4D) measurements.

## Discussion

Protein expression in the inclusion bodies of prokaryote systems was typically a process to be avoided. In this study, we overexpressed human cyclin I protein in the prokaryote system and collected the high yield and high purity inclusion bodies (data not show). By using an overcritical folding process, the inclusion body of cyclin I protein was folded into its functional native state, which was then characterized by ITC (Figure 4A) and Far western blotting (Figure 4B). Moreover, a calcium concentration of about 0.62 mM for cyclin I binding to p21 was required in UV-VIS spectroscopic (Figure 4C) and fluorescence spectroscopic (Figure 4D) measurements. However, a CD-based secondary structural analysis of cyclin I and p21 protein under identical conditions revealed that there were no structural differences when the calcium ion concentrations ranged from 0 mM to 1 mM (data not shown). The results suggest that the effect of cyclin I binding to p21 protein is limited to their hydrophobic core but does not affect the protein's secondary structure. Furthermore, the calcium concentration used in ITC and Far western blot experiments (1 mM) is sufficient for cyclin I binding to p21 protein. Physiologically, the binding of cyclin I and p21 involve the maintenance of cell numbers in post-mitotic tissue [10-12]. Intracellular calcium ion is a secondary messenger involved in multiple signal transduction pathways [27,28], including cellular apoptosis or necrosis pathways [29] at overloaded concentrations. Accordingly, the cyclin I protein exists in the post-mitotic cell and can bind to p21 when the apoptosis signal, a surplus of calcium ions, is present, preventing cellular apoptosis and maintaining cell numbers.

In the thermal stability analysis measured by DSC, the cyclin I protein did not have a signification phase-transition point during the heating process, even in its native state (calcium ion-rich environment), similar to the glassy transition [30]. The DSC profile suggests that cyclin I has no stable tertiary structure and

is an intrinsically disordered protein. Intrinsically disordered proteins usually play a role in signal transduction and cell regulation by binding and regulating their functional partners [13,31]. Interestingly, p21, the functional partner of cyclin I, is also an intrinsically disordered protein [20]. The existence of an interaction between 2 intrinsically disordered proteins is an interesting observation of protein–protein interactions. Although the binding of p21 to cyclin I was proven in this study, the precise functional complex and its mode of regulation remain to be determined.

During the overcritical folding process, we collected folding intermediates and analyzed their secondary structure and hydrophobic core formation by CD and fluorescence spectra, respectively. Interesting, CD analysis revealed that the secondary structure of cyclin I is predominately  $\alpha$ -helical, which is similar to other membranes of the cyclin family [32-34], and the helical ratio of cyclin I protein approaches 50% to 70% in all folding intermediates ( $M_1$  state to native state), indicating that the helix is formed during the early stages of the folding process. Additionally, only a small percentage of random coil (about 20%) formation occurs during the folding process. In combination with DSC results, the small amount of random coil in cyclin I is important for its structural dynamics. Moreover, hydrophobic collapse, as determined by fluorescence, showed a blue shift in  $\lambda_{\max}$  and an increase in intensity, indicating that the hydrophobic core was becoming increasingly stable following the folding process. These results were consistent with changes in particle size as measured by DLS. Moreover, added calcium ions further reduce the cyclin I folding intermediate to its smallest particle size, indicating that the cyclin I protein is most stable in the calcium-rich environment.

In summary, cyclin I is an intrinsically disordered protein with a stable secondary structure, and the energy state and hydrophobic collapse can be used as the indicator of the folding process. Moreover, the direct interaction between 2 intrinsically disordered proteins, cyclin I and p21, is mediated by calcium ions. The interaction between cyclin I and p21 may prevent cellular apoptosis and help preserve cell number in post-mitotic tissue and maintain cellular function.

## **Acknowledgments**

We would like to thank Dr. P.C. Huang in Johns Hopkins University, for their valuable suggestions and discussions on the paper. We would like to thank National Synchrotron Radiation Research Center to provide the CD spectrophotometer in this study. This study was supported in part by grant NSC

## References

- [1] T. Evans, E.T. Rosenthal, J. Youngblom, D. Distel, T. Hunt, Cyclin: A protein specified by maternal mRNA in sea urchin eggs that is destroyed at each cleavage division, *Cell* 33 (1983) 389-396.
- [2] D. Joyce, C. Albanese, J. Steer, M. Fu, B. Bouzahzah, R.G. Pestell, NF- $\kappa$ B and cell-cycle regulation: the cyclin connection, *Cytokine & Growth Factor Reviews* 12 (2001) 73-90.
- [3] J.H. Nugent, C.E. Alfa, T. Young, J.S. Hyams, Conserved structural motifs in cyclins identified by sequence analysis, *Journal of Cell Science* 99 (1991) 669-674.
- [4] J. Pines, T. Hunter, Cyclin-dependent kinases: a new cell cycle motif?, *Trends in Cell Biology* 1 (1991) 117-121.
- [5] M. Pagano, Cell cycle regulation by the ubiquitin pathway, *The FASEB Journal* 11 (1997) 1067-1075.
- [6] T. Nakamura, R. Sanokawa, Y.F. Sasaki, D. Ayusawa, M. Oishi, N. Mori, Cyclin I: A New Cyclin Encoded by a Gene Isolated from Human Brain, *Experimental Cell Research* 221 (1995) 534-542.
- [7] S. Bates, S. Rowan, K. Vousden, Characterisation of human cyclin G1 and G2: DNA damage inducible genes., *Oncogene* 13 (1996) 1103-1109.
- [8] M.R. Jensen, T. Audolfsson, V.M. Factor, S.S. Thorgeirsson, In vivo expression and genomic organization of the mouse cyclin I gene (*Ccni*), *Gene* 256 (2000) 59-67.
- [9] G. Landberg, K. Nilsson, K. Jirström, L. Rydén, R. Kitching, A. Burger, A. Seth, Cyclin I is expressed in human breast cancer and closely associated with VEGF and KDR expression, *Breast Cancer Research and Treatment* 89 (2005) 313-316.
- [10] S.V. Griffin, J.P. Olivier, J.W. Pippin, J.M. Roberts, S.J. Shankland, Cyclin I Protects Podocytes from Apoptosis, *Journal of Biological Chemistry* 281 (2006) 28048-28057.
- [11] P.T. Brinkkoetter, P. Olivier, J.S. Wu, S. Henderson, R.D. Krofft, J.W. Pippin, D. Hockenbery, J.M. Roberts, S.J. Shankland, Cyclin I activates Cdk5 and regulates expression of Bcl-2 and Bcl-XL in postmitotic mouse cells, *The Journal of Clinical Investigation* 119 (2009) 3089-3101.
- [12] P. Brinkkoetter, J. Pippin, S. Shankland, Cyclin I-Cdk5 governs survival in post-mitotic cells, *Cell Cycle* 9 (2010) 1729-1731.
- [13] J. Liu, N.B. Perumal, C.J. Oldfield, E.W. Su, V.N. Uversky, A.K. Dunker, Intrinsic Disorder in Transcription Factors, *Biochemistry* 45 (2006) 6873-6888.
- [14] K. Sugase, H.J. Dyson, P.E. Wright, Mechanism of coupled folding and binding of an intrinsically disordered protein, *Nature* 447 (2007) 1021-1025.
- [15] C.-C. Chang, M.-S. Cheng, Y.-C. Su, L.-S. Kan, A First-Order-Like State Transition for Recombinant Protein Folding, *Journal of Biomolecular Structure and Dynamics* 21 (2003) 247-255.
- [16] C.-C. Chang, P.-Y. Lin, X.-C. Yeh, K.-H. Deng, Y.-P. Ho, L.-S. Kan, Protein folding stabilizing time measurement: A direct folding process and three-dimensional random walk simulation, *Biochemical and Biophysical Research Communications* 328 (2005) 845-850.
- [17] C.-C. Chang, Y.-C. Su, M.-S. Cheng, L.-S. Kan, Protein folding by a quasi-static-like process: A first-order state transition, *Physical Review E* 66 (2002) 021903.
- [18] C.-C. Chang, C.-T. Tsai, C.-Y. Chang, Structural restoration of inactive recombinant fish growth

- hormones by chemical chaperonin and solvent restraint approaches, *Protein Engineering* 15 (2002) 437-441.
- [19] C.-C. Chang, X.-C. Yeh, H.-T. Lee, P.-Y. Lin, L.-S. Kan, Refolding of lysozyme by quasistatic and direct dilution reaction paths: A first-order-like state transition, *Physical Review E* 70 (2004) 011904.
- [20] R.W. Kriwacki, L. Hengst, L. Tennant, S.I. Reed, P.E. Wright, Structural studies of p21<sup>Waf1/Cip1/Sdi1</sup> in the free and Cdk2-bound state: conformational disorder mediates binding diversity, *Proc Natl Acad Sci U S A* 93 (1996) 11504-11509.
- [21] C.C. Chang, C.S. Lin, M.C. Chen, Y.C. Liu, Y.F. Huang, P.Y. Lin, Y.F. Chen, C.S. Chang, L.S. Kan, Folding and Structural Characterization of Recombinant Cyclin-dependent Kinase Inhibitor p21<sup>(Cip1, Waf1, Sdi1)</sup>, *Biophysical Reviews and Letters* 1 (2006) 45-56.
- [22] N. Sreerama, S.Y.U. Venyaminov, R.W. Woody, Estimation of the number of  $\alpha$ -helical and  $\beta$ -strand segments in proteins using circular dichroism spectroscopy, *Protein Science* 8 (1999) 370-380.
- [23] N. Sreerama, R.W. Woody, A Self-Consistent Method for the Analysis of Protein Secondary Structure from Circular Dichroism, *Analytical Biochemistry* 209 (1993) 32-44.
- [24] B.A.W. Lee Whitmore, Protein secondary structure analyses from circular dichroism spectroscopy: Methods and reference databases, *Biopolymers* 89 (2008) 392-400.
- [25] N.J. Greenfield, Using circular dichroism spectra to estimate protein secondary structure, *Nat. Protocols* 1 (2007) 2876-2890.
- [26] J. Lees, A. Miles, R. Janes, B. Wallace, Novel methods for secondary structure determination using low wavelength (VUV) circular dichroism spectroscopic data, *BMC Bioinformatics* 7 (2006) 507.
- [27] N. Agell, O. Bachs, N. Rocamora, P. Villalonga, Modulation of the Ras/Raf/MEK/ERK pathway by Ca<sup>2+</sup>, and Calmodulin, *Cellular Signalling* 14 (2002) 649-654.
- [28] E.L. Arrese, M.T. Flowers, J.L. Gazard, M.A. Wells, Calcium and cAMP are second messengers in the adipokinetic hormone-induced lipolysis of triacylglycerols in *Manduca sexta* fat body, *Journal of Lipid Research* 40 (1999) 556-564.
- [29] R. Rizzuto, P. Pinton, D. Ferrari, M. Chami, G. Szabadkai, P.J. Magalhaes, F.D. Virgilio, T. Pozzan, Calcium and apoptosis: facts and hypotheses, *Oncogene* 22 (2003) 8619-8627.
- [30] Z.H. Chang, J.G. Baust, Physical aging of glassy state: DSC study of vitrified glycerol systems, *Cryobiology* 28 (1991) 87-95.
- [31] A.K. Dunker, V.N. Uversky, Signal transduction via unstructured protein conduits, *Nat Chem Biol* 4 (2008) 229-230.
- [32] E. Petri, A. Errico, L. Escobedo, T. Hunt, R. Basavappa, The Crystal Structure of Human Cyclin B, *cell cycle* 6 (2007) 1342-1349.
- [33] S. Hoepfner, S. Baumli, P. Cramer, Structure of the Mediator Subunit Cyclin C and its Implications for CDK8 Function, *Journal of Molecular Biology* 350 (2005) 833-842.
- [34] K.K. Kim, H.M. Chamberlin, D.O. Morgan, S.-H. Kim, Three-dimensional structure of human cyclin H, a positive regulator of the CDK-activating kinase, *Nat Struct Mol Biol* 3 (1996) 849-855.

**Table 1.** Chemical compositions of refolding buffer.

	Tris buffer, mM	pH	Urea, M	DTT, mM	Mannitol, %	Pefabloc, $\mu$ M
Folding buffer 1	10	11	2	0.1	0.1	0.5
Folding buffer 2	10	11	1	0.1	0.1	0.5
Folding buffer 3	10	11	-	0.1	0.1	0.5
Folding buffer 4	10	8.8	-	0.1	0.1	0.5
Folding buffer 5 (the native buffer)	10	8.8	-	0.1	-	0.5

**Table 2.** The influence of calcium  $\text{Ca}^{2+}$  and zinc  $\text{Zn}^{2+}$  ions on the hydrodynamic diameter  $D_H$  of cyclin I folding intermediates.

Folding state	$D_H$ , nm	$D_H$ , nm $\text{Zn}^{2+}$	$D_H$ , nm $\text{Ca}^{2+}$	$D_H$ , nm $\text{Ca}^{2+}$ and $\text{Zn}^{2+}$
U	$9.95 \pm 1.47$			
$M_1$	$8.94 \pm 0.55$	$7.74 \pm 0.21$	$5.34 \pm 0.01$	$7.13 \pm 0.12$
$M_2$	$6.25 \pm 0.29$	$7.05 \pm 0.26$	$4.73 \pm 0.10$	$7.45 \pm 0.28$
$M_3$	$5.03 \pm 0.25$	$5.92 \pm 0.15$	$4.18 \pm 0.08$	$7.46 \pm 0.31$
$M_4$	$4.74 \pm 0.04$	$4.88 \pm 0.02$	$4.09 \pm 0.01$	$7.79 \pm 0.04$
$M_5$	$5.12 \pm 0.01$	$6.20 \pm 0.20$	$4.41 \pm 0.12$	$12.19 \pm 0.14$

## Figure legends

**Figure 1. The secondary structure analysis of folded cyclin I protein.** (A) Circular dichroism profiles of cyclin I at 20 °C. The CD curves of intermediate states U (denatured), M<sub>1</sub>, M<sub>2</sub>, M<sub>3</sub>, M<sub>4</sub>, and M<sub>5</sub> have been marked in the figure. Due to the high absorption background of urea in the far-UV region of U, data of lower wavelength than 220 nm are not shown. (B) The CD profiles analysis by SELCON3 of folding intermediates of cyclin I.

**Figure 2. Hydrophobic core formation analysis of folding intermediates of cyclin I protein.** The fluorescence spectra of U, M<sub>1</sub>, M<sub>2</sub>, M<sub>3</sub>, M<sub>4</sub>, and M<sub>5</sub> are marked in the figure. The thick-black, dashed, dotted, grey, thin-black, and dashed-dotted lines represent the spectra of cyclin I in the states of U, M<sub>1</sub>, M<sub>2</sub>, M<sub>3</sub>, M<sub>4</sub>, and M<sub>5</sub>, respectively.

**Figure 3. Thermal stability analysis of folded cyclin I in various ion buffers.** Temperature dependence of specific heat capacity of M<sub>5</sub> in Tris buffer pH 8.8 (solid line), M<sub>5</sub> in the Tris buffer with calcium (dashed line) or zinc (dotted line), and M<sub>5</sub> in Tris buffer with both zinc and calcium (dashed-dotted line). The temperature dependence of specific heat capacity for lysozyme (dashed-dotted line) is illustrated as a control.

**Figure 4. Binding analysis of cyclin I and p21 protein.** (A) Enthalpy change ( $\Delta H$ ), corresponding to the binding of p21 to cyclin I in the presence of calcium ( $\text{Ca}^{2+}$ ), is equal to -90.35 KJ/mol (closed circle). In the figure, [L] represents the concentration of p21, [M] represents the concentration of cyclin I. The ITC experiment is shown under identical conditions, except in the absence of calcium (open circle). (B) The identification of p21 by western blot with p21 monoclonal antibody after expression of cyclin I and p21 in BL21 cell lines (left) with rEaGH used as a negative control. Coprecipitation of p21 and cyclin I has been demonstrated by far western blot (right). The  $\lambda_{\text{max}}$  of (C) UV absorption and (D) fluorescence emission with calcium ions ranging from 0 to 1 mM.

Figure 1A

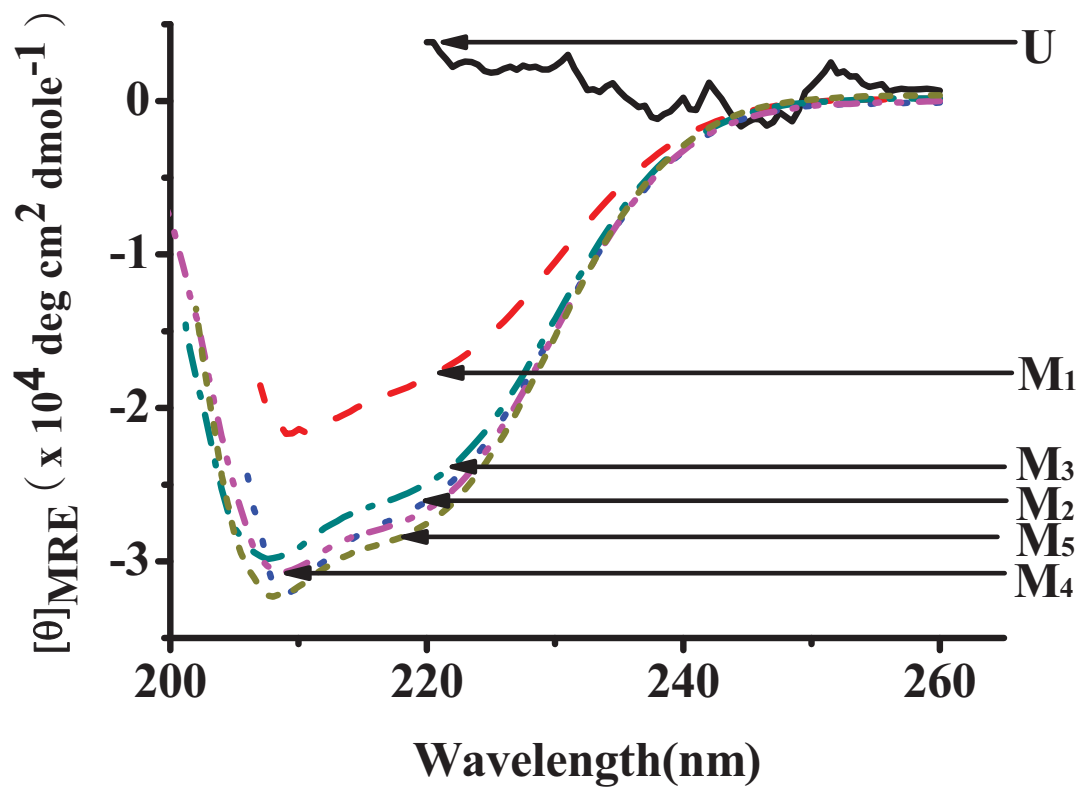


Figure 1B

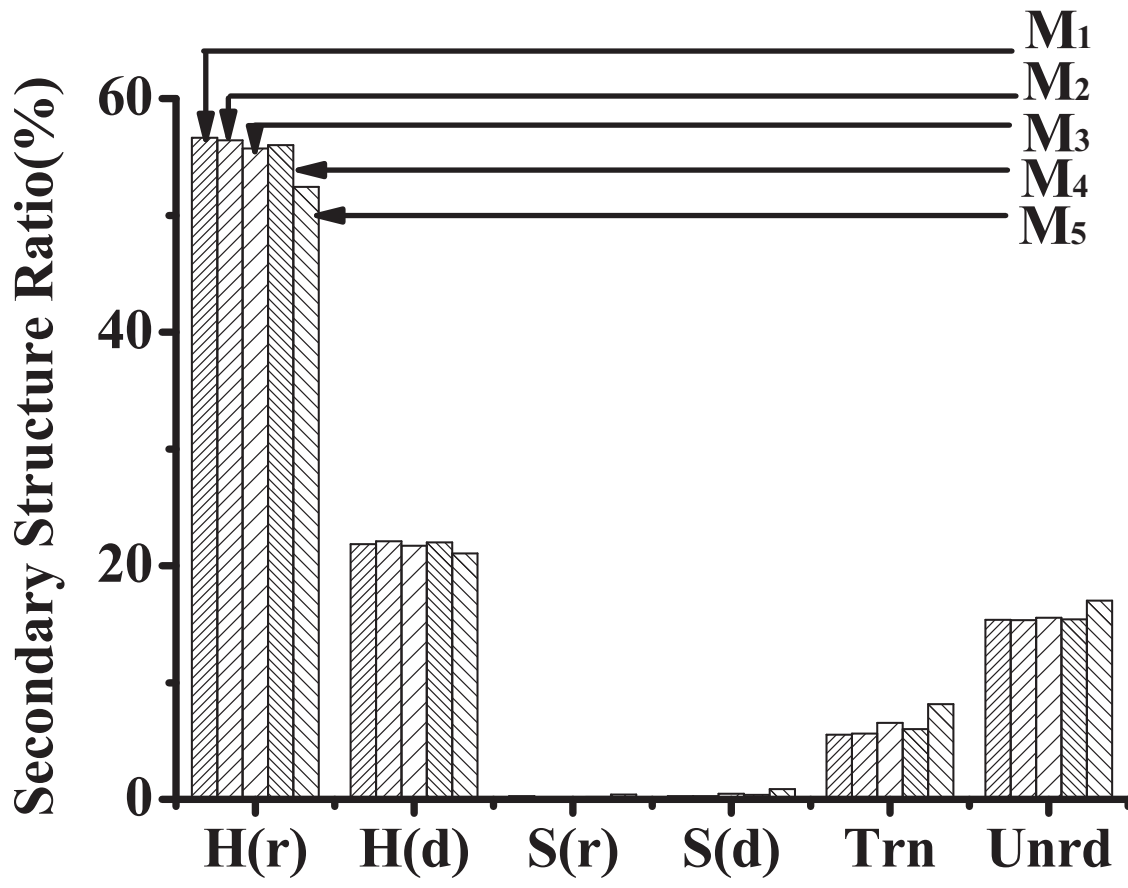


Figure 2

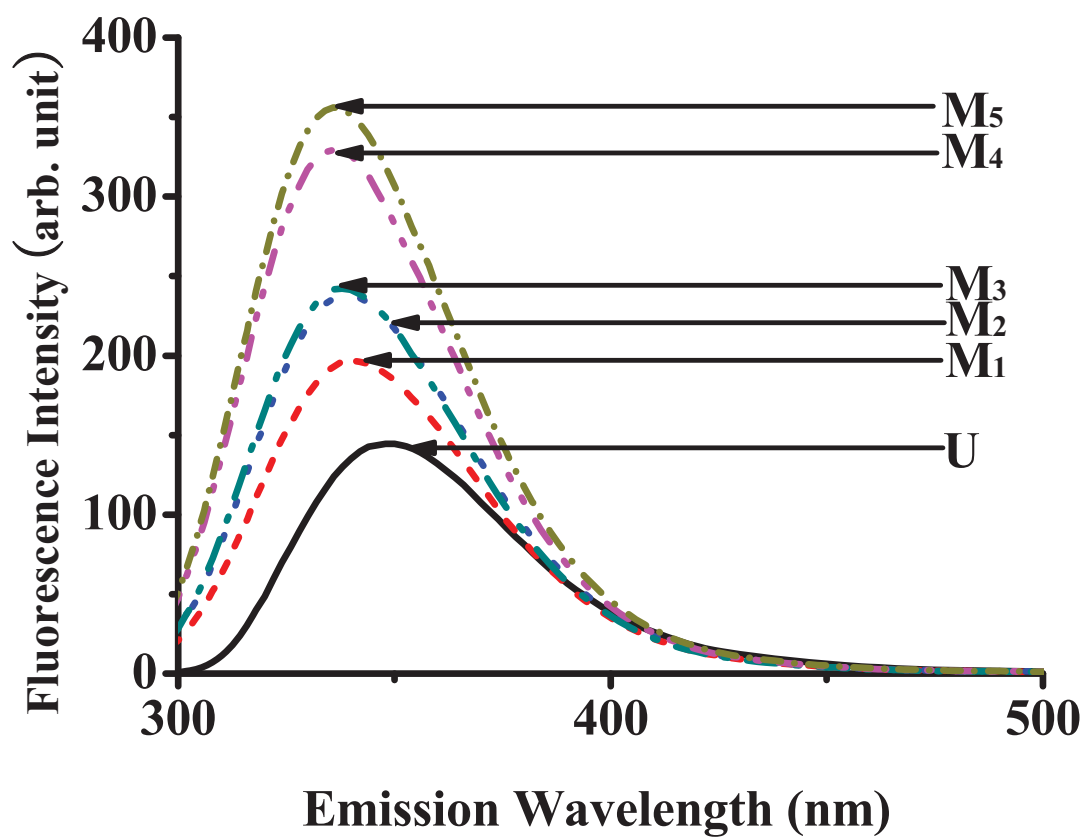


Figure 3

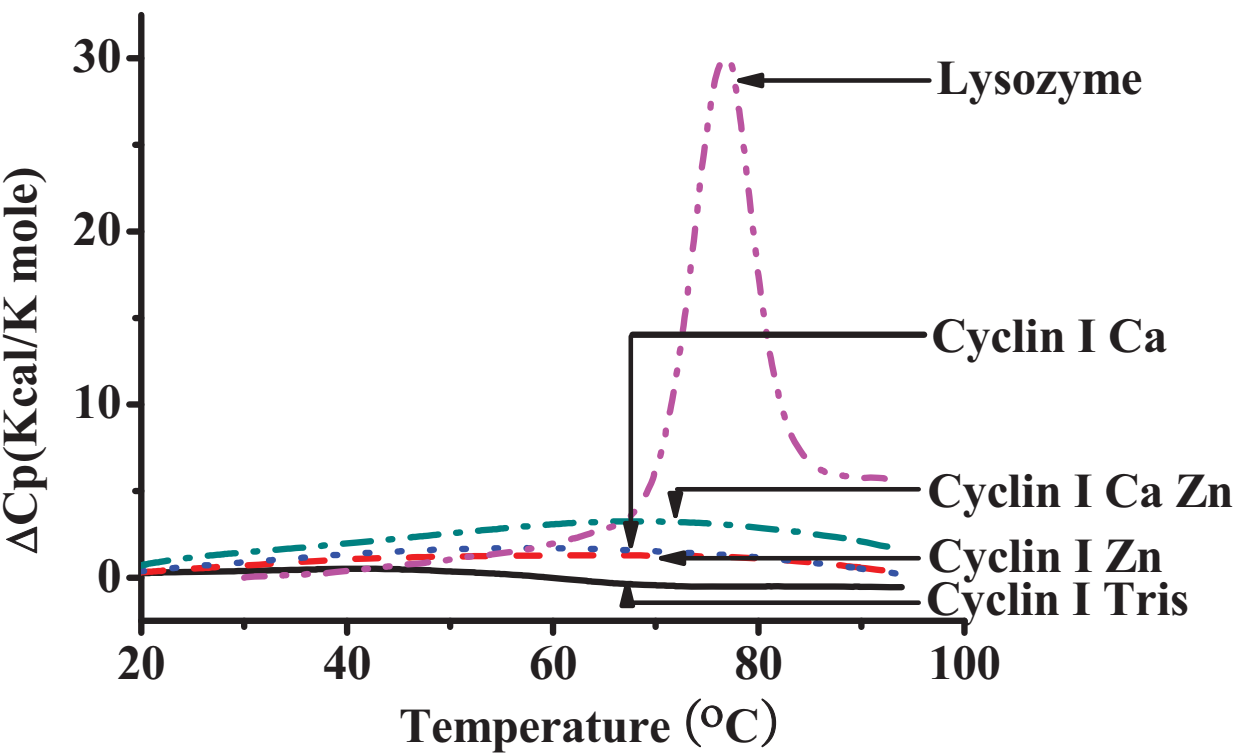


Figure 4A

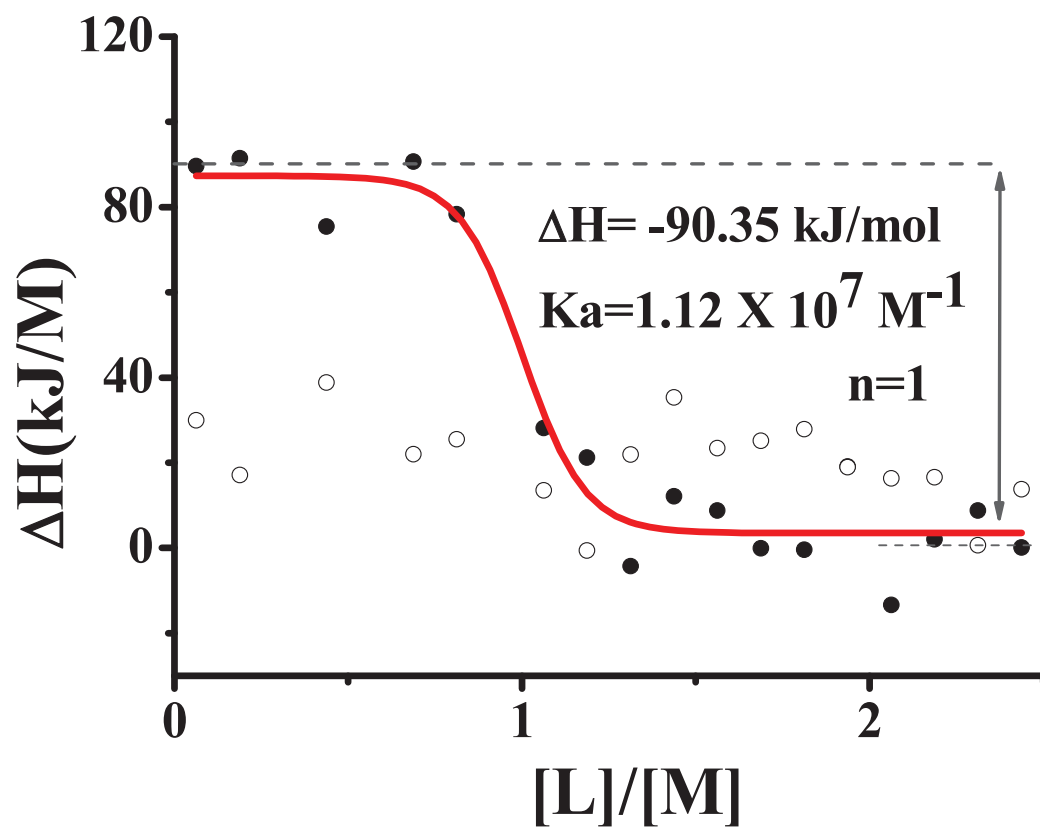
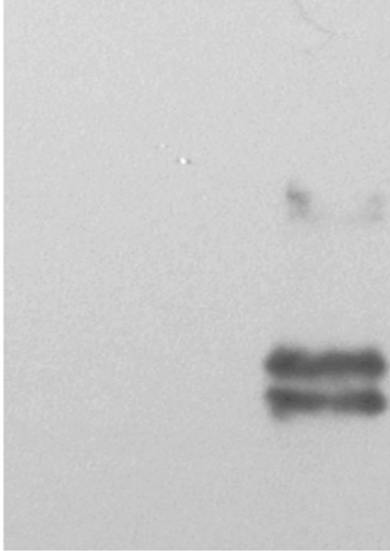


Figure 4B

**(B)**

Western Blot  
Cyclin I rEaGH p21



Far Western Blot  
Cyclin I rEaGH p21

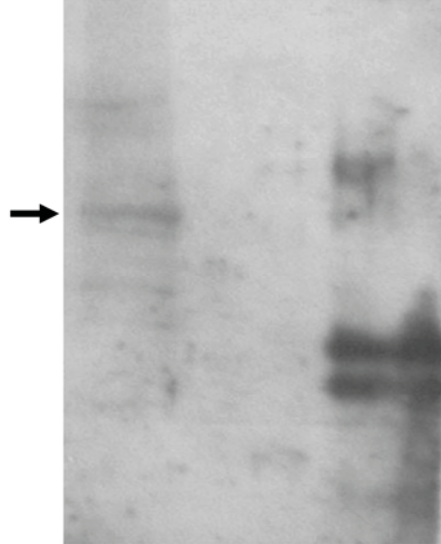


Figure 4C

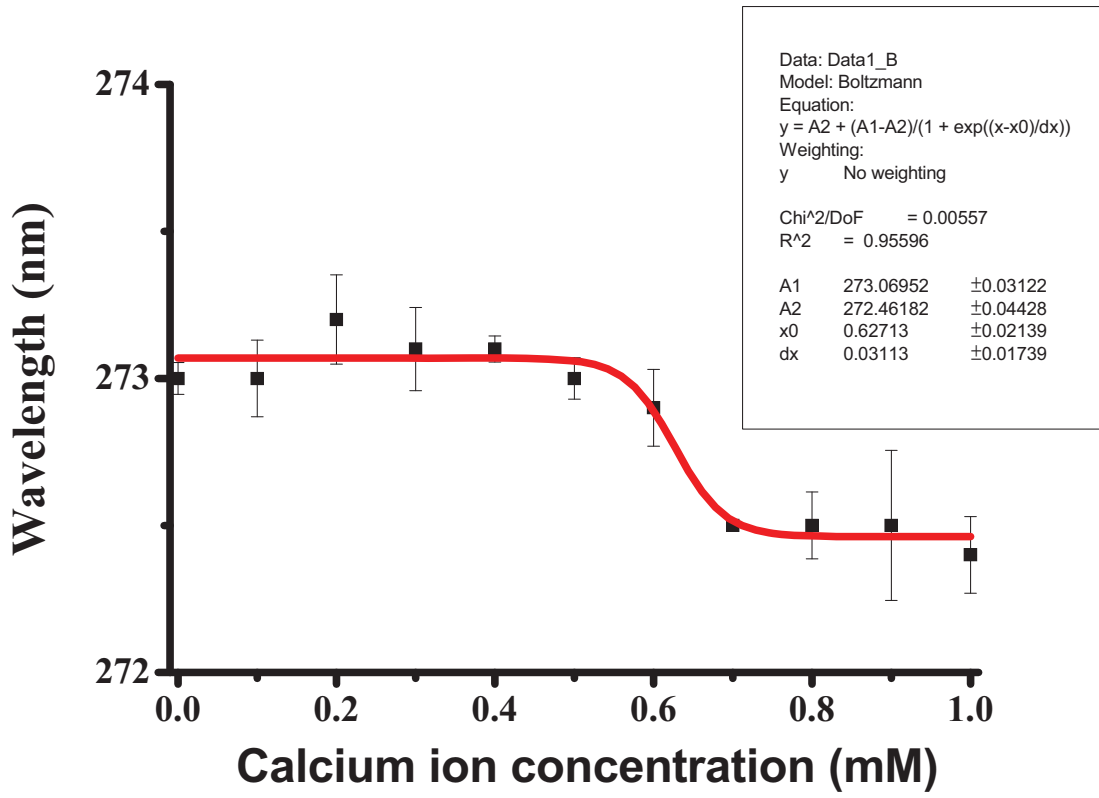
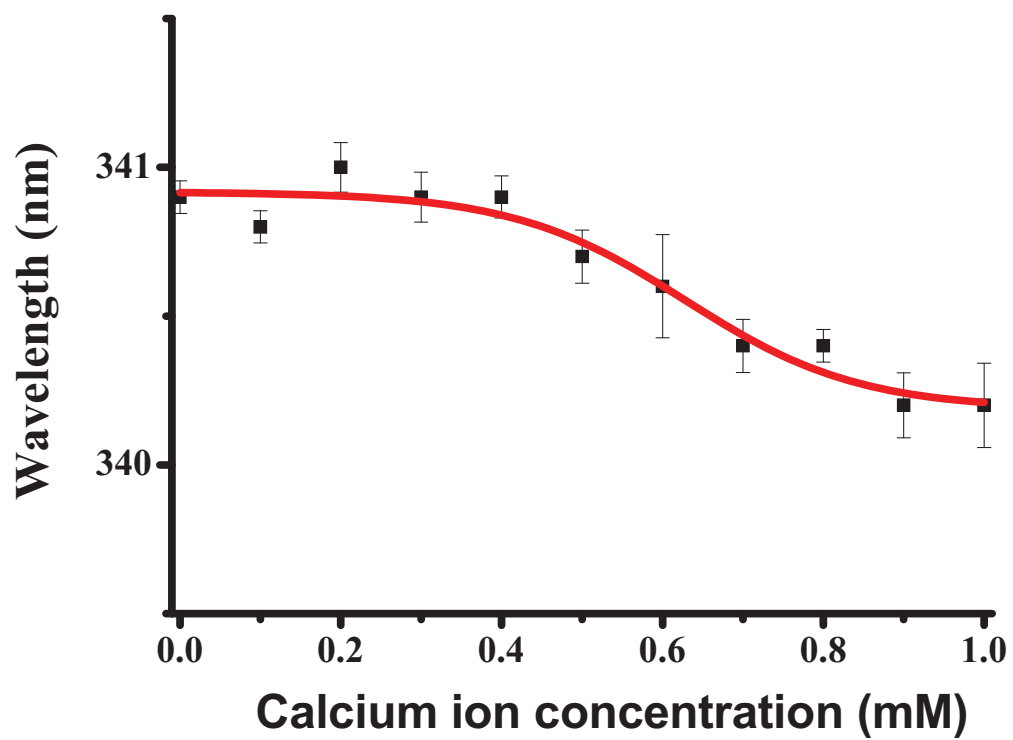


Figure 4D



### Part-III: Protein aggregation: competition reactions between self-stabilization and diffusion limited aggregation in solution

#### Abstract

Protein folding, which is a self-organization process, and aggregation, which is a self-assembly process, may take place spontaneously in a biological system. It is possible that self-organization and aggregation compete with each other frequently during protein folding. It is intriguing to investigate the molecular mechanism for the reaction paths of self-organization or self-assembly. In this study, both reactions of protein folding and aggregation are observed simultaneously, during a direct/off-path refolding process of a reduced/unfolded growth hormone receptor binding protein (GHRBP). Moreover, flat hexagonal plate aggregates of GHRBP molecules are observed through scanning electron microscopy and solution atomic force microscopy. These imaging studies indicated the possibility reaction of aggresome formation which is similar to ice crystal formation. By combining the random walk simulation and experimental data, we surmise that the mechanism of protein aggregation may occur via the diffusion-limited aggregation process (DLA). Meanwhile, the GHRBP self-stabilization time, derived by an autocorrelation function, is found to be  $\sim 14.8 \mu\text{s}$ , which is longer than the secondary structure formation. Namely, the formation of secondary structures may not protect the protein from aggregation. The resultant aggresome, as suggested by Raman and mass spectroscopy, may have been formed by cross-linkages of disulfide bonds and hydrophobic interactions. These results indicated that the diffusion process and concentration of the protein at the initial stage is vital for determination the protein folding or aggregation. The aggregation process of misfolded protein is a parallel process and these misfolded aggregates may possess secondary structure which is similar to  $\beta$ -amyloid or prion.

**Keywords:** Protein folding, diffusion limited aggregation, auto-correlation function, spontaneous folding, Raman spectroscopy, MALDI-TOF mass spectrometry, molecular simulation.

## Introduction

Protein folding, which is a self-organization process, and aggregation, which is a self-assembly process, may take place spontaneously in biological systems by entropically driven force<sup>1-3</sup>. Extensive research has been carried out to study the phenomenon of protein folding and aggregation during the past decades. The ability to control protein folding and hinder aggregation is very important in the production and formation of therapeutic proteins as well as drug production. It has been reported that during the protein folding process, the conformational changes in proteins are involved in the loss of chaperone activity<sup>4</sup>, resulting in protein aggregation and various disease states<sup>5-10</sup>. However, the molecular mechanism remains unknown. It is important to elucidate the mechanism for controlling protein folding and aggregation.

The way in which a chain of amino acids transforms itself into perfectly folded proteins depends on the intrinsic physiochemical properties of the amino acid sequence and on influences of the crowded environment around the protein molecules<sup>11</sup>. Moreover, the topology of the proteins, not their sequence, may play a crucial role during protein folding<sup>12</sup>. As suggested by the “first-order-like phase transition” model of the protein folding reaction, both folded and aggregated protein molecules can be observed during the off-path folding reaction<sup>13-15</sup>. It has been reported that a majority of proteins will aggregate during the folding process *in vitro* in a high concentration system, but not in a low concentration system, suggesting that the aggregation of proteins may be correlated to the concentration of proteins<sup>16</sup>. In general, the kinetic mechanism of the aggregation of condensed matter is believed to be a diffusion-limited aggregation process<sup>17-19</sup>. Therefore, it is important to find out whether the protein aggregation follows the same mechanism.

It has been reported previously that the critical structures of proteins are formed sequentially in a time scale of nano- to micro-seconds during the protein folding process. Based on ultrasonic absorption (UA) and temperature jump (TJ) techniques, it has been reported that secondary structures comprising  $\alpha$ -helices (21 amino acids) can form within 30~160 ns<sup>20</sup>. On the other hand, the beta turn formation takes approximately 6  $\mu$ s<sup>20</sup>. Using photodissociation/rebinding methods, the time required for the formation of a loop comprising of 62 amino acids was found to be around 40  $\mu$ s<sup>20</sup>. Eaton et al.<sup>21</sup> have reported that changes in  $\alpha$ -helix are a temperature-dependent process. An increase in temperature results in an increased number of random coil peptides and decrease in the average helix length of helical peptides<sup>21</sup>. The sequential folding phenomenon may reveal a possible and important mechanism of the initiation stages of protein folding<sup>22</sup>. However, observations

of conformational reshuffling<sup>23</sup> and formation of disulfide bridges<sup>24, 25</sup> during subsequent folding processes indicate the possibility of conformational instability during the initial folding stage. Therefore, comparison of the time required for self-stabilization with that required for the formation of secondary structures during the folding process may reveal the folding/aggregation kinetics mechanism during the early folding stage.

To verify the aggregation mechanism, both experimental approaches and three-dimensional random walk simulations were studied in this work. In order to investigate the protein folding/aggregation process, GHRBP was denatured and the disulfide bonds were reduced. The results indicated that an off-path refolding process of a reduced/unfolded GHRBP might contain a combination of an antagonistic reaction of spontaneous folding and aggregation. Meanwhile, flat, hexagonal plate aggregates of GHRBP were observed through scanning electron microscopy (SEM) and atomic force microscopy (AFM). By combining the random walk simulation and experimental observation, we surmise that the mechanism of protein aggregation may occur via the diffusion-limited aggregation (DLA) process. Meanwhile, the aggregates may have been formed by intermolecular disulfide bonds and/or hydrophobic interactions.

## **Experimental section**

All chemicals were obtained from Merck Ltd. (Rahway, NJ). The denaturing/unfolding buffer was composed of 4.5 M urea with 10 mM Tris base, 0.1 M dithiothreitol (DTT), 0.1 % mannitol, and 0.5 mM a protease inhibitor (Pefabloc). The native buffer was 10 mM Tris HCl with a pH of 8.8.

### **Protein expression and purification**

*E. coli*-carrying modified pET28a-GHRBP expression plasmid<sup>26</sup> was grown in LB broth until the optical absorption at OD<sub>600</sub> reached 0.3. Cells were then grown in LB media with the supplement of 0.1 mM IPTG at 37 °C for 16 h. The protocols used for the isolation of the inclusion body from *E. coli* and for the unfolding were based on our previously described procedures<sup>26</sup>. *E. coli* was harvested through centrifugation at 12000 g for 3 min. The cell pellet was re-suspended and mixed well with ice-cold water and lysed with a cell disruptor (Constant System Ltd. Northants, UK). The total cell lysate was separated into soluble and insoluble portions through centrifugation at 12000 g for 3 min. The inclusion body was collected and washed twice with ice-cold double-distilled H<sub>2</sub>O.

### **Off-path (direct dilution) folding study**

GHRBP were unfolded in the unfolding buffers<sup>13, 26</sup> and diluted to various concentrations (from 41.4

mg/ml to 2 mg/ml). The disulfide bonds were reduced to thiol groups accordingly. The denatured GHRBP was mixed rapidly with 100-fold native buffer<sup>13, 23</sup> by ultrasonication. Next, re-folding was performed. In order to test the temperature effect of the direct folding reaction, the reaction mixtures were incubated at 293, 297, 301, 305, and 309 K for 1 h to reach equilibrium. This equilibrium time is  $10^6$ – $10^9$  times longer than that observed in conventional protein folding studies<sup>23, 27, 28</sup>. Therefore, the aggregation reaction definitely reaches its equilibrium state in 1h. When the direct folding reaction reached equilibrium, the folding solution was centrifuged at 12000 g for 3 min to separate the soluble portion from the aggregation/precipitate. The protein concentration in the soluble portion was determined using a UV spectrometer at 277 nm with the extinction coefficient of GHRBP<sup>13, 26</sup>; the dilution effect was calibrated using a serial dilution curve. The aggregation fraction is equal to [1- (soluble protein/total protein)].

#### **Reduction/oxidation state of sulfur group of cysteine monitored using micro-Raman spectroscopy.**

Raman experiments were carried out using the Ranishow 1000 micro-Raman system (Ranishow Plc, Gloucestershire, UK). 5  $\mu$ l GHRBP solutions having varying folding states (10 mg/ml) were lyophilized on the surface of a platinum plate. The Raman spectra were collected around 2570 and 516  $\text{cm}^{-1}$ ; they represent the stretching frequencies of the S-H bond ( $\nu_{\text{S-H}}$ ) of the reduced cysteine and the S-S bond ( $\nu_{\text{S-S}}$ ) of the oxidized cysteine of GHRBP, respectively<sup>22, 29</sup>. The wave numbers of the Raman spectra were calibrated with silicon. Each spectrum was compared with the same folding state buffer to identify the signal of the protein and solvent, respectively.

#### **MALDI-TOF mass spectrometry**

The samples were prepared by mixing equal volumes of a matrix solution of  $\alpha$ -cyano-4-hydroxycinnamic acid (CHCA) (20 mg/ml) (Aldrich, Steinheim, Germany) in pure methanol and an analyte (protein) solution. 1  $\mu$ l of the resultant solution was deposited on a stainless sample probe and allowed to air-dry. Mass spectra of positively charged ions were acquired on a Bruker Autoflex instrument (Bruker Daltonik GmbH, Bremen, Germany) operated in the linear mode. A total of 500–2500 single-shot spectra were accumulated from each sample. The laser power was adjusted to 37–38%. The acceleration voltage was 20 KV. Flex analysis software packages (Bruker Daltonik GmbH, Bremen, Germany) were used for data processing.

## Protein mean-collision time determination using initial concentration of unfolded protein under a three-dimensional diffusion model

Similar to the observation made in our previous study that unfolded proteins aggregated with each other during the folding process, the mean collision time for protein molecules may indicate the upper bound of protein folding in its stable state. Therefore, the mean collision time for two protein molecules can be estimated based on the direct folding path, as described previously<sup>23</sup>. The concentrations of the protein, which is diluted by the native buffer, can be converted into the mean-distance ( $\bar{X}$ ) between protein molecules in a solution. According to the three-dimensional random walk model, the mean distance ( $\bar{X}$ ) is approximately the root mean square distance ( $X_{rms}$ ) for a protein random walk in three dimensions. The mean collision time for the protein diffusing across this distance can be determined by the following equations.

$$\bar{X} \approx X_{rms} = \langle X^2 \rangle^{\frac{1}{2}} = (6Dt)^{\frac{1}{2}} \quad (\text{Eq. 1})$$

where D denotes the diffusion constant of protein as defined in Eq. 2 by the Stoke-Einstein correlation,

$$D = \frac{kT}{6\pi\eta R_H} \quad (\text{Eq. 2})$$

where  $\eta$  denotes the viscosity of the protein solution. In this study, the unfolded protein was diluted into a native buffer; the dilution factor was 100. Therefore, the  $\eta$  is approximately 1 cp, which is the viscosity of water<sup>23</sup>.  $R_H$  denotes the effective hydration radius of the protein. According to the results of our study as well as other studies, the unfolded protein molecules are about 2.47 times larger than the native protein molecules<sup>13, 14, 23, 26, 30</sup>; the folding process may be a spontaneous process; therefore, the radius of the protein may reduce as an exponential decay function<sup>31</sup>. Meanwhile, the particle size analysis conducted in this study indicates that the hydration radius ( $R_H$ ) of the GHRBP of unfolded protein is 7.53 nm and that of the native state  $R_H$  is 2.75 nm.

The function of  $R_H$  is expressed as below.

$$R_H(t) = R_0(1 + 1.47e^{-ct}) \quad (\text{Eq. 3})$$

Where c is the hydration radius collapse factor. Therefore, the mean collision time during the diffusive process of protein folding can be expressed as follows.

$$1.47X_{rms}^2 \times e^{-ct} - 6D_0t + X_{rms}^2 = 0 \quad (\text{Eq. 4})$$

$$t = \frac{cX_{rms}^2 + 6D_0 \text{ProductLog}\left[\frac{1.47ce^{-\frac{cX_{rms}^2}{6D_0}} X_{rms}^2}{6D_0}\right]}{6cD_0} \quad (\text{Eq. 5})$$

The ProductLog can be expanded as following,

$$\text{ProductLog}\left[\frac{1.47ce^{-\frac{cX_{rms}^2}{6D_0}} X_{rms}^2}{6D_0}\right] = \frac{0.245cX_{rms}^2}{D_0} - \frac{0.1c^2 X_{rms}^4}{D_0^2} + \frac{0.0455c^3 X_{rms}^6}{D_0^3} \dots \dots \dots (\text{Eq. 6})$$

Therefore, the mean collision/diffusion time for a specified initial concentration of unfolded protein can be determined using the above expression.

### **Molecular simulation of protein aggregation**

In order to identify the molecular interactions involved in the protein folding process, a three-dimensional random walk simulation model is used in this study. This model is quite different from Eden's model<sup>19</sup> because the distribution of protein particles is considered randomly distributed in a defined three-dimensional box with a periodic boundary. The size of the simulation box is determined by the number of simulation particles and the mean distance  $\bar{X}$ , obtained from Eq. 1. Because the protein molecules are considered to be in constant Brownian motion, as described in Eq. 1 and 2, protein collision can be monitored and analyzed. In order to simulate the spontaneous protein folding process during the diffusion time, an activation factor of protein aggregation was introduced as follows:

$$A(t) = \frac{e^{-\frac{t}{\tau}}}{(1 + \log(T - 273))} \quad (\text{Eq. 7})$$

where  $\tau$  denotes the folding time constant and has a value of 500;  $T$  denotes the reaction temperature in Kelvin. We set the threshold to be 0.1. If the value  $A$  is lower than the threshold, the proteins will not interact with each other. In other words, the proteins reach a stable state at such a moment. By comparing the number of particles at the start of the process with the number that remained (the number of spontaneous folds), the protein aggregation fraction can be obtained.

### **Molecular image analysis of aggregated proteins through SEM and AFM**

The aggregated proteins were collected on a cover slip and washed with ddH<sub>2</sub>O to remove the salt and non-aggregated protein molecules. The bound water molecules of the sample were removed by lyophilization. The aggregated samples were coated with Pt by sputter. The sample was placed on the stage of the S4300 cold

field emission scanning electron microscope (Hitachi High-Technologies Co., Ltd , Tokyo, Japan), raised to a working distance of 19.4 mm. The sample was imaged at an accelerating voltage of 5 keV and a current of 7  $\mu$ A. The aggregate protein molecules in a solution environment were imaged with the NanoWizard®II BioAFM (JPK Instruments AG, Berlin, Germany) in tapping mode with a line rate of 0.9 Hz.

## Results

### Protein aggregation fraction analysis

Bacterial expression systems were used to express several heterologous proteins<sup>32, 33</sup>. The recombinant proteins which expressed in the cytosol of *Escherichia coli* often form as an inclusion body<sup>34</sup>. These proteins are mostly non-functional, aggregation, and misfolding<sup>34</sup> but in the high purity and yield<sup>35</sup>. In this study, the GHRBP was obtained from the inclusion body with high purity (more than 95 %) after IPTG induction (see fig. S1). Moreover, the GHRBP can be recognized by GHRBP antibody (see fig. S2) and the secondary structure of folded GHRBP (see fig. S3), analyzing by CD, which is similar to our previously study<sup>26</sup>. These data suggest that the folded GHRBP is in its native state.

As indicated in figure 1a, the fraction of aggregation was found to be 0.973 at the final concentration of approximately 0.20 mg/ml. This indicated that most of the GHRBP molecules were aggregated and precipitated. However, the aggregation fraction dropped rapidly when the initial concentration decreased. For instance, when the initial concentration of unfolded GHRBP is 5  $\mu$ g/ml, the fractions of aggregation decreased to 0.020. This indicates that over 98% protein molecules are folded into their native state. The mean collision time at this concentration, derived from Eq. 6, is 119.12  $\mu$ s at 301 K. This time interval is long enough for the unfolded GHRBP to fold into a stable state (Figure 1a).

### Three dimensional random walk simulations

From the simulation, we found that the aggregation fractions were constant even when the number of particles ( $n$ ) was different. The optimal number of particles for simulation is about 216 for a suitable calculation time. In addition, we found a good agreement between the simulation results and the experimental results (Figure 1a), suggesting that the driving force for the random movement of unfolded proteins in the solution is thermal fluctuation. Meanwhile, the particle size of the proteins (the hydration radius) shrinks spontaneously during the diffusive process, as indicated in Eq. 3. The optimal value of the hydration radius collapse factor  $c$  is 0.01.

In addition, the correlations among the precipitation fraction and the lag time ( $\Delta t$ ) fit with the logistic function (Figure 1b) very well. This function is a modified power law, which is consistent with Forrest and Witten's description<sup>19</sup>. This implies that the process may be diffusion-limited aggregation.

It is believed that the thermal fluctuations during protein folding may affect the reaction rate of protein self-stabilization. For the direct folding process, the optimal folding temperature is 301 K (Figure 2). Therefore, the DLA process competes with the spontaneous self-stabilization process in the direct folding reaction at a certain temperature.

### **SEM and AFM images of aggregated GHRBP**

As indicated in figure 3, hexagonal tablet aggregates of GHRBP molecules were observed during SEM (Figure 3a) and AFM (Figure 3b) analysis. The sizes of the aggregates at X and Y axes are approximately from 0.3  $\mu\text{m}$  to 5  $\mu\text{m}$  in diameter. The thicknesses, Z axis, of these hexagonal tablets are approximately 0.1  $\mu\text{m}$  to 0.3  $\mu\text{m}$ , as measured using the SEM image. As indicated in methods section above, we have ruled out the possibility that these tablets aggregate do not correspond to salt aggregates. Meanwhile, similar hexagonal tablets were observed by AFM both in air and solution conditions. During AFM analysis in air phase, the sizes of the aggregated tablets are approximately 3.3  $\mu\text{m}$  at X and Y axis, and 100 nm at Z-axis. The scan rate is 0.8 Hz. Interestingly, the surface is not smooth like the ones observed in SEM analysis, and there is a hole inside the hexagonal plate. The solution images of AFM measurements also indicate that a hexagonal shape was observed and the size of the aggregates is approximately 4.3  $\mu\text{m}$  at X, Y axis and 90 nm at Z axis. The scan rate is 0.8 Hz. Similar to that observed by AFM, there is a hole on the hexagonal plate for the air environment. Furthermore, part of hexagonal (L shape) aggregate was observed by AFM measurements. The length of one edge is approximately 100 nm and the thickness is approximately 30 nm suggesting that the aggregate of GHRBP might not have formed from a single aggregation core.

### **Raman and mass spectroscopy analysis of GHRBP aggresome**

In order to understand the mechanism of protein aggregation, both Raman and MALDI-TOF mass spectroscopy have been used. Raman spectra analysis of aggregated GHRBP displays the S-S stretching mode at 516.6  $\text{cm}^{-1}$  for oxidize disulfide bonds and the S-H bond stretching mode at 2562.1  $\text{cm}^{-1}$  for reduced S-H bonds (Figure 4b). However, the soluble portion of GHRBP in the same reaction contains only the oxidized disulfide bonds (Figure 4a). As indicated in figure 5, the acetonitrile-soluble portion of aggregated protein

contains some monomer of GHRBP with the molecular weight approximately 22.3 kDa. Meanwhile, stable dimer (approximately 44.6 kDa), trimer (approximately 66.8 kDa) and tetramer (approximately 88.8 kDa) of stable polymers were also observed at the same time. Based on Raman spectra analysis, we suggest that these polymers may be linked through inter-molecular disulfide bonds.

## Discussion

### **Both aggregated and soluble proteins are observed in direct folding path.**

According to the data in figure 1, it is obvious that both the soluble and aggregated precipitated fractions are observed. Meanwhile, by analyzing the oxidation states of their disulfide bonds, we found that both the reduced state (S-H) and the oxidized state (S-S) signals were present that corresponds to the unfolded and the folded states. According to the “first-order like phase transition” reaction model<sup>13, 14, 30</sup>, proteins in a direct folding reaction are trapped in a phase transition line where the two states co-exists in the same zone. These data collectively suggest that aggregated and soluble protein can be observed in a direct folding reaction.

### **Determination of folding stabilization time of GHRBP at various temperatures using auto-correlation function**

As described previously, the mean collision time for the GHRBP molecules folding in 0.414 mg/ml was approximately 10.23  $\mu$ s at 309 K. However, from the result shown in figure 1a, the fraction of aggregation was found to be 0.70 at a mean collision time of 10.23  $\mu$ s. This suggested that most of the proteins were unfolded in solution. However, when the initial concentration is decreased to 10.35  $\mu$ g/ml, the mean collision time was found to be approximately 119.12  $\mu$ s at 301 K. This time period is long enough for GHRBP to fold into a stable state, as the fractions of aggregation is decreased to 0.02 (Figure 1a). The observed precipitation (2%) can be attributed to the back ground for the protein molecules that are mixed in the solution. Meanwhile, in a macroscopic experiment such as protein folding, it is impossible to synchronize all the molecules of the proteins to fold from unfolded state to native state at the same time. The mean collision is upper bound for protein stabilization. Therefore, a direct measurement of collision time at the half fraction of protein aggregation is not viable. However, the aggregation reaction time can be obtained using the autocorrelation function (ACF) of the protein aggregation fraction. The correlation function can be expressed as follows:

$$\Gamma(\Delta t) = \langle C(t) \cdot C(t+\Delta t) \rangle \quad (\text{Eq. 8})$$

where  $C(t)$  denotes the aggregation fraction at time  $t$ ,  $\Delta t$  denotes the time interval between the observations, and the value of  $\Gamma(\tau_c)$  is the half-width of the ACF<sup>36</sup> (Figure 1b). The aggregation correlation time ( $\tau_c$ ), which is the time required for GHRBP to stabilize itself in a folding process, is approximately 29.7 to 14.8  $\mu\text{s}$  at 297K and 301 K, respectively, immaterial whether the experimental reaction was synchronized or not. Thus, in low concentrations, proteins have a chance to fold into a stable form before any collisions occur. This phenomenon is consistent with previous studies<sup>16</sup>. Furthermore, the upper bound estimate of the protein folding stabilization time and the time period of protein aggregation are not equal. The time for aggregates formation is far longer than the stabilizing time of protein interaction. Namely, this stabilizing time is the critical time for protein folding into native state.

As mentioned previously, the mean collision time is also an upper bound estimate for protein folding into stable state in the diffusive processes. Thus, if proteins do not fold and settle into a stable state during this period, they may aggregate and precipitate consequently. Therefore, the mean collision time in the folding reaction is the folding stabilizing time of the protein molecules.

#### **Protein aggregation reaction is a diffusion-limited aggregation (DLA) process in solution.**

The data in the figure 1b implies that the aggregation process may follow the diffusion-limited aggregation process. Furthermore, flat hexagonal plate aggregates of GHRBP molecules were observed by SEM (Figure 3a) and AFM (Figure 3b). These aggregated conformations are similar to the ice-crystal. These hexagonal shapes may relate to the intrinsic properties of the unfolded GHRBP. These conformations of the aggregated proteins similar to the ones adopted by the ice-crystal may suggest that the former may be the fractal structure. However, AFM imaging indicated presence of clear hexagonal edge of aggregated piece. This indicated that the aggregation process may not initiate from a single nucleation core of each aggregate. Meanwhile, based on simulation process, we proposed that the aggregated fractions can interact with each other. The fact that our simulation results correlate well the experimental observations indicates that the aggregation process is regulated by the diffusion-collision time among protein molecules. Moreover, the aggregate may not be formed from single nuclear core. This is consistent with the AFM imaging studies. As the aggregation processes among protein molecules are parallel processes, the stabilization time of protein is as fast as 20–30  $\mu\text{s}$ . Thus, our data suggest that the aggregation structure may have been caused by a parallel process and the off-path folding reaction may follow the diffusion limited aggregation (DLA) process.

### **Time scale for protein stabilization is longer than that for secondary structure formation**

As indicated previously, the time period for protein stabilization is approximately 20 to 30  $\mu$ s. It is known that that timescale for the secondary structure formation may be as fast as 100 to 160 ns for a helical structure formation, monitored using laser T jump study<sup>37</sup> or Photolysis<sup>38</sup>. For a  $\beta$ -hairpin formation, it takes approximately 6  $\mu$ s in a laser T jump study.<sup>39</sup> However, formation of a tertiary structure may vary from sub-milliseconds to minutes. It has been reported that the intra-molecular interaction is formed approximately from 100 microseconds to milliseconds<sup>20</sup>. Thus, based on the protein stabilization time, we believe that the protein is stable once the secondary structure and inter-molecular interactions are formed. Therefore, the time scale for monitoring the secondary structure formation may not indicate the actually time scale of protein folding. Moreover, the folding stabilizing time shall be considered as the initial time scale for protein aggresome formation or precipitation. Thus, the exact time scale for the observation of protein aggregation is relatively longer than stabilization time. This study does not only reveal the molecular mechanism of protein aggregation but also indicate the reaction time for the protein to fold into a stable state.

### **The aggresome may be caused by the mis-linked disulfide bonds and hydrophobic interactions.**

In this study, we observed the formation of the tetramer of GHRBP (figure 5). In addition, both oxidized disulfide bonds and free thiol bonds are observed in the aggregated fractions. These results implied that the intermolecular mis-linked disulfide bonds might exist in the aggresome. As indicated in methods section above, these aggregates can be dissolved by sonicating these aggresome with an amphiphilic solvent such as acetonitrile. This indicates that hydrophobic interactions play an important role in the formation of aggresome. The acetonitrile-soluble proteins analyzed using MALDI-TOF mass spectrometer indicated that stable forms of monomer, dimer, trimer and tetramer of GHRBP could be observed in the precipitated portion (Figure 5), but not in the soluble portion (data not shown). Therefore, these aggregates of GHRBP are caused by disulfide mis-linkages and hydrophobic interactions, *in vitro*. However, a native aggresome, such as inclusion body of *E. coli*, did not form oligomers of proteins when the same procedure was used (data not shown). By comparing both the *in vitro* and *in vivo* experiments, we conclude that the hydrophobic interaction is the major factor for the aggresome formation. This suggests that suitable protection chaperones and enzymes that can prevent the formation of mis-linked disulfide bonds are necessary, *in vivo*.

### **Temperature affects the thermal dynamics process of protein folding.**

During the folding process, the thermal fluctuation may affect the reaction rate of protein self-stabilization (Figure 2). By comparing with the first-order-like state transition model<sup>13, 14, 30</sup>, we believe that the forbidden region of direct folding reaction may have been caused by the interactions among unfolded proteins. An over critical reaction regulated by solvent environment and denaturant may play a crucial role to avoid effective collision between proteins, and hence protein folds spontaneously during this period<sup>13</sup>. This phenomenon may explain the possible mechanism and function of molecular chaperones<sup>13, 14, 23, 26, 30</sup> that assist protein folding.

By comparing the functions of activation factor (Eq. 8) and mean collision time (Eq. 6), it is imperative that the aggregation activation factor decreases faster than collision time when the reaction temperature is raised. However, the V-shaped trend of the correlation time ( $\tau_c$ ) versus the reaction temperature (Figure 2) indicates that the reaction rate of the protein that folds spontaneously is not significantly faster than DLA. This makes us further conclude that the direct protein folding is a competitive process between a spontaneous folding and DLA.

## Conclusion

In summary, this is the first study wherein the stabilization time of protein folding has been observed directly and quantified. Depending upon the temperature, it ranges from 14.8 to 29.7  $\mu$ s. The protein folding mechanism in a cell-free system is an antagonistic reaction between spontaneous folding and DLA. The aggregation of proteins during folding process may be caused by intermolecular disulfide bonds mis-linkage and hydrophobic interactions. This observation also indicated that the aggregation process of misfolded protein is a parallel process and these misfolded aggregates may possess secondary structure which is similar to  $\beta$ -amyloid or prion. Namely, these proteins may share similar aggregation mechanism.

## Acknowledgements

We would like to thank Dr. P.C. Huang in Johns Hopkins University and Dr. J.S. Chen in Chung Yuan Christian University, for their valuable suggestions and discussions on the paper. We would like to thank *National Synchrotron Radiation Research Center* to provide the CD spectrophotometer in this study. This study was supported in part by grant NSC 97-2112-M-009-009-YM3 and ATU project.

## References

1. R. Lakshminarayanan, D. Fan, C. Du and J. Moradian-Oldak, *Biophys J*, 2007, **93**, 3664-3674.
2. G. M. Verkhivker, *Biopolymers*, 2004, **75**, 420-433.
3. R. Verma, J. C. Crocker, T. C. Lubensky and A. G. Yodh, *Phys Rev Lett*, 1998, **81**, 4004-4007.
4. D. Singh, B. Raman, T. Ramakrishna and C. M. Rao, *Molecular Vision* 2006, **12**, 1372-1379.
5. K. Sode, S. Ochiai, N. Kobayashi and E. Usuzaka, *International Journal of Biological Sciences*, 2007, **3**, 1-7.
6. D. Eisenberg, R. Nelson, M. R. Sawaya, M. Balbirnie, S. Sambashivan, M. I. Ivanova, A. Madsen and C. Riek, *Accounts of Chemical Research*, 2006, **39**, 568-575.
7. P. Chien, J. S. Weissman and A. H. DePace, *Annual Review of Biochemistry*, 2004, **73**, 617-656.
8. C. M. Dobson, *Nature*, 2003, **426**, 884-890.
9. F. E. Cohen and J. W. Kelly, *Nature*, 2003, **426**, 905-909.
10. D. J. Selkoe, *Nature*, 2003, **426**, 900-904.
11. C. M. Dobson and P. J. Hore, *Nature Structural Biology*, 1998, **5**, 504-507.
12. A. L. Mallam and S. E. Jackson, *Journal of Molecular Biology*, 2007, **366**, 650-665.
13. C.-C. Chang, Y.-C. Su, M.-S. Cheng and L.-S. Kan, *Physical Review E*, 2002, **66**, 021903.
14. Y.-L. Liu, H.-T. Lee, C.-C. Chang and L.-S. Kan, *Biochemical and Biophysical Research Communications*, 2003, **306**, 59-63.
15. C.-C. Chang, P.-Y. Lin, X.-C. Yeh, K.-H. Deng, Y.-P. Ho and L.-S. Kan, *Biochemical and Biophysical Research Communications*, 2005, **328**, 845-850.
16. K. Kuwajima, *Proteins*, 1989, **6**, 87-103.
17. R. García-Mata, Z. Bebök, E. J. Sorscher and E. S. Sztul, *Journal of Cell Biology*, 1999, **146**, 1239-1254.
18. S. R. Forrest and T. A. Witten, Jr., *Journal of Physics A*, 1979, **12**, L109-L117.
19. T. A. Witten and L. M. Sander, *Physical Review Letters*, 1981, **47**, 1400.
20. O. Bieri and T. Kiefhaber, *Biological Chemistry*, 1999, **380**, 923-929.
21. W. A. Eaton, V. Muñoz, S. J. Hagen, G. S. Jas, L. J. Lapidus, E. R. Henry and J. Hofrichter, *Annual Review of Biophysics and Biomolecular Structure*, 2000, **29**, 327-359.
22. H. Roder and W. Colón, *Current Opinion in Structural Biology*, 1997, **7**, 15-28.

23. C.-C. Chang, X.-C. Yeh, H.-T. Lee, P.-Y. Lin and L.-S. Kan, *Physical Review E*, 2004, **70**, 011904.
24. S. Kohei, E. Welker and H. A. Scheraga, *Biochemistry*, 2001, **40**, 15002-15008.
25. E. Welker, W. J. Wedemeyer, M. Narayan and H. A. Scheraga, *Biochemistry*, 2001, **40**, 9059-9064.
26. C.-C. Chang, C.-T. Tsai and C.-Y. Chang, *Protein Engineering*, 2002, **15**, 437-441.
27. P. S. Kim and R. L. Baldwin, *Annual Review of Biochemistry*, 1982, **51**, 459-489.
28. T. Y. Tsong, R. L. Baldwin, P. McPhie and E. L. Elson, *Journal of Molecular Biology*, 1972, **63**, 453-469.
29. S. K. Freeman, ed., *Applications of laser Raman spectroscopy*, Wiley, New York, 1974.
30. C.-C. Chang, M.-S. Cheng, Y.-C. Su and L.-S. Kan, *Journal of Biomolecular Structure and Dynamics*, 2003, **21**, 247-255.
31. L. Cyrus, *Journal of Physical Chemistry*, 1968, **65**, 44-45.
32. M. Zhang, X. Jiang, Z. Su, J. Lin, Q. Xiang, Z. Yang, Y. Huang and X. Li, *Applied Microbiology and Biotechnology*, 2011, 1-9.
33. K. Chen, J. Ye, C. Liu, P. Di, J. Chen, Y. Xiao, H. Li and W. Zhang, *Molecular Biology Reports*, 2011, 1-8.
34. G. Hannig and S. C. Makrides, *Trends in Biotechnology*, 1998, **16**, 54-60.
35. Y.-J. Wang, Y.-D. Liu, J. Chen, S.-J. Hao, T. Hu, G.-H. Ma and Z.-G. Su, *International Journal of Pharmaceutics*, 2010, **386**, 156-164.
36. H. S. Chan and K. A. Dill, *The Journal of Chemical Physics*, 1994, **100**, 9238-9257.
37. B. Gruenewald, C. U. Nicola, A. Lustig, G. Schwarz and H. Klump, *Biophysical Chemistry*, 1979, **9**, 137-147.
38. K. C. Hansen, R. S. Rock, R. W. Larsen and S. I. Chan, *Journal of the American Chemical Society*, 2000, **122**, 11567-11568.
39. P. A. Thompson, W. A. Eaton and J. Hofrichter, *Biochemistry*, 1997, **36**, 9200-9210.

## Figure legends

Figure 1. Fraction of protein aggregation versus diffusion collision time at various temperatures. (a)  $T = 301$  K.

The solid squares and dotted line denoted the experimental results and the simulation results, respectively. (b) The auto-correlation function of the fraction of protein versus diffusion collision time. The horizontal and vertical lines in the figure denoted the fitting of the auto-correlation function by logistic function. The  $\tau_c$  represented the correlation time for which  $\Gamma(\tau_c) = 1/2 \Gamma(0)$ .

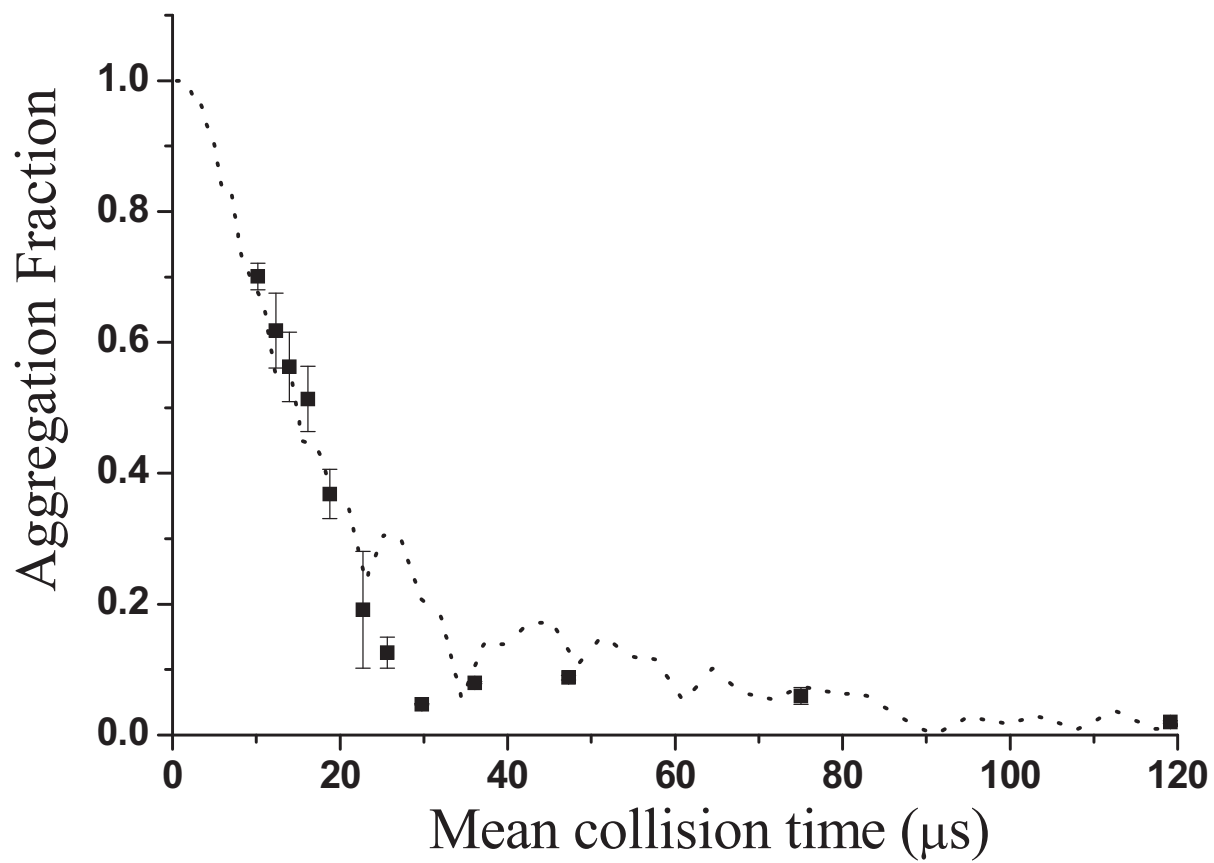
Figure 2. The temperature dependent protein folding time. The thermal fluctuation would affect the reaction rate of protein self-stabilization, and the 301K is the most optimal refolding temperature of GHRBP.

Figure 3. SEM and AFM images of aggregated GHRBP. (a) SEM image of hexagonal aggregates of GHRBP, the GHRBP would be form regular shape in the DLA aggregation process. (b) AFM images of GHRBP aggregates. The aggresome of GHRBP was similar to SEM image but with roughly surface.

Figure 4. Raman shift of GHRBP aggregates and soluble form. (a) The S-S ( $\nu_{S-S}$ ) stretching region. (b) The S-H ( $\nu_{S-H}$ ) stretching region. The gray line and black line denoted precipitated and soluble GHRBP, respectively.

Figure 5. MALDI-TOF mass spectra of acetonitrile soluble GHRBP aggregates. The molecular weight of GHRBP is 22.32 kDa. There are monomer, dimer, trimer and tetramer of the GHRBP. Where the  $m$  denoted the molecule of GHRBP.

**Figure 1a**



**Figure 1b**

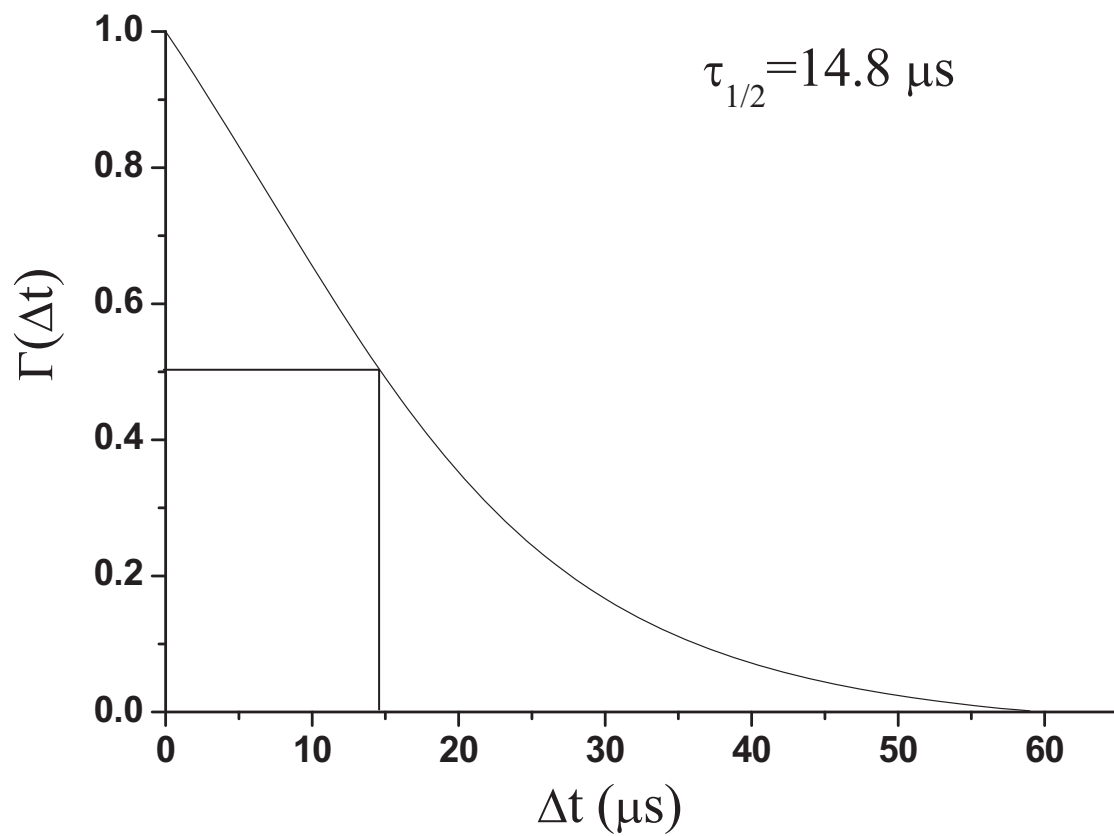
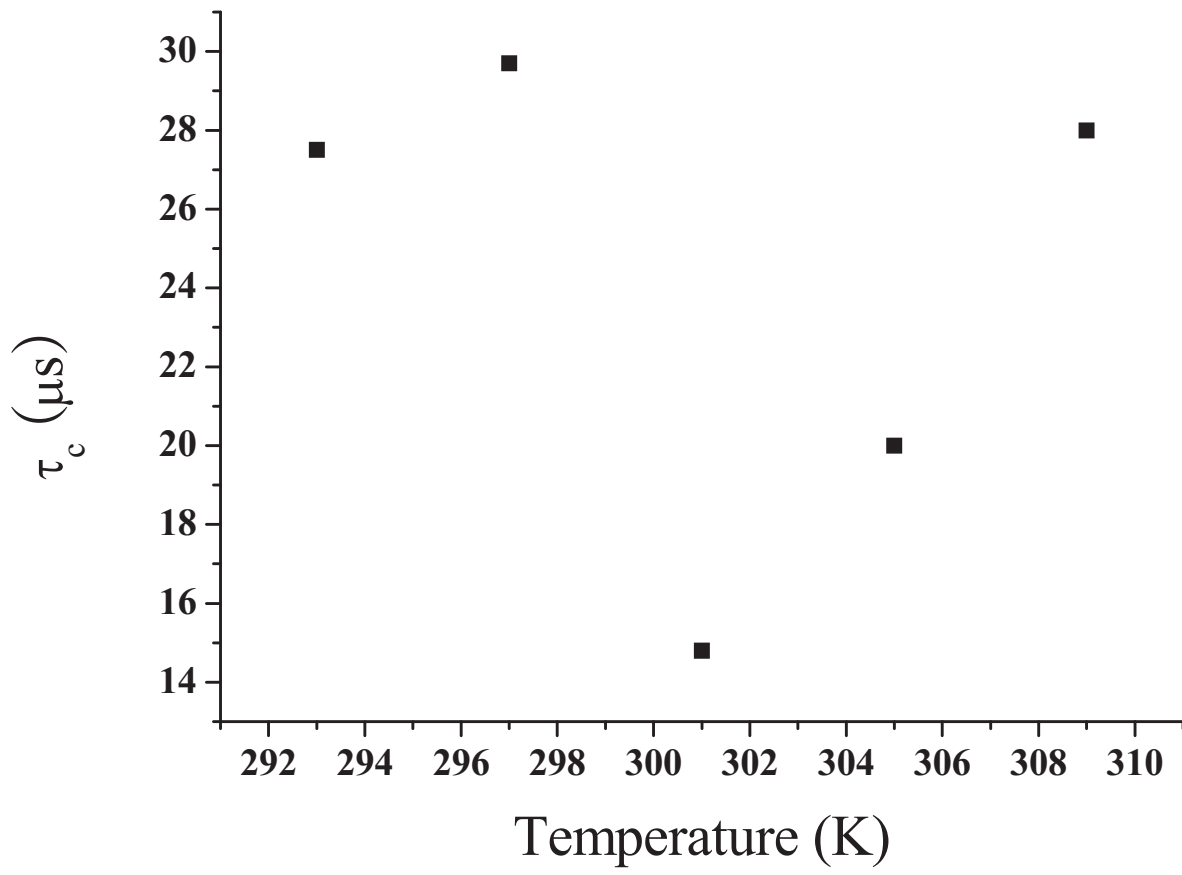


Figure 2



**Figure 3a**

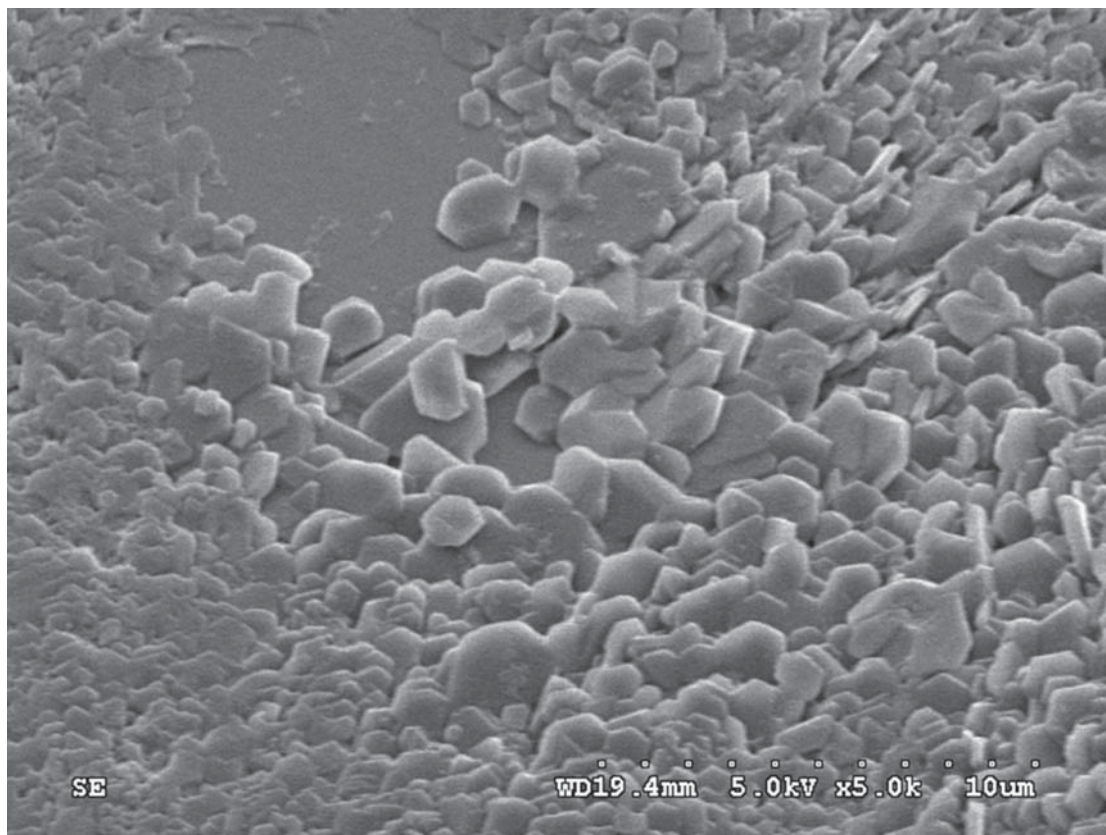


Figure 3b

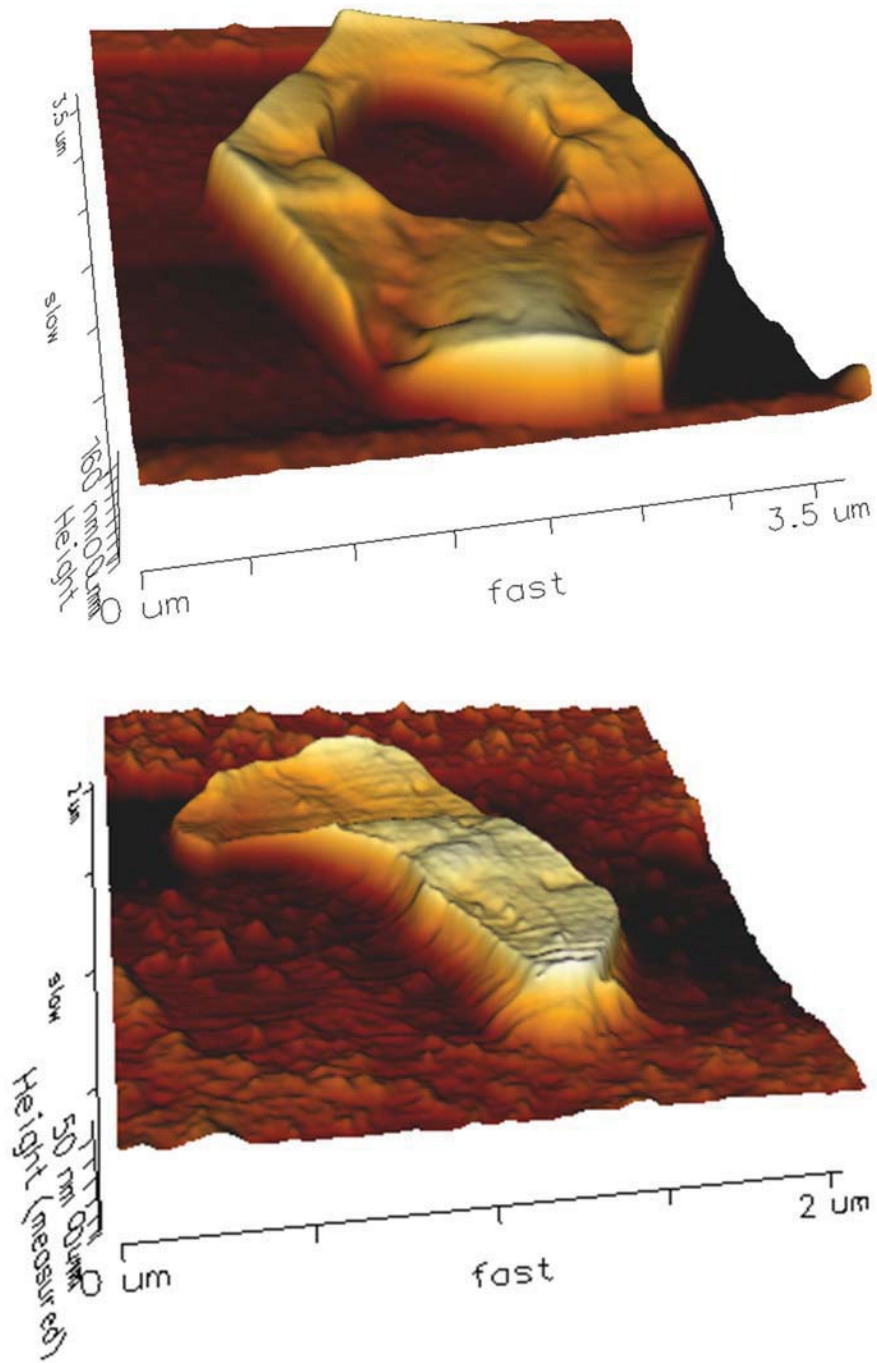
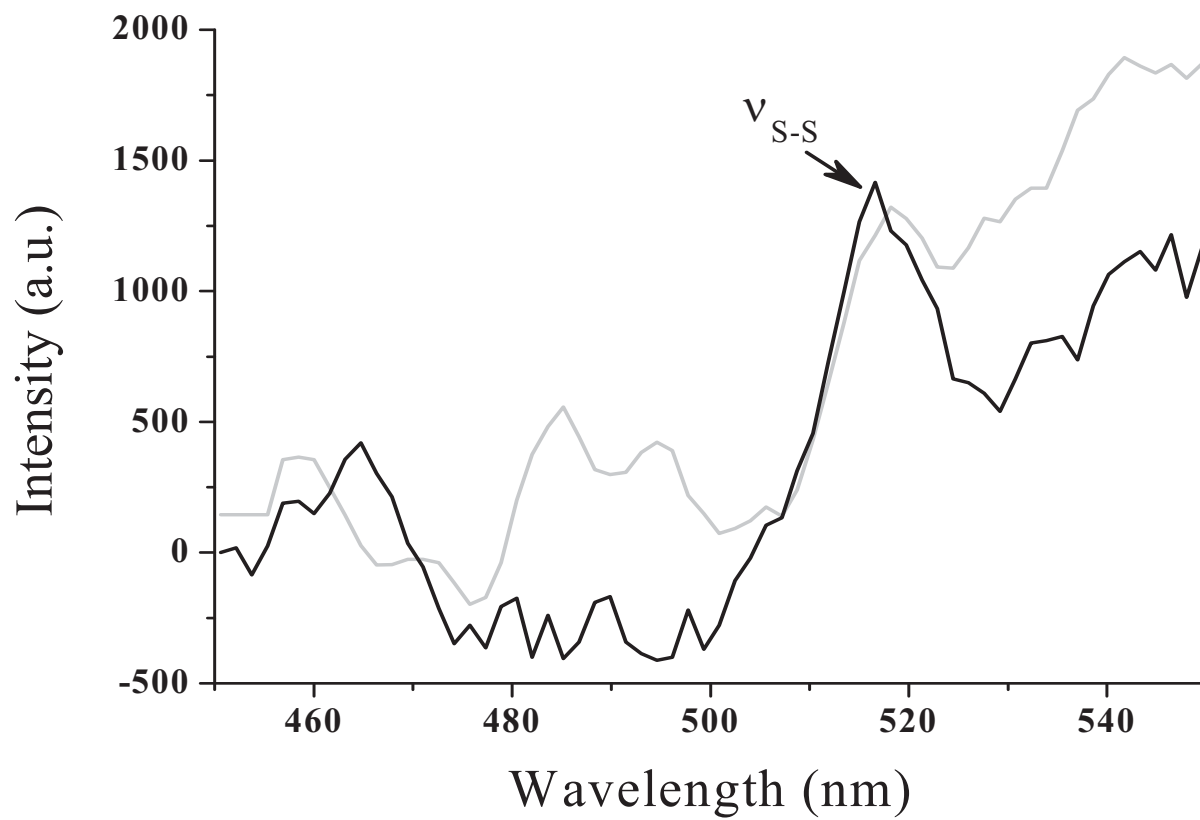


Figure 4a



**Figure 4b**

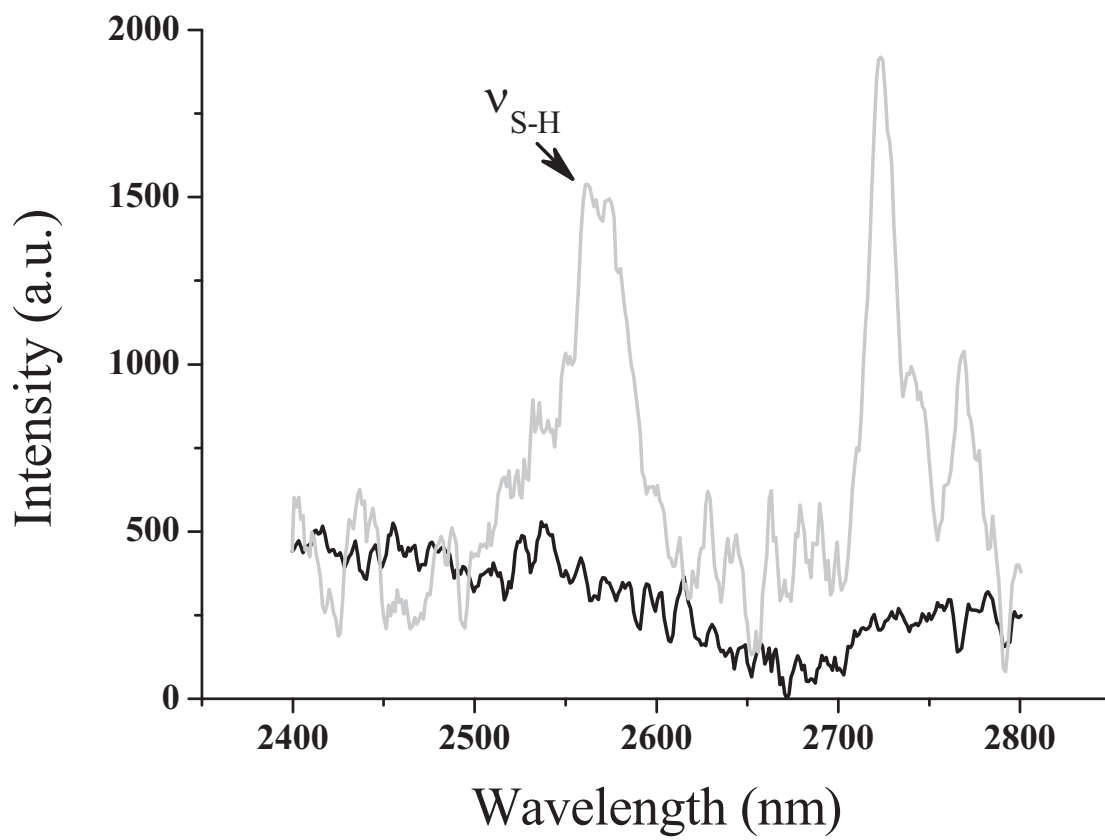
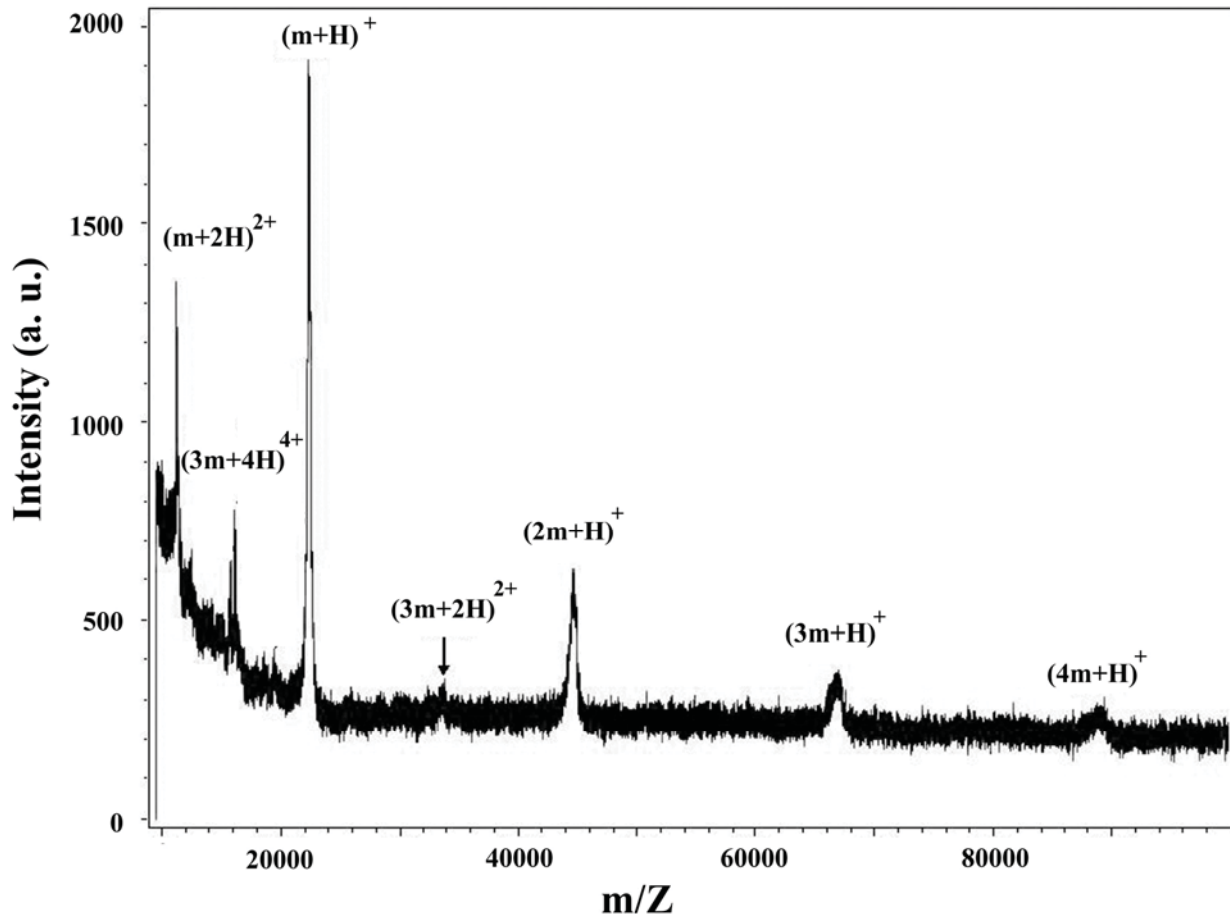


Figure 5



## Laser induced popcornlike conformational transition of nanodiamond as a nanoknife

Chia-Ching Chang,<sup>1,a)</sup> Pei-Hsin Chen,<sup>1</sup> Hsueh-Liang Chu,<sup>1</sup> Tzu-Cheng Lee,<sup>1</sup> Ching-Chung Chou,<sup>1</sup> Jui-I Chao,<sup>1,b)</sup> Chien-Ying Su,<sup>2</sup> Jyh Shin Chen,<sup>2</sup> Jin-Sheng Tsai,<sup>3</sup> Chuan-Mei Tsai,<sup>4</sup> Yen-Peng Ho,<sup>5</sup> Kien Wen Sun,<sup>6</sup> Chia-Liang Cheng,<sup>7</sup> and Fu-Rong Chen<sup>8</sup>

<sup>1</sup>Department of Biological Science and Technology, National Chiao Tung University, Hsinchu, Taiwan 300, Republic of China

<sup>2</sup>Instrument Technology Research Center, National Applied Research Laboratories, Hsinchu, Taiwan 300, Republic of China

<sup>3</sup>National Synchrotron Radiation Research Center, Hsinchu, Taiwan 300, Republic of China

<sup>4</sup>National Nano Device Laboratories, Hsinchu, Taiwan 300, Republic of China

<sup>5</sup>Department of Chemistry, National Dong Hwa University, Hualien, Taiwan 300, Republic of China

<sup>6</sup>Department of Applied Chemistry and Institute of Molecular Science, National Chiao Tung University, Hsinchu, Taiwan 300, Republic of China

<sup>7</sup>Department of Physics, National Dong Hwa University, Hualien, Taiwan 300, Republic of China

<sup>8</sup>Department of Engineering and System, National Tsing Hua University, Hsinchu, Taiwan 300, Republic of China

(Received 22 April 2008; accepted 14 June 2008; published online 22 July 2008)

Nanodiamond (ND) is surrounded by layers of graphite on its surface. This unique structure feature creates unusual fluorescence spectra, which can be used as an indicator to monitor its surface modification. Meanwhile, the impurity, nitroso (C—N=O) inside the ND can be photolyzed by two-photon absorption, releasing NO to facilitate the formation of a  $sp^3$  diamond structure in the core of ND and transforming it into a  $sp^2$  graphite structure. Such a conformational transition enlarges the size of ND from 8 to 90 nm, resulting in a popcornlike structure. This transition reaction may be useful as nanoknives in biomedical application. © 2008 American Institute of Physics. [DOI: 10.1063/1.2955840]

Nanodiamond (ND) has been shown to be nontoxic and is considered one of the most important biocompatible nanomaterials.<sup>1</sup> Its unique fluorescence properties allow observation of its presence in variant wavelengths.<sup>2,3</sup> The surface of ND can be carboxylated; the nanoparticles so modified exhibit high affinity to proteins,<sup>2,4</sup> rendering conjugation possible with DNA,<sup>3,5</sup> lysozyme,<sup>2</sup> and cytochrome c.<sup>6</sup>

ND (average diameter 4–6 nm, Nanodiamond, TI, Switzerland) has been synthesized from the detonation of the mixture of trinitrotoluene and hexogen.<sup>7</sup> Its conformation and composition remain unclear. In this study, we studied the conformation using ultra high resolution field emission transmission electron microscopy (FE-TEM) (JEM-2010F, JEOL, Ltd. Tokyo, Japan), electron energy loss spectroscopy (EELS), field emission scanning electron microscopy (SEM) (Hitachi S-4300, Hitachi High-Technologies Corporation, Tokyo, Japan) and atomic force microscopy (AFM) (D3100, Veeco Instruments Inc, NY, USA) and Raman spectroscopy.

As shown in Fig. 1, both AFM and TEM images indicate that the size of the ND particles are uniform [Fig. 1(a)]. A magnified view inside red circle is shown as an inset in upper right corner, which indicates that the ND contains a 6 nm diamond core and around 1 nm thick graphite shell. The lattice spacing is about 2 Å which may correspond to {111} plane of diamond structure. The inset in the low right corner

is a diffraction pattern from the NDs in the view. It shows a typical electron diffraction ring for diamond. The inset in the low left corner is an AFM image that shows the surface morphology of the ND. Figure 1(b) is a SEM image of ND after laser radiated. The average size of laser radiated ND is about 90 nm. Inset is a TEM image shows the magnified view of ND after laser radiated.

These observations are consistent with the Raman spectral analysis [Figs. 2(a) and 2(b)] and nanobeam EELS spectra analysis [Figs. 2(c)]. As indicated in Fig. 2(a) the ND contains both broaden diamond Raman absorption at 1324  $\text{cm}^{-1}$  and a planar graphite (*G* band) spectrum at 1575  $\text{cm}^{-1}$ . The broaden 1324  $\text{cm}^{-1}$  peak may contain part of the absorption of distortion graphite (*D* band). This core-shell interface structure may create unique surface plasmonic mode and emit the unusual fluorescence spectra in variant wavelengths, as mentioned in previous studies.<sup>2,3</sup>

Elemental data provided by manufacturer showed that there is 9.3% of trace nitrogen inside the structure of the ND. However, previous surface modification study indicated that no nitrogen containing functional group could be observed on the ND surface.<sup>7</sup> We examined the ND with Raman spectroscopy in the range of 500–1100  $\text{cm}^{-1}$ , and detected a very weak signal near 604  $\text{cm}^{-1}$ . This signal was seen only after long (10 min) accumulation [Fig. 2(b)], and is attributable to nitrogen containing functional group nitroso (—C—N=O).<sup>8</sup> By systematic simulation of the nitroso containing molecules from one carbon,  $\text{H}_3\text{C—N=O}$ , to 30 carbons, Tri-adamantane-NO (R—C—N=O), with Gaussian 03 (B3LYP/6–31G (d) Opt(Raman), with scaling factor 0.89), we noted the Raman shift of the bending mode of

<sup>a)</sup> Author to whom correspondence should be addressed. Electronic mail: ccchang01@faculty.nctu.edu.tw. Also at: the Institute of Physics, Academia Sinica, Taipei, Taiwan 11529, R.O.C.

<sup>b)</sup> Also at the Institute of Pharmacology and Toxicology, Tzu Chi University, Hualien, Taiwan 970, R.O.C.

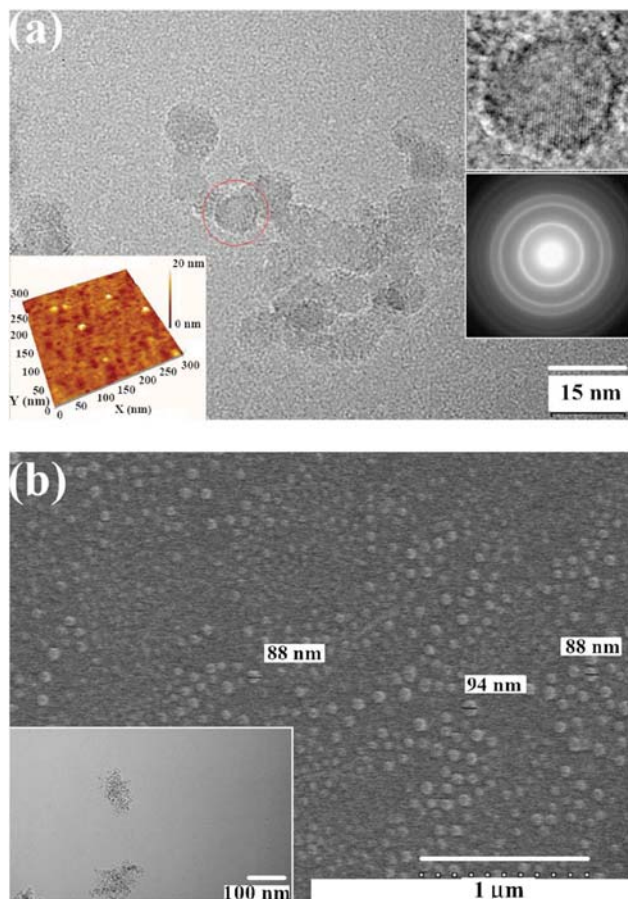


FIG. 1. (Color online) (a) TEM image of ND. A magnified view inside red circle is shown as an inset in upper right corner. The lattice spacing is about 2 Å which may correspond to {111} plane of diamond structure. The inset in the low right corner is a diffraction pattern from the NDs in the view. It shows a typical electron diffraction ring for diamond. The inset in the low left corner is an AFM image that shows the surface morphology of the ND. (b) SEM image of ND after laser radiated. The average size of laser radiated ND is about 90 nm. Inset is a TEM image shows the magnified view of ND after laser radiated.

—C—N of nitroso increased from  $504\text{ cm}^{-1}$  and plateau near  $606\text{ cm}^{-1}$  when the carbon number was larger than ten. On this basis, we surmise that the Raman peak at  $604\text{ cm}^{-1}$  is caused by the bending mode of —C—N=O of nitroso of ND.

Nitroso is an active functional group; dissociation of the C—N bond of nitroso (—C—N=O) is in the range of 225–270 nm of UV light,<sup>8</sup> where nitroso undergoes photolysis and releases nitro monoxide. However, we found that there was no photolysis taking place of the NDs, when irradiated with regular UV light. It is possible that the electronic band gap of ND is around 5.47 eV (or approximately 227.8 nm UV wavelength)<sup>9</sup> and the UV light was absorbed by the diamond structure.

In further test, the possible involvement of photolysis within the ND, we irradiated the ND solution for 30 s with 532 nm; 20 ns, full width at half maximum, Nd:YAG (yttrium aluminum garnet), pulse laser (LS2137U/2, Lotis TII Ltd., Minsk, Belarus); with 140 mW average power; 10 Hz repetition rate; 2 mm beam size. Interestingly, a popcornlike conformational change of ND was observed after the laser irradiation. The size of ND changed from 8 nm [Fig. 1(a)] to approximate 90 nm [Fig. 1(b)]. This observation is consistent

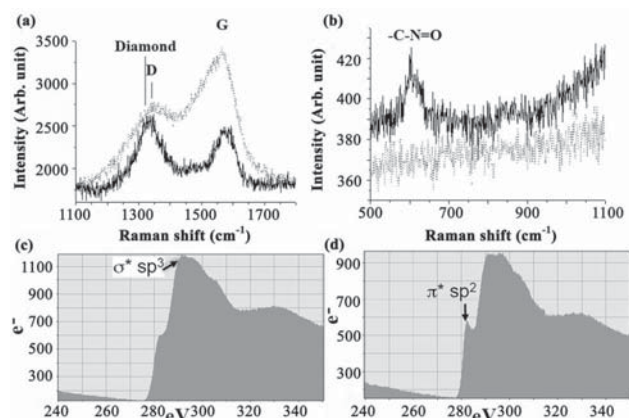


FIG. 2. (a) Raman spectra of the ND (solid line) and laser irradiated ND (dash line) at the range from 1100 to 1800  $\text{cm}^{-1}$ . (b) The Raman range of 500–1100  $\text{cm}^{-1}$ . (c) and (d) are EELS spectra of ND before and after laser radiation, respectively. (c) shows the very weak signal associated with the  $\pi^*$  bond, while (d) shows enhancement of the  $\pi^*$  signal.

with our previous observation.<sup>10</sup> These laser irradiated particles were fragile and no clear granule image could be observed by FE-TEM [Fig. 1(b)] when they were removed from glass substrate. Raman spectra [Figs. 2(a) and 2(b)] indicated that both peaks of nitroso group and diamond structure disappeared after the laser irradiation; instead, there were D (distortion) and G bands of graphite.<sup>11</sup> Similar observation was obtained by surface analysis of the FE-TEM. The transformation from diamond to graphite after laser irradiation is also confirmed from the EELS spectra. Fig. 2(c) and 2(d) are EELS spectra taken from ND before and after laser radiation, respectively. Figure 2(c) shows the very weak signal associated with the  $\pi^*$  bond (at 283 eV), while Fig. 2(d) shows enhancement of the  $\pi^*$  signal. That suggests that laser radiation may promote the transformation of  $sp^3$  to  $sp^2$  bonds for NDs

These results suggested that photolysis of nitroso and conformational change of this ND occurred concomitantly. As shown in previous studies,<sup>7</sup> nitroso groups are buried within the structure of ND which is consistent with the assumption of our previous study.<sup>10</sup> Their photolysis into nitro monoxide (NO) molecules may generate large internal pressure triggering conformational changes (explosion) in ND. This can be envisioned as a transformation of  $sp^3$  tetrahedral diamond core [Fig. 1(a)] into a  $sp^2$  planar graphite conformation, expanding its size, approximately 12 fold [Fig. 1(b)]. This is similar to our previous observation.<sup>10</sup>

Although the 225–270 nm UV light may induce photolysis of CNO group, the ND structure may absorb UV light and protect it. We have observed that ND is stable under both bright light and regular UV nm light irradiation; it does not absorb long wavelength 532 nm light. However, under ultra-high intensity condition (around  $2.2 \times 10^7\text{ W/cm}^2$ ), there is a nonlinear two-photon absorption effect which allows the CNO group of ND to absorb two incident photons of 532 nm. As a result, multiple ND photolyses occur simultaneously. We propose the molecular mechanism of diamond graphite transition of ND involves a popcornlike conformational transition which is a physical explosion reaction, with affecting distance is in submicron range (around 90 nm). Such is the case, ND may be used as a nanoknife in biosystems, in addition to other applications.

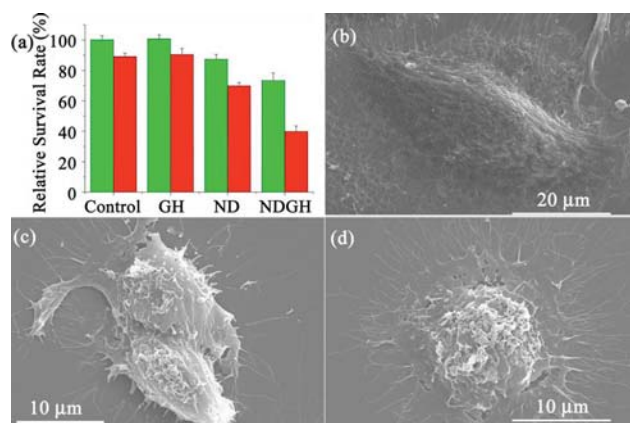


FIG. 3. (Color online) (a) Cell viability assay, (b) SEM images of the A549 cell lines, which were not treated with ND, (c) treated with ND and (d) irradiated with laser following ND treatment. The green bar denotes the cells without laser irradiation and the red bar denotes the cell after laser irradiation and incubation for 24 h.

The feasibility of ND as a nanoknife was indeed tested. We coupled ND to growth hormone (GH), one of the typical growth factors for certain normal tissues and carcinoma. It exerts regulatory functions in controlling metabolism, balanced growth, and differentiated cell expression by acting on specific receptors, GH receptor (GHR), in liver or on cartilage cell surface, triggering a phosphorylation cascade. Thus numerous signaling pathways are modulated and specific gene expression dictated.<sup>12</sup> GH has also been reported to stimulate melanoma cell growth.<sup>12,13</sup> The level of GH receptors is relatively higher in melanocytic tumorous than normal cutaneous cells.<sup>12,13</sup> Similar studies have reported for both mammary epithelial and colorectal cancer cells.<sup>13</sup> GHR is one of the general targets of cancer drug development, as blocking or inhibiting the function of GHR may be a basis for cancer therapy.

The lung cancer cell A549 was used as a model system to be treated with ND linked GH. The graphite surface of ND was first carboxylated by mixing ND with nitrate/sulfate (9:1) at 70 °C and stirred for 24 h. The excess acid was neutralized with 0.1N NaOH and washed with ddH<sub>2</sub>O. The GH was prepared in our laboratory using recombinant techniques as described previously.<sup>14,15</sup> The carboxylated ND molecules were linked by peptide bonding with GH via the zero length cross linkers 1-ethyl-3-[3-dimethylaminopropyl] carbodiimide hydrochloride and *N*-hydroxysuccinimide (Sulfo-NHS) (Pierce Chemical Comp., USA). The reaction was monitored by changes in the fluorescence spectra of the unique fluorescence of ND and autofluorescence of GH. This was followed by examination of MALDI-TOF (matrix-assisted laser desorption ionization-time of flight) mass spectra. Each ND particle was bound with two molecules of GH, forming a NDGH complex (data not shown). The NDGH complex (19 μM) was incubated with the A549 lung cancer cells in culture. After 8 h of incubation, the cells were washed with phosphate buffered saline to remove the non-specific binding complex. The NDGH complex bound to

A549 cell membrane avidly. This was consistent with our previous observation.<sup>16</sup> The cells were then irradiated with the same laser power mentioned above. The results show that approximately 60% of the cells died within 24 h after the irradiation [Fig. 3(a)]. In contrast, less than 10% of the controls cells were found dead under comparable treatment. As shown in Figs. 3(b)–3(d), the cell death can be attributed to the explosion of ND on the cell surface.

In summary, photolysis of nitroso plays a vital role of ND conformational transition. We have developed a NDGH complex, which preferentially kills tumor cells upon high energy pulse laser irradiation. The mechanism may involve the high affinity of NDGH to tumor cell membrane and ND explosion resulted in exposing the high energy locally within hundred nanometers, damaging the membrane leading to cell death. This popcornlike transition reaction of ND is potentially useful as a nanoknife in biomedical application.

We acknowledge support in part from National Science Council, Taiwan, R.O.C. (Grant Nos. NSC 96-2112-M-009-035 and NSC 96-2120-M-259-002). We thank Dr. P. C. Huang for the valuable discussion and suggestion, Dr. Yu-Ching Chang for cell preparation, Dr. Ching-Ping Liu for Gaussian calculation, and Mr. Xin-Yu Lin for TEM measurement. We also thank National center for High-performance Computing for the computing facility; National Tsing Hua University, center for transmission electron microscopy for TEM facility and Instrument Technology Research Center, National Applied Research Laboratories for SEM and AFM facilities.

<sup>1</sup>K.-K. Liu, C.-L. Cheng, C.-C. Chang, and J.-I. Chao, *Nanotechnology* **18**, 325102 (2007).

<sup>2</sup>J.-I. Chao, E. Perevedentseva, P.-H. Chung, K.-K. Liu, C.-Y. Cheng, C.-C. Chang, and C.-L. Cheng, *Biophys. J.* **93**, 2199 (2007).

<sup>3</sup>C. C. Fu, H. Y. Lee, K. Chen, T. S. Lim, H. Y. Wu, P. K. Lin, P. K. Wei, P. H. Tsao, H. C. Chang, and W. Fann, *Proc. Natl. Acad. Sci. U.S.A.* **104**, 727 (2007).

<sup>4</sup>C.-Y. Cheng, E. Perevedentseva, J.-S. Tu, P.-H. Chung, C.-L. Cheng, K.-K. Liu, J.-I. Chao, P.-H. Chen, and C.-C. Chang, *Appl. Phys. Lett.* **90**, 163903 (2007).

<sup>5</sup>H. Huang, E. Pierstorff, E. Osawa, and D. Ho, *Nano Lett.* **7**, 3305 (2007).

<sup>6</sup>L. C. Huang and H. C. Chang, *Langmuir* **20**, 5879 (2004).

<sup>7</sup>A. Krueger, *Chem.-Eur. J.* **14**, 1382 (2007).

<sup>8</sup>A. Keßler, A. Slenczka, R. Seiler, and B. Dick, *Phys. Chem. Chem. Phys.* **3**, 2819 (2001).

<sup>9</sup>S. M. Sze *Physics of Semiconductor Devices*, 2nd ed. (Wiley, New York, 1981).

<sup>10</sup>K.-W. Lin, C.-L. Cheng, and H.-C. Chang, *Chem. Mater.* **10**, 1735 (1998).

<sup>11</sup>Y. Zhou, X. Wang, J. Hadley, S. J. Corey, R. Vasilatos-Younken, *Gen. Comp. Endocrinol.* **144**, 128 (2005).

<sup>12</sup>E. van Garderen, and J. A. Schalken, *Mol. Cell Endocrinol.* **197**, 153 (2002).

<sup>13</sup>X. Yang, F. Liu, Z. Xu, C. Chen, G. Li, X. Wu, and J. Li., *Dig. Dis. Sci.* **49**, 1493 (2004).

<sup>14</sup>C.-C. Chang, C. T. Tsai, and C. Y. Chang, *Protein Eng.* **15**, 437 (2002).

<sup>15</sup>C.-C. Chang, M. S. Cheng, Y. C. Su, and L. S. Kan, *J. Biomol. Struct. Dyn.* **21**, 247 (2003).

<sup>16</sup>C.-Y. Cheng, E. Perevedentseva, J.-S. Tu, P.-H. Chung, C.-L. Cheng, K.-K. Liu, J.-I. Chao, P.-H. Chen, and C.-C. Chang, *Appl. Phys. Lett.* **90**, 163903 (2007).

# Alpha-bungarotoxin binding to target cell in a developing visual system by carboxylated nanodiamond

Kuang-Kai Liu<sup>1,2,3</sup>, Mei-Fang Chen<sup>4</sup>, Po-Yi Chen<sup>1,2,4</sup>,  
Tony J F Lee<sup>1,2,5</sup>, Chia-Liang Cheng<sup>6</sup>, Chia-Ching Chang<sup>3,7</sup>,  
Yen-Peng Ho<sup>8</sup> and Jui-I Chao<sup>1,2,3,9</sup>

<sup>1</sup> Institute of Pharmacology and Toxicology, Tzu Chi University, Hualien 970, Taiwan

<sup>2</sup> Biomedical Nanotechnology Laboratory, Tzu Chi University, Hualien 970, Taiwan

<sup>3</sup> Department of Biological Science and Technology, National Chiao Tung University, Hsin-Chu 300, Taiwan

<sup>4</sup> Neuro-Medical Scientific Center, Tzu Chi General Hospital, Hualien 970, Taiwan

<sup>5</sup> Department of Pharmacology, School of Medicine, Southern Illinois University, Springfield, IL, USA

<sup>6</sup> Department of Physics, National Dong Hwa University, Hualien 974, Taiwan

<sup>7</sup> Institute of Physics, Academia Sinica, Taipei 11529, Taiwan

<sup>8</sup> Department of Chemistry, National Dong Hwa University, Hualien 974, Taiwan

E-mail: [chaoji@mail.tcu.edu.tw](mailto:chaoji@mail.tcu.edu.tw)

Received 22 November 2007, in final form 17 March 2008

Published 14 April 2008

Online at [stacks.iop.org/Nano/19/205102](http://stacks.iop.org/Nano/19/205102)

## Abstract

Biological molecules conjugating with nanoparticles are valuable for applications including bio-imaging, bio-detection, and bio-sensing. Nanometer-sized diamond particles have excellent electronic and chemical properties for bio-conjugation. In this study, we manipulated the carboxyl group produced on the surface of nanodiamond (carboxylated nanodiamond, cND) for conjugating with alpha-bungarotoxin ( $\alpha$ -BTX), a neurotoxin derived from *Bungarus multicinctus* with specific blockade of alpha7-nicotinic acetylcholine receptor ( $\alpha$ 7-nAChR). The electrostatic binding of cND- $\alpha$ -BTX was mediated by the negative charge of the cND and the positive charge of the  $\alpha$ -BTX in physiological pH conditions. Sodium dodecyl sulfate-polyacrylamide gel analysis and matrix-assisted laser desorption ionization time-of-flight mass spectrometry (MALDI/TOF-MS) spectra displayed that  $\alpha$ -BTX proteins were conjugated with cND particles via non-covalent bindings. The green fluorescence of the cND particles combining with the red fluorescence of tetramethylrhodamine-labeled  $\alpha$ -BTX presented a yellow color at the same location, which indicated that  $\alpha$ -BTX proteins were conjugated with cND particles. *Xenopus laevis*'s oocytes expressed the human  $\alpha$ 7-nAChR proteins by microinjection with  $\alpha$ 7-nAChR mRNA. The cND- $\alpha$ -BTX complexes were bound to  $\alpha$ 7-nAChR locating on the cell membrane of oocytes and human lung A549 cancer cells analyzed by laser scanning confocal microscopy. The choline-evoked  $\alpha$ 7-nAChR-mediated inward currents of the oocytes were blocked by cND- $\alpha$ -BTX complexes in a concentration-dependent manner using two-electrode voltage-clamp recording. Furthermore, the fluorescence intensity of cND- $\alpha$ -BTX binding on A549 cells could be quantified by flow cytometry. These results indicate that cND-conjugated  $\alpha$ -BTX still preserves its biological activity in blocking the function of  $\alpha$ 7-nAChR, and provide a visual system showing the binding of  $\alpha$ -BTX to  $\alpha$ 7-nAChR.

<sup>9</sup> Address for correspondence: Institute of Pharmacology and Toxicology, Tzu Chi University, 701, Section 3, Chung-Yang Road, Hualien 970, Taiwan.

## 1. Introduction

Manipulating nanoparticles for biomedical applications has been evaluated in recent years [1–5]. Biological molecules conjugated with nanoparticles can be applied for both diagnostic and therapeutic applications [1, 2, 5, 6]. Semiconductor quantum dots (Qdots) display fluorescent properties without photobleaching that are suitable for advanced bio-imaging [1, 3, 6]. For example, Qdot-coating with a lung-targeting peptide was specifically accumulated in the lung of mice by vessel injection [1]. The visual analysis of the delivery processes of nanoparticle-conjugated therapeutic drugs (or bio-molecules) *in vivo* provides the observation of drug transportation and targeting, which are useful for therapeutic efficacy of such diseases. Unfortunately, the existence of heavy metals such as cadmium (a well-known human toxicant) in Qdots is of concern for medical applications, especially for human treatment. Therefore, alternative nanomaterials containing both biocompatible and detectable properties are highly desirable.

Nanodiamond, a carbon derivative nanomaterial, is a developing nanoparticle for biological applications, which include the advantages of its biocompatibility, non-toxicity, and easily detected intrinsic fluorescence without photobleaching [7–9]. The surface of nanodiamonds provides an exceptional platform for conjugation of biological molecules after chemical modifications [10, 11]. The modified surface of nanodiamonds by carboxylation (carboxylated nanodiamond, cND) presents high affinity for proteins [7, 12]. Besides, the modified nanodiamonds can be conjugated with DNA [10, 13], cytochrome c [14], antigen [15], and growth hormone [16]. However, the biological activity and function of bio-molecules conjugated with cND are still unclear.

Alpha-bungarotoxin ( $\alpha$ -BTX), a neurotoxin derived from *Bungarus multicinctus*, is an antagonist of the  $\alpha$ 7-nicotinic acetylcholine receptor ( $\alpha$ 7-nAChR) of neuronal cells by inducing neuronal damages [17, 18]. Non-neuronal cells (e.g., human lung cancer cells) also expressed  $\alpha$ 7-nAChR [19–21]. The  $\alpha$ 7-nAChR forms a functional homomeric-pentamer nAChR on the cellular membrane to mediate cation (e.g.  $\text{Ca}^{2+}$ ) influx that is activated by an agonist such as choline and nicotine [22–25]. It has been shown that  $\alpha$ 7-nAChR can regulate many physiological functions including cell proliferation [21, 26] and neuroprotection [17, 27].

In the present study, we manipulated the carboxyl group produced on the nanodiamond's surface for conjugating with  $\alpha$ -BTX by imaging and binding to those  $\alpha$ 7-nAChR in *Xenopus laevis*'s oocyte and lung cancer cell. The cND- $\alpha$ -BTX can be visualized on the targeting cells. Furthermore, the cND-conjugated  $\alpha$ -BTX executes the biological function to block the activation of  $\alpha$ 7-nAChR.

## 2. Experimental details

### 2.1. Materials and reagents

The nominal 100 nm nanodiamond powder was from Diamond Innovations (Worthington, OH).  $\alpha$ -BTX,  $\alpha$ -BTX-tetramethylrhodamine ( $\alpha$ -BTX-TMR), and ferulic acid were

purchased from Sigma Chemical Co. (St Louis, MO). HPLC grade acetonitrile (MeCN) was purchased from J T Backer (Phillipsburg, NJ). Formic acid was purchased from Riedel-de Haen (Seelze, Germany). Water was purified using a Milli-Q system (Millipore, Bedford, MA).

### 2.2. A549 cancer cell line

A549 cell line (ATCC, #CCL-185) was derived from the lung adenocarcinoma of a 58 year-old Caucasian male. It has been shown that A549 cells expressed  $\alpha$ 7-nAChR proteins [19–21]. These cells were cultured in RPMI-1640 medium (Invitrogen Co., Carlsbad, CA), which were supplemented with 10% fetal bovine serum (FBS), 100 units  $\text{ml}^{-1}$  penicillin, 100  $\mu\text{g ml}^{-1}$  streptomycin, and L-glutamine (0.03%, w/v). The cells were maintained at 37 °C and 5%  $\text{CO}_2$  in a humidified incubator (310/Thermo, Forma Scientific, Inc., Marietta, OH).

### 2.3. Preparation of cND- $\alpha$ -BTX and cND- $\alpha$ -BTX-TMR

The standard procedure of cND preparation was according to a previous study [14]. Briefly, 0.2 g 100 nm nanodiamond powder was added into a 15 ml acid mixture of  $\text{H}_2\text{SO}_4\text{:HNO}_3$  (3:1) in an ultrasonic bath for incubation of 30 min, and then heated for 30 min. The treated nanodiamonds were washed with distilled water and centrifuged several times. After drying, these cND particles were dispersed in distilled water. For preparing cND- $\alpha$ -BTX and cND- $\alpha$ -BTX-TMR, the cND particles (50  $\text{mg ml}^{-1}$ ) were mixed with  $\alpha$ -BTX (500  $\mu\text{g ml}^{-1}$ ) or  $\alpha$ -BTX-TMR (500  $\mu\text{g ml}^{-1}$ ) in the shaker for 2 h at room temperature. The mixtures were centrifuged at 12 000 rpm for 5 min, and the pellets were washed twice with isotonic PBS (pH 7.4). Finally, the pellet was dissolved in PBS. These cND-protein complexes need to be freshly prepared. To avoid aggregation, the samples were ultrasonicated for 20 min at room temperature before use.

### 2.4. Measurement of particle sizes of $\alpha$ -BTX, cND, and cND- $\alpha$ -BTX

The particle size distributions of  $\alpha$ -BTX, cND and cND- $\alpha$ -BTX were analyzed with a laser light scattering goniometer, BI-200 SM with Brookhaven BI-9000AT software (Brookhaven Instruments, Holtsville, New York, USA).

### 2.5. Bio-atomic force microscopy (Bio-AFM)

To examine the morphology and size of cNDs and cND- $\alpha$ -BTX complexes, these particles were dropped on a mica slice and were analyzed with a Bio-AFM (NanoWizard, JPK Instruments, Berlin). The Bio-AFM was mounted on an inverted microscope, TE-2000-U (Nikon, Japan). A silicon nitride non-sharpened cantilever was used with a nominal force constant of 0.06  $\text{N m}^{-1}$  (DNP-20, Veeco). The images were scanned by using the contact mode. Line scan rates were varied from 0.5 to 2 Hz.

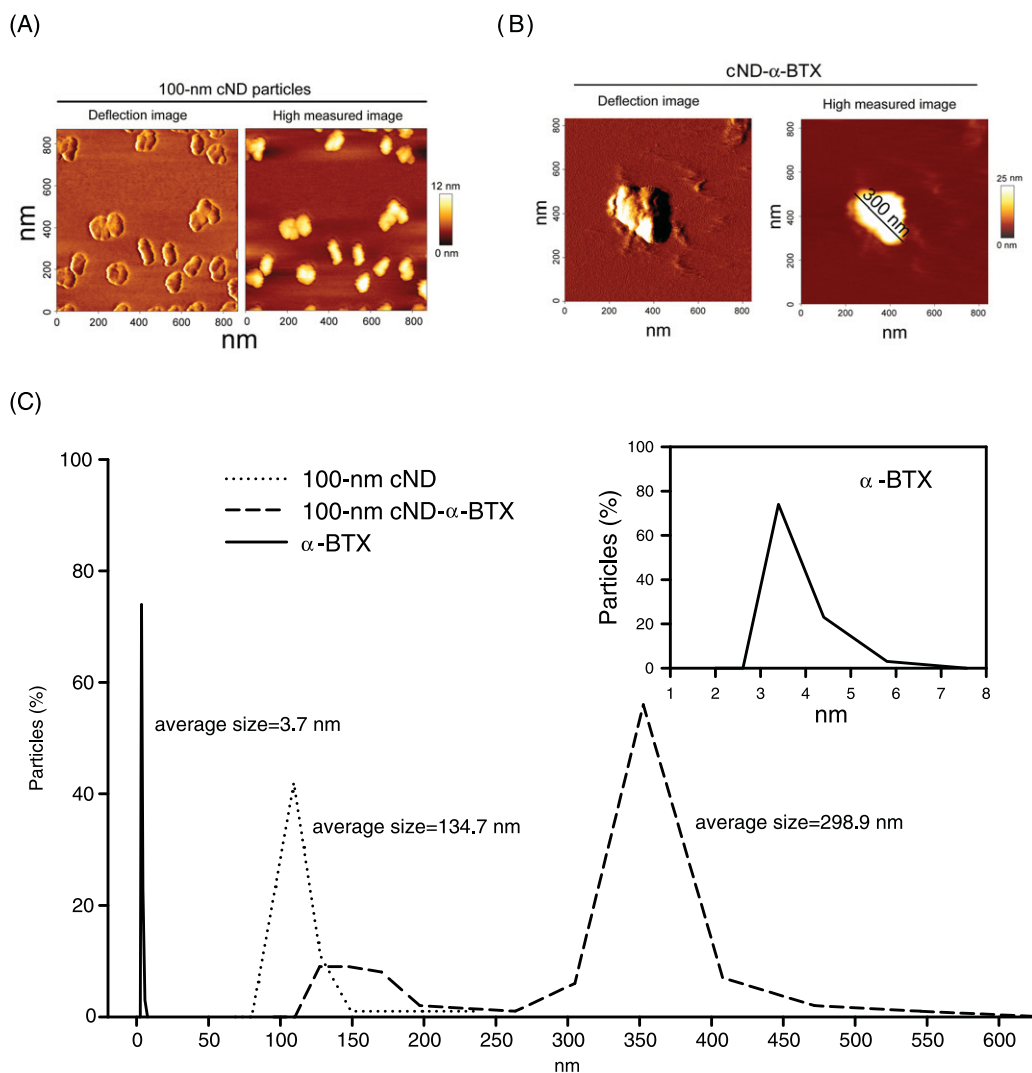


**Figure 1.** Size distributions of cND,  $\alpha$ -BTX, and cND- $\alpha$ -BTX. (A) cND particles and (B) cND- $\alpha$ -BTX complexes were dropped on a mica slice and were analyzed with a Bio-AFM. The deflection image of the Bio-AFM shows the contour and size of cND particles and cND- $\alpha$ -BTX. (C) The particle size distributions of  $\alpha$ -BTX, cND and cND- $\alpha$ -BTX were analyzed by a laser light scattering goniometer. The upper right image was amplified by the size distribution of  $\alpha$ -BTX. The average sizes of molecules were calculated as shown in the figure.

## 2.6. Sodium dodecyl sulfate-polyacrylamide gel (SDS-PAGE) analysis

Briefly, the suspensions of cND,  $\alpha$ -BTX, and cND-BTX were separately subjected to electrophoresis by 12% SDS-PAGE. The indicated molecular weight was loaded by a protein marker reagent (Cambrex, Maine). After electrophoresis, the gel was stained with the coomassie blue buffer (0.1% coomassie blue, 10% acetic acid, and 45% methanol) for 1 h.

## 2.7. MALDI/TOF-MS spectrometry

The cND- $\alpha$ -BTX particles were extensively washed with Milli-Q-filtered water. The supernatant obtained from every washing procedure was analyzed by MALDI/TOF-MS. MALDI/TOF-MS spectra were acquired using an Autoflex time-of-flight mass spectrometer (Bruker Daltonic, Germany) equipped with a 337 nm nitrogen laser (10 Hz, 3 ns pulse width). Spectral data were obtained in the linear mode with

an acceleration voltage of 25 kV. Each mass spectrum was derived from 50 summed scans. Ferulic acid was used as a MALDI matrix, which was prepared by dissolving 12.5 mg of ferulic acid in 1 ml of solvent mixture of 17% formic acid/33% MeCN/50% H<sub>2</sub>O. An aliquot of the sample solution (0.5  $\mu$ l) was mixed with an equal volume of the matrix solution and then applied on the target plate and dried before MALDI/TOF-MS analysis.

## 2.8. Expression of a human $\alpha$ 7-nAChR in *Xenopus laevis*'s oocytes

Stage V and VI oocytes from *Xenopus laevis* were harvested and maintained in the modified ND96 buffer (96 mM NaCl, 2 mM KCl, 1 mM MgCl<sub>2</sub>, 1.8 mM CaCl<sub>2</sub> and 5 mM HEPES, pH 7.6) at 18.5 °C. The human  $\alpha$ 7-nAChR plasmid was kindly provided by Dr Barry J Hoffer (National Institute on Drug Abuse, NIH, Baltimore). The mMessage mMachine kit (Ambion Inc.) was adopted to synthesize capped  $\alpha$ 7-nAChR

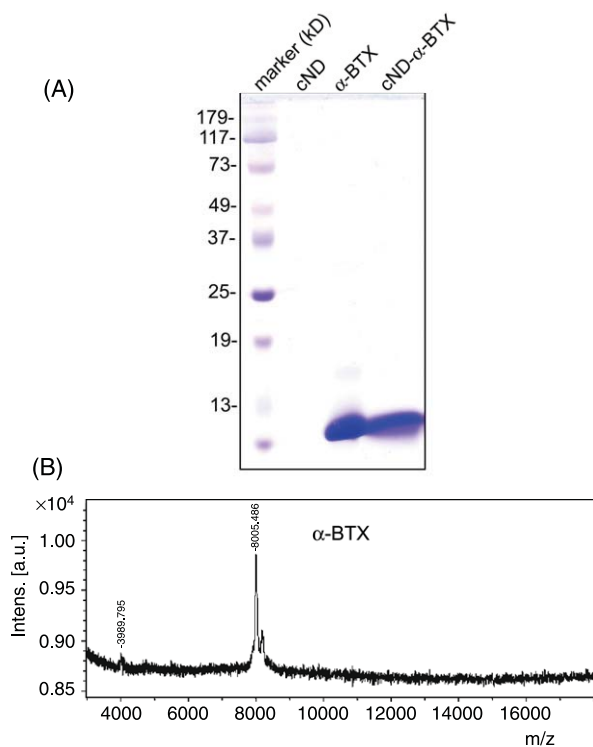


**Figure 2.** Detection of  $\alpha$ -BTX by SDS-PAGE analysis and MALDI/TOF-MS spectrum. (A) The cND particles,  $\alpha$ -BTX, and cND- $\alpha$ -BTX were subjected to electrophoresis by SDS-PAGE. Each well was loaded with 100 nm cNDs ( $500 \mu\text{g ml}^{-1}$ ),  $\alpha$ -BTX ( $20 \mu\text{g}$ ), and  $750 \mu\text{g}$  cND- $\alpha$ -BTX (containing  $20 \mu\text{g}$   $\alpha$ -BTX), respectively. After electrophoresis, the gel was stained with the coomassie blue staining. The left lane indicates the protein marker. (B) The  $\alpha$ -BTX protein was detected by MALDI/TOF-MS from the dissociation of cND- $\alpha$ -BTX particles. The peak at  $m/z$  8005 corresponds to the  $\alpha$ -BTX protein ion.

RNAs *in vitro*. Oocytes were injected with the  $\alpha 7$ -nAChR RNA by using a nanoinjector (Drummond, Inc., Broomall, PA).

### 2.9. Confocal microscopy

A549 cells were cultured on coverslips, which were kept in a 35 mm Petri dish for 16–20 h before treatment. After treatment with  $100 \mu\text{g ml}^{-1}$  cNDs or cND- $\alpha$ -BTX for 4 h, the cells were washed twice with isotonic PBS (pH 7.4) and then were re-cultured in complete medium for 20 h. At the end of incubation, the cells were fixed in 4% paraformaldehyde solution in PBS for 1 h at  $37^\circ\text{C}$ . Then the coverslips were washed three times with PBS, and non-specific binding sites were blocked in PBS containing 10% normal goat serum, 0.3% Triton X-100 for 1 h. The cytoskeleton of  $\beta$ -tubulin protein was stained with anti- $\beta$ -tubulin Cy3 (1:50) for 30 min at  $37^\circ\text{C}$ . Finally, the samples were examined under a Leica confocal laser scanning microscope (Mannheim, Germany) that was equipped with a UV laser (351/364 nm), an Ar laser (457/488/514 nm), and a HeNe laser (543 nm/633 nm).

The oocytes from *Xenopus laevis* were injected with human  $\alpha 7$ -nAChR RNA and then incubated for 2–7 days. After incubation, the vitelline membrane of oocytes was

carefully removed. Thereafter, oocytes were carefully washed twice with the ND96 buffer before treatment with  $100 \mu\text{g ml}^{-1}$  cNDs or cND- $\alpha$ -BTX for 10 min. At the end of treatment, the oocytes were washed with the ND96 buffer and then fixed with in 4% paraformaldehyde solution for 2 h. Subsequently, the oocytes were analyzed with a confocal laser scanning microscope.

### 2.10. Flow cytometry

A549 cells were plated at a density of  $7 \times 10^5$  cells per 60 mm Petri dish in complete medium for 16–20 h. Thereafter, the cells were treated with  $100 \mu\text{g ml}^{-1}$  cND or cND- $\alpha$ -BTX for 4 h. After treatment, the cells were washed twice with PBS and were re-cultured in complete medium for two days. The cells were collected and fixed with ice-cold 70% ethanol overnight at  $-20^\circ\text{C}$ . To avoid cell aggregation, the cell solutions were filtered through nylon membrane (BD Biosciences, San Jose, CA). Finally, the samples were analyzed with a flow cytometer (BD Biosciences). Ten thousand cells were analyzed, and the fluorescence intensity was quantified by a CellQuest software (BD Biosciences).

### 2.11. Two-electrode voltage-clamp recording

The main procedure of two-electrode voltage-clamp recording was described in a previous study [28]. Membrane currents were recorded 2–7 days after the injection. During recording, the oocyte was continuously perfused with the ND96 buffer at a rate of  $7 \text{ ml min}^{-1}$ . Choline ( $0.3 \text{ mM}$ ) was then applied for 1 s directly onto the oocyte. For examining the effects of cND,  $\alpha$ -BTX, or cND-BTX on choline-induced responses, these molecules were dissolved in the ND96 buffer and flowed continuously into the bath chamber for 5 min. Choline responses were examined during treatments. After these molecules were ‘washed off’, the response to choline alone was repeated to obtain an additional control. Two-electrode voltage-clamp recording for the whole oocyte was performed at room temperature by using an OC-725C amplifier (Warner, Inc., Hamden, CT). The borosilicate glass capillaries (1.5 mm, outer diameter) (World Precision Instruments, Inc., Sarasota, FL) were pulled using a P-97 microelectrode puller (Sutter, Inc., Novato, CA). The electrodes were filled with 3 M KCl and had  $0.1$ – $1 \text{ M}\Omega$  resistance. The membrane potential was held at  $-60 \text{ mV}$ . Data acquisition and analysis were performed with a Digidata 1322A and pClamp 9.0 (Axon instruments, Inc., Union City, CA). The traces were filtered at 1 kHz and sampled at 2 kHz. The maximal negative deflection of the current was determined as the current amplitude. To compensate the difference in the  $\alpha 7$ -nAChR expression level, the data were normalized to the current amplitudes before the drug administration and presented as percentages of the choline-induced response.

### 2.12. Statistical analysis

Data were analyzed using Student’s *t* test, and a *p* value of  $<0.05$  was considered as statistically significant in each experiment.

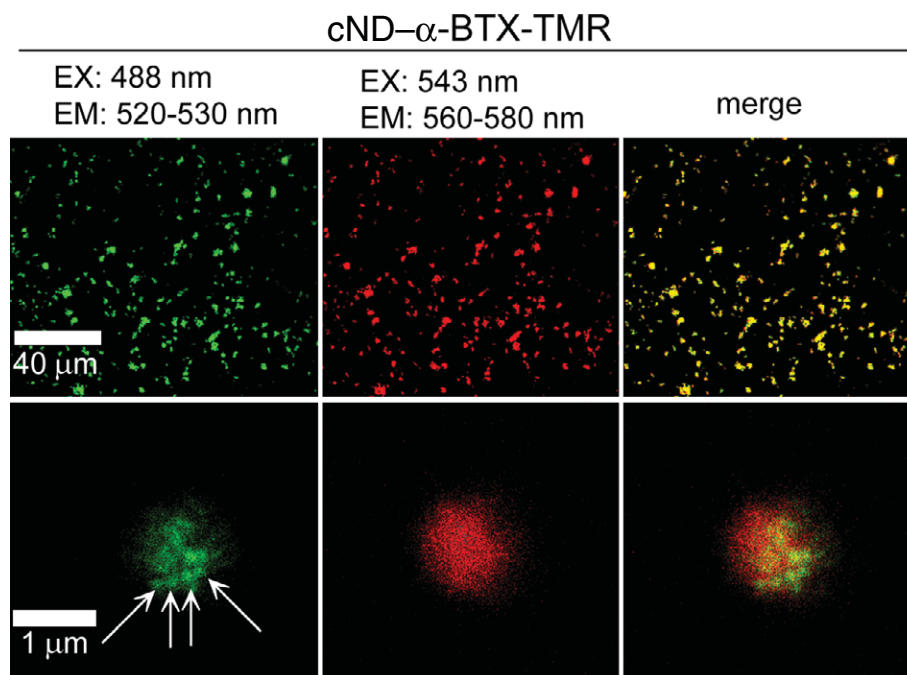


**Figure 3.** Detection of cND- $\alpha$ -BTX-TMR complexes by laser scanning confocal microscopy. The cND particles (750  $\mu$ g) were incubated with  $\alpha$ -BTX-TMR (15  $\mu$ g). After incubation, the cND- $\alpha$ -BTX-TMR complexes were subjected to laser scanning confocal microscopy. The green fluorescence from the cNDs was excited with wavelength 488 nm and the emission was collected in the range of 510–530 nm. Arrows indicate the location of cND particles. The red fluorescence of TMR was excited by the wavelength of 543 nm and then the emission at 560–580 nm was detected. The yellow color in the merged pictures shows cND- $\alpha$ -BTX-TMR complexes.

### 3. Results

#### 3.1. Morphology and size of cND and cND- $\alpha$ -BTX

As shown in figure 1(A), the nominal size of 100 nm cND particles was  $\sim$ 100 nm. The morphology of cND particles was oblong under Bio-AFM observation (figure 1(A)). However, the size of the cND- $\alpha$ -BTX complex was increased to  $\sim$ 300 nm (figure 1(B)). Moreover, a laser light scattering goniometer was used to measure the size distribution of  $\alpha$ -BTX, cND, and cND- $\alpha$ -BTX. The average sizes of  $\alpha$ -BTX and cND were 3.7 and 134.7 nm, respectively (figure 1(C)). The cND particles conjugated with  $\alpha$ -BTX and formed the cND- $\alpha$ -BTX complexes with average size 298.9 nm (figure 1(C)).

#### 3.2. $\alpha$ -BTX conjugated with cND but not covalently binding

To examine the interaction of  $\alpha$ -BTX and cNDs, suspensions of  $\alpha$ -BTX, cND, and cND- $\alpha$ -BTX were loaded onto SDS-PAGE analysis. The amino acid sequence and molecular weight of  $\alpha$ -BTX were shown as a 7.983 kD protein, which contained 74 amino acids [29]. After electrophoresis using SDS-PAGE, the molecular weight of  $\alpha$ -BTX was  $\sim$ 8 kD in the gel (figure 2(A)). The cND particles did not present on the SDS-PAGE gel (figure 2(A)). The sample of cND- $\alpha$ -BTX also presented the  $\alpha$ -BTX protein band (figure 2(A)). In addition, we manipulated  $\alpha$ -BTX released from cND- $\alpha$ -BTX complexes. The molecular weight of  $\alpha$ -BTX was obtained by MALDI/TOF-MS analysis. Figure 2(B) shows that the peak at  $m/z$  8005 was the pattern of the  $\alpha$ -BTX protein ion from the  $\alpha$ -BTX separated samples.

#### 3.3. Dual fluorescence imaging of $\alpha$ -BTX

The tetramethylrhodamine-labeled alpha-bungarotoxin ( $\alpha$ -BTX-TMR) was incubated with cND particles and then subjected to laser scanning confocal microscopy. The cND particles exhibited green fluorescence at 510–530 nm after 488 nm excitation (figure 3, left pictures). The red fluorescence of TMR (excitation wavelength: 543 nm; emission wavelength: 560–580 nm) represented the location of  $\alpha$ -BTX proteins (figure 3, middle pictures). Moreover, the merged pictures showing yellow color indicate the formation of cND- $\alpha$ -BTX-TMR complexes (figure 3, right pictures).

#### 3.4. $\alpha$ -BTX binding on the cell membrane of lung A549 cancer cells

To determine the cND- $\alpha$ -BTX-TMR binding on targeting cells, the human A549 lung cancer cells were treated with these particles and were subjected to confocal microscopy. Both cND and cND- $\alpha$ -BTX-TMR particles were detected on cells that exhibited the green fluorescence from cND signals (figures 4(A) and (B)). The cND particles were taken up into cells but cND- $\alpha$ -BTX-TMR located on the cell membrane of A549 cells (figure 4(A)). The red fluorescence of TMR from cND- $\alpha$ -BTX-TMR indicated that  $\alpha$ -BTX bound on the cell membrane of A549 cells. The black spots of cND- $\alpha$ -BTX-TMR complexes were also observed by phase contrast image (figure 4(B), left). The yellow color also indicated that the cND- $\alpha$ -BTX-TMR complexes were located on the cell membrane of A549 cells (figure 3, right picture).

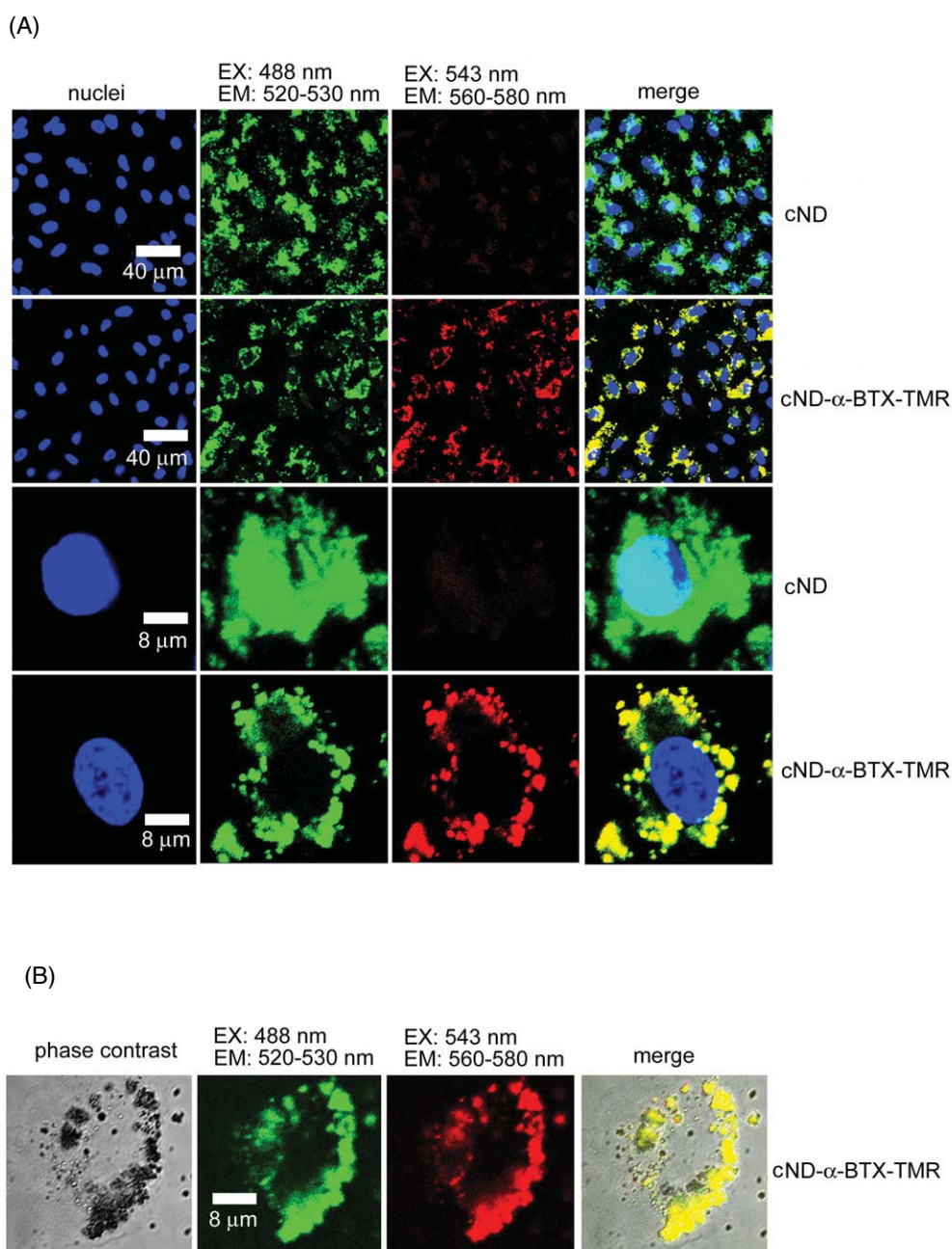


**Figure 4.** Detection of cND and cND- $\alpha$ -BTX-TMR in A549 cells by laser scanning confocal microscopy. (A) and (B), A549 cells were treated with  $100 \mu\text{g ml}^{-1}$  cND or cND- $\alpha$ -BTX-TMR for 4 h and then had 20 h recovery. After cell fixation, the nuclei were stained with Hoechst 33258, which displayed blue fluorescence. The cND particles exhibited the green fluorescence at 510–530 nm after 488 nm excitation. The red fluorescence of TMR was excited with wavelength 543 nm and the emission was collected in the range of 560–580 nm. The black spots of cND- $\alpha$ -BTX-TMR complexes were observed by phase contrast. The yellow color in the merged pictures indicated the location of cND- $\alpha$ -BTX-TMR.

### 3.5. Quantification of cND and cND- $\alpha$ -BTX in A549 cells by flow cytometry

To quantify the level of cNDs and cND- $\alpha$ -BTX binding to A549 cells, the cells were treated with these particles and analyzed by flow cytometry. The fluorescence intensities were increased in A549 cells following treatment with  $50 \mu\text{g ml}^{-1}$  cND or cND- $\alpha$ -BTX (figure 5(A)). The fluorescence intensity was significantly increased  $\sim 2$ -fold after treatment with cNDs and cND- $\alpha$ -BTX (figure 5(B)). However, the fluorescence

intensity of cND was similar to that of cND- $\alpha$ -BTX in A549 cells (figure 5(B)).

### 3.6. cND- $\alpha$ -BTX-TMR binding to $\alpha 7$ -nAChR on cell membrane of *Xenopus laevis*'s oocytes

The human  $\alpha 7$ -nAChR was expressed on *Xenopus laevis*'s oocytes as described in Experimental Details section. The cND particles or cND- $\alpha$ -BTX-TMR bound to oocyte were observed by confocal microscopy. As shown in figure 6, the green fluorescence indicated nanodiamond's signal presenting

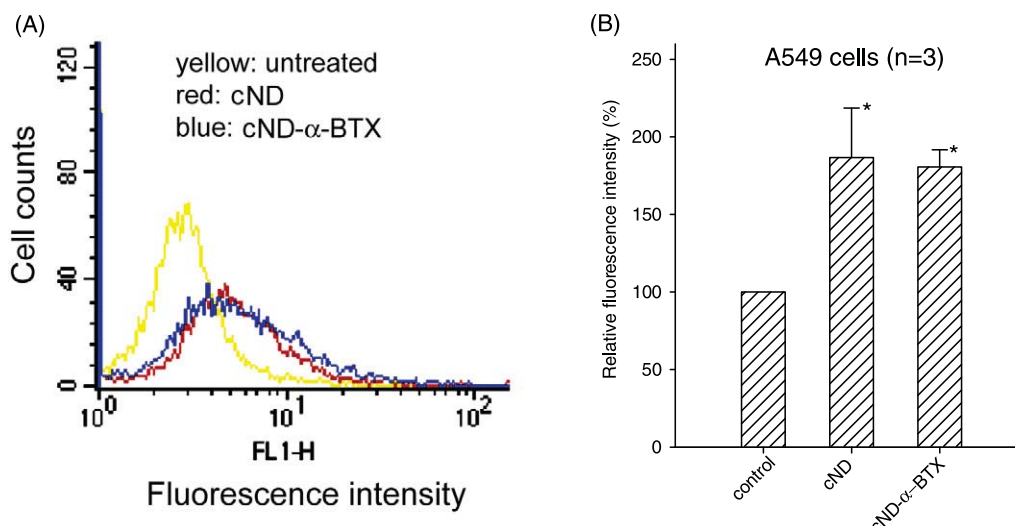


**Figure 5.** Quantified fluorescence intensities of cND and cND- $\alpha$ -BTX in A549 cells by flow cytometry. (A) A549 cells were treated with or without  $100 \mu\text{g ml}^{-1}$  cND or cND- $\alpha$ -BTX for 4 h and then had 20 h recovery. At the end of treatment, the cells were trypsinized and then subjected to flow cytometry analyses. (B) The fluorescence intensity was quantified by a CellQuest software of the flow cytometer. The bar represents mean  $\pm$  S.E. \*  $p < 0.05$  indicates significant difference between untreated and treated samples.

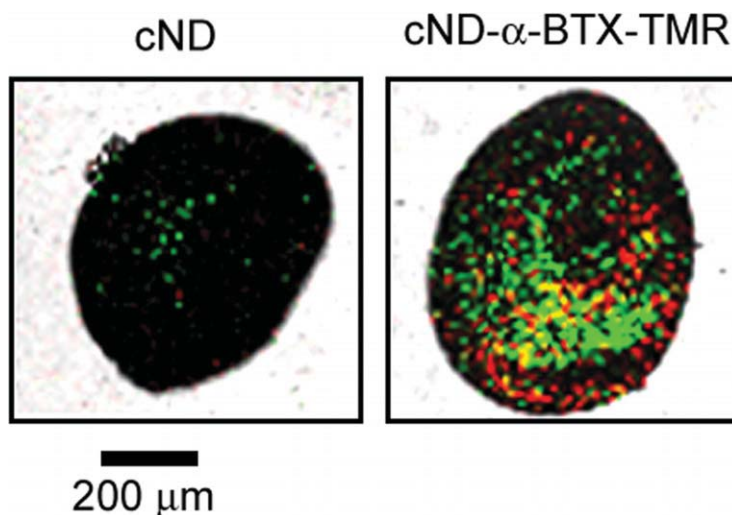


**Figure 6.** Observation of cND- $\alpha$ -BTX binding on the  $\alpha 7$ -nAChR-expressed oocytes. The oocytes from *Xenopus laevis* were injected with the  $\alpha 7$ -nAChR RNA using a nanoinjector. After incubation with cNDs or cND- $\alpha$ -BTX, the oocytes were fixed with 4% paraformaldehyde and were examined under laser scanning confocal microscopy. The green spots indicate the location of cND particles after 488 nm excitation and exhibited emission at 510–530 nm. The red fluorescence of TMR was excited with wavelength 543 nm and the emission was collected in the range of 560–580 nm. The yellow spots indicate the location of cND- $\alpha$ -BTX-TMR.

on the  $\alpha 7$ -nAChR-expressed oocytes. A few cND particles were located on the cell membrane of oocytes following incubation with  $100 \mu\text{g ml}^{-1}$  cND for 10 min (figure 6, left). However, treatment with  $100 \mu\text{g ml}^{-1}$  cND- $\alpha$ -BTX-TMR for 10 min caused high fluorescence intensities of cND and TMR (figure 6, right).

### 3.7. cND- $\alpha$ -BTX inhibits the choline-evoked inward currents by $\alpha 7$ -nAChR on *Xenopus laevis*'s oocytes

The effects of cND and cND- $\alpha$ -BTX on the  $\alpha 7$ -nAChR expressed in oocyte were measured by two-electrode voltage-clamp recording. The apparatus of two-electrode voltage-

clamp recording is shown in figure 7(A). Representative tracings from a continuous recording showed choline-induced inward currents before, during (filled bars) and after 5 min administrations of cND or cND- $\alpha$ -BTX treatment. Treatment with  $12 \mu\text{g ml}^{-1}$  cND did not affect the inward current induced by choline at 0.3 mM; however,  $12 \mu\text{g ml}^{-1}$  cND- $\alpha$ -BTX (containing 30 nM  $\alpha$ -BTX) significantly inhibited  $\alpha 7$ -nAChR-mediated current (figure 7(B)). The inhibition of choline-induced inward currents by cND- $\alpha$ -BTX binding on  $\alpha 7$ -nAChR was irreversible after the addition of fresh choline solution (data not shown). Quantification of current signals showed that cND had little effect on the choline-evoked inward currents (figure 7(C)). In contrast, cND- $\alpha$ -BTX reduced the

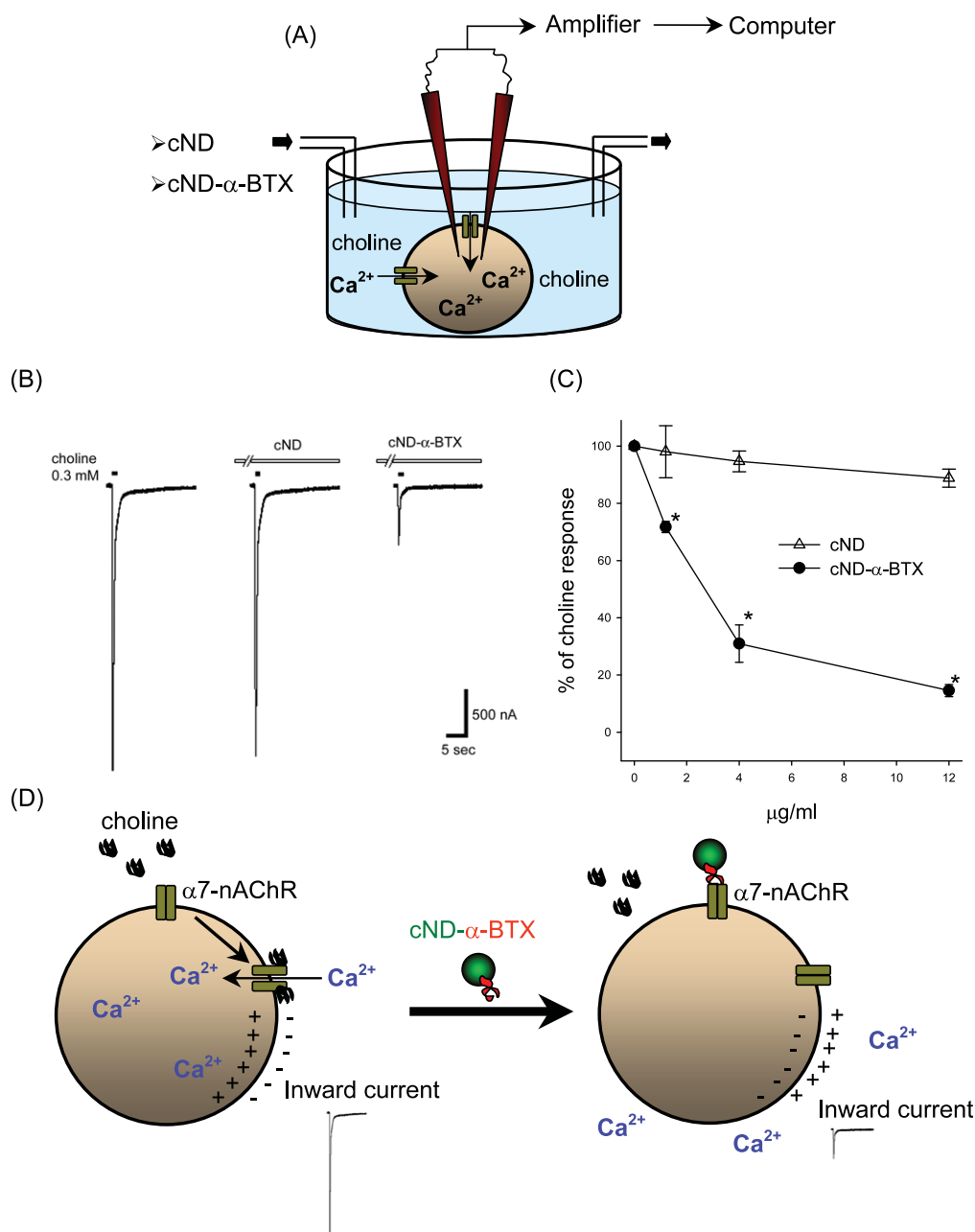


**Figure 7.** Effect of cND and cND- $\alpha$ -BTX on the choline-evoked inward current in the  $\alpha 7$ -nAChR-expressed oocytes. (A) The apparatus of the choline-evoked inward current in the  $\alpha 7$ -nAChR-expressed oocytes. (B) Oocytes were injected with the  $\alpha 7$ -nAChR RNA by using a nanoinjector. After microinjection, the effects of choline, cND, and cND- $\alpha$ -BTX on the  $\alpha 7$ -nAChR-expressed oocytes were measured by two-electrode voltage-clamp recording. Representative tracings from a continuous recording showing choline-induced inward currents before, during, and after 5 min administrations of cND or cND- $\alpha$ -BTX (12  $\mu\text{g ml}^{-1}$ ) treatment. (C) Summary of recordings showing normalized nicotinic responses after 5 min administrations of varied concentrations of cND or cND- $\alpha$ -BTX (0, 1.2, 4, 12  $\mu\text{g ml}^{-1}$ ). Data points were means  $\pm$  S.E from 3–4 successive recordings. \*  $p < 0.05$  indicates significant difference between cND and cND- $\alpha$ -BTX. (D) A model presenting the choline-binding to  $\alpha 7$ -nAChR for evoking inward currents with  $\text{Ca}^{2+}$  influx into oocyte. The green color indicates a cND particle. The red color indicates the  $\alpha$ -BTX protein. Choline evoked the inward current ( $\text{Ca}^{2+}$  influx into oocyte) by binding to the protein subunits of  $\alpha 7$ -nAChR on the cell membrane. The choline-evoked  $\alpha 7$ -nAChR-mediated inward current was blocked by cND- $\alpha$ -BTX.

$\alpha 7$ -nAChR-mediated responses in a concentration-dependent manner (figure 7(C)).

#### 4. Discussion

This is the first report to indicate that cND-conjugated  $\alpha$ -BTX displays the biological activity to block the function of

$\alpha 7$ -nAChR on targeting cells. Importantly, the imaging of  $\alpha$ -BTX revealed by conjugated nanodiamonds on target cells can be detected and quantified by laser scanning confocal microscopy and flow cytometry. This study provides a visual system by cND conjugation with a biological molecule, which is promising for biological applications.

Manipulation of biological molecules by conjugation with nanoparticles is a useful tool for both bio-imaging and drug delivery [1, 2, 5, 6]. Qdots emit fluorescent properties without photobleaching, which have been used in bio-imaging and bio-detection [1, 3, 6]. However, Qdots usually consist of heavy metals such as cadmium, which is well-known to cause a human carcinogen that is of serious concern for medical applications. Previously, we reported that cND particles did not induce cytotoxicity or alter the protein expression profile in human lung cells [8]. Moreover, these particles can be detected by their intrinsic fluorescence and without obvious photobleaching [7, 9]. Therefore, cND provides an ideal alternative nanomaterial because of its biocompatible and spectroscopic detectable properties.

The surface of nanodiamonds provides a unique platform for conjugation of biological molecules after chemical modifications [10, 11]. These cND particles have a high aptitude for protein binding [7, 12]. It has been reported that proteins can be adsorbed by cND via electrostatic interaction, which is strong and suitable for MALDI/TOF-MS analysis [12]. Indeed, cND particles have shown to possess high affinity for binding with  $\alpha$ -BTX proteins. The average size of cND- $\alpha$ -BTX complexes is  $\sim$ 300 nm. The green fluorescence of cND particles combining with the red fluorescence of TMR-labeled  $\alpha$ -BTX presented a yellow color at the same location, which that indicated  $\alpha$ -BTX proteins were conjugated with cND particles. However,  $\alpha$ -BTX can be dissociated from cND- $\alpha$ -BTX complexes presenting on the SDS-PAGE gel and MALDI/TOF-MS spectrum. The PI (isoelectric point) value of  $\alpha$ -BTX is 8.38 in pH 7.4–7.6 (physiological condition used in this study) carrying positive charge. The negative charge of cND particles from the carboxyl group ( $-\text{COO}^-$ ) is electrostatic with the positive charge of  $\alpha$ -BTX from the amino group ( $-\text{NH}_3^+$ ) in physiological pH condition. Therefore, the conjugation of cND and  $\alpha$ -BTX is due to the electrostatic force but not the covalent bonding. In general, electrostatic bonding is very strong. Furthermore, cND- $\alpha$ -BTX reduced the  $\alpha$ 7-nAChR-mediated responses in a concentration-dependent manner. Therefore, the binding affinity of  $\alpha$ -BTX and cND is strong and suitable for bio-applications in those physiological conditions. Although the binding stability of the alpha-BTX-cND complex was not studied in this work, the bonding between cND and  $\alpha$ -BTX under different pH and buffer conditions is currently under investigation.

It has been shown that  $\alpha$ 7-nAChR regulates a wide range of physiological functions [17, 26–28]. The  $\alpha$ 7-nAChRs located on the cellular membrane to mediate cation influx, particularly  $\text{Ca}^{2+}$  in flux [22–25]. The specific  $\alpha$ 7-nAChR is expressed in several human lung cancer cell lines, including A549 cells [19–21]. Moreover, the neuronal  $\alpha$ 7-nAChR displays neuroprotection [17, 27].  $\alpha$ -BTX is a polypeptide composed of 74 amino acids ( $\sim$ 8 kDa) [29]. It is a neurotoxin that binds  $\alpha$ 7-nAChR to induce neuronal damages [17, 18]. Furthermore,  $\alpha$ -BTX can block  $\alpha$ 7-nAChR-mediated downstream signaling pathways [18, 19, 28, 30]. We provided two models of the exogenously expressed  $\alpha$ 7-nAChR in *Xenopus* oocyte and the endogenous  $\alpha$ 7-nAChR in A549

cells and performed cND- $\alpha$ -BTX complexes binding to  $\alpha$ 7-nAChR of target cells. Interestingly, cND-conjugated  $\alpha$ -BTX preserves the biological activity in blocking choline-evoked inward currents in the  $\alpha$ 7-nAChR-expressed oocyte.

In conclusion, we propose a model of a visual system by cND-conjugated  $\alpha$ -BTX that preserves the physiological activity of blocking the function of  $\alpha$ 7-nAChR on targeting cells (figure 7(D)). Although this study provides the model of cND- $\alpha$ -BTX for imaging in human cancerous cell and oocyte *in vitro*, it is expected that the biological applications of nanodiamond-conjugated bio-molecules will be widely used in a variety of systems including bio-imaging, bio-detection, and bio-sensing.

## Acknowledgments

This work was supported by grants from the National Science Council, ROC (NSC 95-2120-M-259-002, NSC 95-2120-M-259-003, NSC 95-2745-B-320-004-URD), and Tzu Chi University (TCMRC-C95005-01).

## References

- [1] Akerman M E, Chan W C, Laakkonen P, Bhatia S N and Ruoslahti E 2002 Nanocrystal targeting *in vivo* *Proc. Natl Acad. Sci. USA* **99** 12617–21
- [2] Michalet X, Pinaud F F, Bentolila L A, Tsay J M, Doose S, Li J J, Sundaresan G, Wu A M, Gambhir S S and Weiss S 2005 Quantum dots for live cells, *in vivo* imaging, and diagnostics *Science* **307** 538–44
- [3] Gao X, Cui Y, Levenson R M, Chung L W and Nie S 2004 *In vivo* cancer targeting and imaging with semiconductor quantum dots *Nat. Biotechnol.* **22** 969–76
- [4] Souza G R, Christianson D R, Staquicini F I, Ozawa M G, Snyder E Y, Sidman R L, Miller J H, Arap W and Pasqualini R 2006 Networks of gold nanoparticles and bacteriophage as biological sensors and cell-targeting agents *Proc. Natl Acad. Sci. USA* **103** 1215–20
- [5] Farokhzad O C, Cheng J, Teply B A, Sherifi I, Jon S, Kantoff P W, Richie J P and Langer R 2006 Targeted nanoparticle-aptamer bioconjugates for cancer chemotherapy *in vivo* *Proc. Natl Acad. Sci. USA* **103** 6315–20
- [6] Dahan M, Levi S, Luccardini C, Rostaing P, Riveau B and Triller A 2003 Diffusion dynamics of glycine receptors revealed by single-quantum dot tracking *Science* **302** 442–5
- [7] Chao J I, Perevedentseva E, Chung P H, Liu K K, Cheng C Y, Chang C C and Cheng C L 2007 Nanometer-sized diamond particle as a probe for biolabeling *Biophys. J.* **93** 2199–208
- [8] Liu K K, Cheng C L, Chang C C and Chao J I 2007 Biocompatible and detectable carboxylated nanodiamond on human cell *Nanotechnology* **18** 325102
- [9] Yu S J, Kang M W, Chang H C, Chen K M and Yu Y C 2005 Bright fluorescent nanodiamonds: no photobleaching and low cytotoxicity *J. Am. Chem. Soc.* **127** 17604–5
- [10] Yang W *et al* 2002 DNA-modified nanocrystalline diamond thin-films as stable, biologically active substrates *Nat. Mater.* **1** 253–7
- [11] Carlisle J A 2004 Precious biosensors *Nat. Mater.* **3** 668–9
- [12] Kong X L, Huang L C, Hsu C M, Chen W H, Han C C and Chang H C 2005 High-affinity capture of proteins by diamond nanoparticles for mass spectrometric analysis *Anal. Chem.* **77** 259–65

- [13] Ushizawa K, Sato Y, Mitsumori T, Machinami T, Ueda T and Ando T 2002 Covalent immobilization of DNA on diamond and its verification by diffuse reflectance infrared spectroscopy *Chem. Phys. Lett.* **351** 105–8
- [14] Huang L C and Chang H C 2004 Adsorption and immobilization of cytochrome c on nanodiamonds *Langmuir* **20** 5879–84
- [15] Kossovsky N, Gelman A, Hnatyszyn H J, Rajguru S, Garrell R L, Torbati S, Freitas S S and Chow G M 1995 Surface-modified diamond nanoparticles as antigen delivery vehicles *Bioconjug. Chem.* **6** 507–11
- [16] Cheng C Y, Perevedentseva E, Tu J S, Chung P H, Chenga C L, Liu K K, Chao J I, Chen P H and Chang C C 2007 Direct and *in vitro* observation of growth hormone receptor molecules in A549 human lung epithelial cells by nanodiamond labeling *Appl. Phys. Lett.* **90** 163903
- [17] Shaw S, Bencherif M and Marrero M B 2002 Janus kinase 2, an early target of alpha 7 nicotinic acetylcholine receptor-mediated neuroprotection against Abeta-(1-42) amyloid *J. Biol. Chem.* **277** 44920–4
- [18] Wang Y, Pereira E F, Maus A D, Ostlie N S, Navaneetham D, Lei S, Albuquerque E X and Conti-Fine B M 2001 Human bronchial epithelial and endothelial cells express alpha7 nicotinic acetylcholine receptors *Mol. Pharmacol.* **60** 1201–9
- [19] West K A, Brognard J, Clark A S, Linnoila I R, Yang X, Swain S M, Harris C, Belinsky S and Dennis P A 2003 Rapid Akt activation by nicotine and a tobacco carcinogen modulates the phenotype of normal human airway epithelial cells *J. Clin. Invest.* **111** 81–90
- [20] Hsu S H, Tsou T C, Chiu S J and Chao J I 2005 Inhibition of alpha7-nicotinic acetylcholine receptor expression by arsenite in the vascular endothelial cells *Toxicol. Lett.* **159** 47–59
- [21] Dasgupta P, Kinkade R, Joshi B, Decook C, Haura E and Chellappan S 2006 Nicotine inhibits apoptosis induced by chemotherapeutic drugs by up-regulating XIAP and survivin *Proc. Natl Acad. Sci. USA* **103** 6332–7
- [22] Bitner R S and Nikkel A L 2002 Alpha-7 nicotinic receptor expression by two distinct cell types in the dorsal raphe nucleus and locus coeruleus of rat *Brain Res.* **938** 45–54
- [23] Castro N G and Albuquerque E X 1995 Alpha-bungarotoxin-sensitive hippocampal nicotinic receptor channel has a high calcium permeability *Biophys. J.* **68** 516–24
- [24] Albuquerque E X, Alkondon M, Pereira E F, Castro N G, Schrattenholz A, Barbosa C T, Bonfante-Cabarcas R, Aracava Y, Eisenberg H M and Maelicke A 1997 Properties of neuronal nicotinic acetylcholine receptors: pharmacological characterization and modulation of synaptic function *J. Pharmacol. Exp. Ther.* **280** 1117–36
- [25] Papke R L, Bencherif M and Lippiello P 1996 An evaluation of neuronal nicotinic acetylcholine receptor activation by quaternary nitrogen compounds indicates that choline is selective for the alpha 7 subtype *Neurosci. Lett.* **213** 201–4
- [26] Trombino S, Cesario A, Margaritora S, Granone P, Motta G, Falugi C and Russo P 2004 Alpha7-nicotinic acetylcholine receptors affect growth regulation of human mesothelioma cells: role of mitogen-activated protein kinase pathway *Cancer Res.* **64** 135–45
- [27] Kihara T, Shimohama S, Sawada H, Honda K, Nakamizo T, Shibasaki H, Kume T and Akaike A 2001 Alpha 7 nicotinic receptor transduces signals to phosphatidylinositol 3-kinase to block A beta-amyloid-induced neurotoxicity *J. Biol. Chem.* **276** 13541–6
- [28] Mozayan M, Chen M F, Si M, Chen P Y, Premkumar L S and Lee T J 2006 Cholinesterase inhibitor blockade and its prevention by statins of sympathetic alpha7-nAChR-mediated cerebral nitroergic neurogenic vasodilation *J. Cereb. Blood Flow Metab.* **26** 1562–76
- [29] Mebs D, Narita K, Iwanaga S, Samejima Y and Lee C Y 1971 Amino acid sequence of-bungarotoxin from the venom of Bungarus multicinctus *Biochem. Biophys. Res. Commun.* **44** 711–6
- [30] Zhang Q, Tang X, Zhang Z F, Velikina R, Shi S and Le A D 2007 Nicotine induces hypoxia-inducible factor-1alpha expression in human lung cancer cells via nicotinic acetylcholine receptor-mediated signaling pathways *Clin. Cancer Res.* **13** 4686–94

# Bridging Biomolecules with Nanoelectronics

Kien Wen Sun  
*National Chiao Tung University*  
Chia-Ching Chang  
*National Chiao Tung University*

11.1	Introduction and Background.....	11-1
11.2	Preparation of Molecular Magnets.....	11-2
	Folding of Magnetic Protein Mn,Cd-MT • Protein: A Mesoscopic System • Quasi-Static Thermal Equilibrium Dialysis for Magnetic Protein Folding	
11.3	Nanostructured Semiconductor Templates: Nanofabrication and Patterning.....	11-6
	Patterned Self-Assembly for Pattern Replication • Fabrication by Direct Inkjet and Mold Imprinting • Nanopatterned SAMs as 2D Templates for 3D Fabrication	
11.4	Self-Assembling Growth of Molecules on the Patterned Templates.....	11-8
11.5	Magnetic Properties of Molecular Nanostructures.....	11-10
11.6	Conclusion and Future Perspectives.....	11-10
	References.....	11-11

## 11.1 Introduction and Background

The field of nanostructures has grown out of the lithographic technology developed for integrated circuits, but is now much more than simply making smaller transistors. In the early 1980s, microstructures became small enough to observe interesting quantum effects. These structures were smaller than the inelastic scattering length of an electron so that the electrons could remain coherent as they traversed them, giving rise to interference phenomena. Studies on the Aharonov-Bohm effect and universal conductance fluctuations led to the field of “mesoscale physics”—between macroscopic classical systems and fully quantized ones.

Now the size of the structures that can be produced is approaching the de Broglie wavelength of the electrons in the solids, leading to stronger quantum effects. In addition to interesting new physics, this drive toward smaller length scales has important practical consequences. When semiconductor devices reach about 100 nm, the essentially classical models of their behavior will no longer be valid. It is not yet clear how to make devices and circuits that will operate properly on these smaller scales. The replacement for the transistor, which must carry the technology to well below 100 nm, has not been identified. It is anticipated that the semiconductor industry will run up against this “wall” within about 10 years.

The current very large-scale integrated circuit paradigm based on complementary metal oxide semiconductor (CMOS) technology cannot be extended into a region with features smaller than 10 nm.<sup>1</sup> With a gate length well below 10 nm, the sensitivity of

the silicon field-effect transistor parameters may grow exponentially due to the inevitable random variations in the device size. Therefore, an alternative nanodevice concept of molecular circuits was proposed that was a radical paradigm shift from the pure CMOS technology to the hybrid semiconductor.<sup>2</sup> The concept combines the advantages of nanoscale components, such as the reliability of CMOS circuits, and the advantages of patterning techniques, which include the flexibility of traditional photolithography and the potentially low cost of nanoimprinting and chemically directed self-assembly. The major attraction of this concept is the incorporation of the richness of organic chemistry with the versatilities of semiconductor science and technology. However, before this, one needs to bring directed self-assembly from the present level of single-layer growth on smooth substrates to the reliable placement of three-terminal molecules on patterned semiconductor structures.

While physics and electrical engineering have been evolving from microstructures, to mesoscopic structures, and now to nanostructures, molecular biologists have always worked with objects of a few nanometers, or less. A DNA molecule, for example, is very long (when stretched out), but it is about 2.5 nm wide with base pairs separated by 0.34 nm. Since the technology has not existed to directly fabricate and manipulate objects this small, various chemical techniques have been developed for cutting, tagging, and sorting large biological molecules. While enormously successful, these methods utilize batch processing of huge numbers of the molecules and rely on statistical interpretations. It is not possible, in principle, to sequence one particular DNA molecule with these techniques, for example. Ideally,

one would like to stretch the DNA straight and simply read the sequence of the base pairs. While we are still far from this goal, nanofabrication techniques promise to bring us much closer.

During recent years, self-assembly has become one of the most important strategies used in biology for the development of complex, functional structures. Self-assembly on modified surfaces is one of the approaches to self-assemble structures that are particularly successful. By the coordination of molecules to surfaces, the molecular systems form ordered systems—self-assembled monolayers (SAMs). The SAMs are reasonably well understood and are increasingly useful technologically. A thin film of diblock copolymers can be self-assembled into ordered periodic structures at the molecular scale (~5–50 nm), and have been used as templates to fabricate quantum dots,<sup>3,4</sup> nanowires,<sup>5–7</sup> and magnetic storage media.<sup>8</sup> More recently, in epitaxial assembly of block-copolymer films, molecular level control over the precise size, shape, and spacing of the order domains was achieved with advanced lithographic techniques.<sup>9</sup> The development of methods for patterning and immobilizing biologically active molecules with micrometer and nanometer scale control has been proven integral to ranges of applications such as basic research, diagnostics, and drug discovery. Some of the most important advances have been in the development of biochip arrays that present either DNA,<sup>10</sup> protein,<sup>11</sup> or carbohydrates.<sup>12</sup> The use of patterned substrates for components of microfluidic systems for bioanalysis is also progressing rapidly.<sup>13–15</sup> Surface modification and patterning at the nanoscale to anchoring protein molecules is an important strategy on the way of obtaining the construction of new biocompatible materials with smart bioactive properties. In fact, surfaces patterned by protein molecules can act as active agents in a large number of important applications including biosensors capable of multifunctional biological recognition. In particular, physical adsorption of proteins onto semiconductor surfaces makes possible to combine the simplicity of the method with the versatility of chemical and physical properties of proteins.

In recent years, there has been substantial attention focused on the reactions of organic compounds with silicon surfaces. The major attraction is the incorporation of the richness of organic chemistry with the versatility of semiconductor science and technology. More recently, it has been demonstrated that TEMPO, 2,2,6,6-tetramethylpiperidinyloxy can bond with a single dangling bond on hydrogen-terminated Si(100) and Si(111) surfaces.<sup>16</sup> Functional organic molecular layers were found to self-assemble on metal<sup>2</sup> and semiconductor surfaces.<sup>17</sup> The technique of self-assembly is one of the few practical strategies available to arrive at one to three-dimensional ensembles of nanostructures. There are many different mechanisms by which self-assembly of molecules and nanoclusters can be accomplished, such as chemical reactions, electrostatic and surface forces, hydrophobic and hydrophilic interactions.

In this chapter, we present most recent advances in the development of techniques in immobilizing a single nanostructure and producing arrays of 3D magnetic protein nanostructures with high throughput on surface modified semiconductor substrates. Well-characterized test nanostructures were prepared

using current state-of-the-art nanofabrication techniques. Both nanoimaging and scanning probe microscopy studies (AFM, SEM, and TEM) on semiconductor nanostructures and these molecular self-assembly systems were performed. The combination of e-beam lithography, scanning probe microscope imaging, spectroscopy, and self-assembly approaches provide not only the high throughput of producing arrays of protein nanostructures but also with highest precision of positioning single nanostructure and/or single molecule.

## 11.2 Preparation of Molecular Magnets

### 11.2.1 Folding of Magnetic Protein Mn,Cd-MT

Metallothionein (MT) is a metal binding protein that binds seven divalent transition metals avidly via its twenty cysteines (Cys).<sup>18</sup> These Cys' form two metal binding clusters located at the carboxyl ( $\alpha$ -domain) and amino ( $\beta$ -domain) terminals of MT.<sup>19</sup> The two clusters were identified as  $\alpha$ -cluster ( $M_4S_{11}$ )<sup>3-</sup>, and the  $\beta$ -cluster ( $M_3S_9$ )<sup>3-</sup> (Figure 11.1),<sup>20–22</sup> where M denotes metal ions (Zn<sup>2+</sup>, Cd<sup>2+</sup>, or others), according to both x-ray crystallographic and NMR studies.<sup>3</sup> MT binds to metals ions via metal-thiol linkages.<sup>19</sup> As shown in Figure 11.1, the ( $M_3S_9$ )<sup>3-</sup> and ( $M_4S_{11}$ )<sup>3-</sup> have the zinc-blende like structure that is similar to the “diluted magnetic semiconductor (DMS)” compounds.<sup>23</sup>

In general, semiconductors are not magnetic. However, a diluted magnetic semiconductor exhibits magnetic properties by doping with Mn and Cd or other II–VI metal ions in certain ratio. The doped metal clusters among the semiconductors are in zinc-blende structures. Meanwhile these semiconductors possess magnetic property only in low temperatures.<sup>23</sup> The magnetic properties may be the result of the d-sp<sup>3</sup> orbital hybridization and the alignment of the electron spins. The bridging sulfur atoms may also contribute to the alignment of the spins of the Mn<sup>2+</sup> ions. Thus, by chelating the Mn<sup>2+</sup> and Cd<sup>2+</sup> with MT (i.e., Mn,Cd-MT), a “magnetic protein” may be obtained.

Recently, the single molecule magnets (SMMs) have attracted much attention.<sup>24</sup> However, the Curie temperature of these molecules has to be as low as 2–4 K<sup>24–26</sup> to avoid the thermal fluctuation among the electron spin within the molecules.<sup>27</sup> To be of practical utilization, it is highly desirable to create a room temperature molecular magnet.<sup>28</sup> With this intention in mind, one has to construct and investigate a new metal binding protein, metallothionein, which sustained characteristic magnetic hysteresis loop from 10 to 330 K. The protein backbone may restrain the net spin moment of Mn<sup>2+</sup> ions to overcome the minor thermal fluctuation. The magnetic-metallothionein (mMT) presented may reveal a possible approach to create high temperature molecular magnet. In order to prepare the Mn,Cd-MT magnetic proteins, the folding mechanism of protein should be introduced.

### 11.2.2 Protein: A Mesoscopic System

Protein is a complex biomolecule that contains a large number of basic residues—amino acids. Therefore, it is not possible to analyze it completely by macroscopic approaches. Meanwhile, it

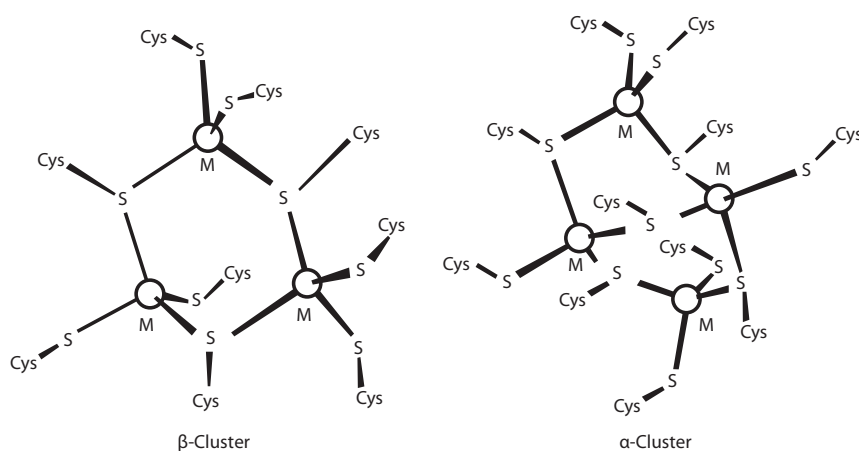


**FIGURE 11.1** Metal binding clusters of metallothionein that was modified from x-ray crystal structure (2). Where the circles denote metal ions  $Zn^{2+}$ ,  $Cd^{2+}$ , or  $Mn^{2+}$ . Each metal ion was linked with protein via metal-thiol bonds.

is not feasible to describe the dynamics of its polypeptide chain behavior by using conventional statistical approaches either. Thus, a protein can be thought of as a mesoscopic system.<sup>29</sup> However, the conformational transition from unfolded state to the native state of a protein may be similar to the conventional phase transition model. In physics, a phase transition is the transformation of a thermodynamic system from one phase to another. In a folding process, proteins follow the thermodynamic theories and transform from the unfolded state to the folded state, where the state is defined as a region of configuration space with minimal potential.<sup>30</sup> Therefore, we named this conformational change as “state transition.”<sup>31</sup> Due to the complexity of a protein folding system, a single experimental study may reveal only a part of the fact of protein folding. Therefore, we should examine the protein-folding problem with multidimensional approaches and integrate the findings to reveal the true mechanism of protein folding.

Protein folding may follow a spontaneous process<sup>29</sup> or a reaction-path directed process<sup>30</sup> *in vitro*. A choice between the two may be determined by the intrinsic properties of proteins, for example, the varying folding transition boundaries. However, a general model, named “first-order-like state transition model,” in which the aggregated proteins exist within finite boundaries can encompass both processes without any conflicts.<sup>31–36</sup> According to this model, the folding path of the protein may not be unique. It can be folded, without being trapped in an aggregated state, via a carefully designed refolding path circumventing the transition boundary, that is, via an overcritical path.<sup>31–36</sup> The intermediates, following an overcritical path, are in a molten globular state,<sup>37</sup> and their behavior is consistent with both a sequential<sup>38</sup> and a collapse model.<sup>39</sup> However, both soluble (folded) and precipitated (unfolded) proteins can be observed in the direct folding reaction path *in vitro*. In terms of the “first-order-like state transition model” language, this can be described as stepping across the state transition line in

the protein folding reaction phase diagram.<sup>31,32</sup> Since in protein refolding it is important to prevent protein aggregation *in vitro*, similarly, in biomedical applications, the revelation of the mechanism of the formation of the two states (unfolded and folded) becomes significant.

Previous studies have indicated that chemical environment,<sup>40</sup> temperature,<sup>41</sup> pH,<sup>42</sup> ionic strength,<sup>43</sup> dielectric constant,<sup>44</sup> and pressure<sup>49</sup>—considered as solvent effects collectively—could affect the fundamental structure, thermodynamics, and dynamics of polypeptides/proteins. The reaction ground state can be expressed as a dual-well potential according to the two-state transition model. The conformational energy, in general, of the unfolded state is relatively higher than that of the native state (Figure 11.1). When the system reaches thermal equilibrium most protein molecules are found in their native state. No unfolded or intermediate states are observable. However, as described previously,<sup>31–36</sup> if a denaturant is added the reaction potential may change accordingly as indicated in Figure 11.1. Then, an unfolded protein may be stable, as it is now at the lowest energy under the newly established equilibrium. The energy of the system can be expressed as follows:

$$H_T = H_p + \lambda H_s \quad (11.1)$$

where  $H_T$ ,  $H_p$ , and  $H_s$  denote the potential energy of the interacting protein-solvent total system, the protein, and the solvent, respectively. The factor,  $\lambda$ , is a weighting factor of the solvent environment ( $0 \leq \lambda \leq 1$ ). It approaches unity when a denaturant is present as pure solvent, and decreases in value as the concentration of the denaturant is reduced.

When  $\lambda$  of the system is changed drastically, direct folding ensues and leads to the release of some of the bound denaturant. According to the Donnan effect in a macromolecule-counter ions interactive system, the diffusion of the bound denaturant can be expressed by Fick’s first law:

$$\vec{J} = -D\nabla n \quad (11.2)$$

where

$n$  denotes the concentration of the denaturant that is dissociated from the protein  
 $D$  denotes the diffusive constant  
 vector  $J$  denotes the flux, respectively, of the solute

According to the Einstein relation

$$D = \frac{kT}{6\pi\eta R_H} \quad (11.3)$$

where

$k$  is the Boltzmann constant  
 $T$  is the temperature in Kelvin  
 $\eta$  is the viscosity of the solvent  
 $R_H$  is the hydration radius of the solutes

Due to the intrinsic diffusion process, the solute exchange processes are not synchronous for all protein molecules. Therefore, the folding rate of protein may not be measured directly by a simple spectral technique, that is, the stopped-flow CD,<sup>45</sup> continuous-flow CD,<sup>46</sup> or fluorescence.<sup>47</sup> However, the reaction interval of protein folding can be revealed by the autocorrelation of reaction time from these direct measurements. The detailed mechanism and an example will be discussed later.

If we look at the energy landscape funnel model of protein folding,<sup>48</sup> it appears that proteins can be trapped in a multitude of local minima of the potential well in a complicated protein system. The native state, though, is at the lowest energy level. When thermal equilibrium is reached, most of the protein molecules are located in the lowest energy state, with a population ratio as low as  $e^{-\Delta E/kT}$ , according to the Maxwell–Boltzmann distribution in thermodynamics. The  $\Delta E$  denotes the energy difference between the native state and a local minimum;  $k$  and  $T$  denote the Boltzmann constant and temperature in Kelvin, respectively. At high concentration (>0.1 mg/mL), however, considerable amount of insoluble protein has been observed in protein folding,<sup>31,33–37,48</sup> indicating that insoluble proteins are at an even lower energy state than the native protein. Therefore, by considering the intermolecular interactions during the protein folding process the reaction energy landscape may be expressed as a three-well model (Figure 11.2). As shown in Figure 11.2, the unfolded protein (U) is in the highest energy state; the native protein (N) is in the lower energy state. However, the intermediate (I) that may cause further protein aggregation/precipitation is in the lowest energy state. Although the energy state of the intermediate/aggregosome is the lowest energy state, the conformational energy of the individual proteins composing the aggregosome may not be lower than the native protein. Namely, in single molecular simulation this extra potential well of intermediate (I) is nonexistent. Therefore, in the conventional energy landscape model (the single molecule simulation model),

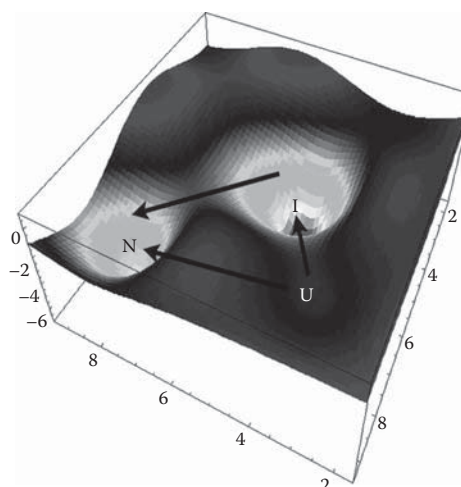


**FIGURE 11.2** Three well model of multi-protein molecules folding reaction. The U denotes the unfolded state. N denotes the native state and I denotes the protein–protein complex (aggregosome) intermediate.

the lowest energy state “I” cannot be observed. According to the Zwanzig’s definition of state, the protein molecules in the intermediate (I) belong to an unfolded state.<sup>13</sup> Hence, in a direct folding reaction, the soluble (N) and the insoluble parts (U) can coexist and they can be observed simultaneously, which is similar to the situation where the phase transition line is crossed in reactions congruent to the “first-order phase transition” model. Therefore, we named the protein folding reaction as “first-order like state transition model” (as shown in Figure 11.3).

The  $\Phi(n_1, n_2, \dots)$  in Figure 11.3 denotes the folding status of protein, where  $n_1, n_2, \dots$  represent the variables affecting the folding status, such as, temperature, concentration of denaturants, etc. The reaction curve indicates an overcritical reaction path of a quasi-static folding reaction. The gray area in Figure 11.3 indicates the state transition boundary of protein folding. The gray line and dash line indicate the reaction path of direct folding. By combining the three-well model (Figure 11.2) and the direct

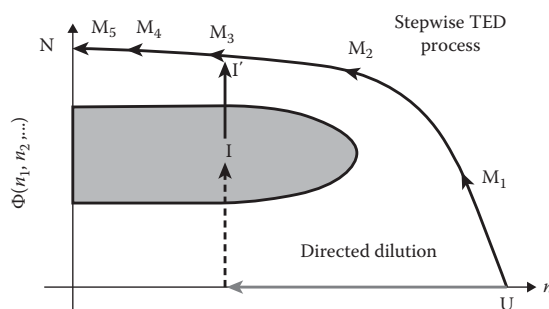


**FIGURE 11.3** The protein folding phase diagram, where the  $\Phi(n_1, n_2, \dots)$  denotes the folding status (the order parameter) of protein. The  $n, n_1, n_2, \dots$  denote the variables that affect the folding status such as temperature, concentration of denaturants, etc.

folding reaction of the “first-order like state transition model” (Figure 11.3), we realized that those folded protein molecules along the direct folding path might fold spontaneously or form aggregates. Spontaneous folding may be driven by enthalpy-entropy compensation.

As indicated previously, the conformation of protein changed with changes of the solvent environment. It seems that the protein may fold spontaneously, such as in Anfinsen’s experiment<sup>44</sup> and direct folding reactions. The protein folding reaction, similar to all chemical reactions, reaches its equilibrium by following the fundamental laws of thermodynamics. Although protein folding has been studied extensively in certain model systems for over 40 years, the driving force at the molecular level remained unclear until recently.

It is known that polymers and macromolecules may self-assemble/self-organize into a wide range of highly ordered phases/states at thermal equilibrium.<sup>49–52</sup> In a condensed solvent environment, large molecules may self-organize to reduce their effective volume. Meanwhile, the number of the allowed states ( $\Omega$ ) of small molecules, such as buffer salt and other counterions in solution, increases considerably. Therefore, the entropy of the system,  $\Delta S = R \ln(\Omega_f/\Omega_i)$ , becomes large, where  $i$  and  $f$  denote the initial and final states, respectively. Meanwhile, the enthalpy change ( $\Delta H$ ) between the unfolded and native protein is around hundreds kcal/mol.<sup>53</sup> Therefore, the Gibbs free energy of the system,  $\Delta G = \Delta H - T\Delta S$ , becomes more negative in this system when the large molecules self-organize.<sup>54</sup> A similar entropy-enthalpy compensation mechanism has been used to solve the reaction of colloidal crystals that self-assemble spontaneously.<sup>55,56</sup>

According to our studies,<sup>31,33–37</sup> the effective diameter of the unfolded protein is about 1.7 to 2.5 fold larger than the folded protein. Therefore, with the same mechanism, those macromolecules (proteins) may tend to reduce their effective volumes and increase the system entropy when thermal equilibrium is reached. The increase in entropy may compensate for the change of the enthalpy of the system and enable the reaction to take place spontaneously. This may be the reaction molecular mechanism of spontaneous protein folding reactions. Meanwhile, a similar mechanism can be adopted into the self-assembly process of magnetic protein in nanopore arrays.

### 11.2.3 Quasi-Static Thermal Equilibrium Dialysis for Magnetic Protein Folding

Due to the intrinsic diffusion process, the solvent exchange rate is slow and thus the variation of  $\lambda$  is slow and can be thought of as quasi-static. Therefore, we named this buffer exchanging process as a quasi-static process. We manipulated the reaction direction of the protein folding through this process. Meanwhile, we can obtain stable intermediates in each thermal equilibrium state. These intermediates may help us reveal the molecular folding mechanism of protein that is to be discussed in Section 11.3. The following is an example of the stepwise folding method,<sup>31,33–37</sup> and the buffers used were described in these studies.

Step 1: The unfolded protein (U) was obtained by treating the precipitate or inclusion body with denaturing/unfolding buffer to make it 10 mg/mL in concentration. This solution was left at room temperature for 1 h. This process was meant to relax the protein structure by urea and pH (acidic or basic) environments. The disulfide bridges were reduced to SH groups and the protein was unfolded completely.

Step 2: The unfolded protein (U) in the denature/unfolding buffer was dialyzed against the folding buffer 1 for 72 h to dilute the urea concentration to 2 M, producing intermediate 1, or  $M_1$ .

Step 3:  $M_2$  was obtained by dialyzing  $M_1$  against the folding buffer 2 for 24 h to dilute urea concentration to 1 M.

Step 4:  $M_3$ , an intermediate without denaturant (urea) in solution, was then obtained by dialyzing  $M_2$  against the folding buffer 3 for 24 h.

Step 5:  $M_3$  was further dialyzed against the folding buffer 4 for 24 h, and the pH changed from 11 to 8.8 to produce  $M_4$ .

Step 6: Finally, the chemical chaperonin mannitol was removed by dialyzing  $M_4$  against the native buffer for 8 h to yield  $M_5$ .

It should be noted that all the equilibrium time of each step is longer than the conventional dialysis time. In general, for the free solvent case the solute may exchange with the buffer completely within hours. However, it is known that the denaturant molecules interact with protein, similar to the Donna effect, and the solute exchange may be slow and needs more time for the system to reach thermal equilibrium, especially for the first refolding stage. The folding time of each process is relatively longer than the regular solvent exchange process. Therefore, we can obtain the magnetic protein that follows a similar process. Protein microenvironment protects the net electron spin of molecules from thermal fluctuation.

The bridging ligands (i.e., sulfur atom, S) between the magnetic ions may be responsible for aligning the electron spin of magnetic ions. As indicated in Figure 11.4, the valance bonding electrons of the bridging Cys may hop between the bonded metal ions, such as  $Mn^{2+}$  and  $Cd^{2+}$ ; whereas the  $Cd^{2+}$  in the  $\beta$  metal cluster is rather important in restraining the orientation of the electron spins of the bridging sulfurs and in aligning the spins of  $Mn^{2+}$  in the metal binding clusters. Therefore, this electron hopping effect may turn the Mn,Cd-MT into a magnetic molecule. However, the protein backbone surrounding the  $\beta$  metal cluster may provide a strong restraining effect to overcome the thermal fluctuations from the environment. Therefore, the magnetization can be observed in room temperature. However, the geometrical symmetry of the spin arrangement in all Mn-MT may cause partial or complete cancellation of detectable magnetization. These results also indicated that the threshold temperature of the molecular magnet might rise to room temperature if the proper prosthetic environment, such as protein backbone, can be linked against the thermal fluctuation of the temperature.

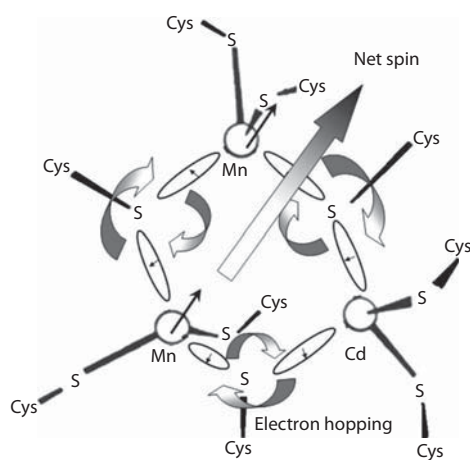


FIGURE 11.4 Proposed electron spin model of Mn<sup>2+</sup> in β metal binding cluster of Mn,Cd-MT-2.

Therefore, we have successfully constructed a molecular magnet, Mn,Cd-MT, that is stable from 10 to 330 K. The observed magnetic moment can be explained by the highly ordered alignment of (Mn<sub>2</sub>CdS<sub>9</sub>)<sup>3-</sup> clusters embedded in the β-domain in which sulfur atoms serve as key bridging ligands. The discovery of magnetic-metallothionein (mMT) may allude to new schemes in constructing a completely different category of molecular magnets.

### 11.3 Nanostructured Semiconductor Templates: Nanofabrication and Patterning

The rapidly developing of interdisciplinary activity in nanostructuring is truly exciting. The intersections between the various disciplines are where much of the novel activity resides, and this activity is growing in importance. The basis of the field is any type of material (metal, ceramic, polymer, semiconductor, glass, and composite) created from nanoscale building blocks (clusters of nanoparticles, nanotube, nanolayers, etc.) that are themselves synthesized from atoms and molecules. Thus, the controlled synthesis of those building blocks and their subsequent assembly into nanostructures is one fundamental theme of this field. This theme draws upon all of the material-related disciplines from physics to chemistry to biology and to essentially all of the engineering disciplines as well.

The second and most fundamental important theme in this field is that the nanoscale building blocks, because of their size being below about 100 nm, impart to the nanostructures that are created from them new and improved properties and functionalities that are still unavailable in conventional materials and devices. The reason for this is that the materials in this size range can exhibit fundamentally new behavior when their sizes fall below the critical length scale associated with

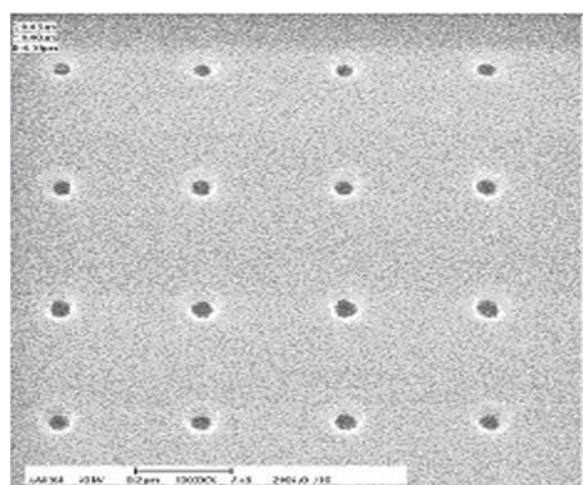
any given property. Thus, essentially any material property can be dramatically changed and engineered through the controlled size-selective synthesis and assembly of nanoscale building blocks. The present juncture is important in the fields of nanoscale solid-state physics, nanoelectronics, and molecular biology. The length scales and their associated physics and fabrication technology are all converging to the nanometer range.

The ability to fabricate structures with nanometer precision is of fundamental importance for any exploitation of nanotechnology. In particular, cost effective methods that are able to fabricate complex structures over large areas will be required. One of the main goals in the nanofabrication area is to develop general techniques for rapidly patterning large areas (a square centimeter, or more) with structures of nanometer sizes. Presently, electron-beam (e-beam) lithography is capable of defining patterns that are less than 10 nm. These patterns can then be transferred to a substrate using various ion milling/etching techniques. However, these are “heroic” experiments, and can only be made over a very limited area—typically a few thousand square microns, at most. While such areas are immediately useful for investigating the physics of nanostructures, the applications we would like to pursue will eventually require a faster writing scheme, and much larger areas. The time and area constraints are determined by the direct e-beam writing. It is a “serial” process, defining single small regions at a time. Furthermore, the field of view for the e-beam system is typically less than 100 nm when defining the nanometer-scale structures. One simply cannot position the electron beam with nm precision over larger areas.

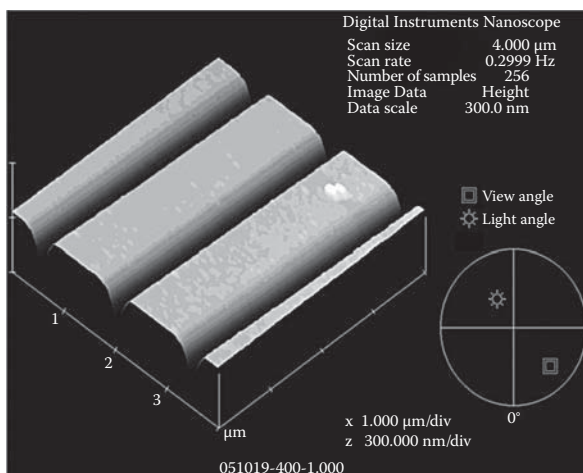
While e-beam lithographic methods are very general, in that essentially any shape can be written, we will also make use of “natural lithography” (tricks). Similarly, advances in the knowledge of the DNA structure has recently been applied to the fabrication of self-organized nm surface structures. There are many such “tricks” that could prove crucial to the success of the projects in allied fields. A list of current methods toward nanofabrication is given below.

#### 11.3.1 Patterned Self-Assembly for Pattern Replication

By exploiting e-beam and focused ion beam lithography, self-assembled monolayers can be patterned into 10–20 nm features that can be functionalized with single molecules or small molecular groupings. These patterned areas will then be used as templates to direct the vertical assembly of stacks of molecules or to direct the growth of polymeric molecules. Schematics of the processes and the possible templates used are shown in Figure 11.5. The initial 2D pattern will thus be translated into 3D nanosized objects. With the capability of the full control over the interfacial properties, it will be possible to release the objects from the templates and transfer them to another substrate, after which the nanopatterned surface can be used again to provide an inexpensive replication technique.



(a)



(b)

AQ1

FIGURE 11.5 E-beam lithography defined (a) nanopores and (b) nanotrenches on silicon templates. (From Sun, 2007. With permission.)

### 11.3.2 Fabrication by Direct Inkjet and Mold Imprinting

This part of the technique will draw on recent advances in printing techniques for direct patterning of surfaces. This involves the use of inkjet printing to deliver a functional material (semiconductor or metal) to a substrate, which is then controlled by patterning in the surface free energy of the substrate, to allow very accurate patterning of the printed material. Currently, devices show channel lengths down to 5  $\mu\text{m}$ , but indications are that geometries can be reduced to submicron dimensions. The method will be concerned with the limits to resolution that can be achieved by this process, and also the structure and the associated electronic structure at polymer–polymer interfaces, such as that between semiconductor and insulator layers in the field-effect device.

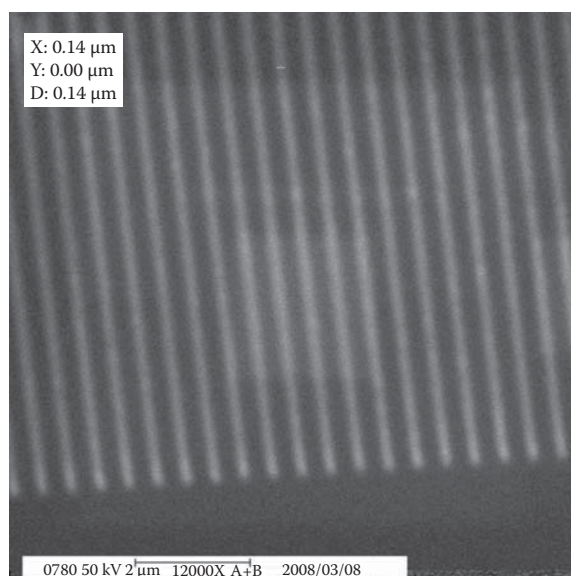


FIGURE 11.6 Nanogratings on silicon templates by using thermal nano-imprinting technique.

In 1995, Professor Stephen Y. Chou of Princeton University invented a new fabrication method in the field of semiconductor fabrication. It is called nano-imprint lithography (NIL).<sup>57</sup> Briefly speaking, this technique was demonstrated by pressing the patterned mold to contact with the polymer resist directly. The patterns on the mold will transfer to the polymer resist without any exposure source. Therefore, the diffraction effect of light can be ignored and the limitation is dependent only on the pattern size of the mold rather than on the wavelength of the exposure light. In Figure 11.6 we show a nano-grating structure made by using the thermal imprinting technique.

Nano-imprint lithography (NIL) technology is a physical deformation process and is very different from conventional optical lithography. This technology provides a different way to fabricate nanostructures with easy processes, high throughput, and low cost. Currently, there are three main NIL techniques under investigation, namely, hot-embossing nano-imprint lithography (H-NIL<sup>57</sup>), ultraviolet nano-imprint lithography (UV-NIL<sup>58</sup>), and soft lithography.<sup>59</sup> Those NIL technologies can be applied to many different research fields, including nano-electric devices,<sup>60</sup> bio-chips,<sup>61</sup> micro-optic devices,<sup>62</sup> micro-fluidic channels,<sup>63</sup> etc.

### 11.3.3 Nanopatterned SAMs as 2D Templates for 3D Fabrication

Modern lithographic techniques (e-beam or focused ion beam (FIB), SNOM lithography) are able to generate topographic (relief) patterns in the 10–50 nm size ranges. As a further step toward more complicated and functional 3D structures, chemical functionalization at a similar size scale is necessary. By exploiting e-beam, FIB, and near-field optical lithography, it is

possible to pattern self-assembled monolayers directly. Using lithography, the SAMs can either be locally destroyed and refilled with other molecules, or the surface of the SAMs can be activated to allow further chemical reactions. The resulting patterned surfaces will be chemically patterned. Patterns can be introduced to incorporate H-bonding, pi-pi stacking, or chemical reactivity. These patterned areas will be used as templates to direct the vertical assembly of stacks of molecules or to direct the growth of polymeric molecules. Large, extended aromatic molecules prefer to stack on top of each other due to pi-pi stacking. These molecules have interesting electronic properties as molecular wires. When surfaces can be patterned to incorporate "seeds" for the large aromatic molecules, the stacking can be directed away from the surface. The initial 2D pattern will thus be translated into 3D nanosized objects. With the full control

over the interfacial properties, it will be possible to release the objects from the templates and transfer them to another substrate, after which the nanopatterned surface can be used again to provide an inexpensive replication technique.

## 11.4 Self-Assembling Growth of Molecules on the Patterned Templates

The self-assembling growth of the MT-2 proteins is demonstrated as follows. One mg/mL magnetic MT in Tris. HCL buffer solution was placed onto the patterned surface, and an electric field with an intensity of 100 V/cm was then applied for 5 min to drive the MT molecules into the nanopores. The sample was then washed with DI water twice to remove the unbounded MT molecules and salts on the surface (the schematic of the process is also shown in Figure 11.7a). Figure 11.8 shows the atomic force microscopy (AFM) image of the template surface with 40 nm nanopores after they were filled by the MT-molecules. Keep in mind that most of the Si surface was still protected by photoresist after the etching processes, which has prevented the MT-molecules from forming strong OH bonds with the Si surface underneath. Therefore, the electrical field-driven MT molecules were all anchored on those areas that were not covered with photoresist. The molecules landing in each pore were then self-assembly grown vertically from the bottom of the pore into the shape of a rod (as shown in Figure 11.8). These molecular nanorods have an average height of ~120 nm above the template surface and a diameter equal to the size of the nanopore.

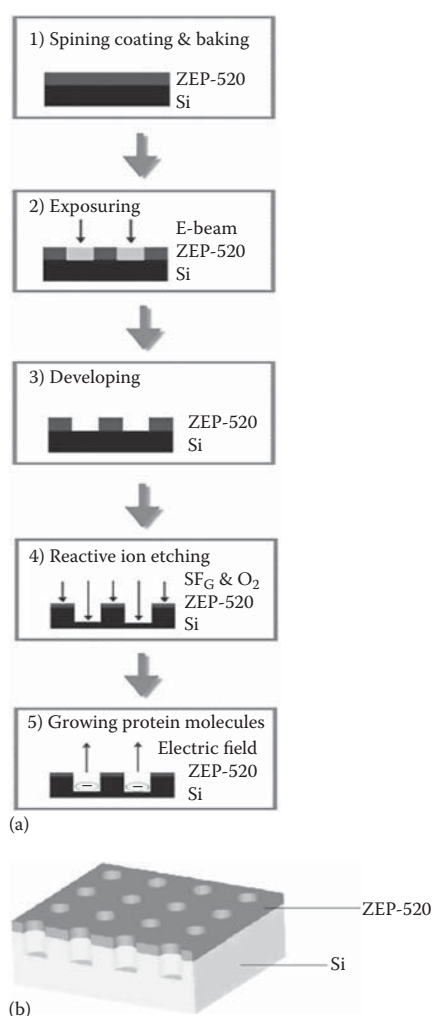


**FIGURE 11.7** (a) Flowchart of the lithography, etching processes, and growth of protein molecules (b) schematics of the patterned templates with nanopores. (From Sun, 2007. With permission.)

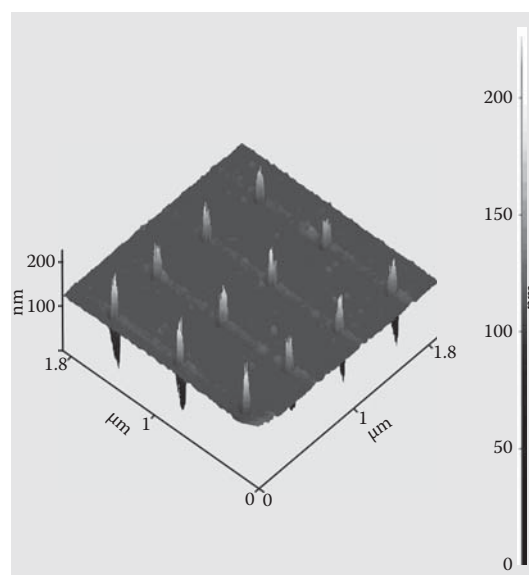


**FIGURE 11.8** Three-dimensional (3D) AFM image of the patterned magnetic molecules. The molecules have self-assembled to grow into a rod shape. (From Sun, 2007. With permission.)

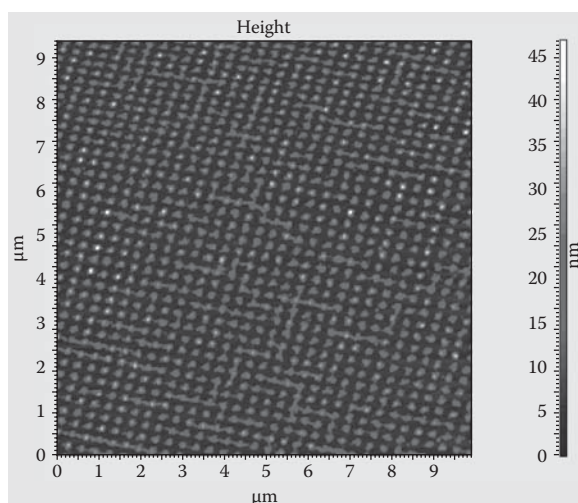


**FIGURE 11.9** Two-dimensional (2D) AFM images of the patterned MT-molecules on the template with pore size of 130 nm and pitch size of 300 nm. (From Sun, 2007. With permission.)

However, experiments on the templates with pore sizes larger than 100 nm gave quite different results. Figure 11.9 shows the two-dimensional AFM image of the template surface with larger pores where we can see that the molecules did not grow vertically above the template surface. Therefore, we were not able to generate 3D images of this type of template. However, judging from the AFM phase images, the MT molecules did form a more

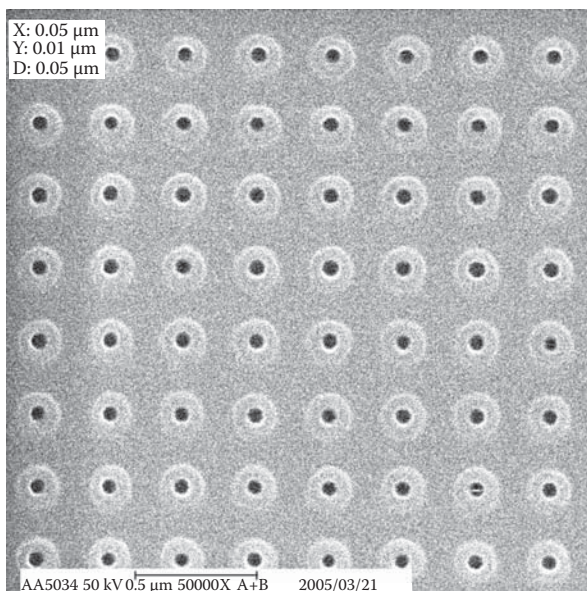
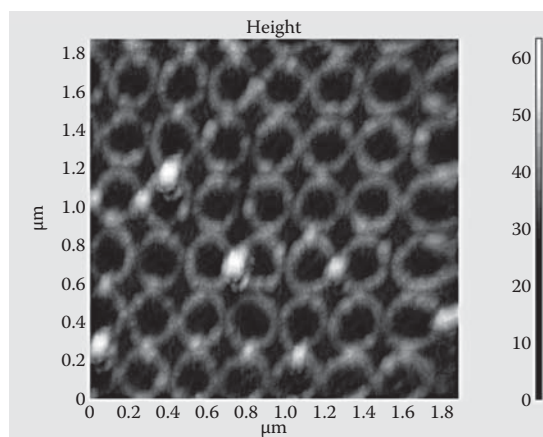


**FIGURE 11.10** SEM image of the Si template shows a ring shape Si exposed area around the circumference of nanopores. (From Sun, 2007. With permission.)

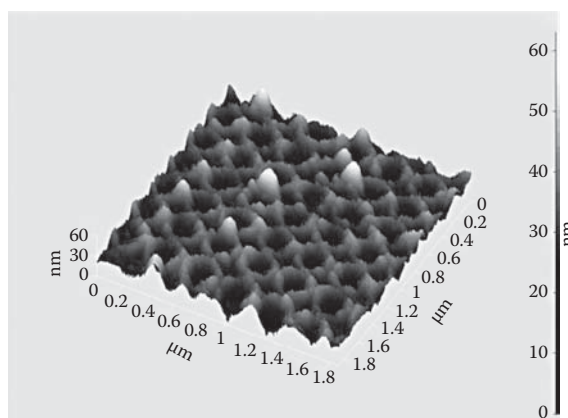
dense structure in the larger pores compared with the case of the smaller pores. On templates with thinner photoresist and smaller pitch sizes (less than 600 nm), we also found that the molecules anchored in the pore can grow laterally toward the neighboring pores (data not shown).

By increasing both the e-beam exposure and dry etching time on the Si surface covered with a thin photoresist layer with a thickness of less than 150 nm, we were able to create a ring-type area with an exposed Si surface along the periphery of the nanopores. The SEM image of this type of template is shown in Figure 11.10. On this particular template, the molecules not only independently grew inside the pores, but they also grew along the circumference of the pores to form molecular rings on the template. Figure 11.11 shows the two-dimensional (2D) and three-dimensional (3D) AFM images of such molecular rings.

In order to gain better control of the formation of molecular nanostructures, it is important to uncover the underlying self-assembling growth mechanism. Molecular self-assembly can be mediated by weak, noncovalent bonds—notably hydrogen



(a)



(b)

**FIGURE 11.11** (a) 2D and (b) 3D AFM images of the patterned MT-molecules. (From Sun, 2007. With permission.)

bonds, ionic bonds (electrostatic interactions), hydrophobic interactions, van der Waals interactions, and water-mediated hydrogen bonds. Although these bonds are relatively insignificant in isolation, when combined together as a whole, they govern the structural conformation of all biological macromolecules and influence their interaction with other molecules. The water-mediated hydrogen bond is especially important for living systems, as all biological materials interact with water. We believe that the first layer of proteins anchored inside the nanopores was bonded with the Si surface dangling bonds. They have provided building blocks for proteins that arrived later. With the assistance of spatial confinement from the patterned nanostructures, the rest of the proteins are able to self-assemble via the van der Waals interactions and perform molecular self-assembly.

### 11.5 Magnetic Properties of Molecular Nanostructures

The magnetic properties of the self-assembled molecular nanorods were investigated with magnetic force microscopy (MFM). We monitored the change of contour of a particular nanorod on the template when an external magnetic field was applied. Figure 11.12a shows the MFM image of the nanorod without the external magnetic field. In Figure 11.12b, a magnetic field of 500 Oe was applied during the measurement with a field direction from the right to left. The strength of the field was kept at a minimum so as not to perturb the magnetic tip on the instrument. In Figure 11.12 we can see clearly that the contour of the

nanorod has changed in shape as compared to the case with no applied field. It indicates that the molecular self-assembly carries a magnetic dipole moment that interacts with the external magnetic field.

### 11.6 Conclusion and Future Perspectives

Success in the synthesis of the magnetic molecules produced from metallothionein (MT-2) by replacing the Zn atoms with Mn and Cd has been demonstrated in this chapter. Hysteresis behavior in the magnetic dipole momentum measurements was observed over a wide range of temperatures when an external magnetic field was scanned. These magnetic MT molecules were also found to self-assemble into nanostructures with various shapes depending on the nanostructures patterned on the Si templates. Data from the MFM measurements indicate that these molecular self-assemblies also carry magnetic dipole momentum. Since the pore size, spacing and shape can easily and precisely be controlled by lithography and etching techniques, this work should open up a new path toward an entire class of new biomaterials that can be easily designed and prepared. The techniques developed in this particular work promise to facilitate the creation of many bio-related nanodevices and spintronics. Magnetic molecular self-assembly may find its use in data storage or magnetic recording systems, as an example. They can also act as spin biosensors and be placed at the gate of the semiconductor spin valve to control the spin current from the source to the drain. More importantly, this work should not be limited to MT-2 molecules

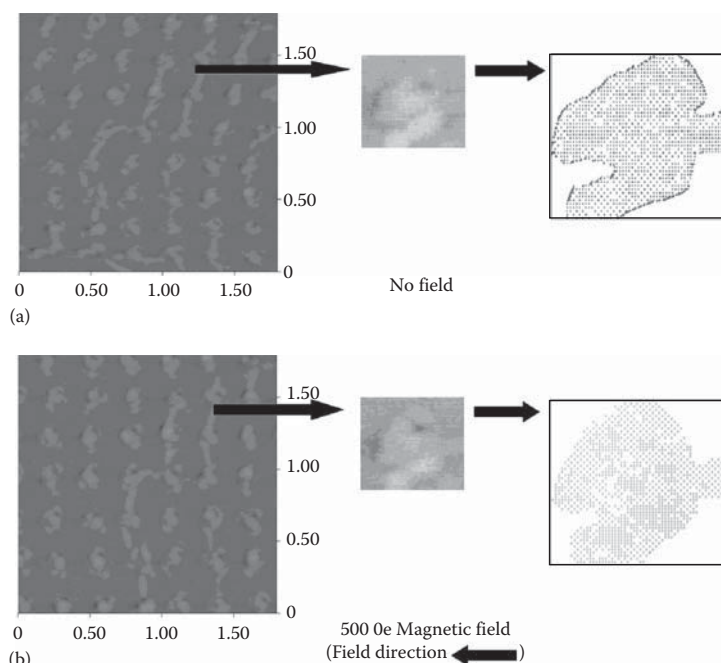


**FIGURE 11.12** MFM images of nanorods (a) without the magnetic field (b) with a 500 Oe magnetic field applied with a field direction from right to left. (From Sun, 2007. With permission.)

and should be extended to other type of molecules and proteins as well. As mentioned in the beginning of this chapter, the various surface patterning techniques developed over the years to interface organic or biological materials with semiconductors have not only provided new tools for controlled 2D and 3D self-organized assemblies, but have also been essential to the creation and emergence of new semiconductor-molecular nanoelectronics as recently discussed by Likharev.<sup>64</sup>

In the future, it is important to develop techniques for growing and characterizing molecular self-assembly, single nanostructure, and molecule on semiconductor templates to bring a measure of control to the density, order, and size distribution of these molecular nanostructures. Using self-assembly techniques, one can routinely make molecular assembly with precise distances between them. Recent explorations of molecular self-assembly have sought to provide transverse dimensions on the mesoscopic nanometer scale. As a general—although not inviolate—rule, these attempts have led to very good local ordering (e.g., nearest neighbors).

We can anticipate, (1) the development of new (supra) molecular nanostructures via the self-assembling method (bottom up technique) and immobilization of single nanostructure or molecule; (2) the design of methods to functionalize molecular self-assembly and devices; (3) an integration of bottom-up and top-down procedures for the nano- and microfabrication of molecularly driven sensors, actuators, amplifiers, and switches; and (4) an increased understanding and appreciation of the science and engineering that lie behind nanoscale processes. All this and more is in the nature of the nanotechnology bonds as it impacts on biology and beyond. In the final analysis, however, the practice of biological synthesis that relies on molecular recognition and self-assembling processes within a very much more catholic framework than is currently being contemplated by most researchers that will dictate the pace of progress in synthesis.

The final goal is to understand this whole notion of what self-assembly is. One needs to really learn how to make use of the methods of organizing structures in more complicated ways than we can do now. On a molecular scale, the accurate and controlled application of intermolecular forces can lead to new and previously unachievable nanostructures. This is why molecular self-assembly (MSA) is a highly topical and promising field of research in nanotechnology today. MSA encompasses all structures formed by molecules selectively binding to a molecular site without external influence. With many complex examples all around us in nature (ourselves included), MSA is a widely observed phenomenon that has yet to be fully understood. Being more a physical principle than a single quantifiable property, it appears in engineering, physics, chemistry, and biochemistry, and is therefore truly interdisciplinary.

## AQ2 References

- Sessoli R., Gatteschi D., Caneschi A., and Novak M.A. (1993), *Nature (London)*, **365**, 141–143.
- Fonticelli M., Azzaroni O., Benitez G., Martins M.E., Carro P., and Salvarezza R.C. (2004), *J. Phys. Chem. B*, **108**, 1898.
- Park M., Harrison C., Chaikin P.M., Register R.A., and Adamson D.H. (1997), *Science (Washington, DC)*, **276**, 1401–1404.
- Li R.R., Dapkus P.D., Thompson M.E., Jeong W.G., Harrison C., Chaikin P.M., Register R.A., and Adamson D.H. (2000), *Appl. Phys. Lett.*, **76**, 1689–1691.
- Thurn-Albrecht T., Schotter J., Kästle G.A., Emlay N., Shibauchi T., Krusin-Elbaum L., Guarini K., Black C.T., Tuominen M.T., and Russell T.P. (2000), *Science (Washington, DC)*, **290**, 2126–2129.
- Kim H.C. et al. (2001), *Adv. Mater.*, **13**, 795–797.
- Lopes W.A. and Jaeger H.M. (2001), *Nature*, **414**, 735–738.
- Cheng J.Y. et al. (2001), *Adv. Mater.*, **13**, 1174–1178.
- Kim S.O., Solak H.H., Stoykovich M.P., Ferrier N.J., de Pablo J.J., and Nealey P.F. (2003), *Nature*, **424**, 411–414.
- Demers L.M., Ginger D.S., Park S.J., Li Z., Chung S.W., and Mirkin C.A. (2002), *Science (Washington, DC)*, **296**, 1836–1838.
- Hodneland C.D., Lee Y.S., Min D.H., and Mrksich M. (2002), *Proc. Natl. Acad. Sci.*, **99**, 5048–5052.
- Houseman B.T. and Mrksich M. (2002), *Chem. Biol.*, **9**, 443–454.
- Chen C.S., Mrksich M., Huang S., Whitesides G.M., and Ingber D.E. (1997), *Science (Washington, DC)*, **276**, 1345–1347.
- Mrksich M., Dike L.E., Tien J.Y., Ingber D.E., and Whitesides G.M. (1997), *Exp. Cell. Res.*, **235**, 305–313.
- Chen C.S., Mrksich M., Huang S., Whitesides G.M., and Ingber D.E. (1998), *Biotech. Prog.*, **14**, 356–363.
- Pitters J.L., Piva P.G., Tong X., and Wolkow R.A. (2003), *Nano Lett.*, **3**, 1431.
- Wacaser B.A., Maughan M.J., Mowat I.A., Niederhauser T.L., Linford M.R., and Davis R.C. (2003), *Appl. Phys. Lett.*, **82**, 808.
- Eaton D.L. (1985), *Toxicol. Appl. Pharmacol.*, **78**, 158–162.
- Robbins A.H., McRee D.E., Williamson M., Collett S.A., Xuong N.H., Furey W.F., Wang B.C., and Stout C.D. (1991), *J. Mol. Biol.*, **221**, 1269–1293.
- Messerle B.A., Schaffer A., Vasak M., Kagi J.H.R., and Wuthrich K. (1992), *J. Mol. Biol.*, **225**, 433–443.
- Boulanger Y., Goodman C.M., Forte C.P., Fesik S.W., and Armitage I.M. (1983), *Proc. Natl. Acad. Sci.*, **80**, 1501–1505.
- Chang C.C. and Huang P.C. (1996), *Protein Eng.*, **9**, 1165–1172.
- Wei S.H. and Zunger A. (1986), *Phys. Rev. Lett.*, **56**, 2391–2394.
- Christou G., Gatteschi D., Hendrickson D.N., and Sessoli R. (2000), *MRS Bull.*, **25**, 66–71.
- Sessoli R., Tsai H.L., Schake A.R., Wang S., Vincent J.B., Folting K., Gatteschi D., Christou G., and Hendrickson D.N. (1993), *J. Am. Chem. Soc.*, **115**, 1804–1816.
- Aubin S.M.J., Dille N.R., Pardi L., Kryzyszek J., Wemple M.W., Brunel L.C., Maple M.B., Christou G., and Hendrickson D.N. (1998), *J. Am. Chem. Soc.*, **120**, 4991.
- Friedman J.R., Sarachik M.P., Tejada J., and Ziolo R. (1996), *Phys. Rev. Lett.*, **76**, 3830–3833.

28. Bushby R.J. and Pailland J.-L. (1995), Molecular magnets, in *Introduction to Molecular Electronics*, M.C. Petty, M.R. Bryce, and D. Bloor (eds.), Edward Arnold, Hodder Headline, London, U.K.
29. Wolynes P.G. (1997), *Proc. Natl. Acad. Sci. U.S.A.*, **94**, 6170–6175.
30. Zwanzig R. (1997), *Proc. Natl. Acad. Sci. U.S.A.*, **94**, 148–150.
31. Chang C.-C., Yeh X.-C., Lee H.-T., Lin P.-Y., and Kan L.S. (2004), *Phys. Rev. E*, **70**, 011904.
32. Welker E., Wedemeyer W.J., Narayan M., and Scheraga H.A. (2001), *Biochemistry*, **40**, 9059–9064.
33. Chang C.-C., Su Y.-C., Cheng M.-S., and Kan L.S. (2002), *Phys. Rev. E*, **66**, 021903.
34. Chang C.-C., Tsai C.T., and Chang C.Y. (2002), *Protein Eng.*, **5**, 437–441.
35. Chang C.-C., Su Y.-C., Cheng M.-S., and Kan L.S. (2003), *J. Biomol. Struct. Dyn.*, **21**, 247–256.
36. Chang C.-C. and Kan L.-S. (2007), *Chinese J. Phys.*, **45**, 693–702.
37. Liu Y.-L., Lee H.-T., Chang C.-C., and Kan L.S. (2003), *Biochem. Biophys. Res. Commun.*, **306**, 59–63.
38. Levy Y., Jortner J., and Becker O. (2001), *Proc. Natl. Acad. Sci. U.S.A.*, **98**, 2188–2193.
39. Creighton T.E. (1993), *Proteins*, W.H. Freeman, New York.
40. Elcock A.H. (1999), *J. Mol. Biol.*, **294**, 1051–1062.
41. Ulrich N.P., Anderlueh G., Macek P., and Chalikian, T.V. (2004), *Biochemistry*, **43**, 9536–9545.
42. Despa F., Fernandez A., and Berry R.S. (2004), *Phys. Rev. Lett.*, **93**, 228104.
43. Seefeldt M.B., Ouyang J., Froland W.A., Carpenter J.F., and Randolph T.W. (2004), *Protein Sci.*, **13**, 2639–2650.
44. Anfinsen C.B., Haber E., Sela M., and White F.H. Jr. (1961), *Proc. Natl. Acad. Sci.*, **47**, 1309–1314.
45. Su Z.D., Arooz M.T., Chen H.M., Gross C.J., and Tsong T.Y. (1996), *Proc. Natl. Acad. Sci.*, **93**, 2539–2544.
46. Roder H., Maki K., Cheng H., and Shastry M.C. (2004), *Methods*, **34**, 15–27.
47. Royer C.A. (1995), *Methods Mol. Biol.*, **40**, 65–89.
48. Misawa S. and Kumagai I. (1999), *Biopolymers*, **51**, 297–307.
49. Dinsmore A.D., Crocker J.C., and Yodh A.G. (1998), *Curr. Opin. Colloid Interface Sci.*, **3**, 5–11.
50. Gast A.P. and Russel W.B. (1998), *Phys. Today*, **51**, 24–30.
51. Pusey P.N. and van Megan W. (1986), *Nature*, **320**, 340–341.
52. Ackerson B.J. and Pusey P.N. (1988), *Phys. Rev. Lett.*, **61**, 1033–1036.
53. Tsong T.Y., Hearn R.P., Warthal D.P., and Sturtevant J.M. (1970), *Biochemistry*, **9**, 2666–2677.
54. Tokuriki N., Kinjo M., Negi S., Hoshino M., Goto Y., Urabe I., and Yomo T. (2004), *Protein Sci.*, **13**, 125–133.
55. Lin K.-H., Crocker J.C., Prasad V., Schofield A., Weitz D.A., Lubensky T.C., and Yodh A.G. (2000), *Phys. Rev. Lett.*, **85**, 1770–1773.
56. Lau A.W.C., Lin K.-H., and Yodh A.G. (2002), *Phys. Rev. E*, **66**, 020401.
57. Stephen Y.C., Peter R.K., and Preston J. R. (1995), *Appl. Phys. Lett.*, **67**, 3114–3116.
58. Bender M., Otto M., Hadam B., Spangenberg B., and Kurz H. (2000), *Microelectron. Eng.*, **53**, 233–236.
59. Xia Y. and Whitesides G.M. (1998), *Angew. Chem. Int.*, **37**, 550–575.
60. Lingjie G., Peter R.K., and Stephen Y.C. (1997), *Appl. Phys. Lett.*, **71**, 1881–1883.
61. Pépin A., Youinou P., Studer V., Lebib A., and Chen Y. (2002), *Microelectron. Eng.*, **61–62**, 927–932.
62. Li M., Tan H., Chen L., Wang J., and Chou S.Y., (2003), *J. Vac. Sci. Technol. B*, **21**, 660–663.
63. Cho Y.H., Lee S.W., Kim B.J., and Fujii T. (2007), *Nanotechnology*, **18**, 465303.
64. Likharev K.K. (2003), Hybrid semiconductor–molecular nanoelectronics. *The Industrial Physicist*, June/July 2003, Forum: 20–23.

## Author Queries

[AQ1] Please provide complete source details to Figures 11.5, 11.7, 11.8, 11.9, 11.10, 11.11, and 11.12.

[AQ2] The following references are one and the same: Refs. 2 and 17 and 46 and 51. Repeated references are deleted both in the list and in the text.

## Chapter 12

# Design of Nanodiamond Based Drug Delivery Patch for Cancer Therapeutics and Imaging Applications

Wing Kam Liu, Ashfaq Adnan, Adrian M. Kopacz, Michelle Hallikainen, Dean Ho, Robert Lam, Jessica Lee, Ted Belytschko, George Schatz, Yonhua Tzeng, Young-Jin Kim, Seunghyun Baik, Moon Ki Kim, Taesung Kim, Junghoon Lee, Eung-Soo Hwang, Seyoung Im, Eiji Ōsawa, Amanda Barnard, Huan-Cheng Chang, Chia-Ching Chang, and Eugenio Oñate

### 12.1 Introduction

The onset and recurrence of cancer is one of the major biomedical quandaries of our time. Currently, surgically removed tumors often leave behind a residual cancer cell population. As not all cancer cells can be detected to ensure complete tumor

---

W. Kam Liu (✉), A. Adnan, A. Kopacz, M. Hallikainen, D. Ho, R. Lam, J. Lee, T. Belytschko, and G. Schatz  
Northwestern University, Evanston, IL, USA

Y. Tzeng  
National Cheng Kung University (NCKU), Tainan, Taiwan

Y.-J. Kim, S. Baik, M. K. Kim, and T. Kim  
Sungkyunkwan University (SKKU), Seoul, South Korea

J. Lee and E.-S. Hwang  
Seoul National University (SNU), Seoul, South Korea

S. Im  
Korea Advanced Institute of Science and Technology (KAIST), Daejeon Science Town, Daejeon, South Korea

E. Ōsawa  
Nanocarbon Research Institute (NCRI), Shinshu University, Nagano Prefecture, Japan

A. Barnard  
Commonwealth Scientific and Industrial Research Organisation (CSIRO), Clayton, VIC, Australia

H.-C. Chang  
Institute for Advanced and Molecular Studies (IAMS), Academia Sinica, Taipei, Taiwan

C.-C. Chang  
National Chiao Tung University (NCTU), Hsinchu, Taiwan

E. Oñate  
International Center for Numerical Methods in Engineering (CIMNE), Barcelona, Spain

removal, systemic and widespread chemotherapy is usually injected into the bloodstream to attempt to target the remaining cancer cells. This can result in devastating side effects because the cancer drugs flow freely throughout the bloodstream with a reduced ability to target-specific regions. This treatment kills both healthy and unhealthy cells, and thus the quality of life of cancer patients is significantly reduced.

A multiscale anatomy of cancer cell, e.g., the breast cancer cell, reveals that a single cancer cell contains a number of characteristic elements including specific biomarker receptors (e.g., folic acid ligands) and DNA molecules, as shown schematically in Fig. 12.1. If these cancer-specific molecules can be intercalated by some functional molecules supplied via an implantable patch, then the patch can be envisioned to serve as a complementary technology with current systemic therapy. The patch has the potential to enhance localized treatment efficiency, minimize excess injections/surgeries, and prevent tumor recurrence, provided that the patch is designed such that a quantitative control on the assembly, loading, and release of such functional groups are ensured.

The creation of a fully optimized biocompatible device capable of local delivery has proven to be very challenging, due to a range of chemical and material problems

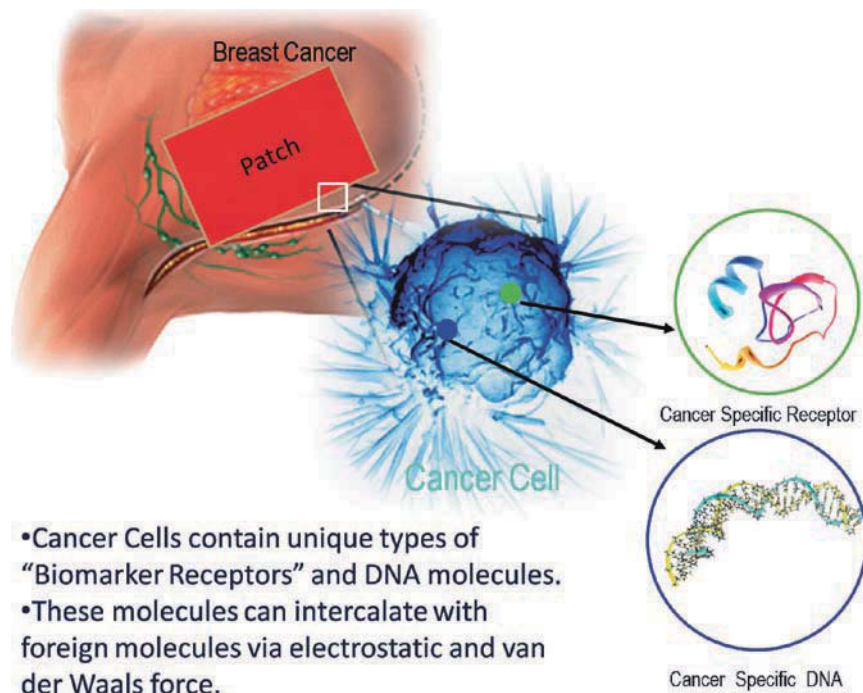


Fig. 12.1 Multiscale anatomy of cancer cell

to be overcome in addition to the pharmacological and biomedical issues. For example, metal-based delivery materials often possess reactive interfaces that can cause cell stress and inflammation, hindering the efficacy of therapy [1, 2]. The selected delivery material must be extremely stable to enable localized release while resisting attack from the immune system, which commonly leads to the breakdown of the device and ultimately to failure of the treatment. Furthermore, systemic nanoparticle-mediated administration of anti-inflammatory compounds is nonlocalized, indiscriminate, dilutes drug efficacy, and lowers drug loading capacities. Therefore, it is important that a technology be developed that can consistently release the cancer drug in a localized and sustained fashion and the fundamental basis of this functionality is understood to drive intelligent device design.

Currently, biodegradable strategies are the preferred option for local drug delivery. This type of device often dissolves between 20 and 30 days after implantation, which is consistent with the timeframe for conclusion of drug release. Sustained treatment using this method requires repeated implantation, which can cause repeated inflammation and side effects that impede cancer treatment [3–5].

Combined imaging/diagnostics and therapy (termed “theranostics”) have made important advances over the past several years, and continued work has been sought to design transformative materials to accelerate the fruition of this roadmap [1–42]. Based on their unique mechanical–chemical properties, it can be envisioned that nanocarbons, such as diamond-based nanomaterials, may serve as optimal platforms for the integrative imaging and treatment of cancer cells. Much of the ongoing research in the emerging field of nanomedicine is based on the use of carbon nanotubes and bucky balls, which challenges their underlying translational relevance and innate compatibility to drug delivery. On the contrary, nanodiamonds (NDs) represent a much more viable alternative, because: (a) they have much higher potential for mass production, yet still possess properties common to nanotubes and bucky balls such as the ultrahigh surface-to-volume ratio, (b) they can improve drug administration efficacy by order of magnitude scale (it has been found from some preliminary mouse studies that 20 times less drug is needed for cancer therapy when it is bound to the NDs compared with administration of the drug alone), (c) they are highly biocompatible (noncytotoxic) as opposed to most carbonaceous materials, and (d) they can be functionalized to chemically link with almost any materials. In this chapter, we outline a framework for the development of an ND-enabled drug delivery system, capable of performing both therapeutics and diagnostics functions, via seamless integration of simulation-based engineering and science (SVE&S) and experimental validations. Our vision is to design a system such that it will be capable of releasing drug for prolonged timescale (in the order of months to a year) over a specific residual cancer cell region, thereby preventing the recurrence of tumor growth. This is a key improvement because widespread/nonspecific drug distribution due to material degradation can be avoided, along with the associated medical complications and unpleasant side effects.

## 12.2 The Drug Delivery Patch

The fundamental requirements for the proposed drug delivery patch are to efficiently detect/diagnose cancer cells and then to deliver therapeutic molecules with a preset dose. In this study, a model drug delivery system is proposed that consists of (a) nanodiamonds (ND), (b) parylene buffer layer, and (c) doxorubicin (DOX) drugs and biomarkers. In its simplest form, an array of self-assembled nanodiamonds is functionalized with DOX and biomarker molecules and is contained inside parylene capsule as shown in Fig. 12.2. Here, parylene polymers serve as the *capsule shell* for the ND complex so that the device integrity is preserved. It can be seen from Fig. 12.2 that the bottom part of the device contains nonporous parylene, and the top part contains porous parylene layers. Parylene is chosen because it is highly biocompatible and also Food Drug Administrations (FDA) approved. The pore size in the parylene layer is in the order of nanoscale and may be fabricated using MEMS-based technology.

It is envisioned that the patch will be implanted in the body after a surgery is commenced to remove residual (and otherwise persistent) cancer cells. The physiological conditions in the vicinity of living healthy cells and cancerous cells are significantly different and can be quantified by different pH levels. The patch is designed such that when it is implanted in the body and comes into contact with cancer cells, the drug molecules will detach from the NDs and flow through the

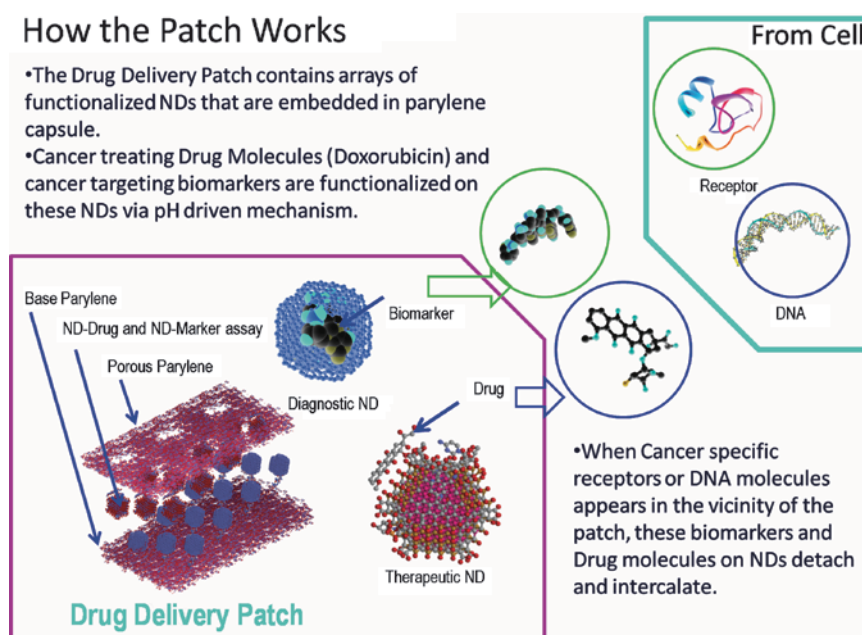


**Fig. 12.2** Schematics of the proposed drug delivery patch. The encircled molecules (biomarkers and drug) are the functional elements detached from ND to attach with the cancer specific molecules of cancer cells

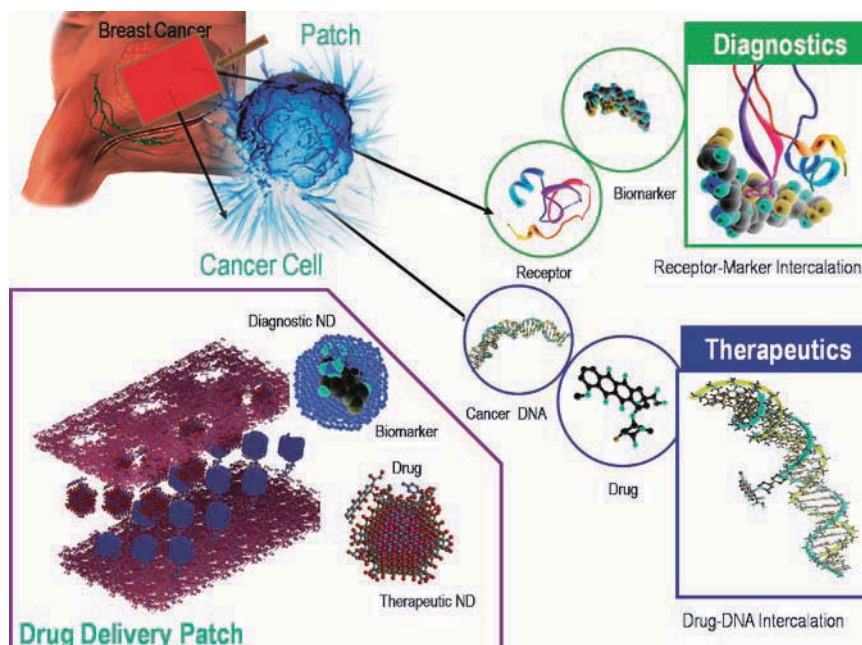


**Fig. 12.3** Schematics of the proposed drug delivery patch with therapeutic and diagnostic functionalities

porous parylene toward cancer cells. The characteristic pH level will dictate the drug “detachment”, and the degree of porosity in the parylene will control the drug “diffusion rate”. Similarly, the ND-biomarker assembly will flow from the device when it comes into contact with cancer-specific receptors. As a result, one device will perform both therapeutic and diagnostic functionalities as schematically shown in Fig. 12.3.

## 12.2.1 Number Effect in Nanoparticles

### 12.2.1.1 What is the Number Effect?

A recent finding suggests that a new attribute of nanoparticles exists, which so far has been neglected but could be unique and generally useful for the smaller nanoparticles such as the primary particles of detonation nanodiamond that we are dealing with in this book. The new attribute is the unexpectedly large number of particles in unit volume or unit weight. This was surprising for us because of our prejudice that nanoparticles are much larger than molecules. There are many reasons for us to acquire this prejudice. Nanoparticles are visible under TEM, whereas molecules are not. There are only a few conventional molecules having such a large size as 1 nm, but a nanoparticle having a diameter of 1 nm (e.g.,  $C_{60}$ )

is the smallest (definition of nanoparticle: 1–100 nm in diameter). Molecules are gauged by Ångstrom unit ( $10^{-10}$  m), whereas nanoparticles are by nm ( $10^{-9}$  m). The truth is that these differences are not really big.

The impact of overwhelmingly large number associated with nanoparticles, especially with single-nano particles, has been noticed by one of the co-authors (E. I. Ösawa) when he spotted a word ‘nanodiamond’ in recent advertisements for sharp pencils (Fig. 12.4). It was interesting to find that a major pencil company claiming to have improved writing performance of their new brand of sharp pencils by *dispersing 400 million particles of nanodiamond into one piece of lead* with 0.5 mm diameter and 60 mm length. *Four-hundred million* particles in such a tiny lead sounded unbelievably large in number. However, the doubt quickly disappeared after simple arithmetic. The number density of the added particles is given by  $400 \times 10^6 / 0.0118 = 3.39 \times 10^{10} / \text{cm}^3$  (the volume of one lead is equal to  $0.0118 \text{ cm}^3$ ). This volume density can be approximately translated into a linear density by taking a cube root of 3230/cm, or 310 nm for average center-to-center distance between the nearest particles. There is certainly a plenty of room to pack 400 million particles in a lead, even if the largest nanodiamond particles with 100 nm diameter were used. In other words, this advertized density sounds great but actually is not really too much for nanoparticles.

Now, if the number of spherical nanoparticles were a decisive factor for the writing performance of lead, how much single-nano buckydiamond (SNBD, the primary particles of detonation nanodiamond) will be needed to pack 400 million particles of them into a lead? It turned out that only 0.5 mg of SNBD per 1 kg of

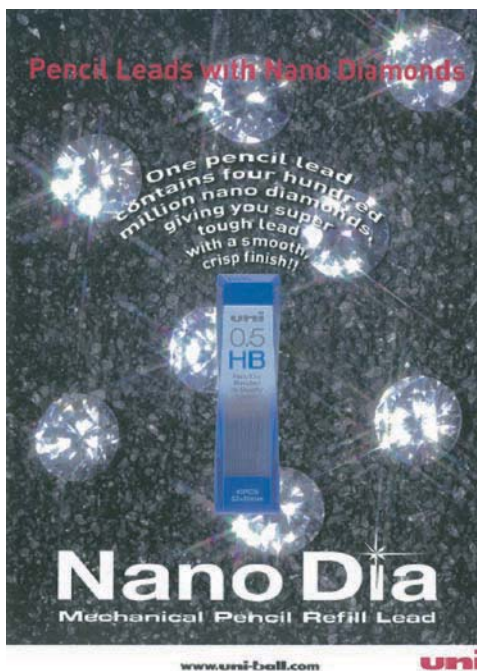


**Fig. 12.4** An advertisement of a new brand of sharp-pencil lead claiming to contain 400 million particles of nanodiamond per piece of lead

**Table 12.1** Basic numbers of SNBD particles

Selected numbers for one SNBD particle	Diameter $D(=2r)$	4.8 nm	100 nm <sup>d</sup>
	Volume $v(=4\pi r^3/3)$	$5.79 \times 10^{-20} \text{ cm}^3$	$5.23 \times 10^{-16} \text{ cm}^3$
	Weight $w(=\rho v)^a$	$1.74 \times 10^{-19} \text{ g}$	$1.64 \times 10^{-15} \text{ g}$
	PW <sup>b</sup> ( $=wN_A$ ) <sup>c</sup>	104,000	$9.88 \times 10^8$
	Number of C atoms	8,660	$8.23 \times 10^7$
Number of particles in 1 g of SNBD $n(=1/w)$		$5.75 \times 10^{18}$	$6.10 \times 10^{14}$

<sup>a</sup> $\rho$  = sp. gr. of diamond = 2.99 g/cm<sup>3</sup> (preliminary results)

<sup>b</sup>“Particulate weight”, a concept corresponding to “molecular weight”

<sup>c</sup> $N_A$  = Avogadro number

<sup>d</sup>A model of agglutinated product of detonation nanodiamond

graphite would be needed to achieve the advertized volume density! It is quite impressive to find how enormous number of particles that tiny amounts of SNBD contain. Basic figures necessary to count the number of SNBD particles are summarized in Table 12.1. The number of particles contained in 1 g of SNBD, which is billion times as large as 5 billion is given in the last line. To be more systematic, the number is the order of quintillion ( $10^{18}$ ).

Actually, such large numbers are beyond our comprehension. We could have some idea on the largeness up to millions ( $10^6$ ) and billions ( $10^9$ ); for example, populations of large cities and countries are of these orders of magnitude. Although it is difficult to grasp the largeness for numbers beyond trillion ( $10^{12}$ ), we should pay attention to the effects of great numbers when dealing with nanoparticles, of which there should be plenty.

Summing up, we learned the following from the above consideration: Nanoparticles are larger than conventional molecules by two to three orders of magnitude. However, as Avogadro Number  $A_N$  is so large that small differences in size between molecule and nanoparticles is not as significantly as it looks. The number of particles per unit weight ( $=A_N/PW$ ) still turns out to be an enormous number which is out of our sense on the large number. This is the essence of number effect, unique in nanoparticles. Number effect does not exist in molecules, nor in microparticles, but only in nanoparticles.

In this regard, nanoparticles may be useful for those uses where enormously large number of particles is critical. One such example of such “number effect” is given below.

### 12.2.1.2 Nanospacers Lubrication

Ever since industrial revolution, oils have been used as practically the sole means for reducing friction between moving parts of all kinds of machines to smoothly transmit power. The major and by far the most critical role of lubricant oil is to provide oil film between touching planes in order to prevent adhesion of the planes by direct or boundary contact under load. However, oil (and grease) film often breaks up when their thickness decreased below a few molecular layers to disastrous

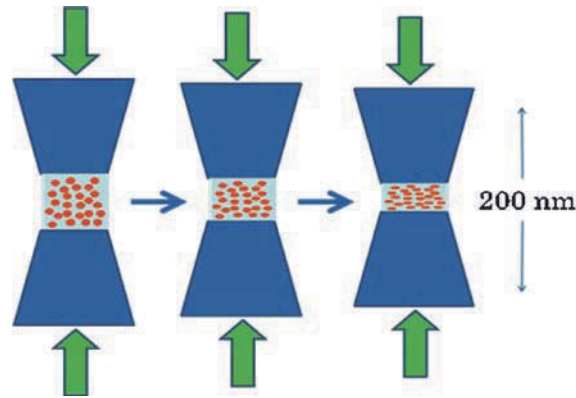


**Fig. 12.5** In nanospacers lubrication, colloidal nanoparticles play the role of adhesion preventing spacers under boundary condition

loss of lubrication. In addition, disposal of the used lubrication oil and grease poses a major cause of environmental destruction and increase emission of  $\text{CO}_2$  gas. Lubrication oil will be forbidden sooner or later.

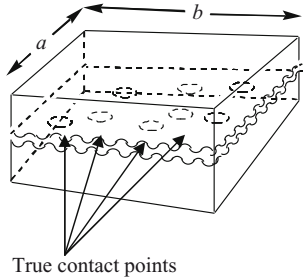
An entirely new lubrication method would be to rely on SNBD particles as the spacers to prevent direct contact between shearing planes of moving parts (Fig. 12.5). While it may seem also possible to use SNBD particles as solid lubricant, actually it is not advisable due to very high tendency for these particles to aggregate to give much larger effective diameters unsuitable to penetrate and cover rough microstructure of surface. We evaluate here colloidal solutions of SNBD dispersed in low-viscosity liquid like water.

One of the critical requirements for lubrication by nanospacers is that there must always be enough number of spacer particles in the true contact areas whenever they were beginning to form themselves under the boundary conditions. We examined the prospect of this requirement for SNBD aqueous colloid by using a classical work of Borden and Tabor [43] who estimated area and number of true contact points under various loads between a pair of polished surface of soft-steel plate having an apparent contact area of  $2000 \text{ mm}^2$  (Table 12.2). To these data, the number effect of dilute aqueous colloid solution of SNBD (Table 12.1) was fitted, as shown below.

Another critical requirement for the nanospacers lubrication is that the spacer particles stay in a thin space between the approaching pair of true contact area without flowing out of the space with the nonviscous solvent. According to our experimental and theoretical analysis [45], SNBD particles are most likely deformed polyhedra with the facets having high electrostatic potentials and supposed to be tightly hydrated in the colloidal solution. Under the boundary lubrication condition, when the tips of the true contact area on the steel surfaces approach to each other across thin colloidal liquid, the shell of hydrated water on the particle surface in the thin colloidal liquid will be attracted to, not repelled by, the steel surface (Fig. 12.5).

If we assume a surface roughness of  $100 \text{ nm}$ , then boundary friction condition will start when the thickness of the colloidal solution pinched between the tipped

**Table 12.2** Area and number of true contact points and number of SNBD spacers present at a true contact point (TCP) between a pair of shearing soft-steel surface (Fig. 12.5) polished to a surface roughness of 100 nm. Concentration of SNBD is 0.01 wt%<sup>a</sup>



Load W kgf	Area of TCP <sup>a</sup> A mm <sup>2</sup>	A/S	No. of TCP	No. of SNBD particles in A 10 <sup>8</sup>
500	5	1/400	35	20.0
100	1	1/2000	22	25.0
20	0.2	1/10000	9	2.1
5	0.05	1/40000	5	0.29
2	0.02	1/100000	3	0.069

<sup>a</sup>Apparent contact area= $a \times b = 2000 \text{ mm}^2$ , thickness of liquid film filling the contact area=average roughness $\times 2 = 200 \times 10^{-6} \text{ mm}$ , volume of liquid film in apparent contact area= $0.40 \text{ mm}^3$ , total number of SNBD particles in 0.01% colloid in this volume= $5.75 \times 10^{18} \times 10^{-2} \times 10^{-5} \times 0.4 = 2.30 \times 10^{11}$

surfaces decreased to about 200 nm. At this point, the number of SNBD particles in the true contact area is equal to a liquid column of 0.01% colloidal solution having a volume of  $200 \times A \text{ nm}^3$  (Table 12.2). The sum of these values over the true contact points are entered in the last column of Table 12.2 in a unit of  $10^8$  particles. Even in the very beginning of boundary condition, 7 million SNBD particles participate in the spacer action (the lowest line of Table 12.2). Number of spacers keeps increasing as the load as well as the number and area of true contact points are increased, up to 2 billion under the highest load included in Table 12.2, to take over the load to prevent adhesion. We feel that these numbers are much more than enough, and in practice the concentration of colloid could be reduced to as low as one ten-thousandth % concentration without increasing friction coefficient.

We have already obtained an excellent friction coefficient of 0.02 in our first experiments on nanospacers lubrication, by measuring friction between poly(acrylamide) gel immersed in SNBD colloidal solutions and a reciprocating sapphire ball under a small but constant load [44]. However, at that time we have not noticed 'number effect' and vaguely thought that low friction should be realized only in considerably high concentration range of 0.1–5 % based on chemical experience. As clearly shown by the analysis of Bowden–Tabor work in the previous section, the tested concentrations were much too high. We plan to repeat the experiments using much dilute colloidal concentrations.

### 12.2.1.3 Remarks on the Number Effect

Discovery of nanospacers lubrication reinforced by the number effect will have significantly large impact. In the traditional lubrication oil, the oil itself played dual

role of adhesion preventive agent and medium. In contrast, nanospacers lubrication consists of adhesion preventive agent and medium as separate components. The function of medium is to disperse the adhesion preventive agent, and there is no need to form liquid film. Therefore, medium can be of low viscosity like water. For environmental protection, water is the best medium, even though it will induce rust on steel. Rusting consists of a series of electrochemical reactions, wherein Fe is oxidized to  $\text{Fe}(\text{OH})_2$  and loose  $\text{Fe}_2\text{O}_3 \cdot x\text{H}_2\text{O}$ . Covering the iron surface with compact oxide layer of  $\text{Fe}_3\text{O}_4$  is considered to be the cheapest, and most efficient antirusting agent as used in the stainless steel. We would predict that eventually highly diluted aqueous SNBD colloid or lubrication water will replace lubrication oil as lubricant, and all the iron parts of machines will be made of highly stable stainless steel. The lubrication water may contain one more component which replaces the fragile hydration shell on the SNBD surface with more durable and tight oil-like layer to avoid mechanical damage to the true contact areas.

Small mass of nanoparticles brings about large number effect. In other words, each single nanoparticle of SNBD has complex geometric and electronic structure which leads to a variety of functions [45], but they come in large numbers; hence, in many cases, we need a very small mass of nanoparticles. In the past, when the smallest available particles were of the order of microns in diameter, we used to prepare microcomposites containing as much reinforcing components as possible. However, the same results can be realized in much smaller proportions of nanoparticles as reinforcing components in nanocomposites. It is likely that Hall–Petch effect works best for nanocomposites. A logical consequence of number effect is that we may wish to design, prepare, and evaluate nanocomposites in terms of the number of particles rather than the weight. Then, we will be more used to handle large number of like billion-and trillion- like astronomers.

## 12.3 Materials and Manufacturing

As mentioned, the essential material systems of the patch are nanodiamond, parylene polymers, drug and imaging molecules. Among these, nanodiamond plays the key role in device performance. In the following sections, nanodiamond manufacturing techniques are provided.

### 12.3.1 *High Frequency Plasma-Enhanced Chemical Vapor Deposition (PECVD) for ND Particles and Film Synthesis and Processing*

The Nano Particle Technology Laboratory (NPTL) is engaged in doing research related to nanoparticle generation, measurement, and some other related applicable research areas such as environment, medical science, energy, new material, element & sensors.

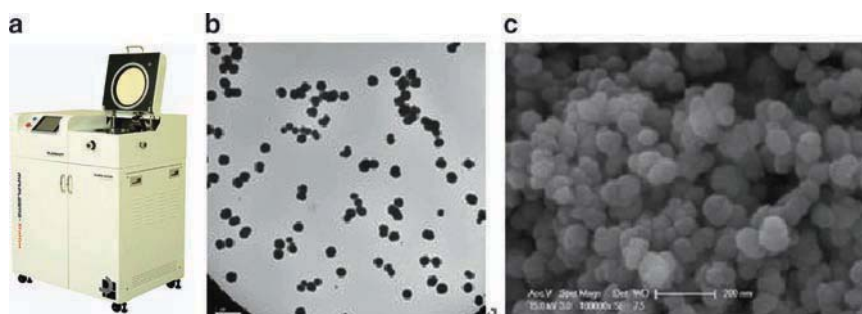


**Fig. 12.6** Plasma System (a) and Synthesized Nanoparticles (b and c)

Nanoparticles are widely studied as a building block for broad applications. Several studies have been performed to generate nanoparticles by liquid- or gas-phase synthesis processes. Compare to liquid-phase synthesis, gas-phase synthesis has many advantages such as high purity, continuous process, and size/structure controllability. However, it is still difficult to manufacture nanoparticles smaller than 10 nm due to coagulation.

Recently, NPTL synthesized Si nanoparticles using RF plasma (Fig. 12.6). In which, the size, composition, and growth of nanoparticles can be easily controlled. The Si nanoparticles synthesized, using inductively coupled plasma, have diameter in the range of 3 nm to a few hundred nm and are very uniform in size (relative standard deviation is less than 0.2). These particles are being applied to secondary battery electrode materials.

Recent research articles [62–76] reveal that nanodiamonds (NDs) in particular possess several characteristics including surface functionalization capabilities, biocompatibility, and versatile deposition and processing mechanisms that make them suitable for advanced drug delivery. NDs have formerly been physically immobilized and functionalized in various ways in order to bind with cytochrome *c*, DNA, antibodies, and various protein antigens.

All prior methods of synthesizing diamond are bulk processes. In such processes, new atoms of carbon arrive at the growing diamond crystal structure having random positions, energies, and timing. Growth extends outward from initial nucleation centers having uncontrolled size, shape, orientation, and location. Existing bulk processes can be divided into three principal methods – high pressure, low pressure hydrogenic, and low pressure nonhydrogenic. The high frequency plasma-enhanced chemical vapor deposition (PECVD) is one of the low pressure or CVD hydrogenic metastable diamond growth process.

PLASMA technology (PECVD) is widely used to synthesis and alters the surface properties of few materials without affecting their bulk properties. Plasma deposition involves the addition of a plasma discharge to the foregoing filament process. The plasma discharge increases the nucleation density and growth rate and is believed to enhance ND and ND film formation. There are three basic plasma

systems in common use: a microwave plasma system, a radio frequency of RF (inductively or capacitively coupled) plasma system, and a direct current or DC plasma system. The diamond growth rate offered by these systems can be quite modest, on the order of  $\sim 1 \mu/\text{h}$ .

In the case of low pressure hydrogenic method, hydrogen gas mixed with methane is introduced through plasma (discharge), dissociating the methane molecule to form the methyl radical ( $\text{CH}_3$ ) and dissociating the hydrogen molecule into atomic hydrogens (H). Hydrogen is generally regarded as an essential part of the reaction steps in forming ND/ND film during CVD and atomic hydrogen must be present during low pressure diamond growth to: (1) stabilize the diamond surface, (2) reduce the size of the critical nucleus, (3) “dissolve” the carbon in the feedstock gas, (4) produce carbon solubility minimum, (5) generate condensable carbon radicals in the feedstock gas, (6) abstract hydrogen from hydrocarbons attached to the surface, (7) produce vacant surface sites, (8) etch (regasify) graphite, hence suppressing unwanted graphite formation, and (9) terminate carbon dangling bonds. Both diamond and graphite are etched by atomic hydrogen, but for diamond, the deposition rate exceeds the etch rate during CVD, leading to diamond (tetrahedral  $\text{sp}^3$  bonding) growth and the suppression of graphite (planar  $\text{sp}^2$  bonding) formation. (Note that most potential atomic hydrogen substitutes such as atomic halogens etch graphite at much higher rates than atomic hydrogen). Similarly, dual DC-RF plasma system is used to deposit hydrogenated diamond like carbon (DLC) films from methane plasma. It has the advantages of separately controlling ion density and ion energy by RF power and DC bias, respectively, over conventional simply capacitive-coupled radio frequency PECVD. The  $\text{sp}^3$  content, hardness, and Young’s modulus of the DLC films increased with increasing RF power at a constant DC bias of  $-200 \text{ V}$  and reached the maximum values at an RF power of  $300 \text{ W}$ , after which they decreased with further increase of the RF power. The DC bias had a similar but greater effect on the structure and properties of the films, owing to a greater influence of the ion energy on the characteristics of the films than the ion current density. D. M. Gruen group in Argonne National Laboratory has been made ND film w/o hydrogen gas using MWCVD Plasma jet method has high deposition rate so that it is considered alternative method for Microwave CVD (MWCVD) and High frequency CVD (HFCVD). Generally, methane gas is extremely diluted only by  $1 \text{ vol}\%$ . The substrate temperature should be over  $700 \text{ C}$  for MWCVD & HFCVD film. If we use RF plasma system, we can conduct the same process at lower temperature which be quite advantage for particle deposition for bio device system.

Apart from synthesis, the capability of high-frequency plasma to modify surface physical and chemical properties without affecting bulk properties is advantageous for the design, development, and manufacture of biocompatible polymers. The plasma treated materials have found various applications in automobiles, microelectronics, biomedical and chemical industries. Specific surface properties, such as hydrophobicity, chemical structures, roughness, conductivity, etc., can be modified to meet the specific requirements of these applications. The major effects observed in plasma treatment of polymer surfaces are cleaning of organic contamination, micro-etching, cross-linking, and surface chemistry modification.

Biomaterials that have contact with the human body need an optimal combination of mechanical properties and surface characteristics that result in superior performance in the biological environment. Physicochemical properties of the surface of the material, such as surface free energy, hydrophobicity, and surface morphology, which influence the cell–polymer interaction, determine the choice of the polymer. Since in general all polymers do not possess the surface properties needed for biomedical applications, radio frequency (RF) plasma treatment plays a crucial role in incorporating them. Surface modification in a controlled fashion, deposition of highly cross-linked films irrespective of the surface geometries, formation of multilayer films, eco-friendly nature, and the prospect of scaling-up make the RF plasma treatment extremely suitable for biomedical applications.

## 12.4 Device Design Roadmap

Over the past couple of years, multiscale modeling and simulations [46–59] have been extensively used to understand properties of solids and structures. We aim to establish a seamless integration of multiple scale computational techniques along with appropriate experimental validation. The design roadmap is schematically shown in Fig. 12.7. In this multiscale analysis, quantum scale (QS) calculation

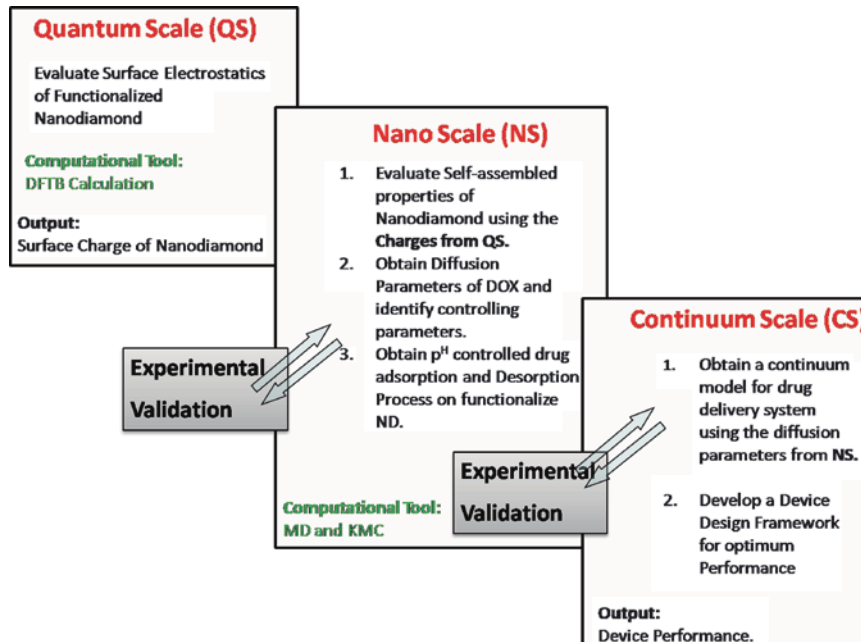


Fig. 12.7 Device design roadmap that includes multi-scale simulation and experimental validation

will predict the structure and surface electrostatics of the functionalized NDs. Information from this scale will be utilized in the atomistic calculations at the nanoscale (NS) to evaluate the self-assembly process of functionalized NDs, their electrostatic interactions with drug molecules/biomarkers as well as their diffusion kinetics. Finally, at the continuum scale (CS), the drug delivery process from the device to the targeted area will be modeled and simulated with information provided from sub scale simulations.

Now, in order for the device to function as an innovative drug delivery system with multifunctional capabilities, some fundamental science issues need to be solved. These include quantitative understanding of

1. Structure, surface electrostatics and self-assembly of NDs so that their packing with functional groups can be efficiently facilitated, under a range of conditions.
2. Drug–ND and biomarker–ND interaction process so that they can be controlled with the physiological condition of cancer cells.
3. Drug–ND and biomarker–ND diffusion process so that drug dose rate and cell imaging efficiency can be identified.
4. Overall design optimization with respect to the integrated patch performance.

In addition, the solutions to these scientific issues need to be verified and validated. To do this, a multi-level uncertainty quantification scheme needs to be developed. There are two facets to this uncertainty analysis: (1) comparing the experimental and theoretical results on each scale (quantum, nano, and continuum), and (2) linking these scales such that uncertainty on one scale can realistically propagate into other scales. The knowledge of the uncertainty present in modeling allows for a more robust and reliable model and patch design.

There are many approaches toward uncertainty analysis on a single scale, most involving an iterative process where experiments are repeated and computational models are refined until a realistic calibration between the two can be made (Xiong, 2009; Kennedy and O'Hagan, 2001). However, a multi-level uncertainty quantification scheme that allows for reliable error propagation across many scales does not currently exist. This is another area of this drug delivery system design that needs to be addressed.

## **12.5 Structure and Surface Electrostatics of Nanodiamonds**

### ***12.5.1 Uncertainty Quantification of ND charge***

The solutions to these scientific issues also need to be verified and validated to ensure model reliability. To do this, a multi-level uncertainty quantification scheme needs to be developed. There are two facets to this uncertainty analysis: (1) comparing the experimental and theoretical results on each scale (quantum, nano, and continuum),

and (2) linking these scales such that uncertainty on one scale can realistically propagate into other scales. The knowledge of the uncertainty present in modeling allows for a more robust and reliable model and patch design.

For example, the surface charges of the NDs discussed in Sect 5.2 can be approached in a variety of ways. A strictly linear projection can be done such that the charge distribution for the larger NDs looks precisely the same as for the smaller NDs. However, this ignores most of the information that is known about the system and assumes a behavior that may not be accurate. As experimental data are limited on this scale, a better understanding of the accuracy of this estimate is important. Errors introduced in this step will propagate throughout the modeled system.

Instead of the this deterministic approach, an estimate of the probability density function (PDF), and therefore the cumulative density function (CDF), of each face of the ND can be generated statistically. The estimated PDF and CDF are developed using a Gaussian-kernel smoothing technique for each of the three truncated octahedral NDs with available DFT calculations. A sample of size  $n$ , where  $n$  is the number of atoms present on the respective faces of the next larger ND, is generated from the current PDF and the sample PDF is generated. These sample functions are used as a projection of the next larger ND.

This projection scheme allows for a good estimate, but it only utilizes data present on the closest ND to determine the surface charges for unknown NDs. A more rigorous scheme can be developed using a bootstrapped and edgeworth expansion [76]. Bootstrapping refers to resampling a data set to estimate the behavior of the entire system. This ideology carries over well for the use in data projection because of the data sub-steps available (in this case, the surface charge distributions of the different sized NDs). More details of the bootstrap method and Edgeworth expansion can be found in Hall [78], but the application to the ND charge distribution will be outlined here.

Each face of the ND truncated octahedron is considered independently because they have dramatically different charge distributions. For example, face 100 can be isolated into three readily available data sets: the first set from the largest ND with 1639 total atoms, the second set from the next largest ND with 1198 total atoms, and the third set from the next largest ND with 837 total atoms. The two smallest NDs (268 and 548 atoms) will not be considered because their results vary from the larger charge distributions that are of interest for this application.

The surface charges for the 100 faces on the three NDs are extracted, and will be referred to in decreasing order of size, respectively  $F_1$ ,  $F_2$ , and  $F_3$ . A random sampling with replacement is done of  $F_1$ ,  $F_2$ , and  $F_3$  to create three more data sets to calculate the projection onto a larger ND, and gives a better projection scheme. From these six data sets, a nested probability distribution can be estimated, and a better understanding of the reliability of the linear projections is available.

The surface charges are only one example of the uncertainty quantification needed in this ND model. There are many approaches toward uncertainty analysis on a single scale, most involving an iterative process where experiments are repeated and computational models are refined until a realistic calibration between the two can be made [79, 80]. However, a multi-level uncertainty quantification

scheme that allows for reliable error propagation across many scales does not currently exist. This is another area of this drug delivery system design that needs to be addressed.

### 12.5.2 Multiscale Analysis of ND charge

The structure of individual nanodiamonds (NDs), described in terms of the degree of crystallinity and characteristic surface chemistry, is crucial to all ND-based technologies. Both crystallinity and surface chemistry affect particle–particle interactions, changing the way individual nanodiamonds self-assemble, and particle–drug interactions responsible for adsorption and desorption of drug molecules. The structure of detonated NDs is still relatively poorly understood, but the past decade has seen a number of seminal computational studies upon which the current understanding is based. [60] Early work utilized thermodynamic (phase stability) theories [63] and first-principles density functional theory (DFT) computer simulations [61] to elucidate the shape of ND, and describe how the shape affects the stability of individual surface facets on small particles (< 2 nm in diameter). While NDs may assume various nominal shapes, including spherical, octahedral, truncated octahedral, cuboctahedral, and cubic morphologies, NDs with truncated octahedral or cuboctahedral morphologies are thermodynamically preferred over other alternative shapes. [63] Similarly, early DFT simulations demonstrated that the preferential graphitization of the (111) surface to form fullerene-like  $sp^2$ -bonded “bubbles” on the surface, giving rise to a special (all-carbon) core–shell structure known as a bucky-diamond. [65] Bucky-diamonds are characterized by a crystalline diamond  $sp^3$ -bonded core, encapsulated by a single- or multi-layer  $sp^2$ -bonded fullerene-like shell that either partially or fully covers the particle surface. The localized (surface)  $sp^3$  to  $sp^2$  phase transition is spontaneous at room temperature, but can be eliminated by coating the surfaces with suitable passivants [66].

A more recent density functional tight binding (DFTB) study [67] examining the crystallinity of somewhat larger NDs (2–3 nm in diameter) confirmed the thermodynamic preference for the truncated octahedral shape, and the localized graphitization of the octahedral (111) facets. The (100) and (110) surface facets were shown to resist graphitization, but exhibited reconstructions containing  $sp^{2+x}$  hybridized carbon atoms. In addition to this, these new results predicted an anisotropic (facet dependent) pattern of charge distributions on ND surfaces. The resultant surface electrostatic potential revealed that the (100) surface facets possess a strong positive electrostatic potential, while the (111) facets possess a negative electrostatic potential depending upon the degree of surface graphitization. This suggests that Coulombic interparticle interactions may be responsible for nanodiamond agglomeration, and that a preferred orientation for particle–particle interactions would produce self-assembled ND agglomerates. This hypothesis was validated via a systematic DFTB study in 2008 [68], which elegantly demonstrated preferred configuration of ND interparticle interactions based on strong, long-ranged Coulombic attractions.

While these studies give some insight into ND electronic structure for ND between 1–3.3 nm in diameter, experimentally available detonation NDs range in size from 4–10 nm [81]. Unfortunately, it is not yet possible to determine the equilibrium structure of charged NDs over this entire size range because of computational constraints. Moreover, experimental results indicate that detonated NDs are heavily functionalized with various functional groups including carboxyl (–COOH) and carbonyls (CO). As conventional DFT and DFTB calculations will be too computationally expensive to treat entire ensembles of structures at experimentally relevant sizes, we have implemented a multiscale approach to nanodiamond simulation, building upon the *ab initio* foundation and extending this knowledge to larger systems. In the first instance, we have employed a projection method to identify charge distributions for larger nanodiamonds, beyond the sizes explored in previous works.

In this method, effective surface electrostatic potentials for smaller NDs that are obtained from DFTB calculations [67] are first analyzed. Figure 12.8 shows normalized surface potentials for truncated octahedral and cuboctahedral geometry [67]. The surface potentials per atom are calculated using the classical Coulomb's law that utilizes the Mulliken charge distributions from DFTB calculation:

$$\Psi_i(r) = \frac{q_i q_j}{4\pi\epsilon\epsilon_0 r_{ij}}, j \neq i \quad (12.1)$$

where  $\psi$  is the surface potential,  $q$ 's are the atomic charges,  $\epsilon$  is the dielectric permittivity and  $r$  is the distances between atoms. Here,  $i$  is a free index and  $j$  is the dummy index and the relation follows Einstein's summation convention.

In the case of the truncated octahedral subset, as shown in Fig. 12.8a, it can be observed that there is a strong correlation between the particle shape and structure of the surfaces, and the sign of electrostatic potential. The (100) surfaces, and the (100)/(111) edges, exhibit a strong positive potential, whereas (like the octahedral particles), some of the graphitized (111) surfaces exhibit a strongly negative potential.

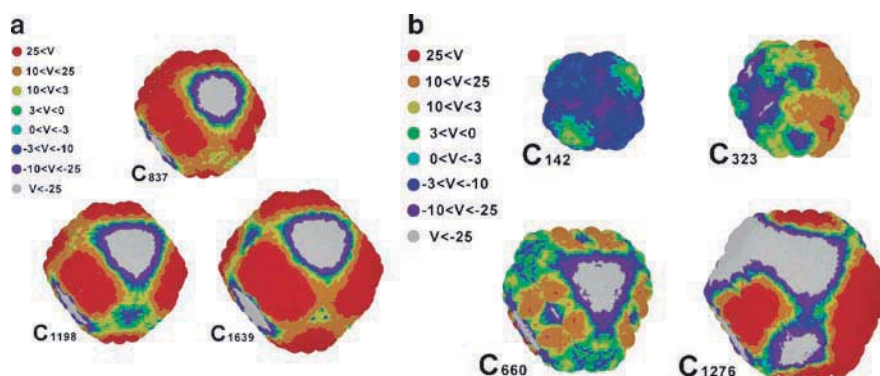


**Fig. 12.8** Normalized surface electrostatic potential for the relaxed structures of the (a) truncated octahedral and (b) cuboctahedral subsets. Here  $C_{xxx}$  refers to xxx carbon atoms in structure, and higher the number the larger is nanodiamond size. The figure is obtained from [67]

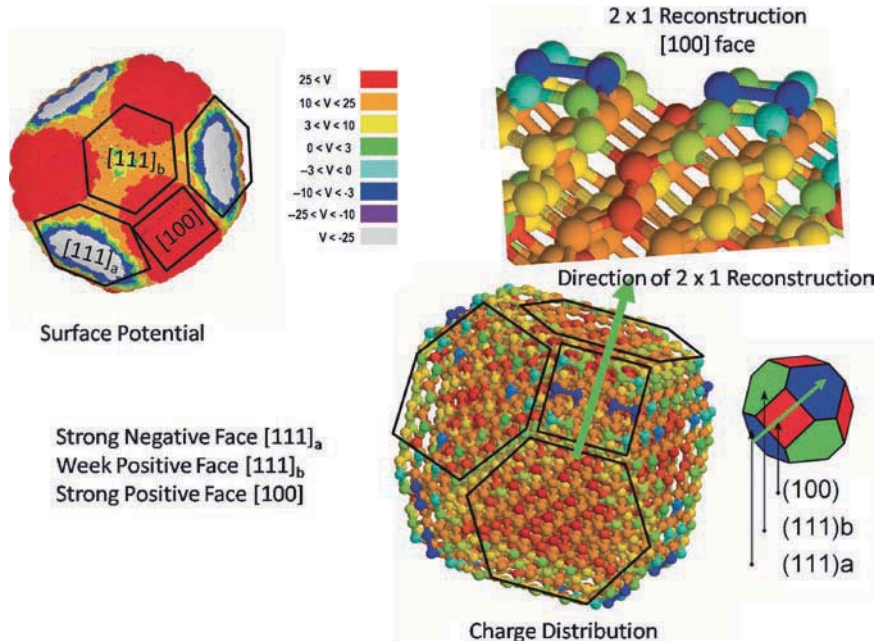


**Fig. 12.9** Charge distribution and corresponding surface potential on truncated octahedral nanodiamond. Note the geometric asymmetry in the overall structure induced by  $2 \times 1$  dimer on the (100) face that in turn causes two distinct distributions of charges and potentials on (111) faces

It is interesting that only half of the (111) surfaces exhibit the strong negative  $V$ , while the remaining (111) surface exhibit much more variation in potential (depending on the position relative to the facet center). This is due to some “artificial” asymmetry in the overall particle shapes. This asymmetry has been introduced on purpose to ensure that the (100) surfaces have the opportunity to form two ideal  $2 \times 1$  dimer rows, but results in rectangular (100) facets, and some (111) facets being slightly larger than others. This is shown in Fig. 12.9.

Since the asymmetry in the (111) surface potentials is not due to cross-linkers, or variations in the core–shell structure [66], but due to geometric asymmetry and imperfect graphitization alone, it can be anticipated that a symmetric geometry would yield a similar potential field on all (111) surfaces if graphitization is homogeneous. With this assumption, the charge and potential distribution with respect to ND size has been analyzed and the relation between charge and surface potential has been explored.

### 12.5.2.1 Charge and Potential on (100) Surface

Figure 12.10(a) shows the charge distribution on (100) surface of a truncated octahedral nanodiamond. In this figure, the surface atoms of the (100) faces are only colorized to identify the charges more clearly. The atoms colored in gray represent

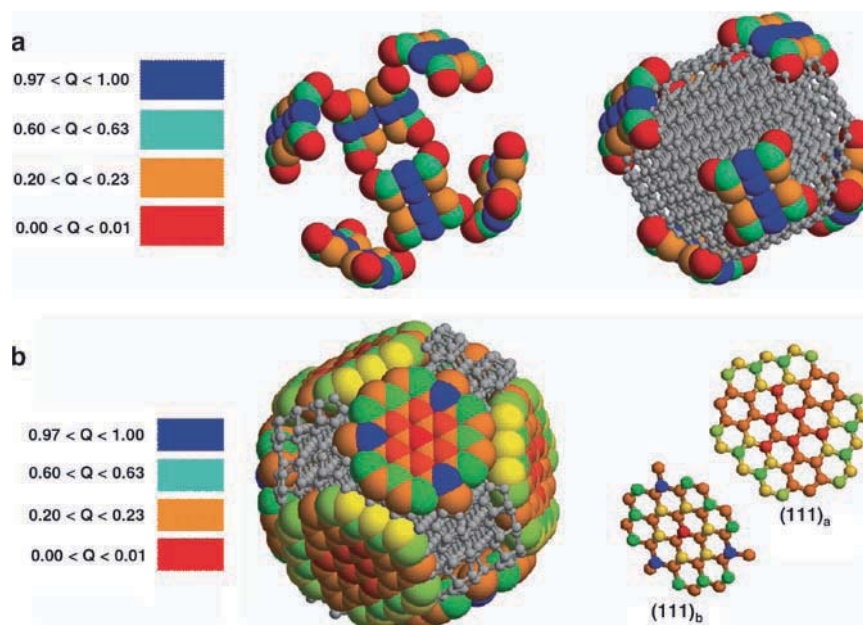


**Fig. 12.10** Charge distribution on (a) (100) and (b) (111) faces of a truncated octahedral nanodiamond

all remaining atoms that do not participate in the (100) terminal atomic layers. It can be noted that there are eight (100) facets on this nanodiamond shape. A closer look at any particular (100) surface reveals that there are four distinct types of positive point charges present. Of these charges, the four corner atoms (colored red) have negligible charges, partly because they are sitting beneath the (100) surface plane. A dramatic reduction in charge is observed for other atoms that are not lying on the surface [67]. Conversely, the rows of atoms perpendicular to the  $2 \times 1$  missing row directions (colored blue) exhibit a considerably higher positive potential. These high values are attributed to the reconstruction itself. This charge projection scheme, we ignored these two extreme charge values, assuming instead that the strong positive charge on the (100) facets of larger ( $>5$  nm) NDs will not be dominated by these atomic-scale reconstructions and negligible charges due to out-of-plane atom sites. With this assumption, we evaluated the average charge  $Q_{average}$  using the relation:

$$Q_{average} = \frac{1}{N} \sum_i^N q_i \quad (12.2)$$

Now, we employed the same procedure to evaluate the average charge for three different nanodiamonds, and the results are plotted in Fig. 12.11a. It can be seen from Fig. 12.11a that charge on (100) faces approaches a constant value (+0.4378 ec) as ND size increases.

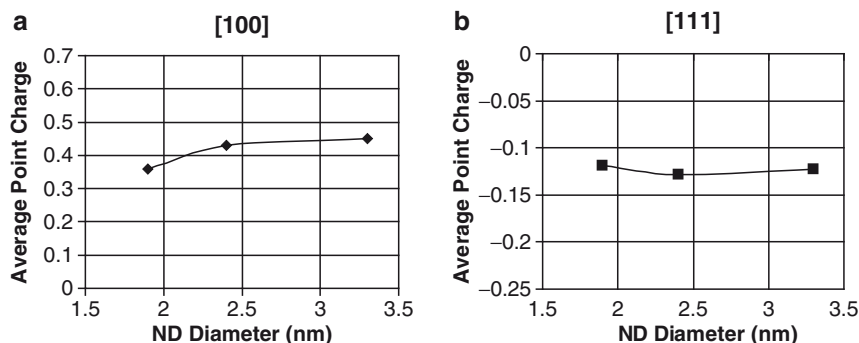
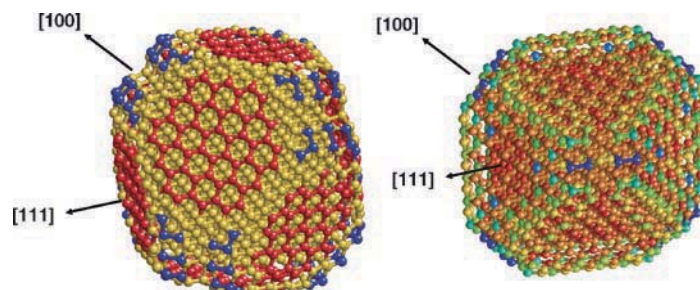


Fig. 12.11 Projected average charge distribution on (a) (100) faces and (b) (111) faces

### 12.5.2.2 Charge and Potential on (111) Surface

Using a similar approach to the (100) surface facets, the charge distribution on a (111) surface of a truncated octahedral nanodiamond is shown in Fig. 12.10b. In this figure, only the surface atoms on the (111) faces are colorized. As before, the atoms colored in gray represent all remaining atoms that do not participate in the (111) terminal atomic planes. It can be noted that there are six (111) faces on this nanodiamond, and it can be identified that the surface geometries of all (111) is not identical. In contrast, the half of the graphitized (111) surfaces exhibits a strongly negative potential (denoted as a type (111)<sub>a</sub> facet), and half exhibits much more variation in potential (denoted as a type (111)<sub>b</sub> facet). This is due to asymmetry in the overall particle shape introduced to preserve the ideal  $2 \times 1$  reconstruction on the [67] facets, but resulting in imperfect graphitization of the (111)<sub>b</sub> facets (as mentioned in Sect. 5.2.1) [67]. In our charge projection analysis, we ignore the contributions from (111)<sub>b</sub> faces with the assumption that the charge distributions of (111)<sub>b</sub> faces would be similar to (111)<sub>a</sub> if the geometric asymmetry in the structure is absent, and graphitization is geometrically homogenous.

Employing an identical procedure to evaluate the average charge for all three nanodiamonds, and the results are plotted in Fig. 12.11b. It can be seen from Fig. 12.11b that the charges on (111) faces approaches a constant value ( $-0.1239$  ec) as ND size increases. Using these two approximated constant charges on (100) and (111) surfaces, the corresponding surface potential is computed and compared with original DFTB calculated data, as shown in Fig. 12.12. In the future, to simulate large nanodiamonds, these constant charges will be utilized to extend this work well beyond the modest length scale accessible to DFT and DFTB simulations.



**Fig. 12.12** Comparison of charge distribution and surface potential between the facet dependent constant charge approximated and DFTB calculated ND surface

## 12.6 ND–Drug Interactions

### 12.6.1 Functionalization of Nanodiamonds

The next phase of calculation involves binding of the DOX to the functionalized NDs. The understanding the drug absorption and desorption profile to and from NDs is the most critical portion of the device design. There is no clear understanding on how many or what types of functional group are present on any ND surface. Some experimental observations [77–85] suggest that the types of functional groups are greatly dependent on the available dangling bonds on ND, whereas the degree of functionalization is dependent on functional group size, shapes, and orientations. In general, it is extremely difficult to quantitatively predict either the types or the number of functional groups present on any surface. It is, however, possible to obtain the upperbound estimate of the functional group by counting the number of potential sites with respect to nanodiamond size. Moreover, it is also possible to identify potential functional elements based on their available valences. For example, it is likely that carboxyl [–COOH] functional group that has valence equals one would attach on (111)/( $\bar{1}\bar{1}\bar{1}$ ) edges because such edges have one dangling bond. Similarly, the carbonyl groups [–CO] with two valence electrons are more likely to attach on (100) faces because each site has two dangling bonds. It can be noted that either of the functional group are negatively charged implying they both should attract positively charged ions. In the future, some phase stability studies will be conducted in the future to quantify more on the possible functional groups.

### 12.6.2 Conjugation With Single-Stranded DNA Through $\pi$ -Stacking

The base of single-stranded DNA (ssDNA) is known to conjugate with  $sp^2$  hybridized carbon structures through  $\pi$ -stacking [84, 85]. A similar mechanism can be adopted

to attach the base of ssDNA to NDs. Once the ssDNA-carbon nanostructure complex is obtained, these can be used as probes to identify target ssDNA with particular sequence [86]. Also, biotinylated ssDNA can be conjugated with carbon nanostructures to provide a platform to link with a variety of biomolecules, including antigen and antibody, through the strong, versatile biotin-avidin interaction [87].

### ***12.6.3 Electrostatic Interactions Between Doxorubicin and Functionalized Nanodiamond***

Typical functionalized NDs and drug molecules contain opposite charges at their surfaces, it has been a natural interpretation that interactions between ND and drug molecules should be straightforward – NDs should attract to drugs as they come into contact. However, recent experiments, however, suggest that NDs usually do not interact with drug molecules in the presence of neutral solutions. The addition of NaCl in the solution improves the interaction dramatically. Moreover, some experiments [6], without any exhaustive conclusion, suggest that drug loading/unloading process may be connected to the pH content of the solution. It has been observed from Dean Ho's experiment [6] that ND and DOX in aqua solution do not adhere to each other. However, a dramatic change in drug adsorption on ND surfaces has been observed with the addition of NaCl (or NaOH) in the solution. The process can be explained from electrokinetic theories involving anionic-cationic interactions. It can be argued that in aqueous solution, without the addition of any other perturbation ions, the repulsive interaction of DOX-DOX and ND-ND is greater than the cohesive interaction of ND-DOX and thus an insignificant amount of DOX can be adsorbed onto the NDs. With the addition of NaCl, the increase of  $\text{Cl}^-$  ions may shift the balanced interactions toward the formation of DOX-ND complexes because cationic DOX is also balanced with anionic  $\text{Cl}^-$  ions. The actual mechanism can be modeled via molecular dynamics simulations and can be contrasted with an electrokinetic theory. A well-validated theory will essentially ease the development of a seamless continuum model for drug delivery.

### ***12.6.4 Fundamental Theory of Electrostatic Interactions Between Charged Particles***

The interactions of charged particles or ions evolve over time, while maintaining a self-balanced total charge in the system of interested must be self-balanced. How the charges are distributed locally in the system and what factors control the local environment are unclear. The Gouy-Chapman double layer model addresses this issue [89].

Considering an infinitely spanned planar interface with a surface potential  $\psi_0$  (V) and a surface charge density  $\sigma_0$  ( $\text{Cm}^{-2}$ ), the Gouy and Chapman model

attempts to describe the distribution of charge and potential in the solution as a function of distance from the surface.

A fundamental result from electrostatics gives the relationship between charge density  $\rho(Cm^{-3})$  and the potential  $\psi_0(V)$  at any point in the domain of interest. This is the classical *Poisson Equation*:

$$\nabla^2\Psi = \frac{\partial^2\Psi}{\partial x^2} + \frac{\partial^2\Psi}{\partial y^2} + \frac{\partial^2\Psi}{\partial z^2} = -\frac{\rho}{\epsilon} \quad (12.3)$$

where  $\epsilon$  is the permittivity of the medium.

In addition, in an electrolyte solution, the charge density depends on the local concentrations of anions and cations, which in turn depends on the location potential through the *Boltzmann Equation*:

$$n_i = n_{i0} \exp\left(-\frac{z_i e \Psi}{kT}\right) \quad (12.4)$$

where  $n_i$  is the number concentration of ion  $i$  at a point where the potential is  $\psi$ ,  $n_{i0}$  is the corresponding concentration in the bulk solution ( $\psi=0$ ),  $z_i$  is the valence of ion  $i$ ,  $e$  is the electron charge,  $k$  is the Boltzmann constant. The equation clearly suggests that when the potential has a sign opposite to the sign of charge, then the location concentrations will be higher than the bulk value and vice versa.

Now combining (12.3) and (12.4), the classical *Poisson–Boltzmann Equation* for electrostatic interactions can be obtained as:

$$\nabla \cdot \epsilon(r) \nabla \Psi(r) = \rho_{bulk} + \sum_i z_i e n_{i0} \exp\left(-\frac{z_i e \Psi}{kT}\right) \quad (12.5)$$

For a one-dimensional system with homogenous dielectric medium, the PB equation can be written as

$$\frac{d^2\Psi}{dx^2} = \frac{2ze n_0}{\epsilon} \sinh\left(\frac{z_i e \Psi}{kT}\right) \quad (12.6)$$

For a system with small potential:

The *sinh* term can be expanded and linearized as:

$$\sinh(\Psi) = \Psi + \frac{\Psi^3}{3!} + \frac{\Psi^5}{5!} + \dots \approx \Psi \quad (12.7)$$

The linearized approximation makes it easier to solve the PB equation.

### 12.6.5 pH-Dependent Adsorption–Desorption

At the ionic level, variation in pH simply means variation in anionic–cationic concentration. As a result, it should be possible to develop a correlation between

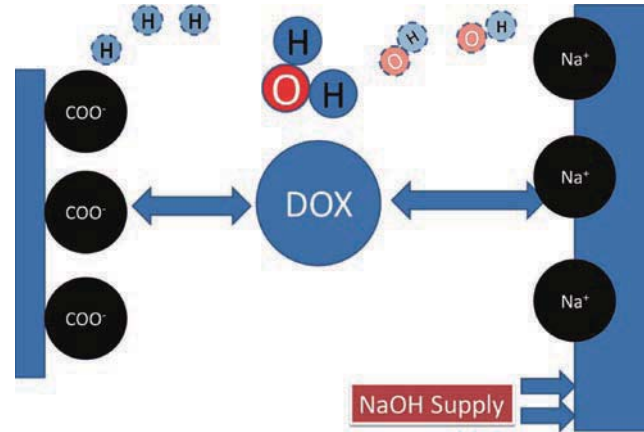


**Fig. 12.13** (a) Basic components of ND-DOX-Parylene drug delivery system. (b) Major diffusion process involved in the drug delivery system. The basic device consists of a non-porous parylene substrate, ND-drug assembly and porous parylene media. Process 1: Drugs are adsorbed on the ND surface via pH-mediated electrostatic interactions between ND-drug and solutions. Once adsorbed on the surface, the centrifuged-out ND-drug assembly is put on the non-porous parylene bath to ensure device integrity. Process 2: Diffusion of ND-drug system is controlled by varying the porous parylene thickness. Controlling is possible between the time frame of 10 min and 2 days. Process 3: pH-controlled drug release

pH level and adsorption-desorption criterion. One such approach is described in following schematic diagram (Fig. 12.13). The notes on Fig. 12.13 will help understand the approach.

## 12.7 ND-Drug Diffusion Through Porous Parylene

### 12.7.1 Fundamental Theory

In principle, diffusion of ND-drug system can be modeled using Fick's Laws of Diffusion which states that:

$$\frac{\partial C}{\partial t} = D \left( \frac{\partial^2 C}{\partial x^2} + \frac{\partial^2 C}{\partial y^2} + \frac{\partial^2 C}{\partial z^2} \right) \quad (12.8)$$

where,  $D$  is the diffusion coefficient. At the continuum level, ND-drug system diffusion through parylene layer should obey this Fick's Law. As the parylene pore radius is at the order of nanometer, it is expected that VDW interaction force will impart contribution on the diffusion process. This could be verified by performing MD/MC simulation on drug diffusion through parylene layers.

Now, once we have the diffusion coefficient determined, we can employ them to develop a continuum model using immersed finite element method.

### 12.7.2 Diffusion Through Porous Parylene and Continuum Model

The focus of this section is on the description and numerical modeling of drug release from the porous parylene matrices. Polymeric matrices can be thought as coherent systems that contain mechanical properties in between those of solids and liquids. The delivery system at the continuum is simply a three-dimensional network comprised of a liquid medium with embedded high molecular weight molecules, similar to that of sponge. Porosity of such matrix systems becomes crucial, as the drug diffusion may occur not only through network meshes but also through the pores. Drug release kinetics may be affected not only by the physical and chemical characteristics of the drug/ND/polymer matrix, but also by many factors including polymer swelling and erosion, drug dissolution and diffusion characteristics from the ND, drug/ND distribution inside the polymer matrix, drug/ND/polymer ratio, and overall system geometry. Upon contact with the release fluids, physiological media, the polymer swells, and release can take place. This implies the transition process of the polymer from the glassy dry state to the rubbery swollen one, where molecular rearrangements of polymeric chains reach a new equilibrium condition. This glassy–rubbery transition increases polymer chain mobility, enabling the drug to dissolve and diffuse through the gel layer. The time required for this transition depends on the relaxation time of the given polymer/solvent system, which in turn is a function of both solvent concentration and temperature. If the relaxation time is much lower than the characteristic time of diffusion, the solvent absorption may be described by means of Fick’s law with a concentration-dependent diffusion coefficient. On the contrary, Fickian solvent absorption with constant diffusivity takes place. If both the relaxation time and the characteristic time of diffusion are about the same, solvent adsorption does not follow Fick’s law of diffusion. Hence, drug release becomes non-Fickian where solvent absorption and drug release depends on the polymer/solvent viscoelastic properties.

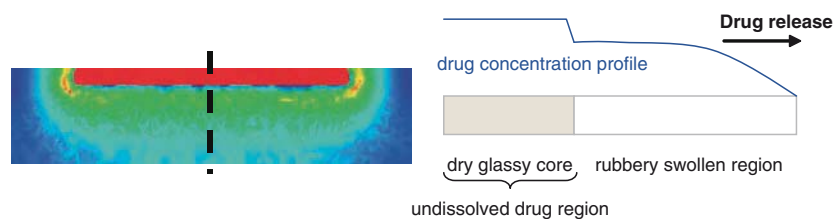


**Fig. 12.14** The external fluid uptake of the drug molecules

At the continuum level, the drug release mechanism from the ND/polymer matrices can be divided into three main fronts: the eroding front separating the release environment from the matrix, the swelling front separating the dry glassy core from the swollen matrix portion, and the diffusion front, which is found between the outer portion of the swollen matrix and the inner part where the drug is not yet completely dissolved. It should be noted that at the matrix/release environment interface, uniform distribution of drug may lead to a burst effect in the release profile followed by a slow release and must be avoided.

Most of the modeling effort at the continuum will be invoked within the immersed finite element method (IFEM). IFEM becomes an ideal platform to treat these kinds of problems due to its capabilities of solving fluid–structure interaction problems. Furthermore, within this framework, new models can be developed to describe drug release from the ND/parylene matrices.

Many simple empirical and semi–empirical approaches have been developed to describe drug release from matrix systems; among them is the one by Higuchi that applies to a planar system:

$$M_t = A\sqrt{D(2C_0 - C_s)C_s t} \quad C_0 > C_s \tag{12.9}$$

where  $M_t$  is the amount of drug released until time  $t$ ,  $A$  is the release area,  $D$  is the drug diffusion coefficient,  $C_0$  is the initial drug concentration in the matrix, while  $C_s$  is the drug solubility. This model, despite its simplicity, may be extended to more complex geometries and porous systems.

Consider an incompressible three-dimensional deformable structure  $\Omega^s$  (as shown in Fig. 12.15), i.e., drug delivery system or a cancer tumor, completely immersed in an incompressible fluid domain  $\Omega^f$ . Both, the fluid and the solid occupy the domain  $\Omega$ , but do not intersect

$$\begin{aligned} \Omega^f \cup \Omega^s &= \Omega \\ \Omega^f \cap \Omega^s &= 0 \end{aligned} \tag{12.10}$$

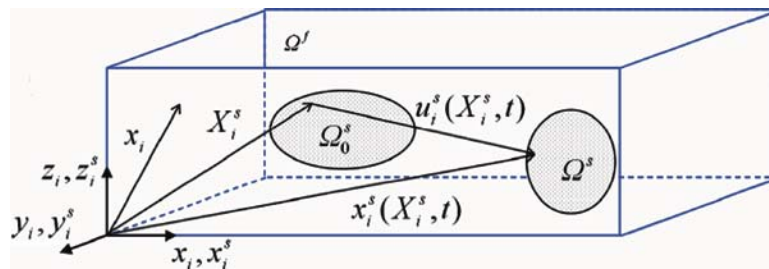


**Fig. 12.15** The Eulerian coordinates in the computation fluid domain  $\Omega^f$  are described with the time invariant position vector  $x_i$ . The solid positions in the initial configuration  $\Omega_0^s$  and the current configuration  $\Omega^s$  are represented by  $X_i^s$  and  $x_i^s(X_i^s, t)$ , respectively

With these assumption, Eulerian fluid mesh is adopted which spans the entire domain  $\Omega$  and a Lagrangian solid mesh is constructed on top of the Eulerian fluid mesh. The coexistence of fluid and solid in  $\Omega^s$  requires some deliberation when developing the momentum and continuity equations. As we know, the inertial force of a particle is balanced with the derivative of the Cauchy stress  $\sigma$  and the external force  $f^{\text{ext}}$  exerted on the continuum

$$\rho \frac{dv_i}{dt} = \sigma_{ij,j} + f_i^{\text{ext}} \quad (12.11)$$

Noting that the solid density  $\rho^s$  is different from the fluid density  $\rho^f$ , i.e.,  $\rho = \rho^s$  in  $\Omega^s$  and  $\rho = \rho^f$  in  $\Omega^f$ , the inertial forces can be divided into two components within the solid domain  $\Omega^s$  in the following manner:

$$\rho \frac{dv_i}{dt} = \begin{cases} \rho^f \frac{dv_i}{dt}, & \mathbf{x} \in \Omega / \Omega^s \\ \rho^f \frac{dv_i}{dt} + (\rho^s - \rho^f) \frac{dv_i}{dt}, & \mathbf{x} \in \Omega^s \end{cases} \quad (12.12)$$

Following the same concept, both the external force  $f_i^{\text{ext}}$  and the Cauchy stress is decomposed as

$$f_i^{\text{ext}} = \begin{cases} 0, & \mathbf{x} \in \Omega / \Omega^s \\ (\rho^s - \rho^f) g_i, & \mathbf{x} \in \Omega^s \end{cases}$$

$$\sigma_{ij,j} = \begin{cases} \sigma_{ij,j}^f, & \mathbf{x} \in \Omega / \Omega^s \\ \sigma_{ij,j}^f + \sigma_{ij,j}^s - \sigma_{ij,j}^f, & \mathbf{x} \in \Omega^s \end{cases} \quad (12.13)$$

It is important to note that the fluid stress in the solid domain in general is much smaller than the corresponding solid stress. Furthermore, since the computational fluid domain is the entire domain  $\Omega$ , hydrostatic pressure is ignored. The fluid–structure interaction (FSI) force within the  $\Omega^s$  is defined as

$$f_i^{\text{FSI}s} = -(\rho^s - \rho^f) \frac{dv_i}{dt} + \sigma_{ij,j}^s - \sigma_{ij,j}^f + (\rho^s - \rho^f) g_i, \mathbf{x} \in \Omega^s \quad (12.14)$$

The fluid–structure interaction force is naturally calculated with the Lagrangian description, where a Dirac delta function  $\delta$  is used to distribute the interaction force from the solid domain onto the computational fluid domain.

$$f_i^{\text{FSI}}(\mathbf{x}, t) = \int_{\Omega^s} f_i^{\text{FSI}s}(\mathbf{X}^s, t) \delta(\mathbf{x} - \mathbf{x}^s(\mathbf{X}^s, t)) d\Omega \quad (12.15)$$

Hence, the governing equation for the fluid domain can be derived by combining the fluid terms and the interaction force as:

$$\rho^f \frac{dv_i}{dt} = \sigma_{ij,j}^f + f_i^{\text{FSI}}, \mathbf{x} \in \Omega \quad (12.16)$$

As we consider the entire domain  $\Omega$  to be incompressible, we only need to apply the incompressibility constraint ( $v_{i,i} = 0$ ) once in the entire domain  $\Omega$ . To define the Lagrangian description for the solid and Eulerian description for the fluid, different velocity field variables,  $v_i^s$  and  $v_i^f$ , are introduced to represent the motions of the solid in the domain  $\Omega^s$  and the fluid within the entire domain  $\Omega$ . The coupling of both velocity fields is accomplished with the Dirac delta function

$$v_i^s(\mathbf{X}^s, t) = \int_{\Omega} v_i(\mathbf{x}, t) \delta(\mathbf{x} - \mathbf{x}^s(\mathbf{X}^s, t)) d\Omega \quad (12.18)$$

The coupling between the fluid and solid domains is enforced via the Dirac delta functions. The nonlinear system of equations is then solved using the standard Petrov-Galerkin method and the Newton–Raphson solution technique. Moreover, to improve the computational efficiency, GMRES iterative algorithm is employed to compute the residuals based on the matrix-free techniques.

## 12.8 Diagnostic Nanodiamonds

### 12.8.1 Imaging Applications as BioMarkers

Organic fluorophores have been widely used to tag antibodies in typical immunological assays including an immuno-fluorescent staining. However, photobleaching of the chromophore limits the life time and long-term stability, resulting in the disability of researchers to investigate specimens repeatedly and over long periods. Nanoscale particles, such as NDs, can be employed to overcome this hurdle. NDs show persistent, nonphotobleaching Raman scattering enabling the detection of the signal from a small amount of molecules. Two distinctive Raman modes, so-called D and G modes, correspond to  $sp^3$  and  $sp^2$  hybridized carbon structures. The NDs will be engineered from the synthesis step to optimize these Raman signals for better sensitivity. Also, a variety of dopants can be incorporated to induce fluorescence in the visible range. These dopants will be optimized to provide high quantum yields.

### 12.8.2 Imaging Functionality of Nanodiamond

Figure 12.16 shows the confocal fluorescence image of 5-nm ND and A549 lung cancer cell. The fluorescence images shown are after 30-min incubation with the

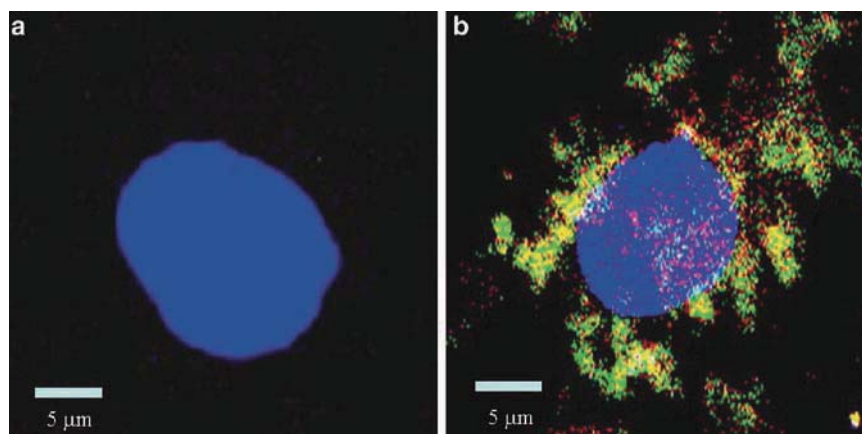


**Fig. 12.16** Fluorescence images of (a) ND only and (a) ND-GH on A549 cancer cell. (a) The nonlabeled ND can be stripped after 30-min incubation with A549 cancer cell. (b) However, the growth hormone-labeled ND can recognized A549 cancer cell specifically

nonlabeled nanodiamond (a) and growth hormone-labeled nanodiamond (b). The right image indicates the labeled nanodiamond can recognized cancer cell specifically. Meanwhile, the non-labeled nanodiamond can be uptake freely after 12 h incubation (data not shown). Therefore, ND may be a good candidate as drug or gene delivery shuttle and indicator in biomedical usage.

The right figures are interactions of growth hormone-labeled NDs (ND-GH) with A549 cell. The A549 cancer cell contains growth hormone receptors on the surface of its cell membrane. Therefore, the NDGHs are located on the cell surface and cannot be observed inside the cell. This images indicated that the modified ND can be used as cancer cell targeting molecules and the optical properties of ND can help us to identify those cancer cells. Namely, functionalized ND can be used in bio-image of cancer research [88].

As shown in Fig. 12.17, the topic of this study in ND-related cancer targeting and treatment is based on the impurity, nitroso, of ND. The nitroso is the residue of the TNT and hexogen during diamonds detonation. This impurity is embedded in the structure of nanodiamonds. However, this molecule can be photo activated and release NO by LASER irradiation.

These accumulated NO, as depicted in Fig. 12.18, will be heated and increase extremely high pressure and facilitate the diamond transform into graphite. This process will enlarge the size of ND tenfolds, as a nanoblast. Therefore, this conformation transition can be used as nanoknife in nanomedicine. This is model to interpret the mechanism of functionalized ND complexes recognize specific target of cell membrane and can be triggered blast as nanoknives for nano medicine.

Cancer cell targeting-ND can be triggered by LASER as nano-knives which can lead cancer cell program death.

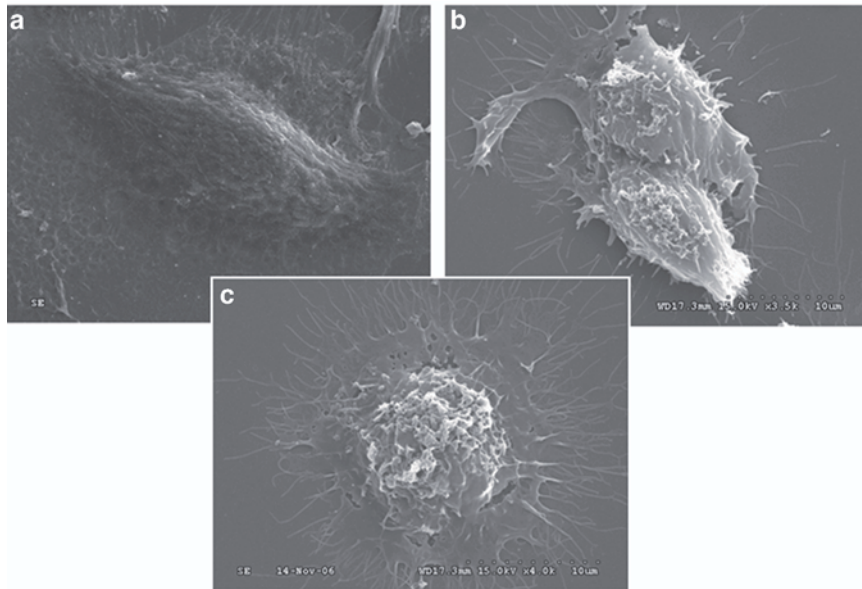


Fig. 12.17 Cancer cell targeting

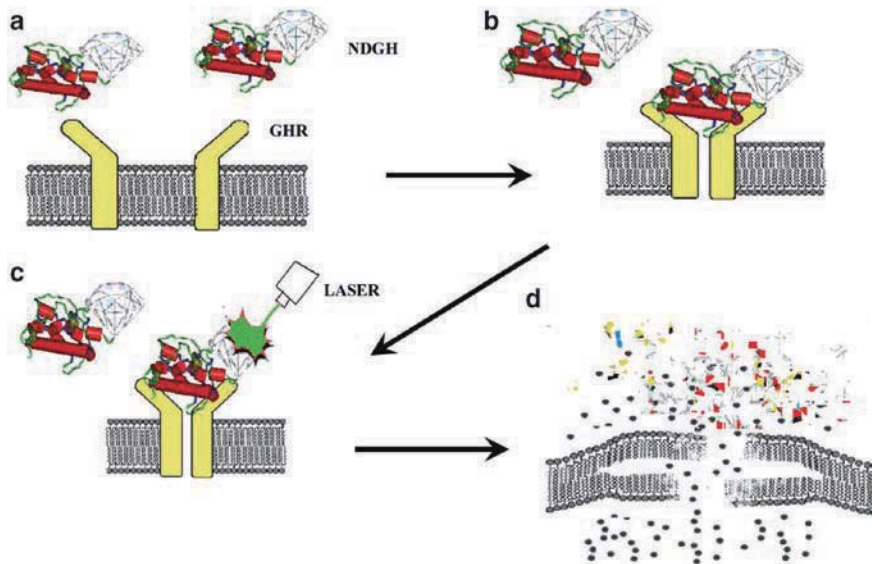


Fig. 12.18 Proposed mechanism of nano-surgery

## 12.9 Summary and Conclusions

In this book chapter, a broad range of materials have been explored as candidates for the imagery/diagnosis and therapeutic release toward cancer. The development of a platform approach toward rationally designed nanocarbon-enabled imagery and drug delivery that is broadly applicable would be an important advance towards material-driven enhancements in therapy. This research unites an emerging global effort towards the application of novel ND platforms, a model nanocarbon system, as imaging agents and drug carriers due to their comprehensively and quantitatively demonstrated biocompatibility and lack of cytotoxicity, as well as their ability to mediate the sustained release of nearly any type of therapeutic. It is imperative that in addition to experimental observation, additional work is required to fundamentally understand the material properties that govern these characteristics so that mechanistic approaches towards optimizing and tuning drug release parameters, and defect-based ND fluorescence can be manipulated to generate scalable, on-demand performance from these technologies [90–93]. It is this marriage of modeling/simulation and experimental validation to design (modeling) and develop (experimental) a multifunctional microfilm device that is simultaneously capable of releasing moiety-functionalized fluorescent NDs for targeted cancer cell imagery and drug–ND hybrids for sustained drug delivery to these cancer cells.

Over the several sections of this book chapter, we have briefly introduced a novel concept to numerically design a multifunctional drug delivery patch system for cancer therapeutic and diagnostic applications. New parameters for coulombic interactions in nanodiamonds have been developed from DFTB calculated results. An uncertainty quantification study has also been performed to demonstrate the multiscale capability of the charge prediction method. These parameters can be employed in large-scale MD simulations to capture the fundamental physics of nanodiamond structure and self-assembly. An upper bound estimate for the loading capacity of functional groups on nanodiamonds is outlined. This estimate will pave the way to understand drug loading capacity of nanodiamond. Research is underway [90–101] to address several fundamental science issues on drug delivery system. For instance, using the newly developed coulombic interaction parameters, the self assembled morphology [95, 99] of ND-clusters will be determined. Such morphology will be helpful in designing efficient patch system. Using ND-drug charge interactions in various physiological environment (characterized by pH), the mechanics of pH-mediated drug loading and unloading from ND will be investigated [94, 97]. Using classical Fick's law of diffusion and van der Waals potentials, drug diffusion through parylene nanopores will be investigated [100]. Finally, a continuum model based on Immersed Finite Element Techniques will be developed to study the overall patch performance.

**Acknowledgment** Financial Support from the US National Science Foundation and the World Class University program (R33-10079) under the Ministry of Education, Science and Technology, Republic of Korea, are greatly appreciated.

## References

1. Niemeyer CM (2001) Nanoparticles, proteins, and nucleic acids: biotechnology meets materials science. *Angew Chem Int ed* 40:4128–4158
2. Michalet X, Pinaud FF, Bentolila LA, Tsay M, Doose S, Li JJ, Sundaresan G, Wu AM, Gambhir SS, Weiss S (2005) Quantum dots for live cells and in vivo imaging. *Diagnostics and beyond*. *Science* 307:538–544
3. Jeong B, Bae YH, Lee DS, Kim SW (1997) Biodegradable block copolymers as injectable drug-delivery systems. *Nature* 388:860–862
4. Jeong B, Bae YH, Kim SW (2000) Drug release from biodegradable injective thermosensitive hydrogel of PEG-PLGA-PEG triblock copolymers. *J Control Rel* 63:155–163
5. Gombotz WR, Pettit DK (1995) Biodegradable polymers for protein and peptide drug delivery. *Bioconj Chem* 6:332–351
6. Huang H, Pierstorff E, Osawa E, Ho D (2007) Active nanodiamond hydrogels for chemotherapeutic delivery. *Nano Lett* 7:3305–3314
7. Huang H, Pierstorff E, Osawa E, Ho D (2008) Protein-mediated assembly of nanodiamond hydrogels into a biocompatible and biofunctional multilayer nanofilm. *ACS Nano* 2:203–212
8. Osawa E (2007) Recent progress and perspectives in single-digit nanodiamond. *Diamond Relat Mater* 16(12):2018–2022
9. Dolmatov VY (2006) Applications of detonation nanodiamond. *Ultrananocryst; Diamond*, 477–527
10. Yeap WS, Tan YY, Loh KP (2008) Using detonation nanodiamond for the specific capture of glycoproteins. *Anal Chem* 80:4659–4665
11. Sakurai H, Ebihara N, Osawa E, Takahashi M, Fujinami M, Oguma K (2006) Adsorption characteristics of a nanodiamond for oxoacid anions and their application to the selective preconcentration of tungstate in water samples. *Anal Sci* 22:357–362
12. Krueger A, Stegk J, Liang Y, Lu L, Jarre G (2008) Biotinylated nanodiamond: simple and efficient functionalization of detonation diamond. *Langmuir* 24(8):4200–4204
13. Krueger A, Liang Y, Jarre G, Stegk J (2006) Surface functionalization of detonation diamond suitable for biological applications. *J Mater Chem* 16(24):2322–2328
14. Barnard AS (2006) Theory and modeling of nanocarbon phase stability. *Diamond and Related Materials* 15(2–3):285–291
15. Barnard AS (2008) Self-assembly in nanodiamond agglutinates. *J Mater Chem* 18(34):4038–4041
16. Mielke SL, Belytschko T, Schatz GC (2007) Nanoscale fracture mechanics. *Annu Rev Phys Chem* 58:185–209
17. Paci JT, Belytschko T, Schatz GC (2006) Mechanical properties of ultrananocrystalline diamond prepared in a nitrogen-rich plasma: a theoretical study. *Phys Rev B* 74:184112-1–184112-9
18. Osawa E (2008) Monodisperse single nanodiamond particulates. *Pure Appl Chem* 80(7):1365–1379
19. Barnard AS, Vlasov II, Ralchenko VG (2009) Predicting the distribution and stability of photoactive defect centers in nanodiamond biomarkers. *J Mater Chem* 19(3):360–365
20. Barnard AS, Sternberg M (2008) Vacancy induced structural changes in diamond nanoparticles. *Journal of Computational and Theoretical Nanoscience* 5(11):2089–2095
21. Chang Y-R, Lee H-Y, Chen K, Chang C-C, Tsai D-S, Fu C-C, Lim T-S, Tzeng Y-K, Fang C-Y, Han C-C, Chang H-C, Fann W (2008) Mass production and dynamic imaging of fluorescent nanodiamonds. *Nature Nanotechnology* 3(5):284–288
22. Fu C-C, Lee H-Y, Chen K, Lim T-S, Wu H-Y, Lin P-K, Wei P-K, Tsao P-H, Chang H-C, Fann W (2007) Characterization and application of single fluorescent nanodiamonds as cellular biomarkers. *Proc Natl Acad Sci USA* 104(3):727–732
23. Sumant AV, Grierson DS, Gerbi JE, Birrell J, Lanke UD, Auciello O, Carlisle JA, Carpick RW (2005) Toward the ultimate tribological interface: surface chemical optimization and nanoscale single asperity properties of ultrananocrystalline diamond. *Adv Mat* 17:1039–1045

24. Naguib NN, Elam JW, Birrell J, Wang J, Grierson DS, Kabius B, Hiller JM, Sumant AV, Carpick RW, Auciello O, Carlisle JA (2006) The use of tungsten interlayers to enhance the initial nucleation and conformality of ultrananocrystalline diamond (UNCD) thin films. *Chem Phys Lett* 430:345–50
25. Sumant AV, Gilbert PUPA, Grierson DS, Konicek AR, Abrecht M, Butler JE, Feygelson T, Rotter SS, Carpick RW (2007) Surface composition, bonding, and morphology in the nucleation and growth of ultra-thin, high quality nanocrystalline diamond films. *Diam Rel Mat* 16:718–24
26. Lee W, Jang S, Kim MJ, Myoung J-M (2008) Interfacial interactions and dispersion relations in carbon-aluminium nanocomposite systems. *Nanotechnology* 19:285701-1–285701-13
27. Steager EB, Kim C-B, Kim MJ (2008) Temperature effects on swarming flagellated bacteria in microfluidic environments. *J Heat Transfer* 130:080908–1
28. Kim YS, Liao KS, Jan CJ, Bergbreiter DE, Grunlan JC (2006) “Conductive thin films on functionalized polyethylene particles. *Chem Mat* 18:2997–3004
29. Jan CJ, Walton MD, McConnell EP, Jang WS, Kim YS, Grunlan JC (2006) Carbon black thin films with tunable resistance and optical transparency. *Carbon* 44:1974–1981
30. Ho YP, Chen HH, Leong KW, Wang TH (2006) Evaluating the intracellular stability and unpacking of DNA nanocomplexes by quantum dots-FRET. *J Control Rel* 116:83–89
31. Zhang J, Zimmer JW, Howe RT, Maboudian R (2008) Characterization of boron-doped micro- and nanocrystalline diamond films deposited by wafer-scale hot filament chemical vapor deposition for MEMS applications. *Diam and Rel Mat* 17:23–28
32. Discher BM, Won YY, Ege DS, Lee JC, Bates FS, Discher DE, Hammer DA (1999) Polymersomes: tough vesicles made from diblock copolymers. *Science* 284:1143–1146
33. Yang Y, Zeng C, Lee LJ (2004) Three-dimensional assembly of polymer microstructures at low temperatures. *Adv Mat* 16:560–564
34. Qi L, Gao X (2008) Quantum dot–amphipol nanocomplex for intracellular delivery and real-time imaging of siRNA. *ACS Nano*, DOI: [10.1021/nl800280r](https://doi.org/10.1021/nl800280r)
35. Discher DE, Ahmed F (2006) Polymersomes. *Ann Rev Bio Eng* 8:323–341
36. Geng Y, Discher DE (2005) Hydrolytic shortening of polycaprolactone-block-(polyethylene oxide) worm micelles. *J Am Chem Soc* 127:12780–12781
37. Ahmed F, Discher DE (2004) Controlled release from polymersome vesicles blended with PEO-PLA or related hydrolysable copolymer. *J Control Rel* 96:37–53
38. Discher DE, Eisenberg A (2002) Polymer Vesicles *Science* 297:967–973
39. Lam R, Chen M, Pierstorff E, Huang H, Osawa E, Ho D (2008) Nanodiamond-embedded microfilm devices for localized chemotherapeutic elution. *ACS Nano* 2:2095–2102
40. Cui Y, Wei QQ, Park HK, Lieber CM (2001) Nanowire nanosensors for highly sensitive and selective detection of biological and chemical species. *Science* 293:1289–1292
41. Baughman RH, Zakhidov AA, de Heer WA (2002) Carbon nanotubes—the route toward applications. *Science* 297:787–792
42. Bianco A, Prato M (2003) Can carbon nanotubes be considered useful tools for biological applications? *Adv Mat* 15:1765–1768
43. Bowden T, Tabor D (1961) Friction and lubrication in solids, Japanese edition. Maruzen, Tokyo, p 27
44. S Mori, A Kanno, H Nanao, I Minami, E Ōsawa, Tribological performance of nanodiamond for water lubrication, Proceedings of the 3 rd International Symposium on Detonation Nanodiamonds: Technology, Properties and Applications, July 1–4, 2008, St. Petersburg, Russia, p. 21–28, Ioffe Physico-Technical Institute
45. Ōsawa E, Ho D, Huang H, Korobov MV, Rozhkova NN (2009) “Consequences of strong and diverse electrostatic potential field on the surface of detonation nanodiamond particles,” *Diam Rel Mater*, 18, doi.org/[10.1016/j.diamond.2009.01.025](https://doi.org/10.1016/j.diamond.2009.01.025).
46. Qian D, Liu WK, Zheng Q (2008) Concurrent quantum/continuum coupling analysis of nanostructures. *Comput Methods Appl Mech Eng* 197(41–42):3291–3323
47. Kopacz AM, Liu WK, Liu ShuQ (2008) Simulation and prediction of endothelial cell adhesion modulated by molecular engineering. *Comput Meth Appl Mech Eng* 197(25–28): 2340–2352

48. Liu Y, Kieseok Oh, Bai JG, Chang C-L, Yeo W, Chung J-H, Lee K-H, Liu WK (2008) Manipulation of nanoparticles and biomolecules by electric field and surface tension. *Comput Meth Appl Mech Eng* 197(25–28):2156–2172
49. Liu WK, Jun S, Qian D (2008) Computational nanomechanics of materials. *Journal of Computational and Theoretical Nanoscience* 5(970–996):2008
50. Liu WK, Kim Do Wan, Tang S (2007) Mathematical foundations of the immersed finite element method. *Computational Mechanics* 39(3):211–222
51. WK Liu, Liu Y, Farrell D, et al (2006) Immersed finite element method and applications to biological systems. *Comp Meth Appl Mech Eng*, 195(1722-1749),
52. Liu WK, Sukky J, Qian D (2006) Computational nanomechanics of materials, *Handbook of theoretical and computational nanotechnology*, M Reith and W Schommers (Eds). 4, 132–191, American Scientific Publishers
53. Liu WK, Park HS, Qian D, Karpov EG, Kadowaki H, Wagner GJ (2006) Bridging scale methods for nanomechanics and materials. *Comput Meth Appl Mech Eng* 195(13–16):1407–1421
54. Liu WK, Park HS, Qian D, Karpov EG, Kadowaki H, Wagner GJ (2006) Bridging scale methods for nanomechanics and materials. *Computer method in applied mechanics and engineering* 195:1404–1421
55. Park HS, Karpov EG, Liu WK (2005) Non-reflecting boundary conditions for atomistic, continuum and coupled atomistic/continuum simulations. *Int J Numer Meth Eng* 64:237–259
56. WK Liu, HS Park, D Qian, EG Karpov, H Kadowaki, GJ Wagner. Bridging Scale Methods for Nanomechanics and Materials”, accepted for publication in *Comput Meth Appl Mech Eng* 2005, special issue in honor of the 60th birthday of Prof. T.J.R. Hughes.
57. Park HS, Karpov EG, Klein PA, Liu WK (2005) The bridging scale for two-dimensional atomistic/continuum coupling. *Phil Mag* 85(1):79–113
58. Park HS, Karpov EG, Liu WK, Klein PA (2005) The bridging scale for two-dimensional atomistic/continuum coupling. *Phil Mag* 85(1):79–113
59. Park HS, Karpov EG, Klein PA, Liu WK (2005) Three-dimensional bridging scale analysis of dynamic fracture. *J Comput Phys* 207:588–609
60. *Applied Mechanics and Engineering*. 198 (15-16), pp 1327–1337, March 2009
61. Barnard AS, Russo SP, Snook IK (2005) *J Comput Theor Nanosci* 2:180
62. AS Barnard, SP Russo, IK Snook (2003) *J Chem Phys* 118, 5094; AS Barnard, SP Russo, IK Snook (2003) *Phys Rev B* 68, 073406
63. AS Barnard, SP Russo, IK Snook (2003) *Philos Mag Lett* 83, 39; AS Barnard, SP Russo, IK Snook (2004) *Diamond Relat Mater* 12, 1867
64. Barnard AS, Zapol PJ (2004) *Chem Phys* 121:4276
65. AS Barnard, SP Russo, IK Snook (2003) *Phys Rev B* 68, 073406
66. AS Barnard, SP Russo, IK Snook (2003) *Int J Mod Phys B* 17 (21) 3865
67. Barnard AS, Sternberg M (2007) *J Mater Chem* 17:4811
68. Barnard AS (2008) *J Mater Chem* 18:4038
69. Harold P Bovenkerk, Thomas R Anthony, James F Fleischer, William F Banholzer, CVD diamond by alternating chemical reactions, US patent 5,302,231, 12 april 1994
70. Dieter M Gruen, Thomas G McCauley, Dan Zhou, Alan R Krauss, Tailoring nanocrystalline diamond film properties US patent, 6,592,839, 15 July 2003
71. Li H, Tao Xu, Chen J, Zhou H, Liu H (2003) Preparation and characterization of hydrogenated diamond-like carbon films in a dual DC-RF plasma system. *J Phys D: Appl Phys* 36:3183–3190
72. Synthesis and Application of Nano-crystalline Diamond Thin Film, KISTI reports, 2005
73. Baik E-S, Baik Y-J, Lee SW, Jeon D (2000) Fabrication of diamond nano-whiskers. *Thin Solid Films* 377–378:295–298
74. Remes Z, Kromka A, Vanecek M, Grinevich A, Hartmannova H, Kmoch S (2007) The RF plasma surface chemical modification of nanodiamond films grown on glass and silicon at low temperature. *Diamond & Related Materials* 16:671–674
75. Hirakuri KK, Minorikawa T, Friedbacher G, Grasserbauer M (1997) Thin film characterization of diamond-like carbon films prepared by r.f. plasma chemical vapor deposition. *Thin Solid Films* 302:5–11

76. Krueger A (2008) New carbon materials. *Chem Eur J* 14:1382–1390
77. [www.kurzweilai.net/meme/frame.html?main=/articles/art0632.html](http://www.kurzweilai.net/meme/frame.html?main=/articles/art0632.html): How to make nano diamond.
78. Hall P (1992) The bootstrap and edgeworth expansion. Springer Series in Statistics. Springer-Verlog, New York
79. Kennedy MC, A O'Hagan (2001) Bayesian calibration of computer models. *Journal of the Royal Statistical Society Series B* 63, 425–464.
80. Xiong Y, Chen W, Tsui K-L, Apley D (2009) A better understanding of model updating strategies in validating engineering models. *Comput Meth Appl Mech Eng* 198(15–16):1327–1337
81. Krüger A, Kataoka F, Ozawa M, Fujino T, Suzuki Y, Aleksenskii AE, Ya. Vul A, Osawa E (2005) Unusually tight aggregation in detonation nanodiamond: Identification and disintegration. *Carbon* 43:1722–1730
82. Panich AM, Shames AI, Vieth HM, Osawa E, Takahashi M, Ya Vul A (2006) Nuclear magnetic resonance study of ultrananocrystalline diamonds. *Eur Phys J B* 52:397–402
83. M Gruen, Shenderova O (2005) Synthesis, properties and applications of ultrananocrystalline nanodiamond. Springer, USA. 217–230
84. Zheng M, Jagota A, Semke ED, Diner BA, Mclean RS, Lustig SR, Richardson RE, Tassi NG (2003) *Nature mater* 2:338
85. Zheng M, Jagota A, Strano MS, Santos AP, Barone P, Chou SG, Diner BA, Dresselhaus MS, Mclean RS, Onoa GB, Samsonidze GG, Semke ED, Usrey M, Walls DJ (2003) *Science* 302:1545
86. Hwang ES, Cao C, Hong S, Jung HJ, Cha CY, Choi JB, Kim YJ, Baik S (2006) *Nanotechnol* 17:3442
87. Chengfan Cao, Jung Heon Kim, Ye-Jin Kwon, Young-Jin Kim, Eung-Soo Hwang and Seunghyun Baik (2009) An immunoassay using biotinylated single walled carbon nanotubes as Raman biomarkers, Accepted to *Analyst*.
88. Cheng C-Y, Perevedentseva E, Tu J-S, Chung P-H, Cheng C-L, Liu K-K, Chao J-I, Chen P-H, Chang C-C (2007) Direct and in vitro observation of growth hormone receptor molecules in A549 human lung epithelial cells by nanodiamond labeling. *Appl Phys Lett* 90:163903 (SCI)
89. Hunter RJ (1981) Zeta potential in colloidal science. Academic, London
90. Wing Kam Liu, Ashfaq Adnan, Adrian Kopacz, Roadmap for nanodiamond-based drug delivery design for cancer therapeutics and diagnostics, 10th US National Congress On Computational Mechanics, Columbus, OH, 2009
91. Wing Kam Liu, Ashfaq Adnan, Adrian Kopacz (2009) Design of nanodiamond-enabled drug delivery system by simulation based science & engineering, ASME International Mechanical Engineering Congress & Exposition, Lake Buena Vista, Florida – November 13–19.
92. Wing Kam Liu, Multiscale design of nanodiamond-based drug delivery system for engineered medicine, coupled problems 2009, Computational Methods For Coupled Problems In Science And Engineering, 8–10 June 2009, Ischia Island, Italy.
93. Wing Kam Liu, Ashfaq Adnan, Adrian Kopacz, Nanoscale Science In Therapeutic And Diagnostic Applications 2009 ASME International Mechanical Engineering Congress & Exposition, Lake Buena Vista, Florida – November 13–19, 2009.
94. Adnan A, Kam Liu Wing (2009) Mechanics of pH mediated adsorption/desorption of doxorubicin drug from functionalized nanodiamond. 10th US National Congress On Computational Mechanics, Columbus, OH
95. Kopacz A, Adnan A, Kam Liu W (2009) Functionalized & self-assembled nanodiamonds for diagnostic and therapeutic applications. 10th US National Congress On Computational Mechanics, Columbus, OH
96. Wing Kam Liu, Ashfaq Adnan (2009) Nanoscale science in therapeutic and diagnostic applications. 10th US National Congress On Computational Mechanics, Columbus, OH
97. Ashfaq Adnan, Wing Kam Liu (2009) Mechanics of pH controlled loading and release of chemotherapeutics from functionalized nanodiamond, 2009 ASME International

- Mechanical Engineering Congress & Exposition, Lake Buena Vista, Florida – November 13–19, 2009
98. Michelle Hallikainen, Ashfaq Adnan, Wing Kam Liu, Predicting nanodiamond structure and surface charge distribution using molecular dynamics and Bayesian statistics. 10th US National Congress On Computational Mechanics, Columbus, OH, 2009
  99. Adrian Kopacz, Ashfaq Adnan, Wing Kam Liu (2009) Equilibrium functionalization and self-assembly of nanodiamond as a platform for engineered medicine”, 2009 ASME International Mechanical Engineering Congress & Exposition, Lake Buena Vista, Florida – November 13–19, 2009
  100. Paul Arendt, Wei Chen, Wing Kam Liu, Ashfaq Adnan, Multiscale design of a simplified nanodiamond based drug delivery system. 10th US National Congress On Computational Mechanics, Columbus, OH, 2009
  101. Wing Kam Liu, Ashfaq Adnan, Adrian Kopacz, Young-Jin Kim, Moon Ki Kim, Multiscale design of nanodiamond-based drug delivery system for cancer therapeutics and diagnostics. 2nd International Symposium On Computational Mechanics (ISCM II) and 12th International Conference On Enhancement And Promotion Of Computational Methods In Engineering And Science (EPMESC XII), November 30 – December 3, 2009, Hong Kong – Macau

# Ni<sup>2+</sup> doping DNA: a semiconducting biopolymer

Peng-Chung Jang Jian<sup>1</sup>, Tzeng-Feng Liu<sup>1</sup>, Chuan-Mei Tsai<sup>2</sup>,  
Ming-Shih Tsai<sup>3</sup> and Chia-Ching Chang<sup>4,5,6</sup>

<sup>1</sup> Department of Material Science and Engineering, National Chiao Tung University, Hsinchu 30050, Taiwan, Republic of China

<sup>2</sup> National Nano Device Laboratories, Hsinchu 30071, Taiwan, Republic of China

<sup>3</sup> Cabot Microelectronic, Chupei, Hsinchu Hsien 302, Taiwan, Republic of China

<sup>4</sup> Department of Biological Science and Technology, National Chiao Tung University, Hsinchu 30050, Taiwan, Republic of China

<sup>5</sup> Institute of Physics, Academia Sinica, Taipei 11529, Taiwan, Republic of China

E-mail: [ccchang01@faculty.nctu.edu.tw](mailto:ccchang01@faculty.nctu.edu.tw)

Received 3 May 2008, in final form 7 June 2008

Published 18 July 2008

Online at [stacks.iop.org/Nano/19/355703](http://stacks.iop.org/Nano/19/355703)

## Abstract

DNA is a one-dimensional nanowire in nature, and it may not be used in nanodevices due to its low conductivity. In order to improve the conducting property of DNA, divalent Ni<sup>2+</sup> are incorporated into the base pairs of DNA at pH  $\geq$  8.5 and nickel DNA (Ni-DNA) is formed. Conducting scanning probe microscopy (SPM) analysis reveals that the Ni-DNA is a semiconducting biopolymer and the Schottky barrier of Ni-DNA reduces to 2 eV. Meanwhile, electrochemical analysis by cyclic voltammetry and AC impedance shows that the conductance of Ni-DNA is better than that of native DNA by a factor of approximately 20-fold. UV spectroscopy and DNA base pair mismatch analyses show that the conducting mechanism of Ni-DNA is due to electrons hopping through the  $\pi$ - $\pi$  stacking of DNA base pairs. This biomaterial is a designable one-dimensional semiconducting polymer for usage in nanodevices.

## 1. Introduction

The structure of double-stranded DNA was reported by Watson and Crick in 1953 [1]. The electron transfer properties of DNA were studied intensively for decades [2–6]. However, the conclusions on DNA conductivity remained contradictory. For example, in 1962, Eley and Spivey were the first researchers who suggested that the  $\pi$ - $\pi$  interactions between the stacked base pairs in DNA could serve as a pathway for charge transportation [2]. Barton *et al* also reported that fluorescence quenching could be caused by the charge on an excited donor leaking to a nearby acceptor [3]. Barton *et al* and Eley and Spivey suggested that DNA was a conducting molecular wire. However, directly measuring the electrical current through DNA molecules which are absorbed on a mica surface indicates that DNA is an insulator [4, 5]. Meanwhile, Porath and Dekker's study demonstrates that DNA is a semiconductor

with a wide bandgap [6]. Since intrinsic DNA conductivity cannot provide a convincing conclusion, a metal-doped DNA, i.e. metallic DNA (M-DNA) [7–11], may be an alternative approach to generate a conducting nanowire.

Recently, an electrochemical technique in which a self-assembled monolayer (SAM) is formed on a metal electrode has been widely applied to study the electron transfer properties of polymers [12–17]. This technique can be used to measure rapid reactions of charge transfer kinetics by monitoring redox indicators in solutions [18, 19]. Further, alternating current (AC) impedance spectrum analysis and equivalent circuit simulation are efficient methods to probe the interfacial characterization of electrodes [20–24].

In this study, we convert native DNA into Ni-DNA. We perform conducting scanning probe microscope (SPM) measurements, and the results reveal that the Ni-DNA is like a semiconductor which is consistent with Porath and Dekker's [6] study and the Schottky barrier of Ni-DNA reduces to 2 eV. The conducting property of this Ni-DNA is at least approximately 20-fold higher than that of native DNA in both

<sup>6</sup> Address for correspondence: Department of Biological Science and Technology, National Chiao Tung University, Hsinchu 30050, Taiwan, Republic of China.

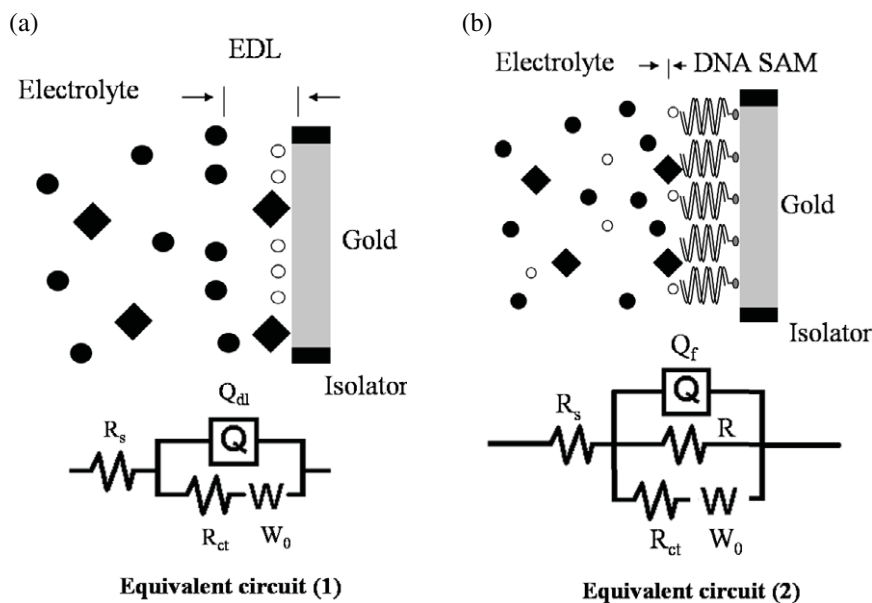


**Figure 1.** The electrochemical systems of the bare gold and DNA-modified gold electrodes. (a) Equivalent circuit 1 for the bare gold electrode and (b) equivalent circuit 2 for the DNA-modified gold electrode in a negative redox probe,  $[\text{Fe}(\text{CN})_6]^{-3}$ , system.  $R_s$  is the solution resistance and  $R_{ct}$  is the charge transfer resistance between electrode and electrolyte. The electrical double layer capacitance is  $Q_{dl}$ ,  $R$  is the resistance through ds-DNA,  $Q_f$  is the DNA film capacitance and  $W_0$  shows the Warburg impedance. Water molecules are represented by (○), electrolyte by (●) and (◆) shows redox-active species.

the DC and AC modes. UV spectroscopy analysis shows that the absorption of Ni-DNA has a redshift, and this redshift indicates the reduction in the bandgap of native DNA by doping with  $\text{Ni}^{2+}$ . Further, DNA base pair mismatch analysis indicates a charge transfer through the  $\pi$ - $\pi$  interactions of DNA base pairs and this is consistent with the suggestion by Eley and Spivey [2].

## 2. Materials and methods

All chemicals were purchased from Merck (Merck Ltd, Taipei, Taiwan). Thirty nucleotide primers (the length is about 10.2 nm) comprising poly-CA and 3'-thiol-modified poly-GT were purchased from Bio Basic Inc. (Markham Ontario, Canada). Further, we designed poly-CA with a single base mutation, which caused a base pair mismatch, for example, G/A and G/T in this duplex.

### 2.1. Ni-DNA preparation

A Ni-DNA duplex with a final concentration of 10  $\mu\text{M}$  was formed in a solution with 20 mM Tris-HCl buffer (pH = 9.0) and 5 mM  $\text{NiCl}_2$ . The excess  $\text{Ni}^{2+}$  was removed by dialysis in the same buffer without  $\text{Ni}^{2+}$ . A similar approach could be used to convert DNA into Ni-DNA in the SAM structure.

### 2.2. Preparation of DNA SAMs

In order to immobilize the DNA duplex on the surface of a gold electrode, the 3' end of the poly-GT was thiolated with  $\text{SH}(\text{CH}_2)_6$ . DNA with a concentration of 2  $\mu\text{M}$  (containing 0.1 M PB buffer and 1 M NaCl) was deposited on the cleaned

gold electrode surface. The gold electrode was capped tightly to maintain the gold surface under moist conditions in order to avoid the problem of solution evaporation. After eight hours' incubation a SAM of DNA was formed. In order to remove the non-covalent bounding physisorbed molecules, the modified gold electrode was immersed in 0.1 M phosphate buffered saline buffer (PBS) for 10 min and then dipped twice in distilled water. This process is relatively harsh than in previous studies [17, 21–23]. Therefore, we believed that most of the physisorbed molecules can be removed under this thorough treatment. The bare gold and DNA-modified gold electrodes are employed in electrochemical analyses and these two systems can be described by cartoons and equivalent circuits, as shown in figure 1.

### 2.3. Scanning probe microscopy measurements

A scanning probe microscope model JSPM-5200 (JEOL, MA, USA) was used for measuring the current–voltage curve of DNA SAMs in the contact mode, and voltage biases were applied from  $-4$  to  $4$  V in vacuum ( $10^{-3}$  Pa) at room temperature. The scan size was  $0.5 \mu\text{m} \times 0.5 \mu\text{m}$  and the scan rate was 0.5 Hz. The tungsten tip curvature radius was approximately 20 nm.

### 2.4. Electrophoresis analysis

Native DNA, Ni-DNA and Ni-DNA with EDTA (ethylenediaminetetraacetic acid) were analysed by electrophoresis. In this experiment, a 2.0% agarose gel containing 3  $\mu\text{l}$  SYBR Green (an asymmetrical cyanine dye) was used; further, an electron field of  $10 \text{ V cm}^{-1}$  was applied for 15 min in

0.5 × TBE (Tris-Borate-EDTA) buffer. Then, the metal chelating property of native DNA, Ni-DNA and Ni-DNA with EDTA was verified by their green fluorescence emission.

### 2.5. Electrochemical measurements

All cyclic voltammetry (CV) and AC impedance measurements were performed using a potentiostat/galvanostat model 273A (EG&G, Gaithersburg, MD, USA) and frequency response detector model 1025 (EG&G, Gaithersburg, MD, USA), and the measurements were recorded using a personal computer. The counter electrode was composed of platinum and the reference electrode was composed of Ag/AgCl. The modified gold electrode was used as the working electrode. The electrolyte was composed of 100 mM KNO<sub>3</sub> and 5 mM K<sub>3</sub>[Fe(CN)<sub>6</sub>] (as a redox probe). In order to investigate the electrostatic interactions among the redox probe, a phosphate backbone and metal ions in the base pair, a positive redox probe comprising 5 mM Ru(NH<sub>3</sub>)<sub>6</sub>Cl<sub>3</sub> in 100 mM KNO<sub>3</sub> was used as a reference. During the CV analysis, the sweeping potential was in the range from −300 to 600 mV at a scan rate 20 mV s<sup>−1</sup>, and this potential was reversed for the K<sub>3</sub>[Fe(CN)<sub>6</sub>] redox probe. For the Ru(NH<sub>3</sub>)<sub>6</sub>Cl<sub>3</sub> redox probe, the sweeping potential was in the range from −400 to 100 mV at a scan rate of 20 mV s<sup>−1</sup>, which was reversed later. During the AC impedance analysis, the impedance was measured by a sinusoidal potential modulation of ±5 mV over the frequency range from 100 kHz to 0.01 Hz at a bias potential of 220 mV versus Ag/AgCl. All electrochemical experiments were performed at room temperature, and the impedance data were analysed by ZSimpWin software (Princeton Applied Research, TN, USA).

### 2.6. UV–visible spectroscopy measurements

In order to investigate the effect of pH on metallic DNA formation, 20 mM Tris-HCl with various pH values (pH 8.0, 8.5, 8.8 and 9.0) was used for synthesizing Ni-DNA; this synthesis was carried out by the approach mentioned in the previous section. Then, the samples were dialysed in 500 ml buffer solution (5 mM Tris-HCl) for 24 h at 4 °C in order to remove the excess Ni<sup>2+</sup> in these samples. The UV absorptions of the samples were measured using a UV–visible spectrophotometer (JASCO V-550, Tokyo, Japan) and found to be in the range from 220 to 320 nm.

## 3. Results and discussion

### 3.1. Ni<sup>2+</sup> incorporation in DNA base pairs

In order to observe the Ni-DNA formation, a SYBR Green is used as an indicator which possesses a planar structure and positive charge and can intercalate into a stacking space between DNA base pairs, which is similar to ethidium bromide (EtBr). The gel electrophoresis results (figure 2) show that the fluorescence of SYBR Green cannot be observed in lane 2. According to the studies of Lee *et al* [7, 9] and Baro *et al* ([26]), Zn<sup>2+</sup> and some other divalent metal ions bind to duplex DNA at pHs above 8 and cause a conformational change. This

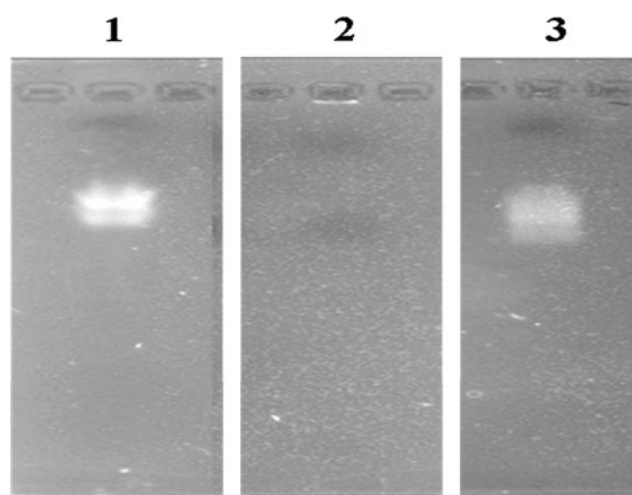


**Figure 2.** The fluorescence image of the SYBR Green of DNA gel. Lane 1, Lane 2 and Lane 3 denote native DNA (30 base pairs), Ni-DNA and Ni-DNA treated with 25 mM EDTA, respectively.

new structure does not bind ethidium bromide (EtBr), due to the electrostatic repulsion, thus a ‘fluorescence assay’ in the presence of EtBr can be used to monitor M-DNA formation. In our study, SYBR Green, with a similar structure and DNA binding mechanism to EtBr, shall share the same mechanism. Therefore, we suggested that the electrostatic repulsion also exists between SYBR Green and metal ions [7, 9, 26]. This result indicates the Ni<sup>2+</sup> replace the imino protons of G and T of DNA and form a stable tetrahedral geometry in an alkali environment (pH ≥ 8.5) which is similar to the previous study [7–9]. However, the fluorescence of SYBR Green can be observed in both the native DNA in lane 1 and 25 mM EDTA (pH = 9.0)-treated Ni-DNA (lane 3). These results indicate that the Ni<sup>2+</sup> can be extracted from base pairing of Ni-DNA by EDTA treatment, and the behaviour of EDTA-treated Ni-DNA is similar to that of native DNA. Further, the SYBR Green dye can again intercalate into EDTA-treated Ni-DNA. These results also show that the Ni-DNA formation is a reversible process. Namely, native DNA can be converted into Ni-DNA by being incubated in the solution with Ni<sup>2+</sup>, as described in the methods section. Meanwhile, this Ni<sup>2+</sup> intercalating structure shortens the gap between each base pair. Therefore, the consequence may change the conductance of DNA.

### 3.2. Ni-DNA is a semiconducting biopolymer

In order to measure the conducting property of Ni-DNA, a DNA SAM structure is formed on the surface of the gold electrode as described previously. Then the electronic characteristics of the Ni-DNA monolayer are directly measured by a conducting SPM in the solid state, and the area-averaged *I*–*V* curves of native DNA and Ni-DNA are shown in figure 3. The measuring structure including a tungsten probe of SPM, DNA SAM and a gold electrode is similar to a Schottky device. Therefore, a semiconductor sigmoid *I*–*V* curve with an approximately 2 V threshold can be observed. However, we find that no significant current can be observed in the native DNA. Meanwhile, the conductance of Ni-DNA is

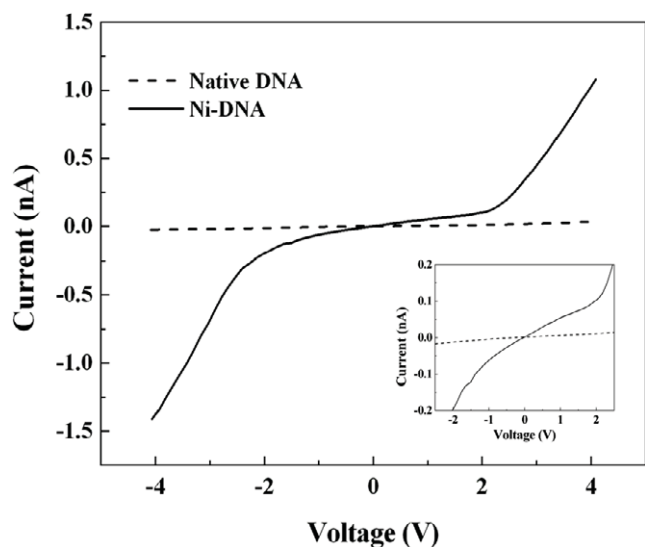


**Figure 3.** Current–voltage curves of the native DNA and Ni-DNA SAMs by conducting SPM.

approximately 20-fold higher than that of the native DNA (figure 3, inset) at a voltage lower than 2 V. The resistivity of the Ni-DNA is approximately  $2.2 \times 10^4 \Omega\text{cm}$ . This resistivity is similar to the semiconductor. Therefore, we can conclude that the Ni-DNA is a semiconducting biopolymer.

The resistivity difference between native DNA and Ni-DNA can be revealed by CV electrochemical analyses.

As shown in figure 4(a), clear redox peaks of  $[\text{Fe}(\text{CN})_6]^{-3}$  and  $[\text{Fe}(\text{CN})_6]^{-4}$  can be observed in the bare gold working electrode owing to the controlling action by CV. The CV curve of the bare gold electrode (figure 4(a)) shows remarkable reduction ( $E_{p,c}$ ) and oxidation ( $E_{p,a}$ ) peaks, and the peak currents are equal. The difference in the potential ( $\Delta E_p$ ) between the redox peaks is approximately 78 mV, and from the well-known behaviour of the CV curve, this small potential difference can be recognized as a diffusion-limited reversible redox reaction [24]. It means that the charge transfer kinetics of the redox reaction is rapid between the redox probe and the bare gold electrode.

The modified gold electrode, which is covered with the SAM of DNA, cannot touch the electrolyte directly. The redox reaction of  $[\text{Fe}(\text{CN})_6]^{-3}$  can be observed only under the condition that the electrons move through the molecules of the SAM. Therefore, the intrinsic conductance of the molecules plays an indispensable role for the migration of electrons. In the case of the SAM of the native DNA, the redox peaks of  $[\text{Fe}(\text{CN})_6]^{-3}$  are not observed (figure 4(b)). This result indicates that the resistance of native DNA is high and that few electrons or holes move through the native DNA molecules. This is consistent with the results of the previously performed conducting SPM measurement. In contrast, in the case of the Ni-DNA SAM, broad redox peaks of  $[\text{Fe}(\text{CN})_6]^{-3}$  and  $[\text{Fe}(\text{CN})_6]^{-4}$  can be observed clearly (figure 4(c)). The large peak separation (is approximately 498 mV) and low peak amplitudes, which are compared to the bare gold electrode, indicate that the charge transfer kinetics is slow between the redox probe and the Ni-DNA modified electrode. This result

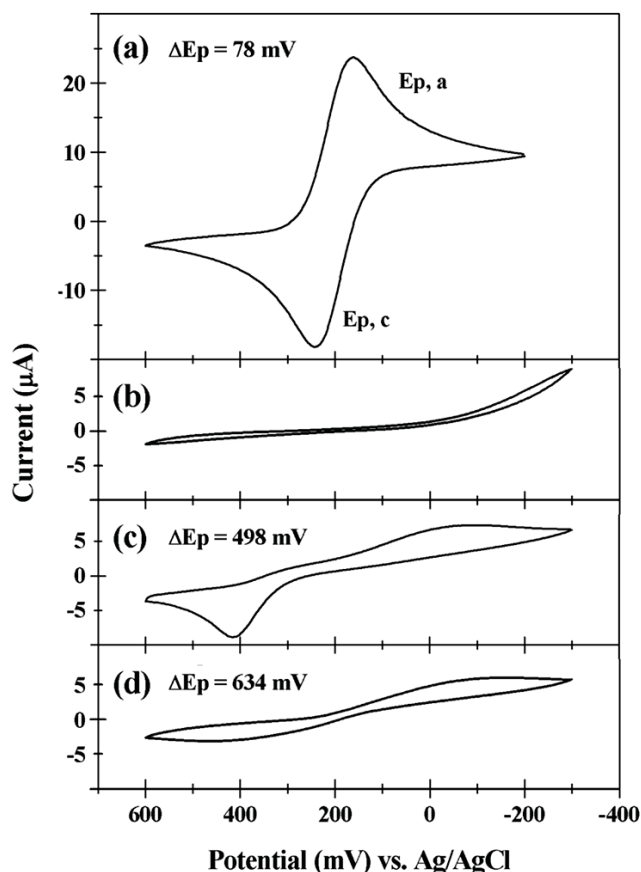


**Figure 4.** Cyclic voltammeteries of the bare gold electrode and modified gold electrodes in the  $[\text{Fe}(\text{CN})_6]^{-3}$  system. (a) Bare gold electrode, (b) native DNA-modified gold electrode, (c) Ni-DNA at pH = 9.0, (d) Ni-DNA after 25 mM EDTA treatment.

indicates that electrons can move through the Ni-DNA in the Ni-DNA SAM-modified gold electrode. This also implies that Ni-DNA is a better conductor than native DNA. However, these redox peaks disappear by treating the Ni-DNA SAM-modified gold electrode with 25 mM EDTA at pH = 9.0 (figure 4(d)). This result also supports the conclusion that the redox reaction that occurs may be attributed to the DNA doped with Ni ions.

According to Peterson's study the surface coverage of DNA molecules depends on the ionic strength of the solution and immobilization time [25]. The theoretical density of a full coverage DNA monolayer should be around  $2.5 \times 10^{13}$  molecules  $\text{cm}^{-2}$ . According to a previous study [25], the maximum probe coverage is achieved (about  $2.75 \times 10^{12}$  probe molecules  $\text{cm}^{-2}$ ) when the concentration of NaCl is 1 M and after 2 h immobilization. In our study, the DNA was incubated in 0.1 M PBS buffer (which contains 1 M NaCl), and immobilized on a gold electrode for 8 h immobilization. Therefore, the estimated density should be higher than  $2.75 \times 10^{12}$  probe molecules  $\text{cm}^{-2}$ . In theory, the SAM structure may contain some holes, but according to our CV analysis in figure 4(b) (no redox peaks), we are sure that the DNA SAM had blocked the gold surface effectively. However, these holes may enhance the signal when the redox probes change to the positive charge. With this density, we are sure that the DNA SAM had blocked the gold surface effectively.

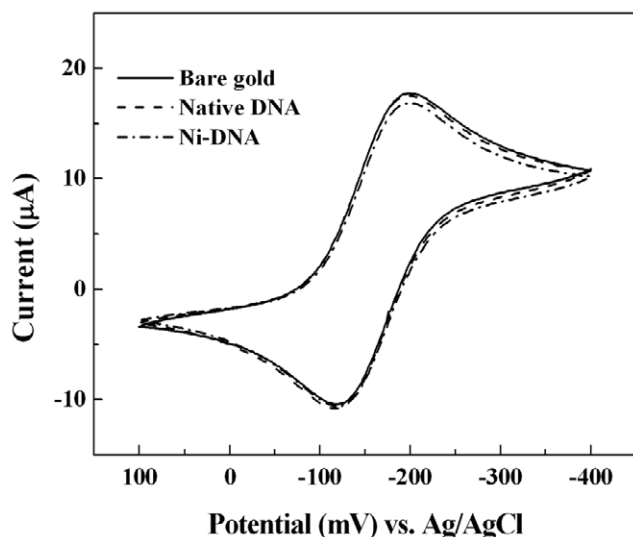


**Figure 5.** Cyclic voltammeteries of the bare gold electrode and modified gold electrodes in the  $[\text{Ru}(\text{NH}_3)_6]^{3+}$  system.

In order to reveal the mass transfer effect of the SAM-modified electrode, which might be affected by the intrinsic property of the SAM, an additional experiment with the positively charged redox probe  $[\text{Ru}(\text{NH}_3)_6]^{3+}$  is performed in the electrochemical measurement. It is interesting to note that remarkable, symmetric and almost identical redox peaks of  $[\text{Ru}(\text{NH}_3)_6]^{3+}$  can be observed for all electrodes in the CV measurements (figure 5). These results show that the charge of the backbone molecules of the SAM is negative and that there is an outflow of positive charge of the redox probe,  $[\text{Ru}(\text{NH}_3)_6]^{3+}$ , which penetrates the SAM and moves directly towards the gold electrode [21, 22, 24].

The charge transfer through the SAM structure may be affected by the charge type of redox probe and the charge type of SAM molecules. Therefore, the charge type of SAM molecules, DNA molecules in this study, can be revealed by negative and positive redox probe tests. Similar observations have been reported by Ruach-Nir's study [27] in the case of negatively charged silica layers on an Au electrode. The negative charge of the silica layer blocked the access of negatively charged  $[\text{Fe}(\text{CN})_6]^{-3}$  ions completely. However, the positively charged  $[\text{Ru}(\text{NH}_3)_6]^{3+}$  ions had free access through the non-porous silica layer and directly react with gold surface. Therefore, we may conclude that it may contain some nanoholes which may enhance the signal of reduction/'non-'reduction current of the positively charged  $[\text{Ru}(\text{NH}_3)_6]^{3+}$  ions. However, the SAM structure is not so patchy that the negative redox probe cannot penetrate freely. These experiments also show that the SAM structures of both electrodes comprise DNA molecules.

### 3.3. AC impedance analysis of native DNA and Ni-DNA

The SAM of DNA between the electrolyte of the solution and electrode plays a role similar to a capacitor. After charging the capacitor at low-frequency alternating current (AC), the charge transportation pathway may go through  $\pi-\pi$

interactions between the stacked base pairs in DNA. Therefore, the equivalent impedance of these SAMs may be revealed by applying different AC frequencies, followed by a simulation using appropriate electron circuits (Randles circuit) [14]. The simulation may also reveal a possible molecular mechanism of electron transport through the molecules of the SAM. The AC impedance analysis (figure 6(a)) indicates that the curve of the bare gold electrode is an almost straight line for all frequency ranges (only a very small semicircle at high frequencies, which is caused by an electrical double layer at the interface between the gold surface and the electrolyte). This impedance characteristic indicates that the electrochemical process results in a diffusion-limited control of the bare gold electrode [22]. However, in the case of the native DNA-modified gold electrode (figure 6(b)), a large-diameter semicircle is observed from a high-frequency to a low-frequency (100 kHz to 0.25 Hz) AC field, which indicates that the impedance of the DNA SAM is controlled by the rate of charge transfer [17, 22]. This large-diameter semicircle of the native DNA SAM (figure 6(b)) is transformed into a smaller semicircle of the Ni-DNA SAM (figure 6(c)), which indicates that the impedance of Ni-DNA is lower than that of native DNA. Namely, the charge transfer between the redox probe and the Ni-DNA modified electrode is faster than that between the redox probe and the native DNA-modified electrode.

Detailed parameters can be simulated by equivalent circuits as follows. The equivalent circuit simulation shows that the interface between the gold surface and the adjacent electrolyte might form an electrical double layer (EDL) (figure 1(a)); the EDL is similar to a simple electrical circuit composed of resistors and a capacitor (figure 1(a)) [14]. The impedance equations ( $R_z$ ) of electrical circuit 1 can be expressed as follows:

$$R_z = R_s + \frac{1}{Q + \frac{1}{R_{ct} + W_0}} \quad (1)$$

$$Q = Q_{dl} \omega^n \left( \cos \frac{n\pi}{2} + j \sin \frac{n\pi}{2} \right) \quad (2)$$

$$W = \frac{1}{W_0} (2\omega)^{-1/2} (1 - j) \quad (3)$$

where the  $R_s$  is the solution resistance and  $R_{ct}$  is the charge transfer resistance between the electrode and the electrolyte.  $Q_{dl}$  is a constant phase element (CPE) that represents the behaviour of a non-ideal capacitor in an electrical double layer system.  $W_0$  (Warburg impedance) is the diffusion impedance. In equation (2),  $\omega$  is the angular frequency; for  $n = 0$ ,  $Q$  is the resistance with  $R = Q_{dl}^{-1}$ , and for  $n = 1$ ,  $Q$  is the capacitance with  $C = Q_{dl}$ . Further, electrical circuit 2 (figure 1(b)) might reveal the conductive behaviour of the DNA-modified gold electrode. The DNA SAM structure on the gold surface can be considered as a polymer-coated metal surface. A report by Janek *et al* reveals that the Randles circuit should be modified further to describe the electron transfer behaviour of the SAM of a conjugated  $\pi$  system [14]. The electrical properties of this coating film (DNA SAM) can be described as a resistor ( $R$ ), and the equivalent circuit is shown

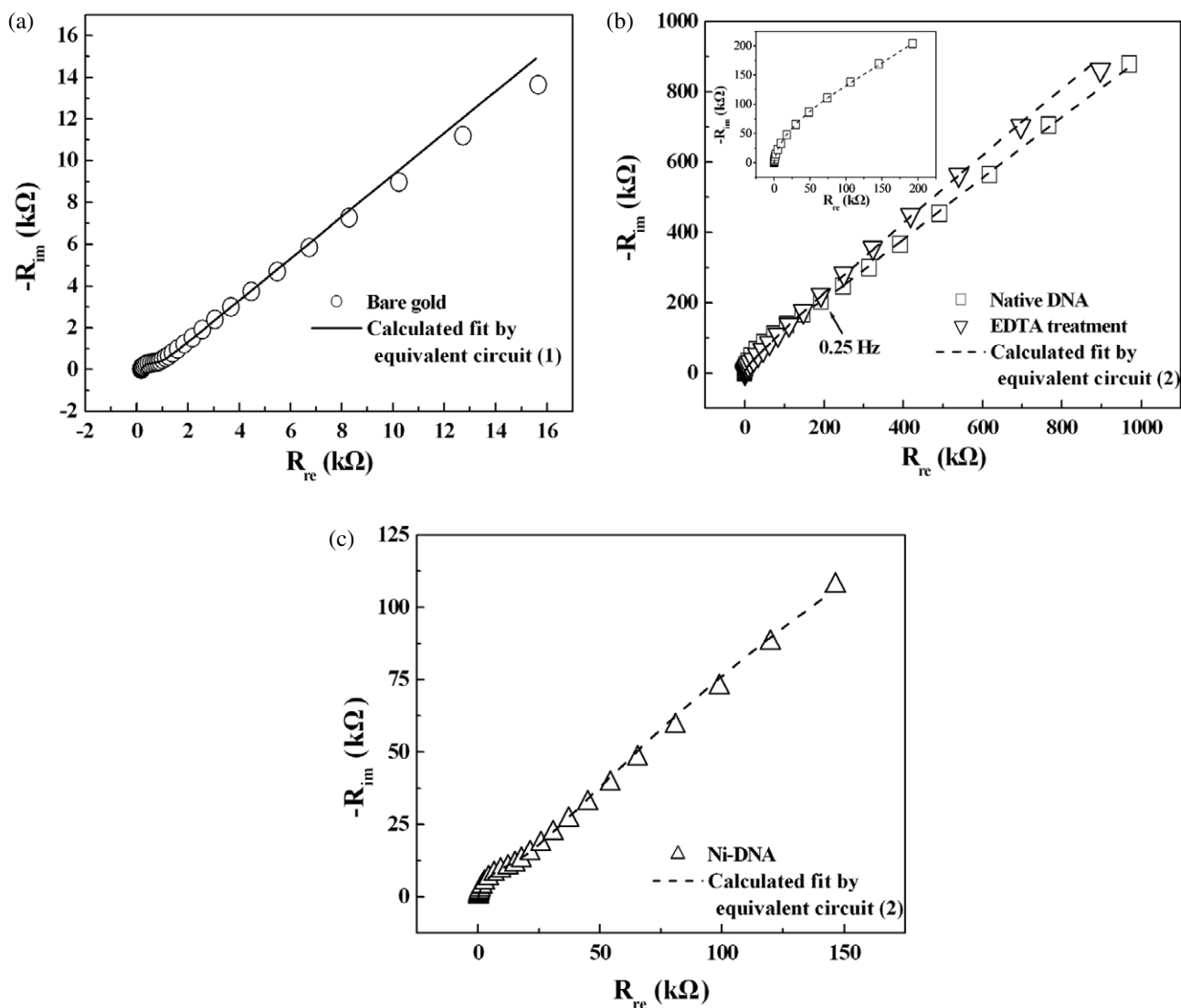


**Figure 6.** AC impedances of the bare gold electrode and modified gold electrodes. (a) Bare gold electrode (circle symbol). (b) Native DNA-modified gold electrode (square symbol) and Ni-DNA modified gold electrode treated with 25 mM EDTA (down-triangle symbol). (c) Ni-DNA modified gold electrode (up-triangle symbol). The straight line indicates the fitting result of a bare gold electrode by equivalent circuit 1 and the dashed lines show the fitting results of modified gold electrodes by equivalent circuit 2.

in figure 1(b). The impedance equations ( $R_z$ ) of electrical circuit 2 can be expressed as follows:

$$R_z = R_s + \frac{1}{Q + \frac{1}{R} + \frac{1}{R_{ct} + W_0}} \quad (4)$$

$$Q = Q_f \omega^n \left( \cos \frac{n\pi}{2} + j \sin \frac{n\pi}{2} \right). \quad (5)$$

In equations (3) and (4) the  $R_{ct}$  is the charge transfer resistance between the electrode and electrolyte, and the  $W_0$  (Warburg impedance) is the diffusion impedance. These two parameters in equivalent circuit 2 had been defined as the impedance caused by the DNA SAM impeding the redox probe directly diffusing to the gold surface and reacting with gold. In other words, the 'leakage resistance' shall be included in these two parameters of DNA SAM. This leakage resistance may be caused by the holes in the SAM, where  $R$  is the resistance

through DNA and  $Q_f$  is the DNA film capacitance. These two electrical circuits can effectively simulate the AC impedance data, as shown in figure 6, and the simulation results are listed in table 1. From these results, we find that both the native DNA and Ni-DNA film are non-ideal capacitors ( $n = 0.8-0.9$ ), and the resistance ( $R$ ) through native DNA is approximately 20-fold higher than that through Ni-DNA (table 1). Namely, Ni-DNA has better conductivity than native DNA, which is consistent with the results of the SPM measurement shown in figure 3.

#### 3.4. Base pair stacking distortion of DNA reduces the conductivity of Ni-DNA

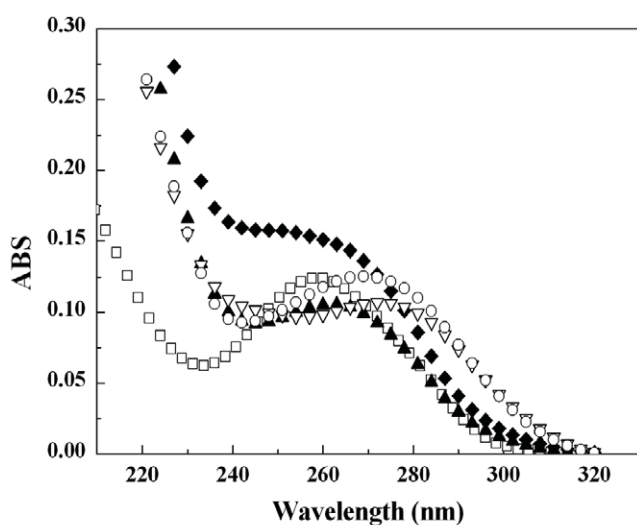
The UV absorption peak of DNA represents the energy absorption for electron excitation from the  $\pi$  state (HOMO) to the  $\pi^*$  state (LUMO) in the conjugated double-bond

**Table 1.** Impedance values for bare gold electrode and modified gold electrodes (the redox probe is  $K_3[Fe(CN)_6]$ ).

	$R_s$ ( $\Omega$ )	$Q_{dl}$ (F)	$Q_f$ (F)	$n$	$R$ ( $\Omega$ )	$R_{ct}$ ( $\Omega$ )	$W_0$ ( $\Omega s^{-1/2}$ )
Bare gold	175.9	$1.94 \times 10^{-6}$		0.86		595.6	$6.66 \times 10^3$
Native DNA	162.3		$7.98 \times 10^{-7}$	0.95	$2.04 \times 10^7$	$1.28 \times 10^5$	$3.37 \times 10^5$
Ni-DNA	175.3		$1.76 \times 10^{-6}$	0.89	$9.85 \times 10^5$	$1.52 \times 10^4$	$4.99 \times 10^4$
EDTA treatment	182.8		$6.43 \times 10^{-7}$	0.93	$3.86 \times 10^7$	$2.74 \times 10^5$	$3.28 \times 10^5$

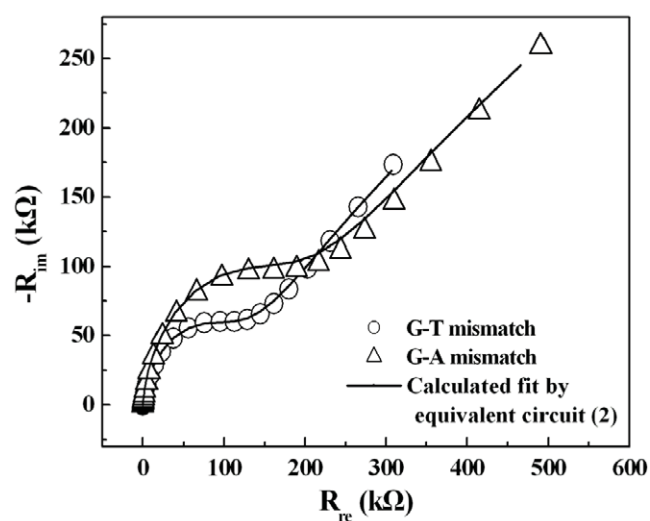
**Table 2.** Impedance values for mismatched DNA SAM-modified gold electrodes (the redox probe is  $K_3[Fe(CN)_6]$ ).

	$R_s$ ( $\Omega$ )	$Q_f$ (F)	$n$	$R$ ( $\Omega$ )	$R_{ct}$ ( $\Omega$ )	$W_0$ ( $\Omega s^{-1/2}$ )
G–A mismatch	192.2	$8.70 \times 10^{-7}$	0.91	$2.27 \times 10^6$	$1.91 \times 10^5$	$1.33 \times 10^5$
G–T mismatch	192.4	$1.05 \times 10^{-6}$	0.89	$1.87 \times 10^6$	$1.21 \times 10^5$	$8.35 \times 10^4$

**Figure 7.** Ultraviolet–visible spectroscopy of the native DNA and Ni-modified DNA at different pH values, where  $\square$  denotes native DNA,  $\blacktriangle$ ,  $\blacklozenge$ ,  $\nabla$ ,  $\circ$  denotes Ni-DNA at pH 8.0, 8.5, 8.8 and 9.0, respectively.

system of purine and pyrimidine bases. Since Ni-DNA has higher conductivity than native DNA and the  $Ni^{2+}$  ions are intercalated in the base pairs of DNA, a clear UV absorption band shift is expected to be observed in Ni-DNA. Therefore, a redshift from 260 to 275 nm of the UV absorption band of Ni-DNA is observed when the pH increases to 8.8 and 9.0 (figure 7). This redshift may be caused by the bandgap reduction between the HOMO and the LUMO of Ni-DNA. Namely, for Ni-DNA, an electron is excited from the  $\pi$  state to the  $\pi^*$  state by less energy. This energy reduction makes the prospect of reducing the resistance ( $R$ ) through DNA and achieving good conduction properties more plausible.

Further, the AC impedance analysis of a single G–A and G–T base pair mismatch of Ni-DNA, which causes base pair stacking distortion and hydrogen bonds changing from 3 to 2, reveals that the noticeable difference AC impedance spectra and the equivalent resistance increases to 2.27 M $\Omega$  or G–A mismatch and 1.87 M $\Omega$  or G–T mismatch (figure 8 and table 2), which are both higher than that of Ni-DNA (the resistance of Ni-DNA is approximately 0.98 M $\Omega$ ). The concerted data reveal that the charge transferred through the

**Figure 8.** AC impedance of Ni-DNA with single G–A mismatch ( $\Delta$ ) and Ni-DNA with single G–T mismatch in the sequence ( $\circ$ ).

DNA might be affected by the interaction of the  $\pi$ – $\pi$  stacking and the hydrogen bonds of DNA base pairs. Therefore, metals chelating in the base pairs of DNA provide additional holes to the base pairs and facilitate the charge transport through the highly ordered one-dimensional nanowire. Namely, the charge transport might be caused by the electron hopping between the base pairs of Ni-DNA and this is consistent with the suggestion by Eley and Spivey [2].

#### 4. Conclusions

From the SPM, CV and AC impedance analyses, we have found that Ni-DNA possesses better conductivity than native DNA. The native DNA effectively self-assembles on the gold surface, and the charge transfer between the redox couple and the modified electrode is restrained because of the higher resistance ( $R$ ) through the native DNA and negatively charged phosphate backbone of DNA. When native DNA is converted into Ni-DNA, the resistance is decreased by approximately 20-fold magnitude. Although the  $Ni^{2+}$  insertion might cause the conformational changes of DNA [7, 9], the new conformation retains duplex formation and the divalent metal ions would replace the imino protons of G and T in the helix and form

a stable tetrahedral geometry [7, 9]. Meanwhile, the results of DNA mismatch experiments have ruled out the structure influences from unexpected structure formation of DNA and the charge transport through the base pairs is causing by the electron-hole effect between base pairs of DNA. Further, the UV spectroscopy analysis also reveals that the Ni<sup>2+</sup> doping decreases the energy gap between the HOMO and the LUMO of DNA. The charge transport might be caused by the electron hopping through the  $\pi$ - $\pi$  interactions between the base pairs of Ni-DNA.

## Acknowledgments

The project is supported in part by NSC grant 96-2112-M-009-035 and ATU-MOE project, Taiwan, ROC. Technical support from the National Nano Device Laboratories of NSC, ROC and the Nano Facility Center of National Chiao Tung University are acknowledged.

## References

- [1] Watson J D and Crick F H C 1953 Molecular structure of nucleic acids; a structure for deoxyribose nucleic acid *Nature* **171** 737–8
- [2] Eley D D and Spivey D I 1962 Semiconductivity of organic substances, part 9. Nucleic acid in the dry state *Trans. Faraday Soc.* **58** 411–5
- [3] Hall D B, Holmlin R E and Barton J K 1996 Oxidative DNA damage through long range electron transfer *Nature* **382** 731–5
- [4] De Pablo P J et al 2000 Absence of dc-Conductivity in  $\lambda$ -DNA *Phys. Rev. Lett.* **85** 4992–5
- [5] Wilson E K 1997 DNA: insulator or wire&quest: flurry of new research, heated debate focuses on biomolecule *C&EN* **24** 33–9
- [6] Porath D, Bezryadin A, de Vries S and Dekker C 2000 Direct measurement of electrical transport through DNA molecules *Nature* **403** 635–8
- [7] Lee J S, Latimer L J P and Reid R S 1993 A cooperative conformational change in duplex DNA induced by Zn<sup>2+</sup> and other divalent metal ions *Biochem. Cell Biol.* **71** 162–8
- [8] Simone S A, Jose M S, Luis S and Felix Z 2006 Geometry and electronic structure of M-DNA (M = Zn<sup>2+</sup>, Co<sup>2+</sup>, and Fe<sup>2+</sup>) *Phys. Rev. B* **73** 205112
- [9] Aich P, Labiuk S L, Tari L W, Delbaere L J T, Roesler W J, Falk K J, Steer R P and Lee J S 1999 M-DNA: a complex between divalent metal ions and DNA which behaves as a molecular wire *J. Mol. Biol.* **294** 477–85
- [10] Wood D O, Dinsmore M J, Bare G A and Lee J S 2002 M-DNA is stabilised in GC tracts or by incorporation of 5-fluorouracil *Nucleic Acids Res.* **30** 2244–50
- [11] Wettig S D, Li C Z, Long Y T, Kraatz H B and Lee J S 2003 M-DNA: a self-assembling molecular wire for nanoelectronics and biosensing *Anal. Sci.* **19** 23–6
- [12] Lee T Y and Shim Y B 2001 Direct DNA hybridization detection based on the oligonucleotide-functionalized conductive *Anal. Chem.* **73** 5629–32
- [13] Drummond T G, Hill M G and Barton J K 2003 Electrochemical DNA sensors *Nat. Biotechnol.* **21** 1192–9
- [14] Janek R P, Fawcett W R and Ulman A 1998 Impedance spectroscopy of self-assembled on Au(111): sodium ferrocyanide charge transfer at modified electrodes *Langmuir* **14** 3011–8
- [15] Miller C, Cuendet P and Gratzel M 1991 Adsorbed  $\omega$ -hydroxy thiol monolayers on gold electrodes: evidence for electron tunneling to redox species in solution *J. Phys. Chem.* **95** 877–86
- [16] Steichen M, Decrem Y, Godfroid E and Buess-Herman C 2007 Electrochemical DNA hybridization detection using peptide nucleic acids and Ru(NH<sub>3</sub>)<sub>6</sub><sup>3+</sup> on gold electrodes *Biosens. Bioelectron.* **22** 2237–43
- [17] Ito T, Hosokaea K and Maeda M 2007 Detection of single-base mismatch at distal end of DNA duplex by electrochemical impedance spectroscopy *Biosens. Bioelectron.* **22** 1816–9
- [18] Finklea H O, Snider D A and Fedyk J 1993 Characterization of octadecanethiol-coated gold electrodes as microarray electrodes by cyclic voltammetry and ac impedance spectroscopy *Langmuir* **9** 3660–7
- [19] Chidsey C E D 1991 Free energy and temperature dependence of electron transfer at the metal-electrolyte interface *Science* **251** 919–22
- [20] Randles J E B 1947 Kinetics of rapid electrode reactions *Discuss. Faraday Soc.* **1** 11–9
- [21] Li C Z, Long Y T, Kraatz H B and Lee J S 2003 Electrochemical investigations of M-DNA self-assembled monolayers on gold electrodes *J. Phys. Chem. B* **107** 2291–6
- [22] Long Y T, Li C Z, Kraatz H B and Lee J S 2003 AC impedance spectroscopy of native DNA and M-DNA *Biophys. J.* **84** 3218–25
- [23] Kelley S O, Boon E M, Barton J K, Jackson N M and Hill M G 1999 Single-base mismatch detection based on charge transduction through DNA *Nucleic Acids Res.* **27** 4830–7
- [24] Chi Q, Zhang J and Ulstrup J 2006 Surface microscopic structure and electrochemical rectification of a branched alkanethiol self-assembled monolayer *J. Phys. Chem. B* **110** 1102–6
- [25] Peterson A W, Heaton R J and Georgiadis R M 2001 The effect on surface probe density on DNA hybridization *Nucleic Acids Res.* **29** 5163–8
- [26] Moreno-Herrero F, Herrero P, Moreno F, Colchero J, Gomez-Navarro C, Gomez-Herrero J and Baró A M 2003 Topographic characterization and electrostatic response of M-DNA studied by atomic force microscopy *Nanotechnology* **14** 128–33
- [27] Ruach-Nir I A, Bendikov T, Barkay Z, Vaskevich A and Rubinstein I 2007 Silica-stabilized gold island films for transmission localized surface plasmon sensing *J. Am. Chem. Soc.* **129** 84–92

## Room temperature negative differential resistance in DNA-based molecular devices

Peng-Chung Jangjian,<sup>1</sup> Tzeng-Feng Liu,<sup>1</sup> Mei-Yi Li,<sup>1,a)</sup> Ming-Shih Tsai,<sup>2</sup> and Chia-Ching Chang<sup>3,b)</sup>

<sup>1</sup>Department of Material Science and Engineering, National Chiao Tung University, Hsinchu 30050, Taiwan

<sup>2</sup>Cabot Microelectronic, Chupei, Hsinchu Hsien 302, Taiwan

<sup>3</sup>Department of Biological Science and Technology, National Chiao Tung University, Hsinchu 30050, Taiwan and Institute of Physics, Academia Sinica, Taipei 11529, Taiwan

(Received 13 November 2008; accepted 5 January 2009; published online 26 January 2009)

A molecular device fabricated from metallic deoxyribonucleic acid (M-DNA) exhibits a negative differential resistance (NDR) behavior. When two gold electrodes were connected by Ni<sup>2+</sup>-chelated DNA, which was converted from  $\lambda$ -DNA, not only was the conductivity of DNA improved, but a NDR device was formed as a full cyclic voltage sweep was applied to measure its current versus voltage characteristics at room temperature and in an ambient environment. Such electronic characteristics of a M-DNA device may have been caused by the redox reactions of Ni ions. This finding provides a simple way to construct electrical nanodevices from biological molecules.

© 2009 American Institute of Physics. [DOI: 10.1063/1.3074502]

Negative differential resistance (NDR) refers to the electrical behavior of some semiconductors in which the electric current decreases with increasing applied voltage over a particular range. NDR is commonly employed in the fields of low-power memory or logic devices, such as Esaki diodes<sup>1</sup> and resonant tunneling diodes.<sup>2</sup> Recently, NDR characteristic have been observed not only in semiconductors but also in organic molecules.<sup>3–5</sup> Various mechanisms of NDR have been proposed for various molecular device systems. They include charging (reduction),<sup>3</sup> redox reaction,<sup>5</sup> structural change,<sup>6</sup> chemical reaction,<sup>7</sup> and the association-dissociation processes<sup>8</sup> of molecules. For example, molecules that contain a nitroamine redox center (2'-amino-4-ethynylphenyl-4'-ethynylphenyl-5'-nitro-1-benzenethiol) that is sandwiched between two metal electrodes exhibit NDR due to a two-step reduction process.<sup>3</sup> Metalloproteins (ferritin) that are embedded in the gap between two single-walled carbon nanotubes yield reproducible NDR peaks during cyclic voltage sweep measurements.<sup>5</sup> This NDR behavior originates in the redox reaction of the transition metal ions in ferritin. To exploit these molecules with NDR properties in nanodevices, detailed knowledge of the molecular electronic characteristics and reliable fabrication processes are both required.

The fact that aromatic heterocycles of DNAs are highly organized has been recently utilized in nanodevices.<sup>9</sup> In 1962, double-stranded DNA with  $\pi$ -electron cores of well stacked bases was suggested to be a pathway for charge transportation.<sup>10</sup> However, discrepancies exist among the measured values of DNA conductivity because of differences in the measuring methods, conditions, or DNA sequences.<sup>11,12</sup> Although the intrinsic conductivity of DNA has not been well characterized, metal-doped DNA, metallic DNA (M-DNA), has been demonstrated to behave as a conductive nanowire.<sup>13</sup> Lee and co-workers discovered M-DNA

formed by the substitution of divalent metal ions (Zn<sup>2+</sup>, Ni<sup>2+</sup>, and Co<sup>2+</sup>) with the imino protons of *G* and *T* of DNA, forming a stable tetrahedral geometry at pH > 8.5. M-DNAs also have better conductivity than the corresponding native forms.<sup>14–16</sup>

In this study, NDR was observed in a M-DNA-based device. Simple lateral metal-molecule-metal (M-M-M) structures were fabricated after pairs of gold electrodes were formed with nanometer gaps on a silica substrate. Ni-DNA, which is derived from  $\lambda$ -DNA, was adopted to connect gold electrodes and act as the active molecule in molecular devices [Fig. 1(a)].

$\lambda$ -DNA was purchased from TOYOBO CO., LTD. (Osaka, Japan). It is comprised of 23 130 base pairs (about

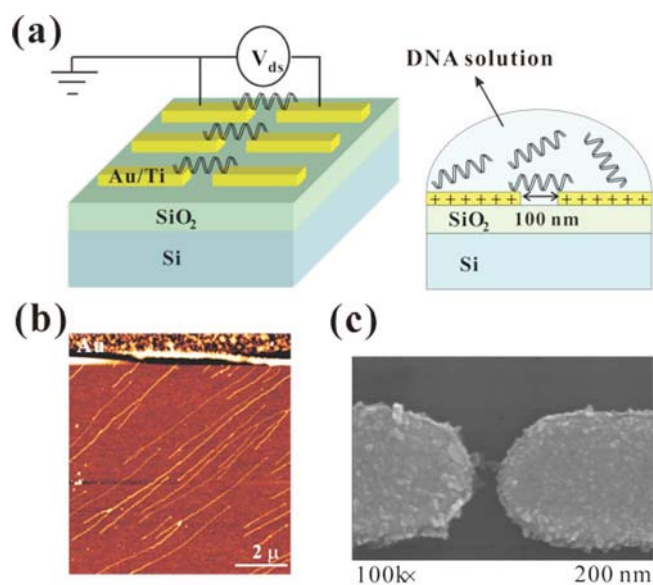


FIG. 1. (Color online) (a) Schematics of the DNA based NDR device (left) and electrostatic trapping (right). (b) AFM image of DNA molecules absorbed on silica oxide after electrostatic trapping process. (c) SEM image of DNA molecules, which are converted into silver wires and bridge on the gap between two gold electrodes.

<sup>a)</sup>Also at National Nano Device Laboratories, Hsinchu 30072, Taiwan.

<sup>b)</sup>Author to whom correspondence should be addressed. Department of Biological Science and Technology, National Chiao Tung University, Hsinchu 30050, Taiwan, R.O.C. Tel.: 886-3-5712121-56958. FAX: 886-3-5733259. Electronic mail: ccchang01@faculty.nctu.edu.tw.

7.9  $\mu\text{m}$ ), with randomly distributed A, G, C, and T bases.  $\lambda$ -DNA was diluted in 10 mM tris-HCl buffer ( $\text{pH}=9.0$ ) to yield a final concentration of 12.5 ng/ $\mu\text{l}$ . Ni-DNA was then converted from the diluted  $\lambda$ -DNA by adding 10 mM tris-HCl and 2.5 mM  $\text{NiCl}_2$  at  $\text{pH}=9.0$  and incubation for at least 8 h.

Standard e-beam lithography and lift-off processes were employed to pattern the nanometer scale electrodes.<sup>17</sup> First, 120 nm  $\text{SiO}_2$  was grown on Si wafers by low-pressure chemical vapor deposition (LB45 Furnace system, ASM, Biltoven, Netherlands). The nanoscale electrode pattern was then transferred to  $\text{SiO}_2$  by evaporating 5-nm-thick titanium (as an adhesion layer) and 50-nm-thick gold using an e-gun evaporator (EBX-8C, ULVAC, Kanagawa, Japan). The resulting electrode gap was 100 nm ( $\pm 10$  nm,  $n=5$ ). Electrical contacts between DNA and the gold electrodes were formed by electrostatic trapping.<sup>18</sup> Both  $\lambda$ -DNA and Ni-DNA solutions were dialyzed against with 2 L double-distilled water for 8 h at 4  $^\circ\text{C}$ , twice, to remove the salt and the excess Ni ions beforehand. Then a drop, around 5  $\mu\text{l}$ , of  $\lambda$ -DNA (or M-DNA) solution was placed on the gap between the electrodes. A voltage of up to 1 V was applied to the electrodes to trap the DNA. (The mean electric field was approximately  $7.85 \times 10^2$  V/m, parallel to the substrate.) After 20 min of incubation, the samples were dried slowly in nitrogen gas and their electronic characteristics were measured using a precision semiconductor parameter analyzer (HP 4156A, AVALON CA, USA).

After the electrostatic trapping process,  $\lambda$ -DNAs were observed under an atomic force microscope (AFM) (NanoWizard II, JPK, Berlin, Germany) in tapping mode. The DNA molecules were absorbed on the silicon oxide, stretched, and oriented toward the electrode [Fig. 1(b)]. A similar phenomenon was also observed in the case of Ni-DNA. According to our previous study,<sup>16</sup> the Ni-DNA molecules remained negatively charged on the backbone as well as native  $\lambda$ -DNA. These negative charges on the DNA molecules are attracted by the positive charges of the electrodes. As expected, more DNA molecules were trapped and some bridged the two electrodes. To confirm that  $\lambda$ -DNAs or Ni-DNAs bridged the two electrodes by electrostatic attraction, the DNA molecules were converted into silver wires by ion exchange,<sup>19</sup> and the SEM image [Fig. 1(c)] revealed the silver nanowire between the 100 nm spaced gold electrodes. Meanwhile, many of the silver nanoparticles were observed on the surfaces of the electrodes. DNA molecules were trapped between these surfaces, bridging the gap between them.

Electrical tests demonstrated that Ni-DNA molecular devices are very stable and their NDR characteristics are reproducible at room temperature in an ambient environment [Fig. 2(a)]. When the voltage applied to M-M-M devices constructed from both  $\lambda$ -DNA and Ni-DNA was swept from  $-10$  to 10 V,  $\lambda$ -DNA [inset in Fig. 2(a)] exhibited a nonlinear  $I$ - $V$  curve with a plateau at low voltage. This semiconductorlike energy gap, which was about 3 eV, has also been reported upon by Porath *et al.*,<sup>11</sup> who measured directly the electrical transport through individual short DNA molecules. This plateau indicates that a contact barrier is present between the junction of  $\lambda$ -DNA and the gold electrodes. When the applied bias voltage reaches a threshold, electrons (or holes) can be injected from the electrode to  $\lambda$ -DNA by tunneling through the contact barrier, and passing through the

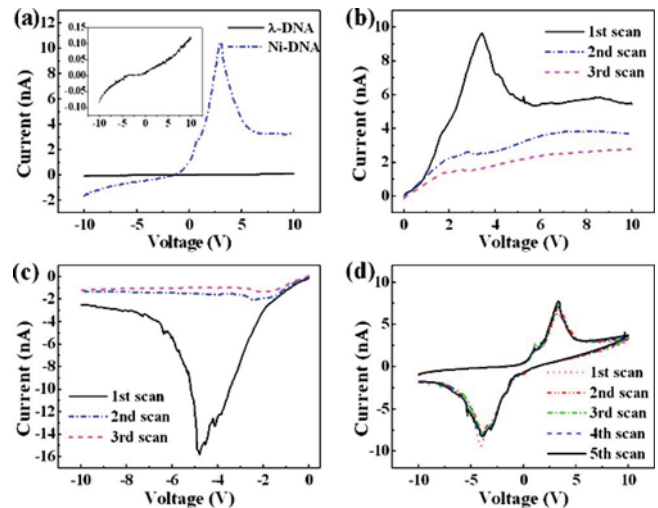


FIG. 2. (Color online) (a) Current-voltage ( $I$ - $V$ ) characteristics of  $\lambda$ -DNA and Ni-DNA, the sweep range from  $-10$  to 10 V. (b)  $I$ - $V$  characteristics of Ni-DNA with positive sweep (0–10 V). (c)  $I$ - $V$  characteristics of Ni-DNA with negative sweep (0–10 V). (d)  $I$ - $V$  characteristics of Ni-DNA with repetitive full cyclic sweeps ( $-10$  V  $\rightarrow$  10 V  $\rightarrow$   $-10$  V). The entire scan rate is 50 mV/s.

DNA molecule.<sup>11</sup> After the  $\lambda$ -DNA was replaced with Ni-DNA, the conductivity of the Ni-DNA device exceeded that of the native DNA device, such that the 3 eV conducting gap of the native DNA device disappeared [Fig. 2(a)]. The inserted metal ions may thus support the formation of a  $d$  band that is aligned with the Fermi level of the electrode.<sup>14</sup> Therefore, electrons (or holes) can be injected without a voltage threshold. The result is comparable with those of previous studies.<sup>14</sup> As well as the improvement in the conductivity of native DNA by Ni ions doped, an interesting NDR behavior was observed. Figure 2(b) plots the  $I$ - $V$  curves of Ni-DNA for successive positive voltage sweeps (0–10 V) at room temperature. An NDR peak was positioned at around 3.50 V with a peak-to-valley ratio (PVR) of 1.78 for the first scan, and the peak disappeared during the subsequent sweep over the same voltage range in the same direction. A negative NDR peak was also observed at about  $-4.70$  V with a PVR of 6.21 when the voltage on the device was swept from 0 to  $-10$  V [Fig. 2(c)]. The negative NDR peak also disappeared upon successive negative sweeps. After the negative NDR peak had been observed, a positive NDR peak reappeared in a positive scan, confirming that both of the NDR peaks were observed when a full cyclic voltage sweep ( $-10$  V  $\rightarrow$  10 V  $\rightarrow$   $-10$  V) was applied [Fig. 2(d)]. Besides the reproducible NDR behavior exhibited by the  $I$ - $V$  curves, hysteresis was observed, possibly associated charge trapping.<sup>20</sup> These reproducible  $I$ - $V$  curves are similar to the reversible redox behavior revealed by the cyclic voltammetry in electrochemical analyses.<sup>16</sup> The DNA-based devices can be reasonably suggested to act as a solid state electrochemical system. Two gold electrodes are the anode and cathode. The phosphate backbone of  $\lambda$ -DNA is the dielectric layer and the Ni ions that dope the  $\lambda$ -DNA act as the electroprobes. The Ni ions undergo redox reactions when the applied voltage approaches the redox potential in the cyclic voltage sweep process. The positive NDR peak corresponds to the oxidation peak of the Ni ions and the negative NDR peak corresponds to their reduction.<sup>5</sup> Namely, the mechanism of NDR in Ni-DNA involves the redox reactions of the Ni ions (oxidation

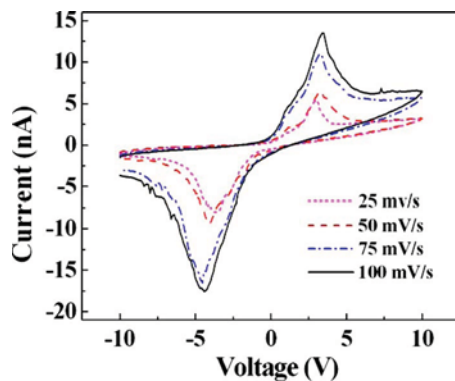


FIG. 3. (Color online)  $I$ - $V$  characteristics of Ni-DNA with full cyclic sweep at a different scan rate.

of  $\text{Ni}^{2+}$  and reduction in  $\text{Ni}^{3+}$ ). Additionally, according to previous studies, Ni-DNA is a decent charge conductor. These characteristics are responsible for the reproducible and stable electrochemical redox reactions of Ni ions during the  $I$ - $V$  scan. Relatively stable  $I$ - $V$  curves were measured during the repetitive full cyclic sweep [Fig. 2(d)].

Significant increases in peak currents with the scan rate were observed (Fig. 3), similar to those of the classical redox reaction parameters in the electrochemical system. The rate of the redox reaction increases with the scan rate increases, increasing the peak current. The  $I$ - $V$  curves are asymmetric and the peak positions are slightly shifted, indicating that the redox reactions of Ni ions are quasireversible, because the charge transfer rate in Ni-DNA molecules varies during a cyclic voltage sweep. Previous investigations demonstrated that a DNA conformational change alters the conductivity.<sup>21</sup> Therefore, the conformational change in negatively charged Ni-DNA may occur during voltage sweep and contribute to the quasireversibility of the Ni redox reaction. Possible causes of such a DNA conformational change include applied bias, and the effect of the transformations between  $\text{Ni}^{2+}$  and  $\text{Ni}^{3+}$  (redox reaction) during the cyclic voltage scan.

In summary, a DNA-based NDR device is implemented using Ni-DNA molecules, which form a bridge between the two gold electrodes by electrostatic trapping. Not only does Ni-DNA serve as a pathway for transporting charges, but also the chelated Ni ions in Ni-DNA become redox centers. Reproducible and stable NDR behaviors are revealed by the  $I$ - $V$  characteristics at room temperature and atmospheric

pressure. This NDR behavior originates the active redox reactions of transition metal ions in DNA. Furthermore, the highest achievable PVR is about 6 in this work. Results of this study demonstrate the potential applications of the above aforementioned molecular devices.

We would like to thank Dr. Shin-Hua Tseng and Dr. Lou-Sing Kan's valuable suggestions and discussion. The project is supported in part by NSC Grant No. 97-2112-M-009-009-MY3 and the ATU-MOE project, Taiwan, R.O.C. Technical supports from the National Nano Device Laboratories of NSC and Nano Facility Center of National Chiao Tung University are acknowledged.

<sup>1</sup>L. Esaki, *Phys. Rev.* **109**, 603 (1958).

<sup>2</sup>T. C. L. G. Sollner, W. D. Goodhue, P. E. Tannenwald, C. D. Parker, and D. D. Peck, *Appl. Phys. Lett.* **43**, 588 (1983).

<sup>3</sup>J. Chen, M. A. Reed, A. M. Rawlett, and J. M. Tour, *Science* **286**, 1550 (1999).

<sup>4</sup>J. D. Le, Y. He, T. R. Hoye, C. C. Mead, and R. A. Kiehl, *Appl. Phys. Lett.* **83**, 5518 (2003).

<sup>5</sup>Q. Tang, H. K. Moon, Y. Lee, S. M. Yoon, H. J. Song, H. Lim, and H. C. Choi, *J. Am. Chem. Soc.* **129**, 11018 (2007).

<sup>6</sup>R. A. Kiehl, J. D. Le, P. Candra, R. C. Hoye, and T. R. Hoye, *Appl. Phys. Lett.* **88**, 172102 (2006).

<sup>7</sup>J. He and S. M. Lindsay, *J. Am. Chem. Soc.* **127**, 11932 (2005).

<sup>8</sup>J. L. Pitters and R. A. Wolkow, *Nano Lett.* **6**, 390 (2006).

<sup>9</sup>S. Nokhrin, M. Baru, and J. S. Lee, *Nanotechnology* **18**, 095205 (2007).

<sup>10</sup>D. D. Eley and D. I. Spivey, *Trans. Faraday Soc.* **58**, 411 (1962).

<sup>11</sup>D. Porath, A. Bezryadin, S. de Vries, and C. Dekker, *Nature (London)* **403**, 635 (2000).

<sup>12</sup>Y. Zhang, R. H. Austin, J. Kraeft, E. C. Cox, and N. P. Ong, *Phys. Rev. Lett.* **89**, 198102 (2002).

<sup>13</sup>P. Aich, S. L. Labiuk, L. W. Tari, L. J. T. Delbaere, W. J. Roesler, K. J. Falk, R. P. Steer, and J. S. Lee, *J. Mol. Biol.* **294**, 477 (1999).

<sup>14</sup>A. Rakitin, P. Aich, C. Papadopoulos, Y. Kobzar, A. S. Vedenev, J. S. Lee, and J. M. Xu, *Phys. Rev. Lett.* **86**, 3670 (2001).

<sup>15</sup>Y. T. Long, C. Z. Li, H. B. Kraatz, and J. S. Lee, *Biophys. J.* **84**, 3218 (2003).

<sup>16</sup>P. C. Jangjian, T. F. Liu, C. M. Tsai, M. S. Tsai, and C. C. Chang, *Nanotechnology* **19**, 355703 (2008).

<sup>17</sup>B. Hartzell, B. McCord, D. Asare, H. Chen, J. J. Heremans, and V. Soghomonian, *Appl. Phys. Lett.* **82**, 4800 (2003).

<sup>18</sup>K. H. Yoo, D. H. Ha, J. O. Lee, J. W. Park, J. Kim, J. J. Kim, H. Y. Lee, T. Kawai, and H. Y. Choi, *Phys. Rev. Lett.* **87**, 198102 (2001).

<sup>19</sup>E. Braun, Y. Eichen, U. Sivan, and G. Ben-Yoseph, *Nature (London)* **391**, 775 (1998).

<sup>20</sup>H. Choi, S. Choi, T. W. Kim, T. Lee, and H. Hwang, *Jpn. J. Appl. Phys., Part 2* **45**, L807 (2006).

<sup>21</sup>N. Kang, A. Erbe, and E. Scheer, *N. J. Phys.* **10**, 023030 (2008).

## Ni<sup>2+</sup>-Enhanced Charge Transport via $\pi$ - $\pi$ Stacking Corridor in Metallic DNA

Shin-Hua Tseng,<sup>†,‡,Δ</sup> Peng-Chung JangJian,<sup>§,Δ</sup> Chuan-Mei Tsai,<sup>¶</sup> Tsai-Mu Cheng,<sup>†</sup> Hsueh-Liang Chu,<sup>†</sup> Yu-Chuan Chang,<sup>†</sup> Wei-Hsien Chung,<sup>†</sup> and Chia-Ching Chang<sup>†||\*</sup>

<sup>†</sup>Department of Biological Science and Technology, <sup>‡</sup>Center for Biomedical and Biological Engineering, and <sup>§</sup>Department of Material Science and Engineering, National Chiao Tung University, Hsinchu, Taiwan Republic of China; <sup>¶</sup>National Nano Device Laboratories, Hsinchu, Taiwan, Republic of China; and <sup>||</sup>Institute of Physics, Academia Sinica, Taipei, Taiwan, Republic of China

**ABSTRACT** The mechanism underlying DNA charge transport is intriguing. However, poor conductivity of DNA makes it difficult to detect DNA charge transport. Metallic DNA (M-DNA) has better conducting properties than native DNA. Ni<sup>2+</sup> may chelate in DNA and thus enhance DNA conductivity. On the basis of this finding, it is possible to reveal the mechanisms underlying DNA charge transport. The conductivity of various Ni-DNA species such as single-stranded, full complement, or mismatched sequence molecules was systematically tested with ultraviolet absorption and electrical or chemical methods. The results showed that the conductivity of single-stranded Ni-DNA (Ni-ssDNA) was similar to that of a native DNA duplex. Moreover, the resistance of Ni-DNA with a single basepair mismatch was significantly higher than that of fully complementary Ni-DNA duplexes. The resistance also increased exponentially as the number of mismatched basepairs increased linearly after the tunneling current behavior predicted by the Simmons model. In conclusion, the charges in Ni<sup>2+</sup>-doped DNA are transported through the Ni<sup>2+</sup>-mediated  $\pi$ - $\pi$  stacking corridor. Furthermore, Ni-DNA acts as a conducting wire and exhibits a tunneling barrier when basepair mismatches occur. This property may be useful in detecting single basepair mismatches.

### INTRODUCTION

DNA is one of the most promising one-dimensional nanomaterials because of its adjustable length and self-assembly properties (1–3). It may be useful as a one-dimensional nanowire or nanodevice in electronic applications; however, it is of great interest to reveal the electrical conduction mechanism of DNA. Recently, both experimental and theoretical studies have demonstrated the conducting behavior of DNA molecules (3–13), yet the mechanism underlying electrical transport remains unclear (3,14). Furthermore, the conductivity of DNA increases dramatically when it is doped with metal ions to form metallic DNA (M-DNA) (10,15,16). As discovered by Lee et al. (17), DNA can be converted into M-DNA by incorporating divalent metal ions (Zn<sup>2+</sup>, Ni<sup>2+</sup>, and Co<sup>2+</sup>) into DNA basepairs at pH levels >8.5, whereby divalent metal ions replace imino protons of the bases in the DNA helix, forming a stable tetrahedral geometry (18). The higher conductance of M-DNA compared to native DNA has been demonstrated by fluorescence assays and electrochemical analyses (18–20). These findings suggest that metal ions in DNA play a vital role in facilitating electron transport. Because the conducting behavior of M-DNA is similar to that of a semiconductor with conducting barriers (10), it probably can be used in metal-containing nanowire systems.

Electrochemical analysis combined with a self-assembled monolayer (SAM), which develops on a conducting surface, has been widely used to directly monitor the conductivity of organic polymers (21–26). For example, the kinetics of charge transfer through a polymer can be analyzed by monitoring redox indicators in solutions (27,28). In addition, analysis of the electrochemical impedance spectrum (EIS) and the equivalent circuit of electrolyte-electrode interface have been widely used to reveal the interfacial interactions between SAM-modified electrodes (10,15,19,29,30). Because the conformation of the SAM structure and redox probes may also affect signal detection (31), suitable detection parameters for metal-doped DNA are required.

In this study, Ni-doped DNA (Ni-DNA) was used to study the conducting mechanism of M-DNA. The conductivity of DNA was enhanced by doping it with Ni<sup>2+</sup> to form Ni-DNA (17,18). The changes in the conductivity of Ni-DNA with various double or single strands and basepair mismatches were studied to investigate the mechanism underlying charge transport through Ni-DNA. The results indicated that charge transport within the Ni-DNA occurs through the Ni<sup>2+</sup>-mediated  $\pi$ - $\pi$  stacking corridor. Further, a single basepair mismatch of G-A or G-T can be detected.

### MATERIALS AND METHODS

#### Materials

All the oligodeoxyribonucleotides—containing 28 or 30 nucleotidyl units—used in this study were purchased from Bio Basic (Markham, Ontario, Canada). These nucleotides had various sequences and a thiol

Submitted July 19, 2010, and accepted for publication January 3, 2011.

<sup>Δ</sup>S.-H. Tseng and P.-C. JangJian contributed equally to this study.

Correspondence: ccchang01@faculty.nctu.edu.tw

Editor: David P. Millar.

© 2011 by the Biophysical Society  
0006-3495/11/02/1042/7 \$2.00

doi: 10.1016/j.bpj.2011.01.005



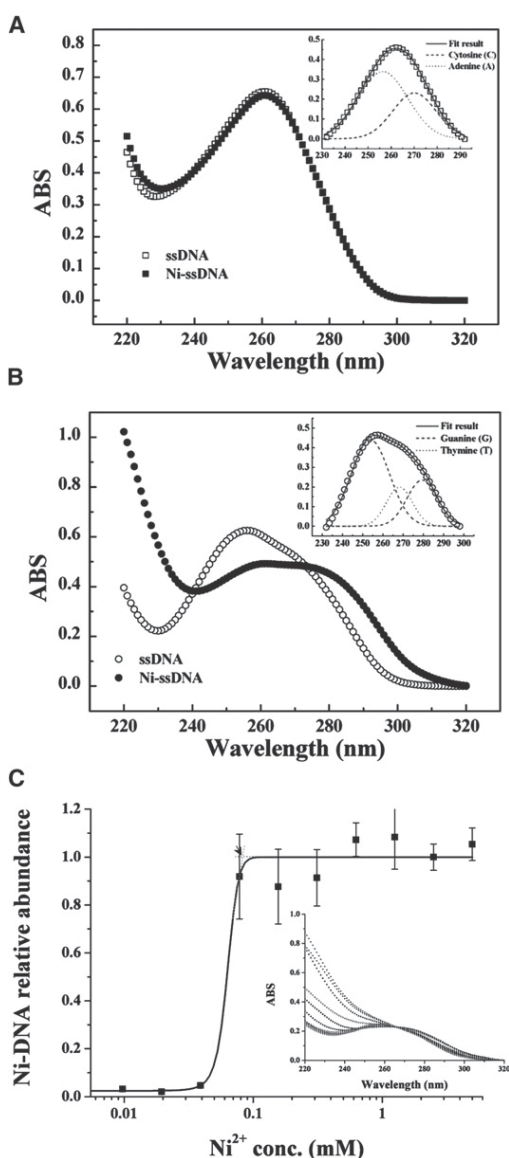


FIGURE 1 Ultraviolet-visible spectroscopic analysis of native ssDNA, Ni-ssDNA, and Ni-DNA. (A and B) Poly-AC (A) and Poly-TG (B) spectra, with open squares and circles denoting the ssDNA of poly-AC and poly-TG, respectively, and solid squares and circles denoting the Ni-ssDNA of poly-AC and poly-TG, respectively. (Insets) Absorption peaks. (C) Relative Ni ion abundance of Ni-DNA (P-fc) versus Ni ion concentration. (Insets) UV absorption peaks from the Ni ion concentration from 4.9  $\mu\text{M}$  to 5 mM (shift from left to right). The saturation line was normalized as 1. Gray dotted lines denote the trend lines for Ni ions bound to DNA; arrow denotes the point of saturation concentration of Ni ions.

at both termini of the DNA bound with one  $\text{Ni}^{2+}$ . Therefore, the 5 mM  $\text{NiCl}_2$  used in this study had reached the saturation concentration, and this approach made the  $\text{Ni}^{2+}$  chelation more efficient. The dissociation constant for Ni ions bound to DNA is  $\sim 6.36 \mu\text{M}$ . Results of the Ni ion chelation assay, which is well fitted with a Gaussian function and the flat saturation line indicating that the affinity of physical absorption of Ni ions to the DNA is weak, shall be ignored. There-

fore, washing the samples with excess buffer twice may be sufficient to remove physically absorbed  $\text{Ni}^{2+}$ .

### Well-stacked basepairs enhance the conductivity of Ni-DNA

According to Peterson's study, surface coverage of DNA molecules depends on the ionic strength of the solution and the time of immobilization (35). According to the previous study (35), maximum probe coverage is achieved ( $\sim 2.75 \times 10^{12}$  probe molecules/ $\text{cm}^2$ ) when the concentration of NaCl is 1 M and the immobilization duration is 2 h. In this study, we determined the DNA density of the SAM incubated in 0.1 M PBS buffer (containing 1 M NaCl) and immobilized on a gold electrode for 8 h. The changes in the resonance frequency ( $\Delta f$ ) determined by measuring the QCM and  $\sim -89.89 \pm 5.06 \text{ Hz}$  ( $n = 3$ ) and  $\sim 9.18 \times 10^{12} \pm 5.17 \times 10^{11}$  ( $n = 3$ ) molecules/ $\text{cm}^2$  according to the Sauerbrey equation (36):

$$\Delta f = \frac{-2f_0^2 \Delta m}{A(\mu_q \rho_q)^{1/2}}, \quad (1)$$

where  $\Delta f$  denotes the change in the resonance frequency (Hz),  $f_0$  is the basic resonance frequency,  $\Delta m$  is the mass of the molecules absorbed onto the gold electrode ( $\text{g}/\text{cm}^2$ ),  $A$  is the surface area of the electrode ( $\text{cm}^2$ ),  $\mu_q$  is the shear coefficient of the quartz crystal of QCM ( $\text{g}/\text{cm} \times \text{s}^2$ ), and  $\rho_q$  is the density of the quartz crystal.

After 8 h of incubation, the probe coverage was  $9.18 \times 10^{12}$  molecules/ $\text{cm}^2$ ; this is higher than that observed in a previous study ( $\sim 2.75 \times 10^{12}$  molecules/ $\text{cm}^2$ ) (35,37) when the incubation duration was 2 h. This indicates that a longer incubation time has higher coverage under the same conditions.

Based on the results of previous studies (8–10,20,34), it was believed that Ni-DNA would have better conductivity than the native form and that the doped metal ions play a vital role in facilitating electron transport. However, the metal ions not only may enter DNA basepairs but also may bind to the phosphate backbone by electrostatic attraction (38) during the metallization process. Thus, both types of  $\text{Ni}^{2+}$  doping may contribute to the improvement in DNA conductivity. We found that the CV curve of the bare gold electrode (Fig. 2 A, inset) included the reduction ( $E_{p,c}$ ) and oxidation ( $E_{p,a}$ ) peaks of  $(\text{Fe}(\text{CN})_6)^{-3/4}$  (reversible redox reaction) during potential sweeps, whereas the redox peaks disappeared after the gold surface was coated with native ssDNA (P-ss) or fully complementary DNA (P-fc) SAMs (Fig. 2, A and B). This indicated that the native-DNA SAMs acted as barriers against penetration of the redox probe (10,37) and that the gold surface was completely blocked by the native DNA. The native-DNA SAMs may provide an insulating layer to the gold electrode surface, and thus, less charge transfer would occur between the redox probe and the gold electrode.

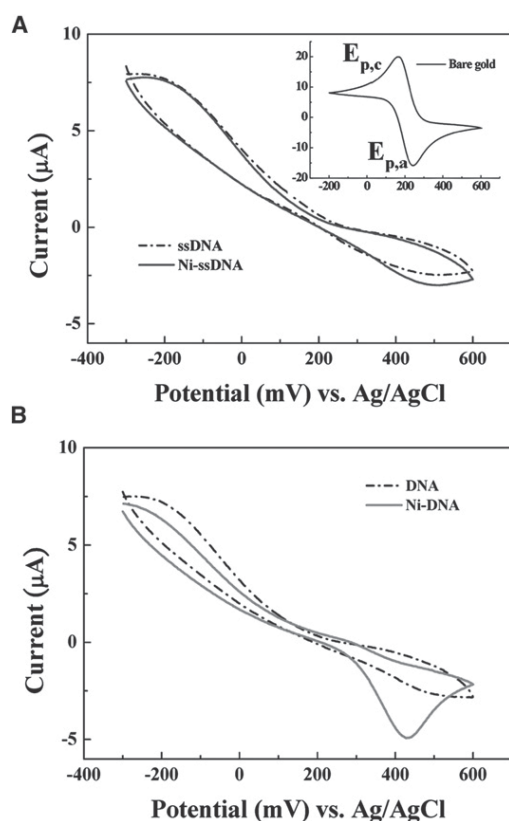


FIGURE 2 CVs of DNA SAMs modified with a gold electrode in the  $(\text{Fe}(\text{CN})_6)^{-3/-4}$  system. (A) ssDNA (dash-dotted line) and Ni-ssDNA (solid line). (B) Full-complementary DNA (P-fc; dash-dotted line) and Ni-DNA (solid line). (Inset) CV of the bare gold electrode.

After  $\text{Ni}^{2+}$  doping, the CV curve of the Ni-ssDNA was almost the same as it was for the native form (Fig. 2 A), whereas the oxidation peak of the redox probe was observed in the Ni-DNA (Fig. 2 B). Therefore, the charges can be transferred between the redox probes and the gold electrode through the Ni-DNA. Although the ssDNA and DNA molecules were incubated in the same  $\text{Ni}^{2+}$  solution (pH 9.0), and the nickel ions might bind to the phosphate backbone (38) or the nucleotide bases of the ssDNA, there was no charge transport via Ni-ssDNA (Fig. 2 A). The only reason for this is that the nickel ions were inserted into the DNA duplex with well-stacked basepairs, and DNA conductivity was enhanced (Fig. 2 B) (10,18,20). Meanwhile, there may be few physically absorbed Ni ions at the phosphate backbone of the DNA (38); their binding affinities are weak and do not affect the electron transport and thus can be ignored.

The insertion of nickel ions, therefore, acts as a bridge to facilitate the transportation of charge through the ordered  $\pi$ -electron system of basepair stacking (39) and dominates the conduction behavior of Ni-DNA. On the basis of the red shift of UV absorption spectra, we think that the incorporation of metal ions may result in a reduction of the original DNA band gap and also an increase in the overlap between the  $\pi$  states of the bases (14). These results indicate

that the incorporation of nickel ions converts double-stranded DNA into a conducting wire through the improvement in charge transport via the  $\pi$ - $\pi$  stacking corridor.

Moreover, after the SAM is formed, its structure may prevent  $\text{Ni}^{2+}$  release from Ni-DNA; hence, there are fewer  $\text{Ni}^{2+}$  ions in the solution. The Berliner Blue complex ( $\text{Ni}_3(\text{Fe}(\text{CN})_6)_2$ ) may be formed, but the relative amount is extremely small and can be neglected. The complex has very low solubility ( $K_{sp} = 1.3 \times 10^{-15}$ ) (40), and even a small amount may precipitate at the bottom of the reaction chamber. However, the proposed blue precipitate was not observed in our study. Moreover, the gold electrode is placed at the top of the reaction chamber and made to face the bottom of the tube. Therefore, formation of the Berliner Blue complex may not affect our detection.

### Electron tunneling through the discontinuity of the $\text{Ni}^{2+}$ -mediated $\pi$ - $\pi$ stacking corridor

To further confirm the conducting mechanism, electric behavior of Ni-DNA was investigated after introducing basepair mismatches to avoid nickel ion chelating and create obstacles in the path of the  $\pi$ - $\pi$  stacking corridor. The charge transfer resistance of Ni-DNA was inspected by EIS, and the electrical behavior of the DNA SAMs on a gold surface was fitted by a modified Randles equivalent circuit (Fig. 3, inset) (10,20,24). The EIS of both fully complementary Ni-DNA and the mismatched sequences (R-AC, R-2AC, or R-3AC) were well simulated by the modified Randles equivalent circuit (Fig. 3). Therefore, all electrical parameters of the DNA-modified gold electrodes were extracted from the impedance spectrum results and were based on this model. The calculated conducting resistance ( $R$ ) of the Ni-DNAs was 0.93, 1.40, 2.66, and 5.34 M $\Omega$  for fully complementary, single A-C mismatches, two A-C mismatches, and three A-C mismatches, respectively. In other words, the resistance of Ni-DNA increased when the

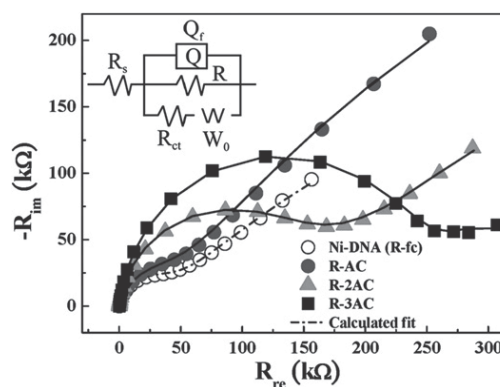


FIGURE 3 EIS of Ni-DNA (R-fc) and its mismatch derivatives R-AC, R-2AC, and R-3AC. (Inset) Modified Randles equivalent circuit. All sequences are shown in Table 1. Open circles denote Ni-DNA (R-fc); solid circles denote Ni-DNA (R-AC); solid triangles denote Ni-DNA (R-2AC), and solid squares denote Ni-DNA (R-3AC). Lines denote the fitting results.

number of successive mismatched basepairs increased. This confirms our findings that the charge transfer in Ni-DNA goes through the Ni<sup>2+</sup>-mediated  $\pi$ - $\pi$  stacking corridor. If a basepair mismatch occurs in a DNA sequence, the mismatched site may cause distortion of the  $\pi$ -stack (41,42) and serve as a potential barrier for charge transport (Fig. 4 A). When  $\Phi$  was defined as the barrier height for the A-C mismatch and the barrier width ( $d$ ) was estimated as 6.8 Å, 10.2 Å, and 13.6 Å for one A-C, two A-C, and three A-C mismatches, respectively, from an x-ray structure (43), the resistance of the mismatched Ni-DNA increased exponentially with respect to the barrier width (Fig. 4 B).

Previous theoretical studies indicate that electrons are transported within the native DNA, and molecular calculation studies generally accept that DNA conductivity can be explained by the tunneling model (44,45). We mentioned in our study that charge transfer in Ni-DNA occurs through the Ni<sup>2+</sup>-mediated  $\pi$ - $\pi$  stacking corridor and a basepair mismatch in the DNA sequence; the mismatched site may cause distortion of the  $\pi$ -stack (41,42) and result in a gap serving as a potential barrier for charge transport (Fig. 4 A). Hence, the resistance change in a single-basepair mismatch can be revealed by the tunneling model. The detailed mechanism derived is shown below.

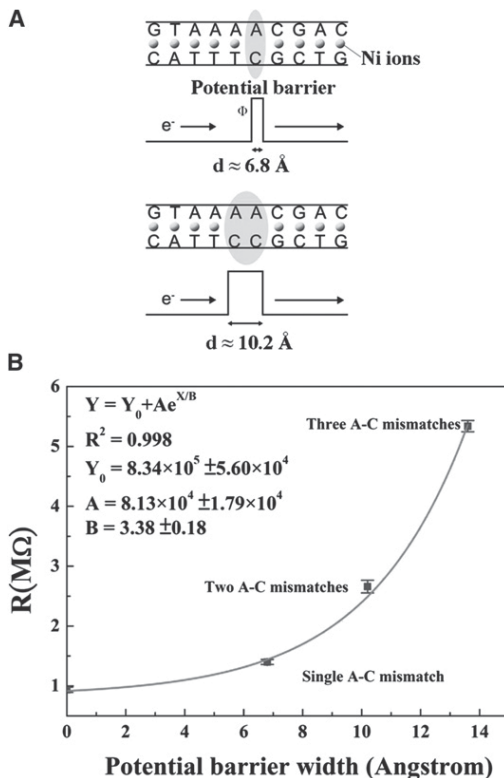


FIGURE 4 (A) A schematic illustration of the mismatch-induced potential barrier in Ni-DNA. (The spheres represent Ni ions.) (B) Charge transport resistances of Ni-DNA increase exponentially with the width of the barrier induced by basepair mismatches. Numbers after the  $\pm$  sign are standard deviations ( $N = 3$ ).

Based on Simmons electric tunnel effect model (46,47), when two conducting electrodes (Ni<sup>2+</sup> chelating in the basepairs of DNA) are separated by a sufficiently thin gap (the span between basepairs of DNA), current can flow between the two electrodes by means of the electric tunneling effect. Meanwhile, the potential barriers in tunnel junctions, current density  $j$ , and voltage in a tunnel junction can be presented as

$$j = j_0 \left\{ \Phi \exp(-A\Phi^{1/2}) - (\Phi + eV) \exp[-A(\Phi + eV)^{1/2}] \right\}, \quad (2)$$

where  $\Phi$  denotes the mean value of the potential barrier in tunnel junctions,  $V$  denotes the voltage across the gap,

$$j_0 = [e/(2\pi h)] \bullet [1/(c\Delta d)^2], \quad (3)$$

$$A = [(4\pi c\Delta d)/h](2m)^{1/2}, \quad (4)$$

and

$$c = 1 - [1/(8\Phi^2\Delta d)] \int_{d_1}^{d_2} [\varphi(x) - \Phi]^2 dx; \quad (5)$$

$m$  is the mass of the electron,  $h$  is Planck's constant, and  $\Delta d$  is the distance between two barrier limits at the Fermi level.

In this study,  $V$  across the gap is relatively small. Therefore, Eq. 2 reduces to

$$j = j_L \Phi^{1/2} V \exp(-A\Phi^{1/2}) \quad (6)$$

where  $j_L = (2m^{1/2}/\Delta d)(e/h)^2$ ,  $\Phi = (\varphi_1 + \varphi_2)/2$ , and  $\Delta d = d$ .  $\varphi_1$  and  $\varphi_2$  are the barrier heights at the interfaces between electrodes 1 and 2, respectively, and the insulator (the vacancy in the empty gap between basepairs of DNA; and  $d$  is the gap between the nickel ions (electrodes) at either side of the mismatched basepairs of DNA.

Therefore,

$$j = (e^2/dh^2)[2m\Phi]^{1/2} V \exp[-(4\pi d/h)(m\Phi)^{1/2}]. \quad (7)$$

In Eq. 7, it is assumed that  $m$ ,  $\varphi_1$ , and  $\varphi_2$  in both electrodes are constants and independent of energy. Therefore, the current density,  $j$ , is a linear function of  $V$ . The resistance,  $R$ , is Ohmic. According to Ohm's law, for a constant voltage  $V$ ,  $R$  can be expressed as

$$\begin{aligned} R &\propto j^{-1} \\ R &\propto \exp(\beta d) \end{aligned} \quad (8)$$

where  $\beta$  denotes the constant  $(4\pi/h)(2m\Phi)^{1/2}$ .

Therefore, when the basepair mismatch increases, the distance  $d$  increases linearly, and consequently, the resistance of Ni-chelating DNA increases exponentially. This result is consistent with the Simmons model and our derivation. Therefore, we may assume that the electric passage through the vacant space of DNA follows the tunneling model.

Moreover, this tunneling mechanism also indicates that the gap between each two nickel ions in the space between basepairs of DNA is small and will be constant. Nickel ions will bind to all binding sites in Ni-DNA, the basepairs of which are shown in Fig. 4 A. On the other hand, if the nickel ions chelate randomly with a lot of vacancy,  $d$  of Ni-DNA varies, and the resistance fluctuates significantly. However, this phenomenon was not observed in our study. Therefore, we assume that each basepair chelated one nickel ion in Ni-DNA. This is consistent with our experiment mentioned previously (35).

The fitting results are shown by a solid line in Fig. 4 B. The  $\beta$  value was  $\sim 0.30 \text{ \AA}^{-1}$ , which is consistent with the findings for the  $\pi$ -stack-mediated charge transfer in native DNA (44,46). These results also suggest that the sensitivity of Ni-DNA-mediated charge transfer relies on the stacking and basepair stability within the DNA helix.

### Identification of G-T and G-A mismatches by Ni-doped DNA

According to the conducting mechanism of Ni-DNA, it is possible to use Ni-DNA as a biosensor to detect mismatches. For example, conventional DNA/DNA hybridization approaches do not facilitate easy detection of a single G-A or G-T mismatch, because DNA with a single basepair mismatch has high thermodynamic stability (45,48). However, such a mismatch can be readily identified in Ni-DNA by EIS analysis (Fig. 5). The calculated resistances ( $R_{\text{GA}}$  and  $R_{\text{GT}}$ ) of the single G-A and G-T mismatched Ni-DNA ( $2.07 \pm 0.06 \text{ M}\Omega$  and  $1.60 \pm 0.07 \text{ M}\Omega$ , respectively) were both higher than those of a fully complementary sequence ( $R_{\text{fc}}$ ;  $0.94 \pm 0.04 \text{ M}\Omega$ ). It is interesting to note that a G-T mismatch had less effect on conductivity than a G-A mismatch. It is known that an A-C (49) or G-T (50) mismatch can form a stable Wobble basepairing in nature, causing little conformational change in the backbone of its DNA, yet allowing intercalation of  $\text{Ni}^{2+}$  into this basepair structure. With intercalated  $\text{Ni}^{2+}$ , the electronic

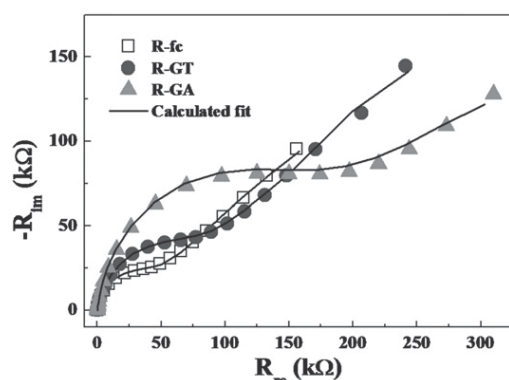


FIGURE 5 EIS of Ni-DNA ( $R_{\text{fc}}$ ) and its mismatch derivatives  $R_{\text{GT}}$  and  $R_{\text{GA}}$ . Open squares, solid circles, and solid triangles represent  $R_{\text{fc}}$ ,  $R_{\text{GT}}$ , and  $R_{\text{GA}}$ , respectively. Lines denote the fitting results.

structure of the DNA base-stacking is rather subtly perturbed. This perturbation may result in a barrier for DNA-mediated charge transport, which requires a higher energy to overcome, as indicated by the increase in charge transfer resistance. For a homopurine G-A mismatch, carbonyl-amino, amino-amino, and/or amino-carbonyl basepairs may be formed (51); the backbone and basepair stacking may be greatly distorted from their native conformation. This distortion not only changes the distance between the flanking nickel ions in the DNA but also blocks the  $\pi$ - $\pi$  interactions between the basepairs. Thus, the electrochemical DNA sensors for detecting mismatches based on Ni-DNA-mediated charge transport are sensitive to the electronics of the  $\pi$ -stack.

### SUMMARY

In this study, UV absorption spectra of Ni-immersed ssDNA and dsDNA confirmed that nickel ions can bind to T and G bases of DNA. Moreover, CV results indicate that the  $\text{Ni}^{2+}$ -mediated  $\pi$ - $\pi$  stacking corridor provides a path for electron transport in Ni-DNA, and the EIS data also demonstrate that the resistance of Ni-DNA increases when basepair mismatches exist in DNA, forming an obstacle in the conducting channel; this increased resistance can be explained by the quantum-mechanical tunneling effect using the Simmons model. Therefore, the conducting mechanism of metalized DNA is via the  $\text{Ni}^{2+}$ -mediated  $\pi$ - $\pi$  stacking corridor. We surmise that the native DNA may also follow a similar mechanism. This mechanism helps us to design a simple scheme to detect a single basepair mismatch of G-A or G-T, as well. In this way, it will be possible to diagnose some mutation hot spots in specific genes.

We thank Dr. P. C. Huang and Dr. L. S. Kan for their valuable suggestions and discussion. Technical support was provided by the National Nano Device Laboratory of the National Science Council and the Nano Facility Center of National Chiao Tung University.

This project was supported in part by a National Science Council grant (97-2112-M-009-009-YM3) and the ATU-MOE Project, Taiwan, Republic of China.

### REFERENCES

1. Aviram, A., and M. A. Ratner. 1974. Molecular rectifiers. *Chem. Phys. Lett.* 29:277–283.
2. Mirkin, C. A., R. L. Letsinger, ..., J. J. Storhoff. 1996. A DNA-based method for rationally assembling nanoparticles into macroscopic materials. *Nature.* 382:607–609.
3. Hwang, J. S., S. W. Hwang, and D. Ahn. 2003. Electrical conduction measurement of thiol modified DNA molecules. *Superlattices Microstruct.* 34:433–438.
4. Cuniberti, G., L. Craco, ..., C. Dekker. 2002. Backbone-induced semi-conducting behavior in short DNA wires. *Phys. Rev. B.* 65:241314.
5. de Pablo, P. J., F. Moreno-Herrero, ..., E. Artacho. 2000. Absence of dc-conductivity in  $\lambda$ -DNA. *Phys. Rev. Lett.* 85:4992–4995.
6. Fink, H.-W., and C. Schönberger. 1999. Electrical conduction through DNA molecules. *Nature.* 398:407–410.

7. Hwang, J. S., K. J. Kong, ..., S. W. Hwang. 2002. Electrical transport through 60 base pairs of poly(dG)-poly(dC) DNA molecules. *Appl. Phys. Lett.* 81:1134–1136.
8. Jangjian, P.-C., T. Liu, ..., C.-C. Chang. 2009. Room temperature negative differential resistance in DNA-based molecular devices. *Appl. Phys. Lett.* 94:043105.
9. Jangjian, P.-C., T.-F. Liu, ..., C.-C. Chang. 2009. DNA mismatch detection by metal ion enhanced impedance analysis. *Chin. J. Phys.* 47:740–747.
10. Jangjian, P.-C., T.-F. Liu, ..., C.-C. Chang. 2008. Ni<sup>2+</sup> doping DNA: a semiconducting biopolymer. *Nanotechnology.* 19:355703.
11. Lee, J. S., L. J. P. Latimer, and R. S. Reid. 1993. A cooperative conformational change in duplex DNA induced by Zn<sup>2+</sup> and other divalent metal ions. *Biochem. Cell Biol.* 71:162–168.
12. Li, X.-Q., and Y. Yan. 2001. Electrical transport through individual DNA molecules. *Appl. Phys. Lett.* 79:2190–2192.
13. Yoo, K. H., D. H. Ha, ..., H. Y. Choi. 2001. Electrical conduction through poly(dA)-poly(dT) and poly(dG)-poly(dC) DNA molecules. *Phys. Rev. Lett.* 87:198102.
14. Alexandre, S. S., J. M. Soler, ..., F. Zamora. 2006. Geometry and electronic structure of M-DNA (M = Zn<sup>2+</sup>, Co<sup>2+</sup>, and Fe<sup>2+</sup>). *Phys. Rev. B Condens. Matter.* 73:205112–205115.
15. Lee, T. Y., and Y. B. Shim. 2001. Direct DNA hybridization detection based on the oligonucleotide-functionalized conductive polymer. *Anal. Chem.* 73:5629–5632.
16. Rakitin, A., P. Aich, ..., J. M. Xu. 2001. Metallic conduction through engineered DNA: DNA nanoelectronic building blocks. *Phys. Rev. Lett.* 86:3670–3673.
17. Wood, D. O., M. J. Dinsmore, ..., J. S. Lee. 2002. M-DNA is stabilised in G\*<sub>C</sub> tracts or by incorporation of 5-fluorouracil. *Nucleic Acids Res.* 30:2244–2250.
18. Li, C. Z., Y. T. Long, ..., J. S. Lee. 2003. Electrochemical investigations of M-DNA self-assembled monolayers on gold electrodes. *J. Phys. Chem. B.* 107:2291–2296.
19. Güllü, Ö., M. Çankaya, ..., A. Türüt. 2008. DNA-based organic-on-inorganic semiconductor Schottky structures. *Appl. Surf. Sci.* 254:5175–5180.
20. Long, Y.-T., C.-Z. Li, ..., J. S. Lee. 2003. AC impedance spectroscopy of native DNA and M-DNA. *Biophys. J.* 84:3218–3225.
21. Chidsey, C. E. D. 1991. Free energy and temperature dependence of electron transfer at the metal-electrolyte interface. *Science.* 251:919–922.
22. Finklea, H. O., D. A. Snider, ..., I. Rubinstein. 1993. Characterization of octadecanethiol-coated gold electrodes as microarray electrodes by cyclic voltammetry and AC impedance spectroscopy. *Langmuir.* 9:3660–3667.
23. Ito, T., K. Hosokawa, and M. Maeda. 2007. Detection of single-base mismatch at distal end of DNA duplex by electrochemical impedance spectroscopy. *Biosens. Bioelectron.* 22:1816–1819.
24. Janek, R. P., W. R. Fawcett, and A. Ulman. 1998. Impedance spectroscopy of self-assembled monolayers on Au<sup>111</sup>: sodium ferrocyanide charge transfer at modified electrodes. *Langmuir.* 14:3011–3018.
25. Miller, C., P. Cuendet, and M. Graetzel. 1991. Adsorbed. omega-hydroxy thiol monolayers on gold electrodes: evidence for electron tunneling to redox species in solution. *J. Phys. Chem.* 95:877–886.
26. Steichen, M., Y. Decrem, ..., C. Buess-Herman. 2007. Electrochemical DNA hybridization detection using peptide nucleic acids and [Ru(NH<sub>3</sub>)<sub>6</sub>]<sup>3+</sup> on gold electrodes. *Biosens. Bioelectron.* 22:2237–2243.
27. Chi, Q. J., J. Zhang, and J. Ulstrup. 2006. Surface microscopic structure and electrochemical rectification of a branched alkanethiol self-assembled monolayer. *J. Phys. Chem. B.* 110:1102–1106.
28. Kelley, S. O., E. M. Boon, ..., M. G. Hill. 1999. Single-base mismatch detection based on charge transduction through DNA. *Nucleic Acids Res.* 27:4830–4837.
29. Desikan, R., S. Armel, ..., T. Thundat. 2007. Effect of chain length on nanomechanics of alkanethiol self-assembly. *Nanotechnology.* 18:424028.
30. Randles, J. E. B. 1947. Kinetics of rapid electrode reactions. *Discuss. Faraday Soc.* 1:11–19.
31. Akkerman, H. B., R. C. G. Naber, ..., B. de Boer. 2007. Electron tunneling through alkanedithiol self-assembled monolayers in large-area molecular junctions. *Proc. Natl. Acad. Sci. USA.* 104:11161–11166.
32. Kang, J., L. Zhuo, ..., X. Wang. 2005. Electrochemical behavior of dopamine at a quercetin-SAM-modified gold electrode and analytical application. *J. Solid State Electrochem.* 9:114–120.
33. Becker, W. M., L. J. Kleinsmith, and J. Hardin. 2006. *The World of the Cell.* Benjamin Cummings, San Francisco.
34. Aich, P., S. L. Labiuk, ..., J. S. Lee. 1999. M-DNA: A complex between divalent metal ions and DNA which behaves as a molecular wire. *J. Mol. Biol.* 294:477–485.
35. Peterson, A. W., R. J. Heaton, and R. M. Georgiadis. 2001. The effect of surface probe density on DNA hybridization. *Nucleic Acids Res.* 29:5163–5168.
36. Buttry, D. A., and M. D. Ward. 1992. Measurement of interfacial processes at electrode surfaces with the electrochemical quartz crystal microbalance. *Chem. Rev.* 92:1355–1379.
37. Yang, M., H. C. M. Yau, and H. L. Chan. 1998. Adsorption kinetics and ligand-binding properties of thiol-modified double-stranded DNA on a gold surface. *Langmuir.* 14:6121–6129.
38. Duguid, J. G., V. A. Bloomfield, ..., G. J. Thomas, Jr. 1995. Raman spectroscopy of DNA-metal complexes. II. The thermal denaturation of DNA in the presence of Sr<sup>2+</sup>, Ba<sup>2+</sup>, Mg<sup>2+</sup>, Ca<sup>2+</sup>, Mn<sup>2+</sup>, Co<sup>2+</sup>, Ni<sup>2+</sup>, and Cd<sup>2+</sup>. *Biophys. J.* 69:2623–2641.
39. Liu, T., and J. K. Barton. 2005. DNA electrochemistry through the base pairs not the sugar-phosphate backbone. *J. Am. Chem. Soc.* 127:10160–10161.
40. Juszczyk, S., C. Johansson, ..., G. Malecki. 1994. Ferromagnetism of the Me<sub>3</sub>[Fe(CN)<sub>6</sub>]<sub>2</sub>·H<sub>2</sub>O compounds, where Me=Ni and Co. *J. Phys. Condens. Matter.* 6:5697–5706.
41. Drummond, T. G., M. G. Hill, and J. K. Barton. 2003. Electrochemical DNA sensors. *Nat. Biotechnol.* 21:1192–1199.
42. Roy, S., H. Vedala, ..., W. Choi. 2008. Direct electrical measurements on single-molecule genomic DNA using single-walled carbon nanotubes. *Nano Lett.* 8:26–30.
43. Watson, J. D., and F. H. C. Crick. 1953. Molecular structure of nucleic acids; a structure for deoxyribose nucleic acid. *Nature.* 171:737–738.
44. Kelley, S. O., R. E. Holmlin, ..., J. K. Barton. 1997. Photoinduced electron transfer in ethidium-modified DNA duplexes: dependence on distance and base stacking. *J. Am. Chem. Soc.* 119:9861–9870.
45. Abad-Valle, P., M. T. Fernández-Abedul, and A. Costa-García. 2007. DNA single-base mismatch study with an electrochemical enzymatic genosensor. *Biosens. Bioelectron.* 22:1642–1650.
46. Kelley, S. O., and J. K. Barton. 1999. Electron transfer between bases in double helical DNA. *Science.* 283:375–381.
47. Simmons, J. G. 1963. Electric tunnel effect between dissimilar electrodes separated by a thin insulating film. *J. Appl. Phys.* 34:2581–2590.
48. Brown, T., W. N. Hunter, ..., O. Kennard. 1986. Molecular structure of the GA base pair in DNA and its implications for the mechanism of transversion mutations. *Proc. Natl. Acad. Sci. USA.* 83:2402–2406.
49. Gao, X. L., and D. J. Patel. 1987. NMR studies of A.C mismatches in DNA dodecanucleotides at acidic pH. Wobble A(anti).C(anti) pair formation. *J. Biol. Chem.* 262:16973–16984.
50. Allawi, H. T., and J. SantaLucia, Jr. 1998. NMR solution structure of a DNA dodecamer containing single G.T mismatches. *Nucleic Acids Res.* 26:4925–4934.
51. Greene, K. L., R. L. Jones, ..., W. D. Wilson. 1994. Solution structure of a GA mismatch DNA sequence, d(CCATGAATGG)<sub>2</sub>, determined by 2D NMR and structural refinement methods. *Biochemistry.* 33:1053–1062.